Dissertation

submitted to the

Combined Faculties for the Natural Sciences and for Mathematics

of the Ruperto-Carola University of Heidelberg, Germany

for the degree of

Doctor of Natural Sciences

Put forward by Dipl. Phys. Stefan Schmitt

Born in Heidelberg, Germany

Date of oral examination: 03. February 2016

The Dynamics of Reactive Halogen Species at the Dead Sea Valley

Abstract

Reactive halogen species (RHS) have a significant impact on the chemical composition of the atmosphere. With its high halite abundance and unique topography the Dead Sea Valley (DSV) is predestined for the investigation of RHS. In the frame work of this thesis, two extensive measurement campaigns were carried out at the DSV in May 2012 and November 2014. The comparison of MAX-DOAS and LP-DOAS data with meteorological measurements indicates strong impact of transport process on the observed trace gas dynamics. The strong depletion of NO_2 mixing ratios during daytime coincides with increased RHS abundance and suggests the formation of halogenated nitrate compounds. These are assumed to enhance the release of RHS from aerosol surfaces by heterogeneous processes. Elevated, confined layers of BrO of up to 50 pptv suggest the release of reactive bromine compounds from aerosol surfaces. The correlation of IO with surface waves indicates abiotic iodine release as a result of increased gas exchange at the water surface. For the first time, gaseous molecular iodine (up to 70 pptv) was detected at the DSV serving as a precursor for reactive iodine. Further, first direct evidence for reactive chlorine chemistry at the DSV was found by the detection of OClO at mixing ratios of up to 6 pptv.

Zusammfassung

Reaktive Halogenverbindungen (RHV) haben einen starken Einfluss auf die chemische Zusammensetzung der Atmosphäre. Durch das erhöhte Vorkommen an Halogeniden und die einzigartige Topographie ist das Tote Meer (TM) ein idealer Ort zur Erforschung von RHV. Im Rahmen dieser Arbeit wurden zwei intensive Messkampagnen am TM durchgeführt. Der Vergleich von MAX-DOAS und LP-DOAS mit meteorologischen Messungen zeigt einen starken Einfluss von Transportprozessen auf die beobachtete Spurenstoffdynamik. Die starke Abnahme von NO_2 während des Tages, bei gleichzeitig erhöhten Vorkommen von RHV, weist auf die Bildung von halogenierten Stickstoffverbindungen hin. Diese können die Freisetzung von RHV an Aerosoloberflächen verstärken. Erhöhte, abgehobene Schichten von BrO mit bis zu 50 pptv deuten auf die Freisetzung von reaktiven Bromverbindungen an Aerosoloberflächen hin. Die Korrelation von IO mit Wellen deutet auf eine abiotische Jodfreisetzung als Folge von erhöhtem Gasauschtausch an der Wasseroberfläche hin. Zum ersten mal konnte molekulares Jod (bis zu 70 pptv) in der Gasphase am TM nachgewiesen werden und als Vorläufer für reaktives Jod identifiziert werden. Weiter, konnte durch den Nachweis von OClO mit bis zu 6 pptv erstmals die reaktive Chlorchemie am TM beobachtet werden.

To my wife Hanna and my son Johann

Contents

Parts of this work have already been published in Holla et al. [2015]. For the sake on consistency, the published data from 2012 has been reanalyzed to be comparable to the data which was acquired in 2014 within the framework of this thesis.

1

Motivation

Despite being the place with lowest continental elevation on earth, the Dead Sea Valley provides a joint connection between a variety of geological sciences. Geologists investigate the tectonics which causes local earth quakes and sinkholes in the coastal region of the lake. The tectonic activity is also assumed to influence the intake of ground water into the Dead Sea as well as the formation of groundwater springs below the water surface, which leads to a potential influence on the water composition.

The air in the Dead Sea Valley is known for its curing effect on respiratory diseases, while the chemical composition of the brine and mud at the coastlines is used to treat skin diseases and arthritis. Further, the unique altitude of 420 m below mean sea level leads to a reduced amount of ultra violet radiation during daytime. Further, the increased oxygen amount due to high pressure have been identified to be beneficial for medical purposes.

Reactive halogen species play an important role in atmospheric chemistry. Due to their high reactivity and the ability to take part in auto catalytic reactions, already small amounts of RHS can have a large impact on the chemical dynamics and the resulting chemical composition of the atmosphere. Atomic bromine, e.g. formed by the fast photolysis of molecular bromine (Br_2) during day time, can react with ozone forming bromine monoxide (BrO). BrO has the ability to undergo a self reaction forming again the photolytic unstable Br_2. Thus, this cycle can transform larger amounts of ozone (two to three orders of magnitude larger than the BrO amount) into oxygen barely without the dissipation of BrO.

This so called ozone depletion events (ODEs) in the presence of BrO have already been observed at polar regions (Simpson et al. [2007], Pöhler et al. [2010] and Liao et al. [2011]) as well as at the Dead Sea (Hebestreit et al. [1999], Tas et al. [2006]).

Further, halogen oxides like BrO or IO can react with nitrogen dioxide (NO_2), which is mostly attributed to biomass burning, industrial emissions and automotive traffic, forming halogenated nitrate compounds $BrONO_2$, $IONO_2$. These compounds can be taken up by aerosols followed by the release of additional amounts of RHS. With a strong anthropogenic influence leading to enhanced emissions of pollutants, NO_2 potentially plays a major role for the RHS chemistry at the Dead Sea. The southern part of the Dead Sea consists of industrial evaporation ponds which are used by the Israeli Dead Sea Works and the Jordanian Arab Potash Company to extract minerals from the brine. This makes the Dead Sea an unique place to investigate the impact of nitrogen oxides on the halogen chemistry.

In the past several measurements focused on the gas phase chemistry of Bromine were carried out and revealed volume mixing ratios of up to 150 pptv (volume mixing ratios, parts per trillion, 10^{-12})(Tas et al. [2006], Hebestreit et al. [1999]) which is factor of 80 higher compared to the marine BrO background (Lampel [2014]). However the release mechanisms and source characteristics are still unclear. Recent studies by Holla et al. [2015] showed that the largest abundance of BrO is found in so called elevated layers which are confined in terms of altitude and located a few hundred meters above the ground level of the valley. This implies that the emission of the high reactive, short-lived trace gas BrO, can not solely be attributed to the water surface or saline soil at the bottom of the Dead Sea Valley, but more likely to heterogeneous processes on aerosols or other, more stable precursors which allow transportation in higher altitudes.

Iodine monoxide (IO) was solely observed by Zingler and Platt [2005] during measurements over the evaporation ponds at amounts of 6 pptv, which is a factor of ten larger compared to the marine background (Lampel [2014]). Since, organisms are sparse in the Dead Sea brine, biogenic release of iodine (like ob-

served over macro algaes at the Irish coast, Ball et al. [2010], Horbanski [2015])
can be ruled out and is most likely attributed to inorganic release, which is also
worthwhile to investigate. Evidence for reactive chlorine chemistry at the Dead
Sea were not found to date. However, it is likely to play a role in the processes
involving RHS at the Dead Sea.

The main goal of this thesis is to investigate the dynamics of reactive halogen
species with respect to heterogeneous chemistry and local meteorology to gain
more knowledge about the sources and source signatures. Two extensive field
campaign were carried out at the Dead Sea Valley in May 2012 and November
2014. Several instruments based on the Differential Optical Absorption Spec-
troscopy (DOAS) were deployed to measure a variety of trace gases simulta-
neously at a time resolution of minutes. DOAS is a remote sensing technique,
which provides a contact-free measurement of trace gas mixing ratios with a sen-
sitivity down to the pptv range. Especially for highly reactive halogen species,
the contact-free measurement is crucial. Multi-Axis(MAX)-DOAS instruments
were deployed to retrieve vertical distributions of trace gases inside the valley by
using scattered sunlight measured under different elevation angles. Thus, mete-
orological driven transportation and the investigation of RHS release processes
in elevated altitudes can be observed. A Long Path(LP)-DOAS instrument, was
set up at the evaporation ponds in Ein Bokek with an absorption path entirely
over the water surface. In combination with the MAX-DOAS instruments, the
LP-DOAS data gives insight about the trace gas gradients near the water surface
and, hence, the emission potential of the brine with respect to reactive halogen
species.

With its high abundance of gaseous reactive halogen species, the Dead Sea Val-
ley is predestined to investigate chemical processes with sufficient accuracy and
time resolution. Further, the abundance of NO_2 and aerosols provides a potential
setting for heterogeneous RHS chemistry. The topography of the valley leads to
transport processes of air masses which provide an additional source of informa-
tion concerning the possible sources of RHS (precursors, aerosols or the water
surface itself). If monitored, the variety of parameters provides an exceptional
data set which can serve for upcoming model studies and can be transferred to

other regions, where the observation of RHS abundance is instrumentally limited (e.g. open ocean, polar regions, stratosphere).

The investigation of the gas phase chemistry above the Dead Sea lake will not only be beneficial for atmospheric scientists but also for in the role of halides in water and soils. Further, it may provide additional information for physicians supporting the knowledge about the curing effect of respiratory diseases by the Dead Sea's atmosphere.

Outline of the thesis

This thesis is separated in four main parts. Part I provides fundamental information about the topography, meteorology, water composition and halogen chemistry at the Dead Sea Valley. Part II describes the methods of data acquisition and analysis used in this thesis. The results from field studies are presented in Part III. In Part IV, the results are discussed and the conclusion is drawn.

Part I

Fundamentals

2

The Dead Sea Valley

2.1 Topography

The Dead Sea Valley is situated 30 km east of Jerusalem within the rift zone between the African and the Arabic plate. A topographic profile is given in figure 2.1. The lake at the bottom of the valley has a west to east width of approximately 20 km and a length of 90 km in north-south direction and is divided in two parts. The northern part, marked in blue in the profile maps, is the natural basin with an water surface altitude of 415 m below sea level.

The southern part (marked in cyan in the map) consists of artificial evaporation ponds, which are run by the Israeli Dead Sea Works company and the Jordanian Arab Potash company to harvest minerals from the brine to produce fertilizers. The water surface level of the southern ponds is 20 m above the water surface of the northern, natural Dead Sea basin. Pump stations located on the southern end of the northern basin continuously transport water into the southern basins. The evaporation leads to an over saturation of the brine and to precipitation of minerals which are harvested by dredgers. The dam between the eastern and western evaporation ponds has a width of about 500 m and represents the border between Israel and Jordan. Vehicles are regular passing the dam to patrol the evaporation ponds or to transport materials to the large construction site. The construction site was located at the northern end of the evaporation ponds near Ein Bokek during the measurements which were performed in May 2012 and are presented in this thesis. It will be shown later, that the emissions from

the construction sites (mainly nitrogen dioxide, NO_2) has a large potential to influence the chemistry of reactive halogens species at the Dead Sea.
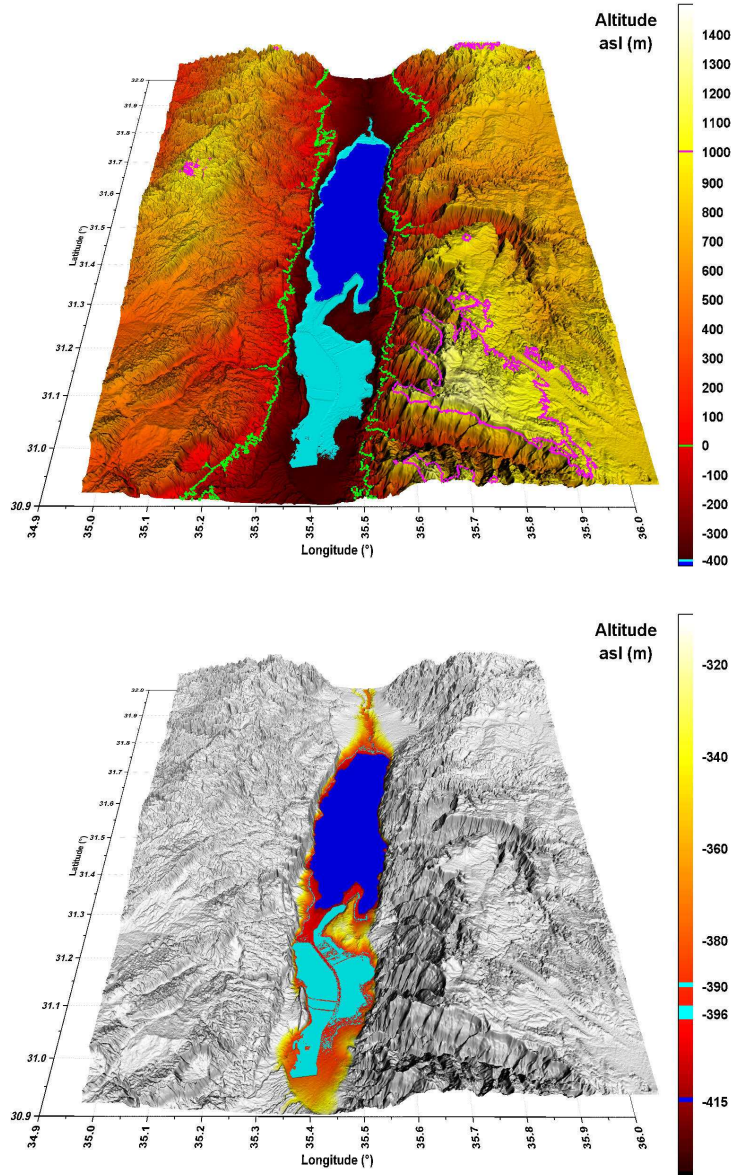
Fig. 2.1: Topographic map of the area around the DOAS instruments at Masada and Ein Bokek. The green line represents sea level altitude while the purple line represents the upper rim of the valley at 1 km on Jordanian side. The lower plot illustrates small scale height differences inside the valley. Data adapted from Shuttle Radar Topographic Mission (SRTM), Jarvis et al. [2008].

Apart from groundwater runoff and precipitation, the Jordan river is the only water inlet of the Dead Sea. During the last years, water drainage from the Jordan river for agricultural use has been drastically increased. Apart from that, the Judean Mountains between the Mediterranean Sea and the Dead Sea are causing a rain shadow effect leading to a low precipitation of around 50-100 mm per year. During the last 30 years, the water level of the Dead Sea lowered by 50 m to approximately 415 m below sea level. Current decrease rates are estimated to 1 m per year.

Elevation profiles at latitudes of measurements presented in this thesis are shown in figure 2.2. The valley has slopes of up to 36% steepness (e.g. at Masada). On the Israeli side, the altitude of the upper rim of the valley between 0 and 200 m above sea level. At Jordanian side, the upper rim reaches altitudes of 1000 m and more (indicated also by the magenta elevation line in figure 2.1.
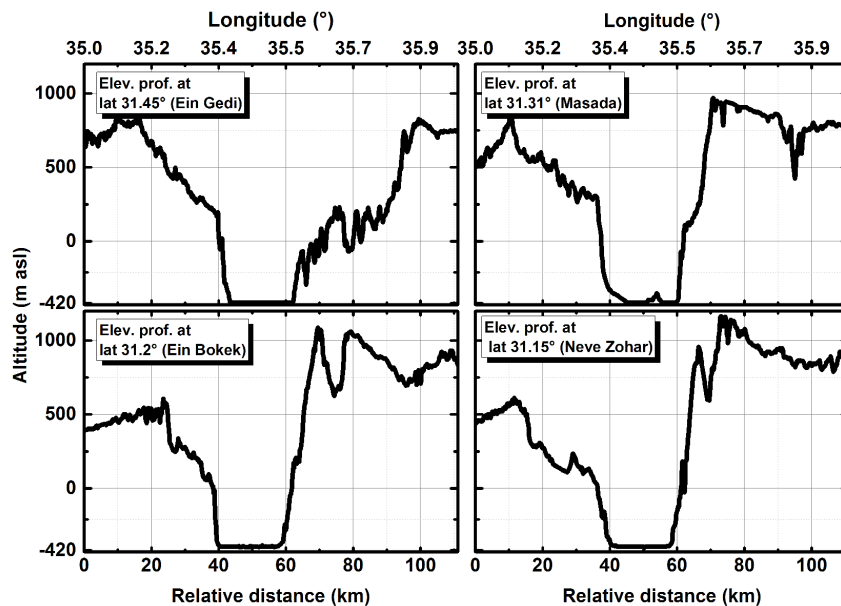
Fig. 2.2: Elevation profiles at Ein Gedi, Masada, Ein Bokek and Neve Zohar (see plot labels). Data adapted from Shuttle Radar Topographic Mission (SRTM), Jarvis et al. [2008].

Segal et al. [1983] investigated the wind system at the Dead Sea by numerical simulations and found out that the topography of the valley often leads to local, small scale wind systems. The temperature difference between the water surface of the lake and the soil at the coastline causes air to rise at the valley slopes with vertical wind speeds of up to 1 m/s (according to Schmitz [2009]). This so called "sea breeze" winds can transport air masses in higher altitudes thus have a strong impact on the horizontal distribution of trace gases and the exchange of air masses between the valley and its surrounding. Further, Segal et al. [1983] showed that the sea breeze can form vertical circulation cells with a convergence zone in the middle of the lake (illustrated in figure 2.3). These cells may confine the air masses of the Dead Sea valley from those of its environment. In the evening, soil temperature decreases due to the lack of solar radiation and the sea breeze collapses. Cold air masses are gravitationally pulled down the valley slopes creating so called catabic winds. Since the catabic winds are formed on both, the western and the eastern slopes, they result in northerly or southerly winds at significantly stronger wind speeds of up to 8 m/s (according to Schmitz [2009]) bottom of the valley.
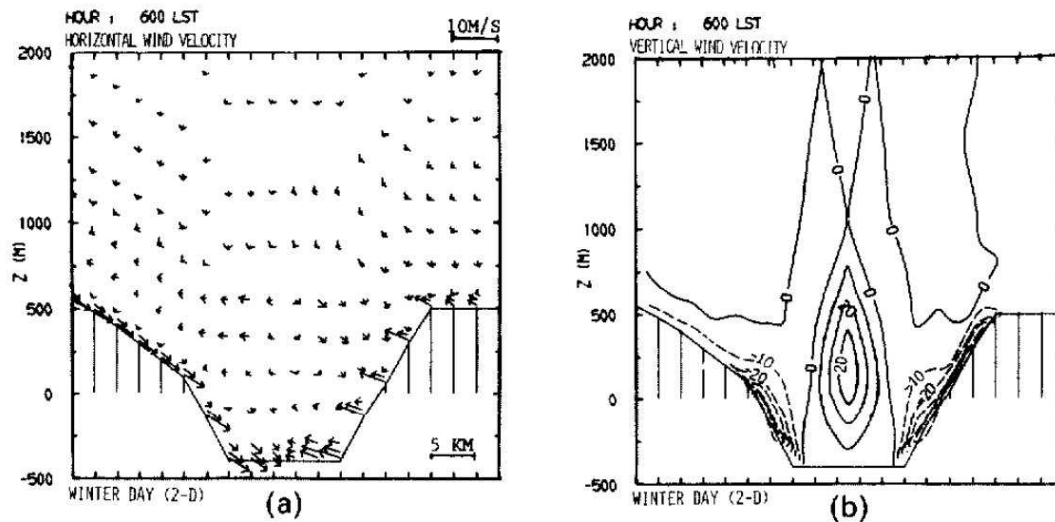
Fig. 2.3: Numerical simulation of the wind field at the Dead Sea Valley by Segal et al. [1983]. **Left:** Horizontal wind vectors. **Right:** Vertical wind speeds in cm/s.

2.2 Water composition

The salinity of the Dead Sea water is about 33%, a factor of ten higher compared to ocean sea water. Further it contains high amounts of magnesium, calcium, bromide and potassium. Lyday [2003] reports a total bromine content of one billion tons dissolved in the brine of the Dead Sea. Israel is currently one of the market leaders in the production of bromine. An extensive description of the chemical composition of the Dead Sea brine can be found in Niemi et al. [1997] and Nissenbaum [1977]. An overview of the their findings is given in table 2.1. In 1997, the Dead Sea reached maximum concentration of NaCl (saturation) as a result to the decreasing freshwater input. After 1977, the NaCl concentration is continuously decreasing due to precipitation of halites to the ground of the lake. Approximately 99% of all anions are chlorine, the rest are mainly bromine anions (Oren [2010]). Niemi et al. [1997] point out the exceptional high bromine amount is most likely caused by precipitation of chloride minerals over a long time period. Further, Oren [2010] report a pH value of 5.8 to 6 which makes the Dead Sea brine acidic.

Species	mg/L in DSW	mg/L in OSW	$\frac{\text{DSW}}{\text{OSW}}$
Br	4600	65	70
Cl	196940	18980	10
I	(*)0.0084	(*)0.006	(*)1.4
Na	38510	10556	3.6
K	6500	380	17
Mg	36150	1272	30 - 33
Ca	16380	400	90
SO_4	580	2649	0.22
HCO_3	230	140	1.6
total dissolved ions	299890	34441	8.7
	mass ratio in DSW	mass ratio in OSW	
1000Br/Cl	23.4	3.4	
Cl/Br	43	294	
Na/Cl	0.3	0.86	
K/Cl	0.03	0.02	
Mg/Cl	0.27	0.1	
Ca/Cl	0.07	0.02	
Ca/Mg	0.27	0.19	

Table 2.1: Chemical composition of the Dead Sea water (DSW) compared to ocean sea water (OSW). Data taken from Niemi et al. [1997]. (*) measured by Nissenbaum [1977].

3

Halogen Chemistry at the Dead Sea Valley

The following section describes the role of halogens in the troposphere with focus on the Dead Sea Valley. Further, heterogeneous processes involving halogen species are discussed, which are assumed to play a major role for the chemical processes at the Dead Sea.

3.1 Bromine

The atmospheric chemistry of reactive bromine is relatively well researched and understood. Several publications report increased amounts of bromine monoxide in polar regions (Frieß et al. [2011], Pöhler et al. [2010], Sihler et al. [2012]) but also at mid-latitudes in volcanic plumes (Hönninger et al. [2004a]Bobrowski et al. [2007]) and at the Dead Sea Valley (Hebestreit [2001], Tas et al. [2006]). The measured BrO concentrations were about a factor of up to 80 higher compared to the marine background of 2 pptv (Lampel [2014]).

Further several observations report increased BrO amounts parallel to rapidly decreasing ozone levels from values of 30 to 40 ppbv down to values close to zero. These so called ozone depletion events (ODE) could be addressed to an auto catalytic process of BrO which can transforms large amounts of ozone in to oxygen (Hausmann and Platt [1994], Tuckermann et al. [1997]). ODEs represent the strong relevance of reactive bromine species for the atmosphere because

already small amounts of several pptv BrO can lead to a depletion of several ppbv of ozone. The following reactions describe the ODE mechanism:

Atomic bromine can react with ozone forming BrO and oxygen. However BrO is quickly photolyized within the order of minutes which leads again to the formation of ozone via reaction 3.3 leaving reaction 3.1 to 3.3 a null cycle in terms of ozone depletion.

$$Br + O_3 \longrightarrow BrO + O_2 \tag{3.1}$$

$$BrO \xrightarrow{h\nu} Br + O \tag{3.2}$$

$$O + O_2 \longrightarrow Br + O_3 \tag{3.3}$$

However, BrO can undergo a self reaction which leads to the formation of two bromine radicals or molecular bromine which is quickly photoed during daytime forming again bromine radicals. The formation of OBrO via reaction 3.6 can be neglected against the other two channels (Papayannis et al. [1999], Butkovskaya et al. [1983]). Each bromine radical can react with ozone via reaction 3.1.

$$BrO + BrO \longrightarrow 2\,Br + O_2 \tag{3.4}$$

$$BrO + BrO \longrightarrow Br_2 + O_2 \tag{3.5}$$

$$BrO + BrO \longrightarrow OBrO + Br \tag{3.6}$$
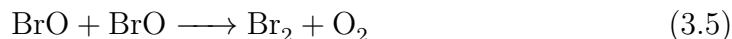
Further heterogeneous processes play an important role since they can lead to exponential increasing bromine amounts in the gas phase. Hyperbromous acid (HOBr), which is formed by the reaction of BrO with the peroxy radical HO_2 (reaction 3.7) can enter the liquid phase of water or water droplets (aerosols). Within the liquid phase, HOBr can react with bromide and hydron forming molecular Br_2. Br_2 which can degas from the water surface and form two Br

radicals by photolysis which can further react with ozone forming BrO. This process, described by the net reaction 3.10, leads to an exponential increase in reactive bromine in the gas phase and is therefor called *bromine explosion* (Platt and Janssen [1995], Platt and Lehrer [1997]). Figure 3.1 shows a sketch of the heterogeneous mechanisms leading to a degassing of Br_2 and BrCl from the water surface or aerosol surface. Obviously, the bromine explosion contributes significantly to ozone depletion events, which have been also observed at the Dead Sea Valley by Hebestreit et al. [1999] and Tas et al. [2006].

$$BrO + HO_2 \longrightarrow HOBr + O_2 \qquad (3.7)$$

$$HOBr_{(aq)} + Br^-_{(aq)} + H_{(aq)}^+ \longrightarrow Br_{2(g)} + H_2O_{(aq)} \qquad (3.8)$$

$$Br_2 \xrightarrow{h\nu} 2\,Br \qquad (3.9)$$
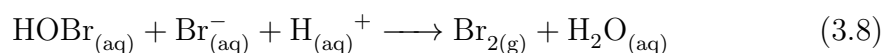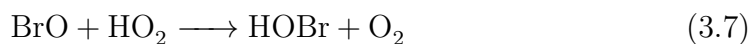
Net reaction from reactions 3.7 to 3.9 and 3.1:

$$BrO \longrightarrow 2\,BrO. \qquad (3.10)$$

The interaction of BrO with nitrogen oxides, especially NO_2, is also believed to enhance the release of Bromine compounds from aerosol surfaces due to the hydrolysis of $BrONO_2$ (Cao et al. [2014]). $BrONO_2$ is formed via the fast reaction of BrO and NO_2 (reaction 3.11, $k_289K = 1.8 \times 10^{-11}$ com^{3}molec^{-1}s^{-1}, Atkinson et al. [2007]). The uptake of $BrONO_2$ of aerosols with high halite content can result in degassing of Br_2, BrCl and Cl_2.

$$BrO + NO_2 \longrightarrow BrONO_2 \qquad (3.11)$$
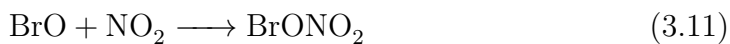
Deiber et al. [2004] investigated the uptake rates of $BrONO_2$ and $ClONO_2$ on the surface of droplets of pure water and solutions of NaBr and NaCl at a temperature range between 273 K and 280 K. They found out that the uptake rate of $BrONO_2$ increased from 0.024 to 0.039 with increasing the temperature from 273 K to 280 K (doubling of the uptake rate within a temperature increase of
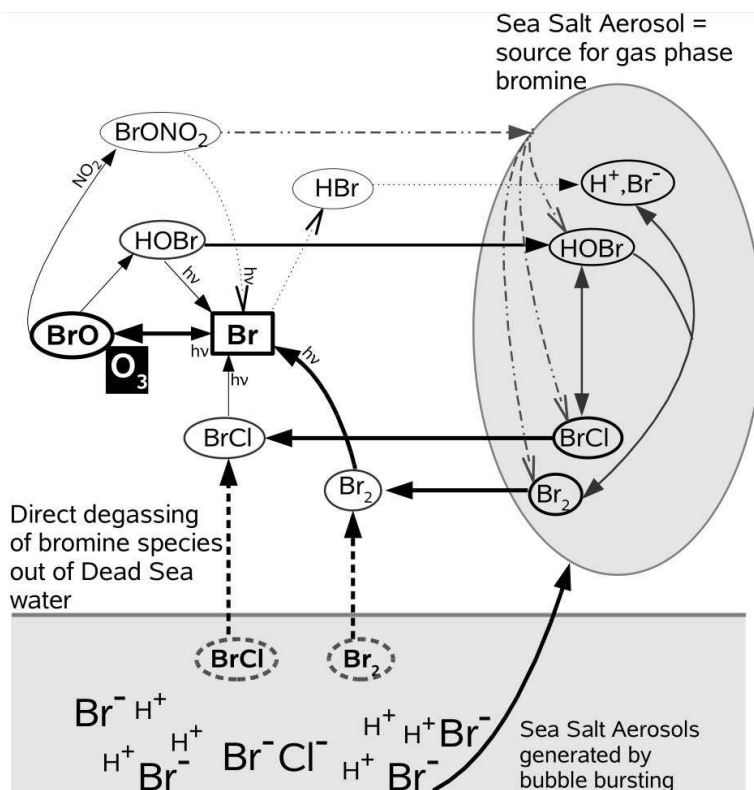
Fig. 3.1: Sketch of heterogeneous mechanisms leading to the release of reactive bromine from the water surface or aerosol surface. By the uptake of BrONO₂ and HOBr followed by the release of Br₂, the amount of bromine in the gas phase is doubled. Adapted from Smoydzin and von Glasow [2009]

10 K). In contrast, the uptake rate of $ClONO_2$ was not affected by a temperature change in this range. The strong temperature dependency may be relevant for the difference of total BrO abundance in summer and winter season. The authors explain the temperature dependency of the uptake of $BrONO_2$ with the higher activation energy for the hydrolysis of $BrONO_2$ (equation 3.12).s

$$BrONO_{2(aq)} + H_2O_{(aq)} \longrightarrow HOBr_{(aq)} + NaNO_{3(aq)} \tag{3.12}$$

According to the equation 3.13 proposed by Aguzzi and J. Rossi [1999], the formation of BrCl from the reaction of $BrONO_2$ with NaCl could be observed.

$$BrONO_{2(aq)} + NaCl_{(aq)} \longrightarrow BrCl_{(aq)} + NaNO_{3(aq)} \tag{3.13}$$

Further, they observed a significant variation of the uptake rate of $BrONO_2$ at different concentrations of NaBr in water droplets. The measured uptake coefficients ranged from 0.032 to 0.062 at NaBr concentrations from 0.01 to 1 M (M = mol/liter). The observed product was Br_2, formed via reaction 3.14.

$$BrONO_{2(aq)} + NaBr_{(aq)} \longrightarrow Br_{2(aq)} + NaNO_{3(aq)} \qquad (3.14)$$
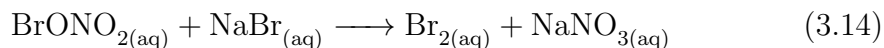
During the investigation of $ClONO_2$ uptake on droplets of NaCl solution, the authors observed Cl_2 as the only product according to reaction 3.15, also proposed by Aguzzi and J. Rossi [1999]. However, they state that HOCl is most likely formed as an intermediate product leading to the formation of Cl_2, according to the findings of Gebel et al. [2001].

$$ClONO_{2(aq)} + NaCl_{(aq)} \longrightarrow Cl_{2(aq)} + NaNO_{3(aq)} \qquad (3.15)$$
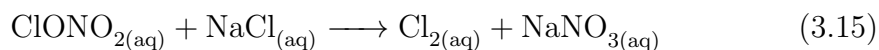
Hence, one can conclude that the formation and uptake of $BrONO_2$ and $ClONO_2$ by aerosols at the Dead Sea is most likely. By forming photochemically unstable products like Br_2, Cl_2 and BrCl, these mechanisms may strongly enhance the observed abundance of reactive halogen species during daytime. For rates of photolysis and thermal decomposition of $BrONO_2$ and $ClONO_2$, see table 3.1.

Species	photolysis rate	conditions	reference
$IONO_2$	$3.0 \pm 2.1 \cdot 10^{-3}$ s^{-1}	SZA $\approx 20°$ - $30°$	Joseph et al. [2007]
$BrONO_2$	$1.3 \cdot 10^{-3}$ s^{-1}	SZA $60°$, surface albedo 25%, sea level	Deters et al. [1998]
	$2.2 \cdot 10^{-3}$ s^{-1}	SZA $20°$, surface albedo 25%, sea level	Deters et al. [1998]

Species	thermal decomposition rate	conditions	reference
$IONO_2$	$(7 - 130) \cdot 10^{-6}$	290K	Saiz-Lopez et al. [2012]
$BrONO_2$	$7.8 \cdot 10^{-6}$	290K	Orlando et al. [1996]

Table 3.1: Photolysis frequencies and thermal decomposition rates of $BrONO_2$ and $IONO_2$.

During measurements in the arctic, Frieß et al. [2011] observed elevated layers of BrO in altitudes of 100 to 200 m above ground. This is a strong evidence for

precursors which have a sufficient long live time to be are vertically transported before releasing short-lived bromine compounds. At the Dead Sea Valley, the water bromide content is exceptionally high (see section 2.2). Thus, a release of reactive bromine species from the water surface or aerosol surface is very likely.

Although the mechanisms of BrO are well studied, the origin of the initial Bromine, which is needed to start the exponential release processes still not fully understood. It is assumed that BrCl and Br_2 can degas from the water surface or the surface of sea salt aerosols once the H^+ concentration is high enough (Smoydzin and von Glasow [2009]; Vogt et al. [1996]; von Glasow and Crutzen [2007]). Another possible release process is the photo dissociation of organic bromine compounds. However, due to their long photolytic lifetime in the troposphere, organic bromine compounds can be ruled out as a major source for reactive bromine near ground level.

3.2 Iodine

Iodine monoxide IO has been reported by several measurements in Mace Head, Ireland (6 pptv Alicke et al. [1999]), in the southern Indian ocean (9 pptv, Hönninger [2002]) and the open ocean (1 pptv, Lampel [2014]). Laboratory studies by Ball et al. [2010] showed, that large amours of I_2 are emitted by macro algeas like *Laminaria digitata* which are highly abundant at the Irish coastline. During daytime, I_2 is quickly photolysed forming atomic iodine which reacts with ozone forming IO. More recent field studies of Horbanski [2015] showed that a dominant part of reactive iodine in coastal areas is emitted by the algaes species *Ascophyllum nodosum*, which is a less potent emitter than *Laminarai digitata*. However, it is much more abundant in the intertidal zone where it is exposed to oxidative stress during low tide.

Similar to bromine, iodine can also lead to the destruction of atmospheric ozone. However, the self reaction of IO leads predominantly to the formation of iodine dioxide (OIO) which is likely to polymerize to iodine oxides of higher order and finally form particles (O'Dowd and Hoffmann [2005], Saiz-Lopez et al. [2012]).

In contrast to the self reaction of BrO, the total amount of iodine radicals is not conserved. Thus, the ozone destruction potential of iodine is very weak compared to BrO. Reactions 3.16 describe the channels and branching ratios for the self reaction of IO with an absolute rate coefficient of k_{298K} = 9.9 x 10^{-11} cm^3 $molec^{-1}s^{-1}$ (Atkinson et al. [2007]).

$$
\begin{aligned}
IO + IO &\longrightarrow & I_2 + O_2 & \quad (< 5\%) \\
&\longrightarrow & 2I + O_2 & \quad (11\%) \\
&\longrightarrow & I + OIO & \quad (38\%) \\
IO + IO + M &\longrightarrow & I_2O_2 + M & \quad (46\%)
\end{aligned}
\tag{3.16}
$$
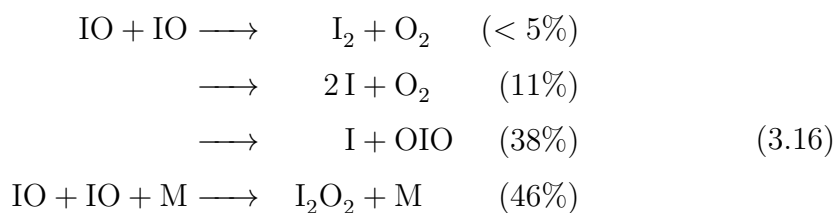
To date, there is only one publication about the detection of reactive iodine species at the Dead Sea Valley. In August 2001, Zingler and Platt [2005] performed two weeks of LP-DOAS measurements over water at the evaporation ponds near Ein Bokek, similar to the measurements performed in this work. Significant IO mixing ratios with peak values of 6 pptv to 10 pptv at detection limits of 0.3 and 2 pptv, respectively, were found regularly during daytime. The authors discussed several potential organic and inorganic sources for IO. Organic sources are quite unlikely since there is only sparse organic activity in the brine of the Dead Sea. Further, the environment of the potential organisms is not influence by fast changes (i.e. tide) resulting in iodine emissions induced by oxidative stress, like it is the case for the intertidal macro algae, e.g. at irish coastlines.

Possible inorganic source are assumed to be driven by the release of iodine species from the water surface directly by photochemical reactions or by the reaction with ozone in the liquid phase. Carpenter et al. [2013] showed that I_2 and HOI are formed by the mechanisms illustrated in figure 3.2, bottom. This implies the reaction of gaseous ozone with aqueous iodide via reactions 3.17 and 3.18:

$$
H^+_{(aq)} + I^-_{(aq)} + O_{3(g)} \longrightarrow HOI_{(g)} + O_{2(g)}
\tag{3.17}
$$

$$H^+_{(aq)} + HOI_{(aq)} + I^-_{(aq)} \rightleftharpoons I_{2(g)} + H_2O \tag{3.18}$$
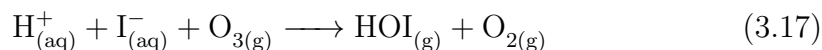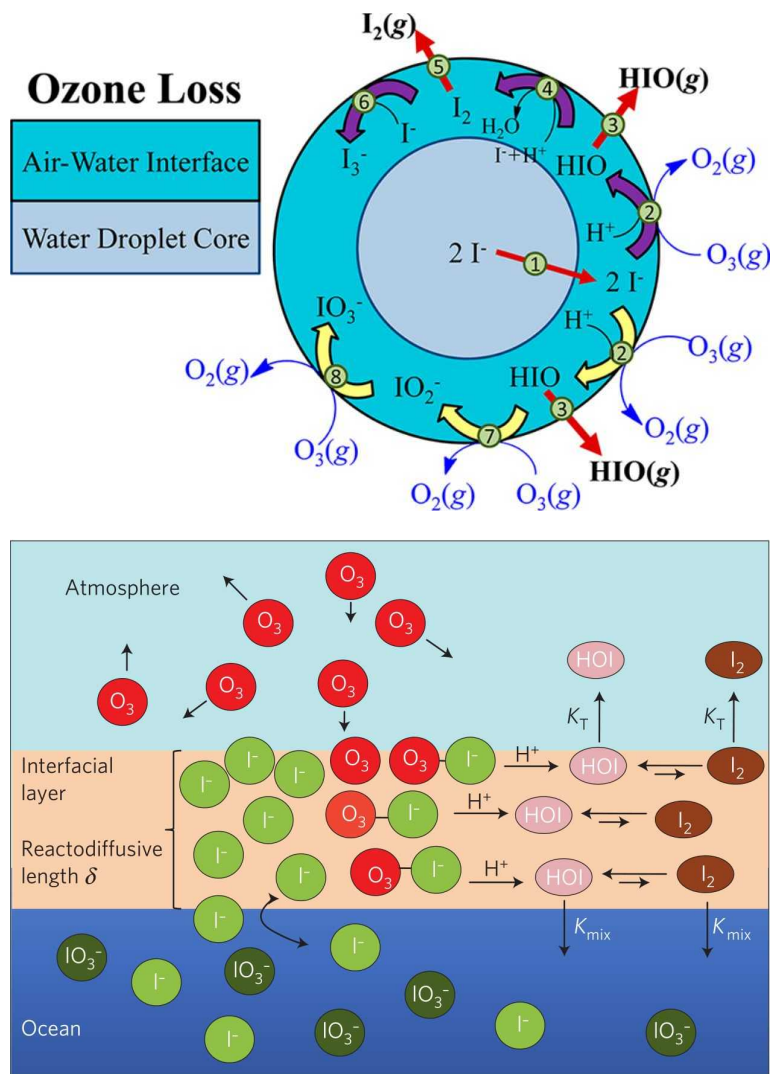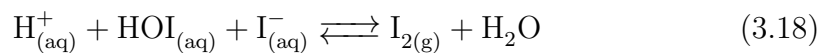
Fig. 3.2: **Top:** *Uptake of ozone of aerosol surface followed by the release of I_2 and HOI. Adapted from Pillar et al. [2013].* **Bottom:** *Illustration of the release of I_2 and HOI from water surface by the reaction of ozone with iodide. K_T and K_{mix} represent the mass transfers between aqueous to gas phase and interfacial layer to bulk water below. Adapted from Carpenter et al. [2013].*

The authors assume that the rate of reaction 3.17 is strongly dependent on accommodation and reaction at the surface layer of the water and therefore driven by the deposition velocity of ozone. Measurements with two independent techniques revealed a near linearly increase of I_2 and HOI emissions with an increase of gaseous ozone and aqueous I^-. During daytime, I_2 and HOI are quickly photolysed forming IO via reaction

$$I_2 + h\nu \longrightarrow 2\,I \tag{3.19}$$

and

$$HOI + h\nu \longrightarrow HO + I \tag{3.20}$$

leading to

$$I + O_3 \longrightarrow IO + O_{2.} \tag{3.21}$$

Further, Pillar et al. [2013] performed laboratory studies on microdroplets and observed the production of I_2 and HOI from aerosolized iodide solutions (0.01 - 100 μM) when exposed to 50 ppbv of ozone (see sketch in figure 3.2, top). This indicates, that the findings of Carpenter et al. [2013] can also be transferred from the bulk water surface to sea salt aerosols. It is assumed that the uptake of ozone on aerosols is significantly contributing to the halogen-driven ozone destruction in the tropical Atlantic. However, since the BrO abundance at the Dead Sea is exceptionally high, the dominating mechanism for ozone destruction is likely to be the auto catalytic self reaction of BrO.

3.3 Chlorine

Only little is known about the role of chlorine in the tropospheric halogen chemistry. Since the absorption cross section of chlorine monoxide (ClO) peaks in the deep UV (below 300 nm) it it very hard to detect small amounts in the lower pptv range. MAX-DOAS is not suitable for ClO measurements which is due to the low intensity of scattered sunlight in the deep UV. Active DOAS instruments like LP-DOAS are required. However, below 300 nm, the sensitivity,

which is proportional to the length of the absorption path is strongly limited by attenuation caused aerosols.

Measurements by Bobrowski et al. [2007] and, more recently Gliß et al. [2015] revealed significant amounts of chlorine dioxide (OClO) in volcanic plumes. OClO mixing ratios of 300 pptv parallel to 2.7 ppbv of BrO were observed. OClO is formed by the reaction of ClO with BrO ($k_{298K} = 6.8$ x 10^{-12} cm^3 $molec^{-1}s^{-1}$ by Atkinson et al. [2007]) or, at similar rates, with IO ($k_{298K} = 6.6$ x 10^{-12} cm^3 $molec^{-1}s^{-1}$ by Atkinson et al. [2007]).

$$BrO + ClO \longrightarrow Br + OClO \tag{3.22}$$

$$IO + ClO \longrightarrow I + OClO \tag{3.23}$$

Gliß et al. [2015] stated, that the relatively low ratio of ClO to BrO can be explained by the reaction of ClO with methane which has a large atmospheric abundance of approximately 1.8 ppmv (Seinfeld and Pandis [2006]). This suppresses the self reaction of ClO, and thus an "explosion-like" behavior which is the case for BrO. During daytime, OClO is quickly photolyzed leading to typical lifetimes of seconds to few minutes (according to Gliß et al. [2015], table 3.2) forming again ClO.

$$OClO \xrightarrow{h\nu} ClO + O \tag{3.24}$$

OClO photolysis rate	SZA
7.1 x 10^{-2} s^{-1}	34°
5.1 x 10^{-2} s^{-1}	62°

Table 3.2: OClO photolysis rates at different solar zenith angles (SZAs). Adapted from Gliß et al. [2015]

The absorption cross section of OClO peaks in the visible wavelength region which facilitates to measure it with a sensitivity of a few pptv using DOAS. OClO is predominantly formed by the reaction of ClO with BrO or IO and

can be used as an indicator for inter-halogen chemistry. Further, the abundance of ClO can be estimated if OClO, BrO and IO are simultaneously monitored. Assuming equilibrium state, the temporal variation of OClO is defined as

$$\frac{d}{dt}[\text{OClO}] = 0 = [\text{ClO}](k_{3.22}[\text{BrO}] + k_{3.23}[\text{IO}]) - J[\text{OClO}] \qquad (3.25)$$

leading to the calculated equilibrium ClO

$$[\text{ClO}] = \frac{J[\text{OClO}]}{(k_{3.22}[\text{BrO}] + k_{3.23}[\text{IO}])} \qquad (3.26)$$

Part II

Methods

4

Differential Optical Absorption Spectroscopy - DOAS

4.1 Theory

Absorption spectroscopy is a method to gain insight about the chemical and physical composition of a medium by its interaction with electromagnetic radiation. The Lambert-Beer law describes the wavelength dependent attenuation of electromagnetic radiation with initial intensity $I_0(\lambda)$ when passing through a medium of length L, described by equation 4.1, where $\sigma_i(\lambda)$ and c_i are the pressure and temperature dependent absorption cross section and concentration of absorber species i. Since the concentration of an absorber can vary along the light path, it also depends on l.

$$I(\lambda, L) = I_0(\lambda) \exp\left(-\int_0^L \sum_i \sigma_i(\lambda, p, T) \ c_i(l) \ dl\right) \qquad (4.1)$$

The optical density $\tau(\lambda,\text{L})$ is defined by

$$\tau(\lambda, L) = \ln\frac{I_0(\lambda)}{I(\lambda, L)}. \qquad (4.2)$$

and describes the optical properties of the observed medium. Usually known quantities are the initial intensity $I_0(\lambda)$, the absorption length L as well as the absorption cross sections $\sigma_i(\lambda, p, T)$ (from literature data). For the case of only one absorbing species which is homogeneously distributed along the light path, the concentration c can be retrieved by measuring I(λ, L):

$$c = \ln\left(\frac{I_0(\lambda)}{I(\lambda, L)}\right) \frac{1}{\sum_i \sigma_i(\lambda, p, T)\ L} = \frac{\tau(\lambda)}{\sum_i \sigma_i(\lambda, p, T)\ L} \tag{4.3}$$

When probing atmospheric air masses, elastic an inelastic scattering on molecules and aerosols, described by Rayleigh and Mie scattering, has also to be taken into account. Including scattering in the Lambert-Beer law leadS to equation 4.4.

$$I(\lambda, L) = I_0(\lambda)\ \cdot\ \exp\left(-\int_0^L \sum_i \sigma_i(\lambda, p, T)\ c_i(l)\ + \epsilon_R(\lambda, l) + \epsilon_M(\lambda, l)\ dl\right) \tag{4.4}$$

$\epsilon_R(\lambda, l)$ and $\epsilon_M(\lambda, l)$ represent the corresponding extinction coefficients. In case of the atmosphere, wavelength dependencies are λ^{-4} for Rayleigh and approximately $\lambda^{-1.3}$ for Mie scattering (Seinfeld and Pandis [1998]).

Probing the Earth's atmosphere implies a larger number of absorbers which makes it hard to distinguish between the different contributions and to retrieve the individual concentrations. DOAS, first introduced by Platt et al. [1979], reduces the complexity of this problem by exploiting the different characteristic wavelength dependencies of trace gas absorption and scattering processes. DOAS separates broad and differential (narrow) absorption structures of absorbing species with strongly wavelength dependent cross sections σ' from those with weaker wavelength dependency σ^B (see figure 4.1). Applying this frequency separation, one can rewrite equation 4.1:

$$I(\lambda, L) = I_0(\lambda)\ \underbrace{\exp\left(-\int_0^L \sum_i (\sigma'_i(\lambda, p, T))\ c_i(l)\ dl\right)}_{\text{strong } \lambda \text{ dependency}}$$

$$\cdot\ \underbrace{\exp\left(-\int_0^L \sum_i \left(\sigma_i^B(\lambda, p, T)\ c_i(l) + \epsilon_R(\lambda, l) + \epsilon_M(\lambda, l)\right)\ dl\right)}_{\text{weak } \lambda \text{ dependency}}\cdot \tag{4.5}$$

The first exponential function has a weak wavelength dependency and the second a strong dependency. Defining $I_{(0,B}(\lambda))$ as the combination of the broad part with the initial intensity $I_{(0}(\lambda))$, which has also a broad character in most DOAS applications, one can define the differential optical density τ' (equation 4.6).
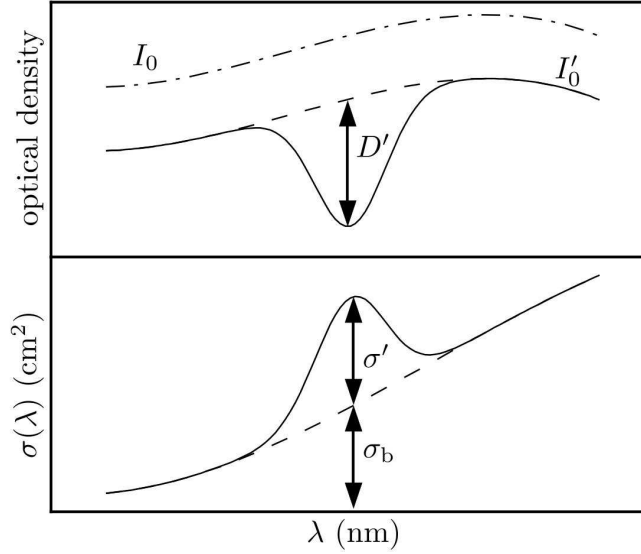
Fig. 4.1: Separation of cross sections in broad (σ^B) and narrow (σ') absorption features leading to the differential optical density τ'. Adapted from Platt and Stutz [2008]

$$\tau'(\lambda, L) = \ln \frac{I_{0,B}(\lambda)}{I(\lambda, L)} = \int_0^L \sum_i (\sigma'(\lambda, p, T) \ c_i(l)) \ dl. \qquad (4.6)$$

During measurements of scattered sunlight (MAX-DOAS, see below) the length of the light path is not known exactly and has to be retrieved by complex algorithms which simulated the radiation transport along the line of sight. Therefore, another useful quantity is defined by the slant column density S_i, which describes the amount of absorber species i integrated over the, yet unknown, light path L (equation 4.7).

$$S_i = \frac{\tau'_i}{\sigma'_i} = \int_0^L c_i(l) \ dl \qquad (4.7)$$

4.2 Measurement procedure

The measurement of the wavelength dependent intensities $I(\lambda)$ and $I_0(\lambda)$ is usually done by spectrometers. Since the instrumental properties (e.g.spectral resolution, non-linearity of the dispersion, noise of the detector) have a strong influ-

ence on the observed signals, they have to be characterized and considered during the analysis. Figure 4.2 shows a sketch describing the procedure of a DOAS measurement. The light $I_0(\lambda)$ from a known light sources passes the measurement
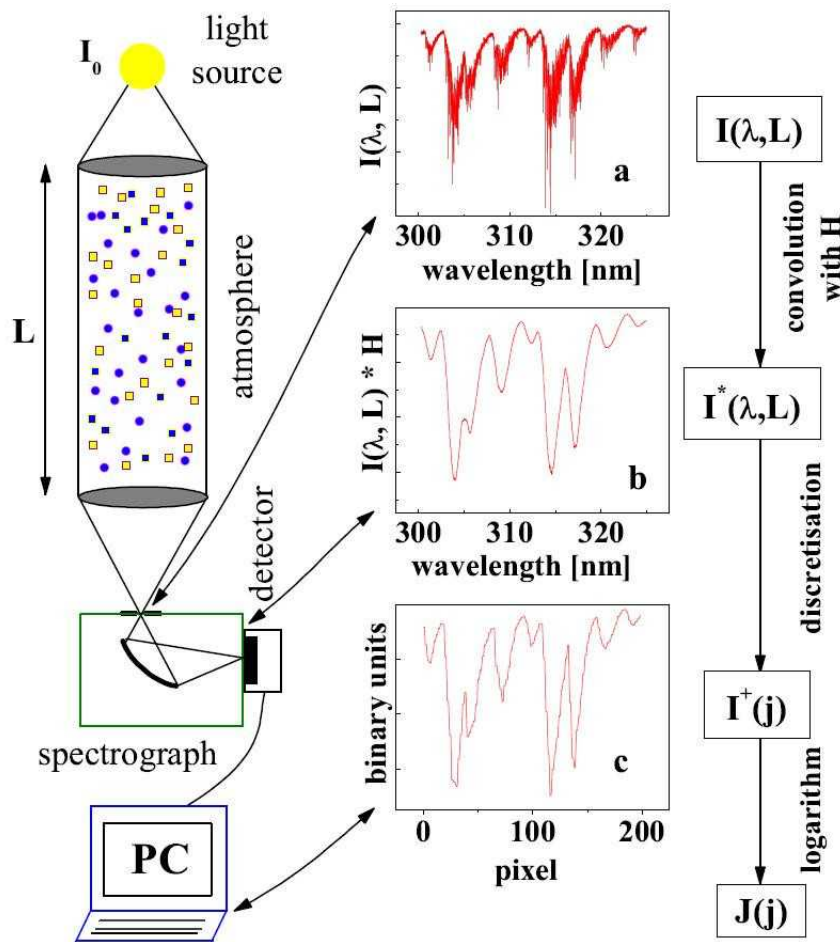
Fig. 4.2: Sketch of the DOAS measurement procedure illustrating how the incident intensity $I(\lambda,L)$ is convolved $(a \rightarrow b)$ and discretized $(b \rightarrow c)$ by the spectrometer unit during a DOAS measurement. Adapted from Stutz and Platt [1996]

volume, in this case, the atmospheres and enters the spectrometer. The spectral resolution of the spectrometer is defined by the width of its entrance slit, which is typically between 50 to 100 μm. The finite resolution leads to a loss of spectral information. Mathematically, this can be described by a convolution of the

incident light $I_0(\lambda)$ with the instrument function $H(\lambda)$ leading to the intensity distribution $I^*(\lambda)$ behind the entrance slit.

$$I^*(\lambda) = I_0(\lambda) * H(\lambda) = \int I_0(\lambda') \cdot H(\lambda - \lambda') \, d\lambda' \tag{4.8}$$

Today, mostly CCDs are used for the detector which is mounted to the spectrograph. Due to its finite pixel size, each pixel detects an interval of wavelengths. The width of this interval depends on the properties of the optical bench of the spectrometer (dispersive element) and the pixel size of the detector. The incident light intensity $I^*(\lambda)$ gets discretized leading to the measured signal $I^+(\lambda)$ which is described by the integral over the wavelength interval detected by pixel j plus the readout noise N_j of the corresponding detector pixel and additive, instrumental signals C which are discussed below.

$$I_j^+(\lambda) = \int_{\lambda(j)}^{\lambda(j+1)} I^*(\lambda') \, d\lambda' + N_j + C. \tag{4.9}$$

The wavelength to pixel mapping $\lambda(j)$ is measured by calibration lamps which distinct emission lines (mercury or neon emission lamps). The wavelengths of the emissions lines are known from the literature. $\lambda(j)$ can usually be described by a polynomial of the order of two or three, depending on the total width of the spectral range of the instrument. Therefore, only three to four emission lines need to be measured to obtain the wavelength to pixel mapping polynomial (equation 4.10, with polynomial coefficients a_k).

$$\lambda(j) = \sum_{k=0}^{n=2,3} a_k \, j^k \tag{4.10}$$

To enhance the data quality, the dark current signal D, which every sensor suffers from, has to be corrected. It is caused by randomly generated electrons and holes in the CCD which are proportional to the temperature via the Boltzmann factor $e^{-E/k_B T}$ and the integration time t of the scan. To reduce the dark current signal, the detectors are often cooled down to temperatures between -40° and 20°, whereas the sensor temperature depends on the circumstances of the exper-

iment. By blocking the entrance slit of the spectrometer, the dark current signal of the CCD can be measured. Usually, rather long integration times t_D of 10 to 30 seconds are chosen to obtain a significant signal D. To correct for dark current, D has to be subtracted from the measurement $I^+(\lambda)$ after being weighted corresponding to the integration time of t of $I^+(\lambda)$.

Further, most detectors add an artificial signal to the measured signal, the so called offset signal O. Thus, negative values caused by noise are avoided. This has the advantage, that analogue digital converter (ADC), which converts the photo currents of the CCD into digital data, does not need to "waste" a bit of its dynamic range on the sign. The offset signal is proportional to the number of averaged scans n per spectrum and can be obtained by recording a spectrum at minimal exposure time, and, hence minimal dark current, and a large number of scans n_O. The correction is done by weighting the offset signal with the number of scan of the measured intensity signal and subtracting it from $I^+(\lambda)$. Thus, the corrected spectrum $I_c^+(\lambda)$ is defined by equation 4.11, where n and t are number of averaged scans and integration time of the measured spectrum $I^+(\lambda)$.

$$I_c^+(\lambda) = I^+(\lambda) - \frac{n}{n_O}\, O - \frac{t}{t_D}\, D \qquad (4.11)$$

4.3 DOAS evaluation

In the following, measured spectra are assumed to be corrected for dark current and offset signal and will be denoted by $I(\lambda)$. To obtain the optical density from the measured data, equation 4.5 has to be applied on the measured spectra. During the analysis, the broad part of the exponential function gets approximated by the so called DOAS polynomial (Platt et al. [1979]) of the order of 2 to 4 depending on the spectral range of the analysis. Equation 4.12 shows the optical density after applying the DOAS polynomial with coefficients a_i and instrumental noise N. Further the slant column density S from equation 4.7 is used to substituted the integral.

$$\tau = \ln \frac{I_0(\lambda)}{I(\lambda, L)} = \underbrace{\left(\int_0^L \sum_i \sigma_i'(\lambda, p, T) \, c_i(l) \right) \, dl + a_i \lambda^i}_{\text{narrow (strong } \lambda \text{ dependency)}} + N$$

$$= \sum_i \sigma_i'(\lambda, p, T) \int_0^L c_i(l) \, dl + a_i \lambda^i + N \qquad (4.12)$$

$$= \sum_i \sigma_i'(\lambda, p, T) \, S_i + a_i \lambda^i + N$$

To obtain the slant column densities which carry the information of the concentration of absorber I, a model function F needs to be constructed. Since, the measurement of absorption cross sections $\sigma_i'(\lambda, p, T)$ with a sufficient accuracy is not trivial, usually literature data is used. However, the literature data is often recorded at a different and much higher resolution. Equation 4.13 recaps the effect of the entrance slit of the spectrometer which is described by the convolution with the instrument function H.

$$I(\lambda) \, * \, H = \left(I_0(\lambda) \, e^{-\tau(\lambda)} \right) \, * \, H(\lambda)$$

$$\approx (-I_0(\lambda) \, \tau(\lambda)) * \, H \qquad (4.13)$$

$$= -I_0(\lambda) \sum_i S_i \left(\sigma_i'(\lambda, p, T) * H(\lambda) \right)$$

At small optical densities τ, the exponential function can be approximated by applying the Taylor expansion which allows the adaption of the high resolution literature data to the usually lower resolution of the DOAS instrument. However, this approach only works with small optical densities but is legitimate when observing less abundant trace gases and, hence weak absorptions (which was the case for the measurements performed in this thesis).

Using the convoluted literature cross sections $\sigma_i^*(\lambda, p, T)$ the model function F can finally described by equation 4.14 with $a_i \lambda^i$ representing the DOAS polynomial.

$$F(\lambda) = \sum_i S_i \, \sigma_i^*(\lambda, p, T) + a_i \lambda^i \qquad (4.14)$$

The data of this thesis was analysied using the software DOASIS (Kraus [2006]), which uses a combination of a least-squares fit and a Levenberg-Marquardt (Lev-

enberg [1944], Marquardt [1963]) fit is used to adapt the model function $F(\lambda)$ to the measured optical density $\tau(\lambda)$ in a given wavelength range (k_1 to k_2) by minimizing the chi square value given by:

$$\chi^2 = \sum_{k_i=k_1}^{k_2} \left(\tau(k_i) - F(k_i) \right)^2 \tag{4.15}$$

The difference between the measured optical density and the modeled function is called the residual spectrum $R(\lambda)$. If the model function is an optimal representation of τ, $R(\lambda)$ should by dominated by the readout noise N of the CCD. If an absorber is missing in the model function F, the residual spectrum is dominated by this absorber once its optical density islarger than the read out noise. This makes the $R(\lambda)$ a useful indicator for the quality of the model function and, hence, the quality of the DOAS analysis. Usually, the root mean square value (RMS) of the residual spectrum $R(\lambda)$ is used as its scalar representation.

4.4 Fit error and detection limits

For all DOAS data analyzed within this thesis, the measurement errors where defined by the 2σ-interval from the least squares algorithm which was. Further, the detection limits were defined by twice the measurement error, according to Stutz and Platt [1996].

4.5 DOAS instruments

Depending on the field of application, DOAS instruments can be realized with different hardware setups. The following section describes the Long Path (LP)-DOAS and the Multi-AXial (MAX)-DOAS techniques, which were applied during the measurement campaigns carried out within the framework of this thesis.

4.5.1 Long Path-DOAS
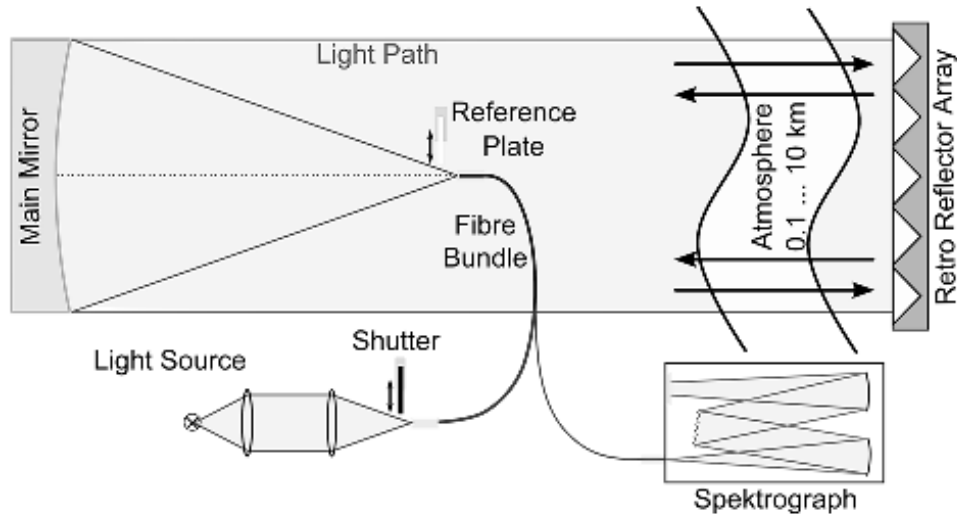
Fig. 4.3: Simplified sketch of a LP-DOAS setup. The light of a light source is coupled into one end of a fiber bundle and is sent through the atmosphere. A retro reflector sends the light back to the telescope where it gets coupled into receiving fibers leading to a spectrometer. The y-shaped mutli fibrer bundle enables the combination of sending and receiving unit into one single telescope. Adapted from Sihler [2007], modified by D. Pöhler, pers. comm.

Long Path DOAS is the most original form of DOAS instruments. Early setups consisted of two telescope units. An emitting unit and a receiving unit. Light from the emitting telescope was send over a distance of several kilometers before being received by the other telescope. To reduce the effort of setting up to complex units at the ends of the light path, today's LP-DOAS instruments combine emitting and receiving unit into one telescope. A sketch of such a setup is illustrated in figure 4.3. The core of the instrument is the y-shaped fiber bundle (single core diameter typically 100 to 200 μm) which combines the emitting fiber, coming from the light source and the receiving fiber leading to the spectrometer (Merten et al. [2011]). The combined end of the fibers is located close to the focal point of the main mirror. The light from the light source (xenon arc lamp or high power LED) is coupled into the corresponding fiber. The main mirror parallelizes it and

sends through the atmosphere onto a retro reflector. The retro reflector sends the light back to the main mirror. The position of the combined end of the fiber bundle is slightly out of the focal point of the main mirror leading to a slightly blurred image. Sending and receiving fibers of the bundle are closely neighbored (distance of about 50 μm) which enables the received light to enter the the fiber leading to the spectrometer.

To record a reference spectrum $I_0(\lambda)$, a reference plate (usually a sand blasted scattering plate made from Aluminium) is moved in front of the combined end of the fiber bundle. Thus, the light from the sending fibers is almost directly coupled into the receiving fibers without traversing the atmospheric measurement path.

During daytime, the telescope also receives sunlight light which is reflected by the terrain behind the retro reflector or scattered into the field of view by aerosols. To account for this so called "background intensity", spectra with blocked light source are recorded regularly recorded by using a shutter (see figure 4.3). By recording the background spectra with the same acquisition settings (integration time and number of averaged scans), the data can be corrected for back ground intensity by a simple subtraction (see also LP-DOAS analysis, section 5.2.3).

Since the light path is determined by twice the distance between the telescope and the retro reflector and can easily obtained by GPS, the trace gas concentrations can directly by calculated via the slant column densities obtained from the fit result.

4.5.2 Multi Axis-DOAS

Multi Axis (MAX)-DOAS, introduced by Hönninger et al. [2004b] is a passive remote sensing method which uses scattered sunlight to measure the trace gas concentrations in the atmosphere. Figure 4.4 illustrates the measurement geometry of MAX-DOAS. The spectral composition of scattered sunlight $I(\lambda, \alpha)$ is measured under different telescope elevation angles α and (usually) evaluated against a spectrum $I_0(\lambda, 90°)$acquired with the telescope pointed in zenith direction.
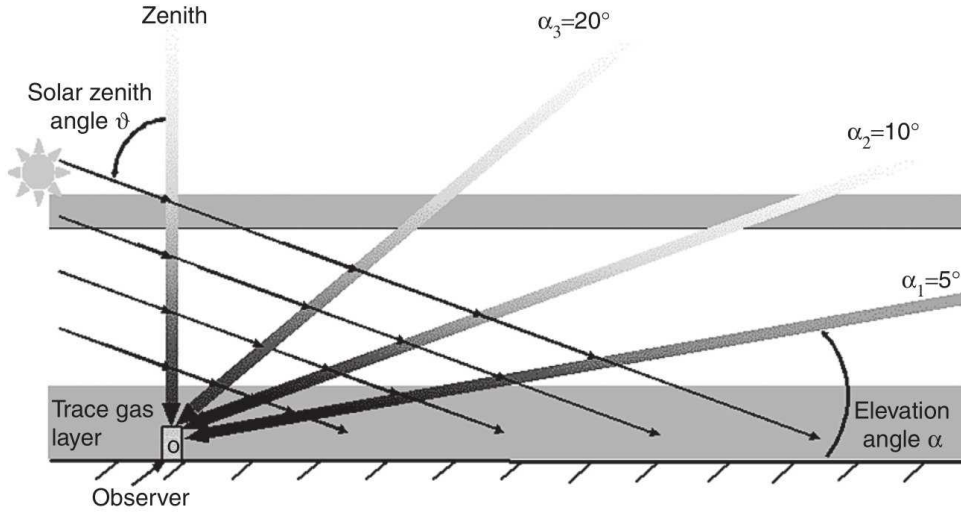
Fig. 4.4: Sketch of a MAX-DOAS measurement geometry. Scattered sunlight is measured under different telescope elevation angles α_1 to α_3 leading to different proportions of absorption paths in the lower trace gas layer. Adapted from Platt and Stutz [2008].

Since $I_0(\lambda, 90°)$ is not free of atmospheric absorption structures, the resulting optical density $\tau(\lambda, \alpha)$ carries information about the differential slant column density (dSCD), which is different to the total SCD. The dSCD describes the difference in absorption strength observed at telescope elevation angles α smaller 90° compared to $\alpha = 90°$. Measuring at multiple elevation angles provides information about the vertical distribution of atmospheric absorbers. At small elevation angles with viewing directions close to the horizon, the light path is located in a distinct altitude while at larger angles, several altitudes averaged. Thus the sensitivity or information content at instrument altitude is significantly higher compared to altitudes above or below the instrument. A typical sequence of elevation angles for ground based measurements is 20∘, 10∘, 5∘, 2∘, 1∘ and 0∘ at which the low increment for small elevations is chosen due to the increased sensitivity at instrument altitude.

Assuming that the concentration of an absorber is confined to the first few kilometers of altitude above instrument level, the dSCD measured under elevation angle α can be approximated with the total SCD. By introducing the so called air mass factor A, the SCD can be converted into vertical column densities (VCD),

which describe the concentration of an absorber integrated vertically along the atmosphere.

$$A = \frac{S}{V} \tag{4.16}$$

The air mass factor is nicely illustrated by the more simple geometry of direct
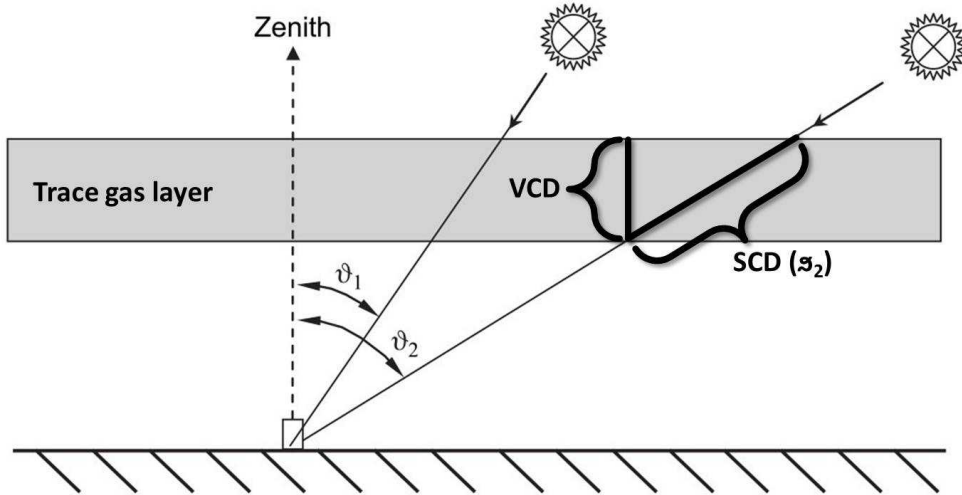
Fig. 4.5: Sketch of the measurement geometry of direct sunlight DOAS. The vertical column density (VCD) can be approximated from the measured slant column density and the solar zenith angle ϑ. Adapted from Platt and Stutz [2008].

light DOAS, where the telescope always points at the sun and therefore linking its elevation angle to the solar zenith angle ϑ. Assuming no contribution by scattered sunlight, the air mass factor A, describing the proportionality between the slant column density along the light path and the vertical column density, described by a simple trigonometric relation leading to equation 4.17.

$$A = \frac{S}{V} \approx \frac{1}{cos(\theta)} \tag{4.17}$$

However, in the case of scattered sun light DOAS, the air mass factors are more complex and need to be calculated by radiation transfer models which makes the quantitative evaluation of MAX-DOAS measurements much more complex compared to direct sunlight DOAS.

MAX-DOAS instruments do not rely on a artificial light source which facilitates a small and lightweight design with low power consumption. Thus, MAX-DOAS instruments can easily be deployed in remote areas and on mobile platforms. Further, the ability to measure vertical distribution of trace gases makes MAX-DOAS a valuable method for the investigation of the chemical composition of the lower troposphere atmosphere.

4.6 Retrieval of absolute trace gas concentrations from MAX-DOAS data

Inverse modeling

The finite number of telescope elevation angles of MAX-DOAS measurements do not provide sufficient information to describe the atmospheric state in terms of vertical trace gas distributions. However, a satisfactory solution of this under-determined problem is the application of inverse methods combined with *a priori* information (i.e. *a priori* vertical profiles). The following section gives a brief introduction the inverse methods which where used for the retrieval of vertical trace gas profiles in this thesis. For further details, see Rodgers [2000] and Jacobs [2007].

Inverse modeling enables the estimation of a state vector $\mathbf{x}$, describing the state of the system which is investigated, in our case, the vertical distribution of trace gases in the atmosphere. The measurement of its observables is represented by the observation vector $\mathbf{y}$. The so called *forward model* F describes the relationship between the true state $\mathbf{x}$ and the observations $\mathbf{y}$ and can be interpreted as the measurement procedure (e.g. the instrument which projects the atmospheric state $\mathbf{x}$ on the acquired data $\mathbf{y}$):

$$\mathbf{y} = F(\mathbf{x}, \mathbf{b}) + \varepsilon. \tag{4.18}$$

The vector $\mathbf{b}$ is called parameter vector and describes the model variables which will not be retrieved (e.g. temperature, pressure, humidity, ...). Errors from the

measurement, the forward model and the model parameters are described by the error vector ε. By the inversion of equation 4.18, one can obtain the state vector $\mathbf{x}$ at given measurements $\mathbf{y}$. This is done by minimizing the cost function χ^2 which describes the squared, error weighted difference between the atmospheric state $\mathbf{x}$ and the measurement $\mathbf{y}$. Using the matrix notation, the inversion can be described in a more general way by

$$\chi^2(\mathbf{x}) = [F(\mathbf{x}) - \mathbf{y}]^T \ S_\varepsilon^{-1} \ [F(\mathbf{x}) - \mathbf{y}] + [\mathbf{x} - \mathbf{x}_a]^T \ S_a^{-1} \ [\mathbf{x} - \mathbf{x}_a] \,, \qquad (4.19)$$

with S_ε being the diagonal error covariance matrix which is defined by the square of the measurement errors, and S_a the *a priori* error covariance matrix.

For F being linear in $\mathbf{x}$,

$$F(\mathbf{x}) = \mathbf{K}\mathbf{x} \qquad (4.20)$$

and replacing F in equation 4.18 leading to

$$\mathbf{y} = \mathbf{K}\mathbf{x} + \varepsilon, \qquad (4.21)$$

an analytically solution can be found. If F is not linearly in $\mathbf{x}$, the Jacobian matrix $\mathbf{K}$ has to be linearized By Taylor expansion around an initial *a priori* value and re-calculated iteratively. For atmospheric trace gas retrieval, $\mathbf{K}$ are usually called *weighting functions* since they describe how strong the measurements are influenced by a variation of the atmospheric state, which can be described by the following equation

$$\mathbf{K} = \frac{\partial F(\mathbf{x})}{\partial \mathbf{x}}. \qquad (4.22)$$

Applying Bayes' theorem (Rodgers [2000]), the maximum *a posteriori* (MAP) solution $\mathbf{x}$', which is equivalent to the minimum of the cost function (equation 4.19) is obtained by

$$\mathbf{x}' = \mathbf{x}_a + \mathbf{G}(\mathbf{y} - \mathbf{K}\mathbf{x}_a) \qquad (4.23)$$

Further, the gain function $\mathbf{G}$ is defined by the variation of the retrieved state $\mathbf{x}$' of the atmosphere against the observables $\mathbf{y}$.

$$\mathbf{G} = \frac{\partial \mathbf{x'}}{\partial \mathbf{y}} \tag{4.24}$$

This leads to the definition of the averaging kernels $\mathbf{A}$

$$\mathbf{A} = \mathbf{GK} = \frac{\partial \mathbf{x'}}{\partial \mathbf{x}} \tag{4.25}$$

which represent the sensitivity of the MAP solution $\mathbf{x'}$ to the true state $\mathbf{x}$. By replacing 4.25 and 4.21 into 4.23 yields a MAP which is proportional to $\mathbf{A}$ and $\mathbf{G}$

$$\mathbf{x'} = \mathbf{Ax} + (\mathbf{I}_n - \mathbf{Ax})\mathbf{x}_a + \mathbf{G}\,\varepsilon \tag{4.26}$$

where I_n is the n-dimensional identity matrix. The contributions of the different terms of equation 4.26 on the solution are described in the following:

1. $\mathbf{Ax}$: contribution of the true state $\mathbf{x}$

2. $(\mathbf{I}_n\text{-}\mathbf{Ax})\mathbf{x}_a$: contribution from *a priori*, also called *smoothing error*

3. $\mathbf{G}\varepsilon$: contribution of random observational error, also called *retrieval error*

Ideally, the smoothing error should be zero. However, often it dominates the total retrieval errors since relatively small measurement errors can be achieved by state of the art instrumental setups.

HEIPRO retrieval algorithm

The vertical aerosol and trace gas profiles in this thesis where retrieved using the HEIPRO (implemented by Yilmaz [2012]) algorithm based on the radiation transfer model SCIATRAN 2 (Rozanov et al. [2002] and Rozanov et al. [2005]). HEIPRO is divided in two parts, a sketch is illustrated in figure 4.6. The aerosol retrieval is based on the measured MAX-DOAS SCDs of the oxygen collision complex O_4. The vertical O_4 distribution is proportional to the squared vertical profile of oxygen and is therefore supposed to be known. Given suitable temperature and pressure, its known distributions serves as an *a priori* profile for the aerosol inversion. Further, O_4 is chemically inert. Variations of measured SCDs
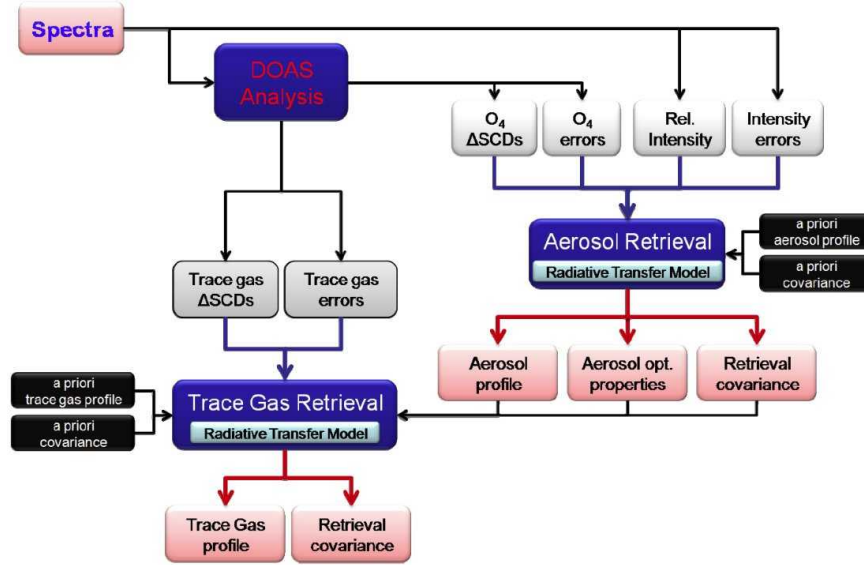
Fig. 4.6: Sketch of the HEIPRO retrieval algorithm. Measured O_4 are used to retrieve aerosol optical properties which provide air mass factors for the retrieval of trace gas profile. Adapted from Yilmaz [2012].

from the expected SCDs are proportional to variations of the absorption path length which again is proportional to the aerosol optical properties of the atmosphere. The product of the aerosol retrieval is given in extinction (km^{-1}) at the wavelength of the O_4 absorption band, which was used in the DOAS analysis and in the retrieval.

Once the aerosol properties of the atmosphere, and hence, the air mass factors of the elevation angles of the measurement are modeled, the trace gas retrieval can be performed. Finding a suitable *a priori* profile is not as obvious as in the aerosol case, since there is no justification of a exponentially decreasing vertical profile for every trace gas species. Therefor, the *a priori* covariance must be appropriately chosen.

5

Instrumental

This chapter gives an overview about the specifications of the instruments which were applied during the two field campaigns in 2012 and 2014 at the Dead Sea. The methods of data acquisition of the instruments and settings for the DOAS analysis are described.

All spectral data acquired within the framework of this thesis was analyzed using the JScript compatible software DOASIS (Kraus [2006]). DOASIS is capable of performing all necessary mathematical operations needed for the DOAS analysis including a Levenberg-Marquardt algorithm for non-linear fitting of literature cross sections to the measured spectra. The analysis algorithms were written in JScript and executed by DOASIS. Since LP- and MAX-DOAS are probing different atmospheres using different light sources, the analysis configurations of the two measurement techniques are different in terms of wavelength ranges, spectral corrections and trace gas species fitted to the spectral data.

In section 5.1.5, the impact of instrument driven stray light (IDSL) on the DOAS analysis is discussed. Large residual structures could be assigned to IDSL in the case of compact spectrometers made by Avantes. By using appropriate corrections, the residual structures could be lowered significantly.

5.1 MAX-DOAS instruments

5.1.1 Hardware setup

MAX-DOAS Ein Bokek 2012
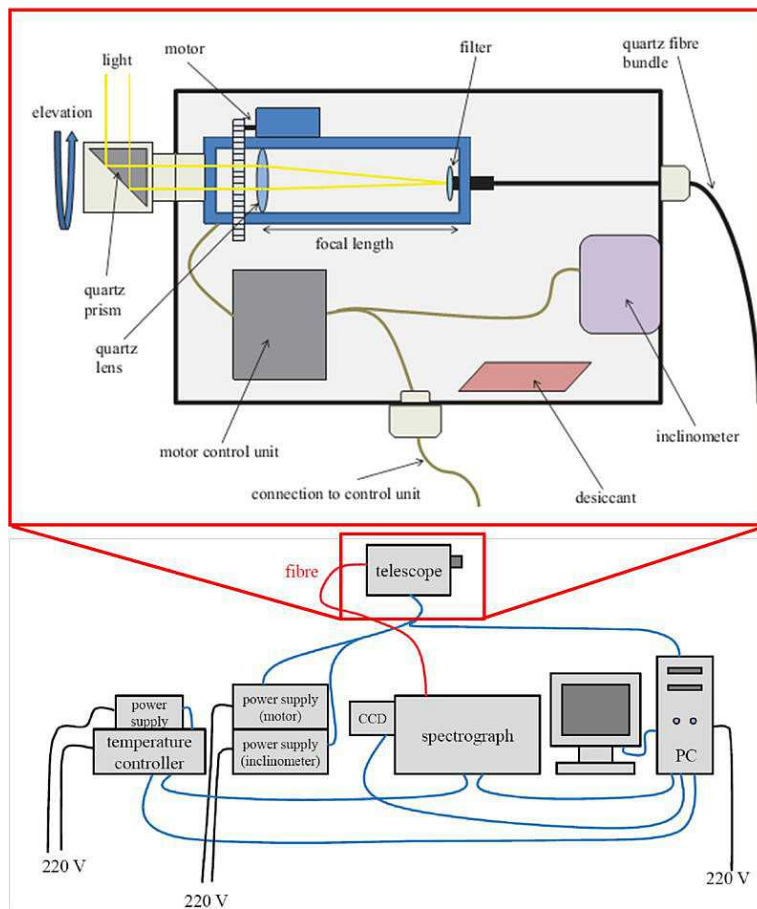
Fig. 5.1: Scheme of the MAX-DOAS instrument at Ein Bokek in 2012. Adapted from Holla [2013].

The MAX-DOAS instrument located at Ein Bokek is described in detail in Holla [2013] and Holla et al. [2015]. Figure 5.1 shows a scheme of the setup. The hardware components and their properties are listed in Table 5.1. The scanner unit consists of a fused silica prism movable by 360° using a brush-less DC motor

. The prism reflects the light on a fused silica lens with a focal length of 100 mm. The lens focusses the light on a multi fiber bundle consisting of 37 circular arranged single fibers. The fiber bundle guides the light to the spectrometer (Acton 300i with Andor DU 440-BU CCD). At the entrance of the spectrometer, the fibers of the bundle are vertically arranged thus forming the entrance slit.

Component	Description
Telescope	Rotatableprism and lens with f = 100 mm and diam 21.4 cm. FOV = 0.5°.
Optical fiber configuration	Multi fiber bundle. 37 x 100μm. Circular arranged at telescope. Vertically arranged at spectrometer.
Spectrometer optical bench	Acton Spectra 300i. Focal length 300mm, f-number f/4. Spectral range 327 nm to 470 nm. Temperature stabilized to 36°.
Spectrometer camera	Andor DU 440-BU back-illuminated CCD cooled to -30°. 2048 x 512 pixels. 13.5 μm x 13.5 μm per pixel.
Data acquisition	PC with MS-DOAS software by U. Frieß.

Table 5.1: List of hardware specifications of the Ein Bokek MAX-DOAS instrument used during the campaign in 2012 at the Dead Sea.

MAX-DOAS Masada top 2012
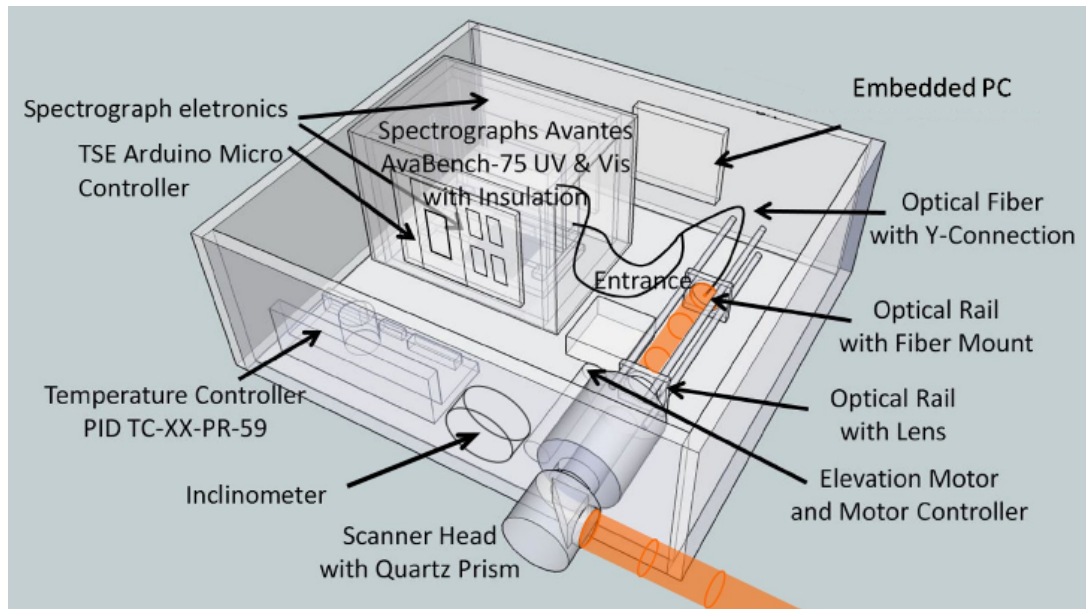
Fig. 5.2: Scheme of the MAX-DOAS instrument at Masada top in 2012. Adapted from Nasse [2014].

The MAX-DOAS instrument positioned at Masada top in 2012 has already been deployed in several field campaigns and has been described in detail in the works of Holla [2013], Nasse [2014] and Zielcke [2015]. Table 5.2 gives an overview of the instrument components. A scheme of the instrumental setup is shown in 5.2. All components are placed in an aluminium box with a size of 50 cm x 40 cm x 20 cm. The scanner of the telescope can be moved by 360°. An inclinometer corrects the elevation angle of the telescope, if the instrument is not placed horizontally or is mounted on a moving platform (e.g. car, plane or ship). Scattered sunlight enters the telescope and is reflected by a prism made of fused silica. A lens (f = 100 mm) focuses the light on a multi fiber bundle consisting of six 100 μm fibers which are circularly arranged. Three of the six fibers guide the light to the UV spectrometer and Vis spectrometer respectively. The spectrometers are mounted on an aluminium base which is temperature stabilized to 20°C. The

whole spectrometer unit is covered in insulation. An embedded PC runs the measurement software and stores the spectral data.

Component	Description
Telescope	Rotatableprism and lens with f = 100 mm and diam 21.4 cm. FOV(UV Spec) = 0.27°, FOV(Vis Spec) = 0.32°. Inclinometer for elevation correction.
Optical fiber configuration	Multi fiber bundle. 6 x 100μm. Circular arranged at telescope. 3 fibers vertically arranged at each spectrometer.
UV Spectrometer	Avantes ULS2048x64 Focal length 75mm, f-number f/7. Built-in BG3 filter. 100 μm entrance slit. Spectral range 287 nm to 450 nm. Temp. stabilized at 20°. Hamamatsu back-thinned detector S10420-1106-01. 2048 x 64 pixels. Pixel size 14 μm x 14 μm.
Vis Spectrometer	Avantes ULS2048L-U2 Focal length 75mm, f-number f/7. 100 μm entrance slit. Spectral range 430 nm to 565 nm. Temp. stabilized at 20°. Sony ILX511B CCD. 2048 pixels. Pixel size 14 μm x 200 μm
Data acquisition	embedded PC (Lippert CRR-LX800) with MS-DOAS software by U. Frieß.

Table 5.2: List of hardware specifications of the Ein Bokek MAX-DOAS instrument used during the campaign in 2012 at the Dead Sea.

MAX-DOAS Masada bottom 2014
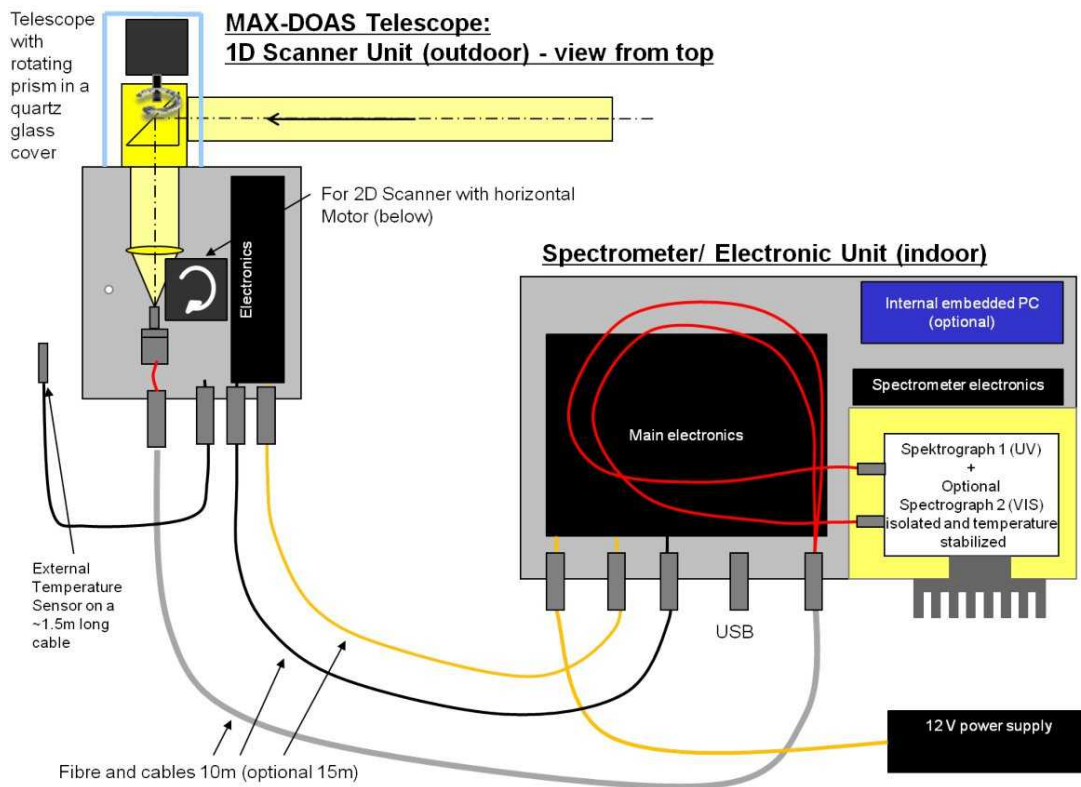
Fig. 5.3: Scheme of the EnviMeS MAX-DOAS instrument at Masada bottom in 2014. Adapted from Pöhler [2014].

This section describes the MAX-DOAS instrument, which was used for the measurements at the bottom of the mountain fortress Masada in 2014. The instrument was built by EnviMeS and consists of two parts (figure 5.3): 1) The scanner unit containing the telescope optics is connected with the spectrometer unit via cables and an optical fiber bundle of 10 m. 2) The telescope consisting of a rotatable prism and a lens. A stepper motor with step size of 0.1° is used to rotate the prism. A tilt sensor mounted on the back of the prism ensures a correct elevation angle of the telescope. The accuracy of the tilt sensor is better than 0.2°. The prism reflects the light on a lens which focuses it on a multi fiber bundle consisting of seven single fibers with a core diameter of 100 μm each. Six circular

arranged fibers guide light to the UV spectrometer. At the entrance slit of the spectrometer, the fibers are vertically arranged. The seventh, centered fiber of the bundle guides the light to the Vis spectrometer. Table 5.3 gives an overview about the optics and spectrometers of the instrument.

Component	Description
Telescope	Rotatableprism and lens with f = 100 mm and diam 21.4 cm.
	FOV(UV Spec) = 0.3°, FOV(Vis Spec) = 0.2°.
	Tilt sensor for elevation correction.
Optical fiber	Multi fiber bundle. 6 x 100μm.
configuration	Circular arranged at telescope.
	6 fibers vertically arranged at UV spectrometer.
UV Spectrometer	Avantes ULS2048x64 Focal length 75mm, f-number f/7. Built-in BG3 filter.
	100 μm entrance slit. Spectral range 296 nm to 459 nm. Temp. stabilized at 20°.
	Hamamatsu back-thinned detector S10420-1106-01.
	2048 x 64 pixels. Pixel size 14 μm x 14 μm.
Vis Spectrometer	Avantes ULS2048L-U2 Focal length 75mm, f-number f/7.
	100 μm entrance slit. Spectral range 440 nm to 583 nm. Temp. stabilized at 20°.
	Sony ILX511B CCD. 2048 pixels. Pixel size 14 μm x 200 μm
Data acquisition	External notebook with MS-DOAS software by U. Frieß.

Table 5.3: List of hardware specifications of the EnviMeS MAX-DOAS instrument used during the campaign in 2014 at the Dead Sea at Masada bottom.

MAX-DOAS Neve Zohar, Ein Gedi, mobile 2014
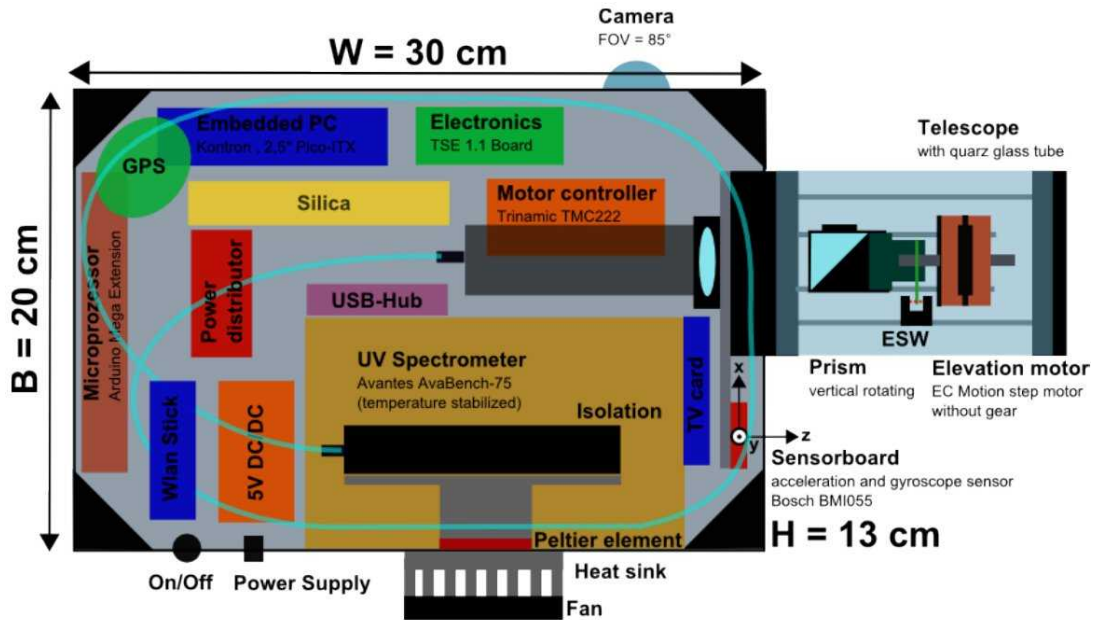
Fig. 5.4: Scheme of the ISA MAX-DOAS instrument which was used for the measurements at Neve Zohar, Ein Gedi and for mobile measurements along the Dead Sea in 2014. Adapted from Penth [2014].

During the campaign at the Dead Sea in November 2014, mobile MAX-DOAS measurements were performed applying the newly developed compact instrument **I**nertial **S**ensor-based **A**ttitude compensating (ISA) MAX-DOAS was applied for the first time. The instrument was developed within the framework of a master's thesis at the Institute of Environmental Physics Heidelberg by Penth [2014] with focus on mechanically precise MAX-DOAS measurements on fast moving platforms. A detailed description can be found in this work. Figure 5.4 shows a sketch of the extreme compact setup of the instrument. All components are arranged in a water proof enclosure with dimensions 30 cm x 20 cm x 13 cm. The design of the scanner unit is similar to that of the EnviMeS instrument Pöhler [2014]. A rotatable prism reflects the light on a lens which focuses it on a fiber. The fiber is connected to a temperature stabilized UV spectrometer. The combination of an acceleration sensor and a gyroscope provides a fast responding

elevation correction which is crucial during measurements on moving platforms (e.g. car, plane, ship), see Penth [2014] for detailed description of the tilt control algorithm. An embedded PC controls the measurement procedure. A built-in web cam and a GPS receiver collect supportive data. An overview of the hardware specifications can be found in Table 5.4.

Component	Description
Telescope	Rotatableprism and lens with f = 75 mm and diam 21.4 cm. FOV(UV Spec) = 0.3°, FOV(Vis Spec) = 0.2°. Tilt sensor for elevation correction.
Optical fiber	Mono fiber with diameter of 400μm.
Spectrometer	Avantes ULS2048x64 Focal length 75mm, f-number f/7. 100 μm entrance slit. Spectral range 296 nm to 460 nm. Temp. stabilized at 20°. Hamamatsu back-thinned detector S10420-1106-01. 2048 x 64 pixels. Pixel size 14 μm x 14 μm.
Data acquisition	Embedded PC Kontron pITX-SP with MS-DOAS software by U. Frieß.

Table 5.4: List of hardware specifications of the ISA MAX-DOAS instrument which was used for mobile measurements and stationary measurements at Neve Zohar and Ein Gedi during the campaign in 2014 at the Dead Sea.

5.1.2 Characterization of instrumental driven stray light (IDSL) of Avantes AvaBench-75 spectrometers.

Due to their small dimensions, compact spectrometers tend to suffer from instrumental driven stray light (IDSL) (see also Schmitt [2011]). The dependency of IDSL on the spectral nature of the incident light is strongly variable. On the one hand, it can be caused by the unwanted reflectivity of interior walls or housings of optical components leading to a constant stray light intensity uniformly distributed over the spectrometers spectral range (IDSL type A). On the other hand, IDSL can also have a strong wavelength dependency (IDSL type B). This can be caused by the zeroth order light which reaches again one of the main mirrors of the spectrometer leading to a non-diffusive reflection. The mirror may reflect this light back on the grating or directly on the sensor which leads to highly wavelength dependent stray light contributions. Other sources

can be light from outside the spectrometer which penetrates through holes in the spectrometer housing.

IDSL can have a significant negative effect on retrieved column densities and residual structures. However, while type A can be partly corrected during a DOAS analysis (see chapter 4), type B is very difficult to handle.

During laboratory measurements, the IDSL of the compact Avantes (Type AvaBench-75 (ULS2048x64-U2)) spectrometers of the EnviMeS MAX-DOAS and ISA MAX-DOAS instrument were characterized. The light of a tungsten lamp was parallelized by a UV fused silica lens, send through an optional color glass filter and focused on the fiber bundle of the instrument by usng a second lens. Several color glass filters (SCHOTT OG530, GG475, RG610, RG665, thickness 3 mm see figure 5.5) were chosen to block light in the wavelength range of the corresponding spectrometer (similar to Frieß [2001]). The observed signal contains only IDSL when using the filter. It is important to note that the EnviMeS MAX-DOAS has an already build-in SCHOTT BG3 bandpass filter which was not yet installed in the ISA MAX-DOAS instrument during the measurements that were made during this thesis. The BG3 filter has a thickness of 1 mm, is permanently mounted behind the entrance slit of the spectrometer and blocks light in the range from 450 nm to 700 nm (figure 5.5). Using the OG530, RG610 and RG665 on the EnviMeS MAX-DOAS will result in nearly the same spectrum. Therefore, only the OG530 filter was used in case of the EnviMeS instrument.

The measurements were performed in the following way. First, the spectrum $I_{NoFilter}(\lambda)$ of the tungsten lamp without the color glass filter was recorded at a fixed exposure time and number of scans, with λ describing the wavelength of the light. Then a lamp spectra $I_{Filter}(\lambda)$ with the filter was recorded with the same settings. Further, a background spectrum with no lamp was recorded to correct for dark current and electronic offset of the corresponding spectrometer.

The wavelength range of the spectrometers of both MAX-DOAS instruments is approximately 300 to 460 nm. In this spectral range the filters have transmittance of below 10^{-5} and therefore block the major part of the incident light (see figure
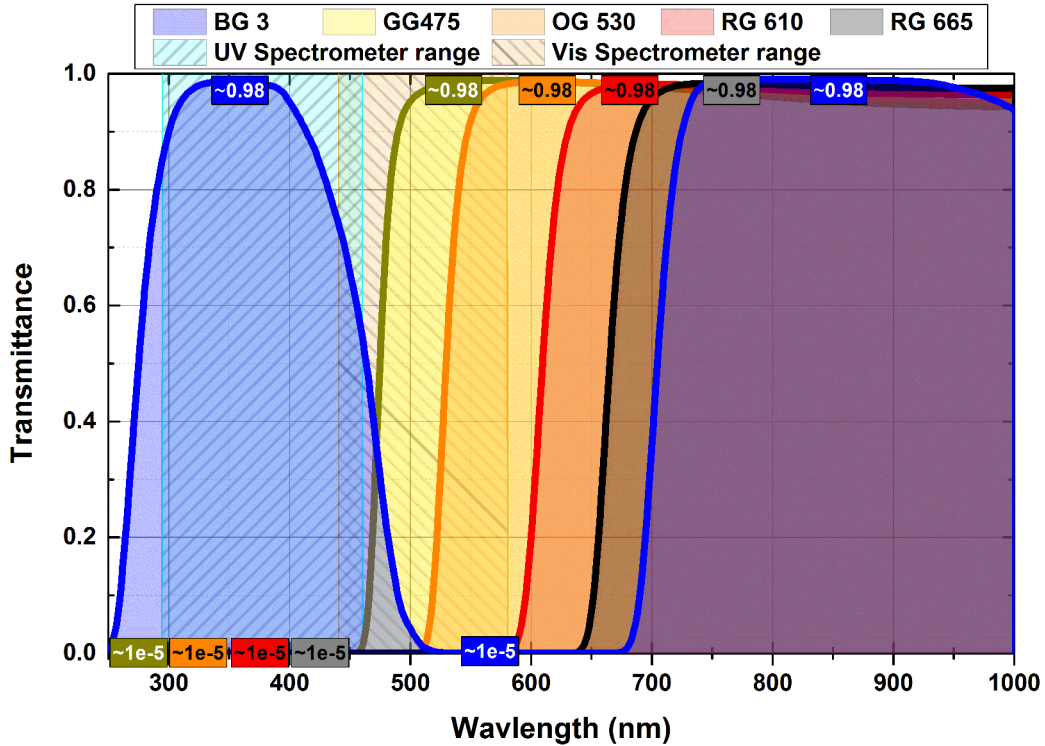
Fig. 5.5: Transmittance curve of the SCHOTT edge filters GG475 (dark yellow), OG530 (orange), RG610 (red), RG665 (black), the EnviMeS MAX-DOAS build-in SCHOTT BG3 band pass filter (blue) and the spectral range of the Avantes Spectrometers of the EnviMeS and ISA MAX-DOAS instruments (turquoise and orange shaded). All filters have a thickness of 3 mm. The colored labels show characteristic transmissions at the minima and maxima of the corresponding filter transmission curve.

5.5). Figure 5.6 shows spectra of the tungsten lamp taken without filter (upper plot) and with the OG530 filter (lower plot), both corrected for dark current and offset signal. The intensity of the spectrum recorded with the OG530 filter has a mean amplitude of 1 % to 2 % of the incident intensity which can be addressed to IDSL. The strongly wavelength dependent features at 312 nm and 380 nm are likely to be caused by non-diffuse reflection inside the spectrometer (IDSL type B, as mentioned above).

IDSL can be quantified by the ratio of stray light intensity $I_{Stray}(\lambda)$ to light intensity $I_0(\lambda)$ which is coupled in to the spectrometer. $I_{NoFilter}(\lambda)$ is the sum of
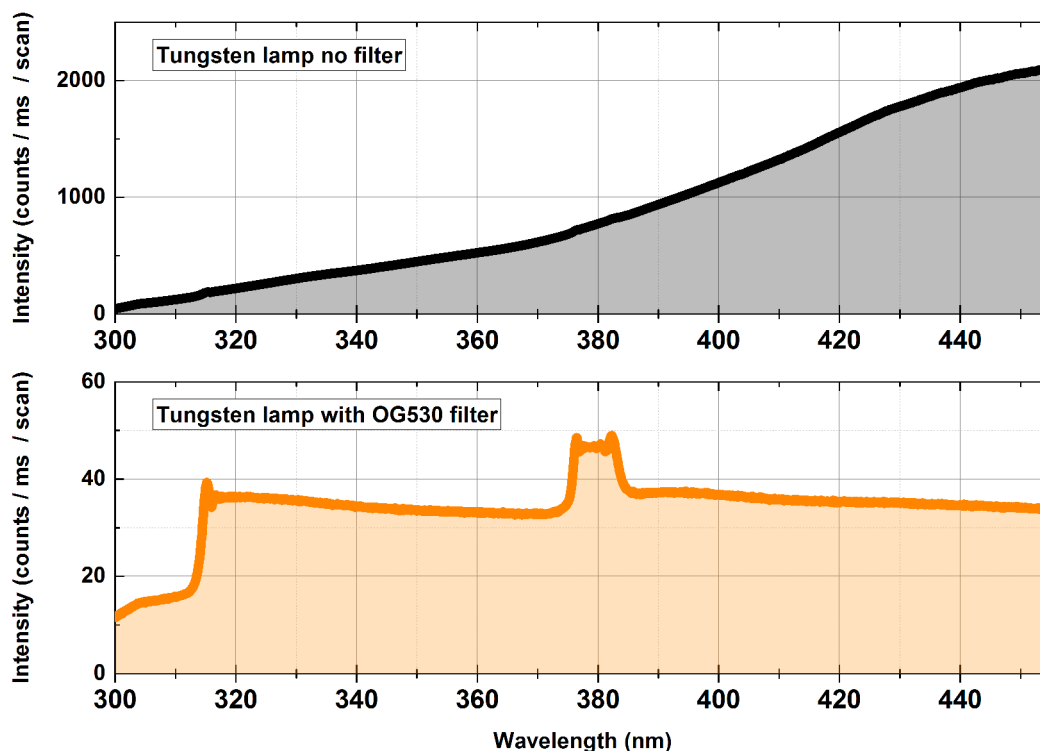
Fig. 5.6: **Top:** *Spectrum of a tungsten lamp recorded with the ISA MAX-DOAS instrument normalized to exposure time and number of scans.* **Bottom:** *Spectrum of the tungsten lamp using the OG530 filter which has a transmittance below 10^{-5} for light at wavelengths shorter than 530nm. The signals amplitude is about 1 % to 2 % of the incident intensity and can be addressed to instrument driven stray light. Both spectra were corrected for dark current and offset signal.*

the pure lamp spectrum plus stray light so the stray light intensity $I_{Filter}(\lambda)$ has to be subtracted to get $I_0(\lambda)$ (equation 5.1).

$$I_0(\lambda) = I_{NoFilter}(\lambda) - I_{Filter}(\lambda) \tag{5.1}$$

The contribution $S(\lambda)$ of IDSL on the measured light of an instrument can be calculated using equation 5.2. Dividing $I_{Filter}(\lambda)$ by $I_0(\lambda)$ provides the ratio of stray light and incident light. However, this would strongly dependent on the intensity distribution of the used light source and overestimates the stray light to light ratio at wavelengths where $I_0(\lambda)$ is small (e.g UV range vs. visible range of

tungsten lamp or scattered sunlight). By multiplying the ratio with a normalized lamp spectrum the spectral characteristic of the lamp is no longer affecting the result.

$$S(\lambda) = \frac{I_{Filter}(\lambda)}{I_0(\lambda)} \; \frac{I_0(\lambda)}{max\,[I_0(\lambda)]} = \frac{I_{Filter}(\lambda)}{max\,[I_0(\lambda)]} \tag{5.2}$$

This method is similar to how most manufacturers of spectrometers characterize their instruments as it apparently results in lower percentage of stray light. However, these characterizations are often done with a wide spectral range of several hundreds nanometers covering the peak wavelength of the used light source. The IDSL value in the manufacturer data sheets is calculated with respect to the global maximum of the light source leading to IDSL values below 10^{-3} for the Avantes spectrometers. The wavelength range of the MAX-DOAS spectrometers covers only a small part of the used light source excluding its peak (tungsten lamp used in laboratory measurements as well as solar spectrum during field measurements). With respect to DOAS, quantifying the additive contribution of IDSL on the measured intensity limited to the spectral range of the spectrometer using equation 5.2 is reasonable.

Instrument driven stray light of Avantes Spectrometers

Figure 5.7 shows the calculated stray light contributions of the EnviMeS and ISA MAX-DOAS instruments measured with a tungsten lamp. The combination of the built-in BG3 and OG530 filter indicates that the main contribution of IDSL originates from light in the wavelength range above 700 mn. Figure 5.7 bottom shows the IDSL signal of the ISA MAX-DOAS spectrometer, which has no built-in BG3 filter. The differences between the curves measured with different filters indicate that up to 25 % of the IDSL signal is caused by light between 500 and 650 nm (difference of GG475 and RG665 curve) while the dominant part of the IDSL (75 %) originates again from the range above 650 nm. The built-in BG3 filter of the EnviMeS instrument is positioned directly behind the entrance slit of the spectrometer. In this position the filter creates stray

light and contributes to the total IDSL signal (D. Pöhler, pers. communication). Thus, the total amount of IDSL is slightly higher for the EnviMeS MAX-DOAS. The differential IDSL structures at below 320 nm and at 380 nm occur in both spectrometers. However, they are shifted towards shorter wavelengths in the EnviMeS spectrometer which may be explained by a difference in the optical setups of the two Avantes spectrometers leading to different IDSL properties.
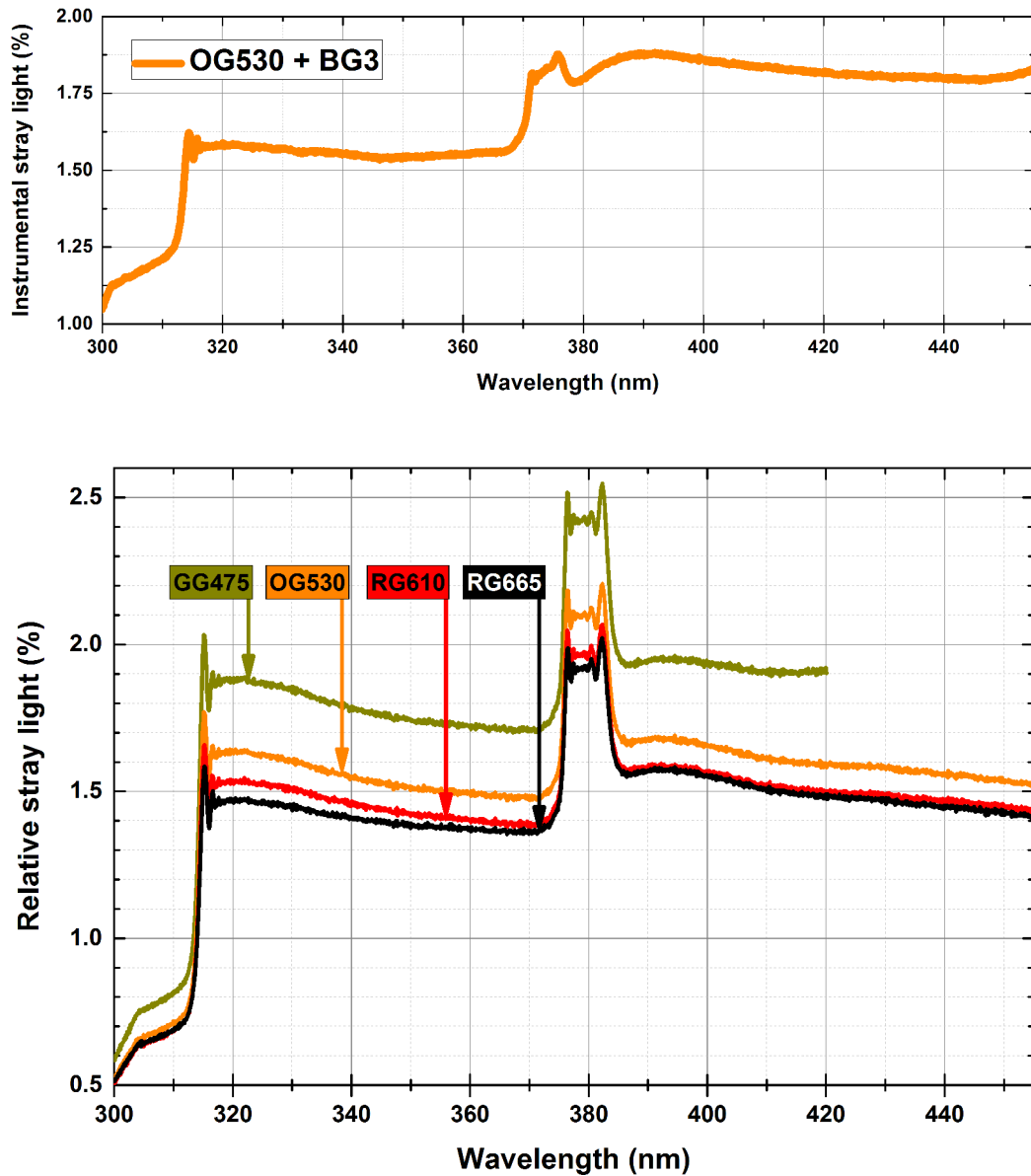
Fig. 5.7: The figure shows the measured instrument driven stray light of Avantes spectrometer measured with color glass filters GG475 (dark yellow), OG530 (orange), RG610 (red) and RG665 (black). **Top:** Stray light of the EnviMeS MAX-DOAS instrument which has a permanent build-in SCHOTT BG3 filter. The slight difference between the curves is caused by lamp instabilities. **Bottom :** Stray light of the ISA MAX-DOAS which has no build in BG3 filter. The different amplitudes of the curves indicate the spectral origin of the stray light signal. The dominating part (about 75 %) of the stray light originates from above 650 nm. Only 25 % originate from between 500 nm and 650 nm.

Differential IDSL structures

The differential structures at 315 nm and 380 nm seem to originate from light in the red and IR wavelength range. This can be shown by applying a high pass filter on the measured stray light calculated with formula 5.2 and dividing the curves measured with filters GG475, OG530 and RG610 by the one measured with RG665. Figure 5.8 shows the result. The division by the RG665 curve reduces the structures by approximately 80 % meaning that mainly light from the range above 650 nm is causing the differential stray light structures. However, the spectral properties tungsten lamp which was used to characterize the IDSL signal of the EnviMeS and ISA MAX-DOAS might not be representative for field measurements. Especially in the range above 650 nm, the tungsten lamp might have a higher intensity relative to the UV/vis range compared to scattered sunlight.
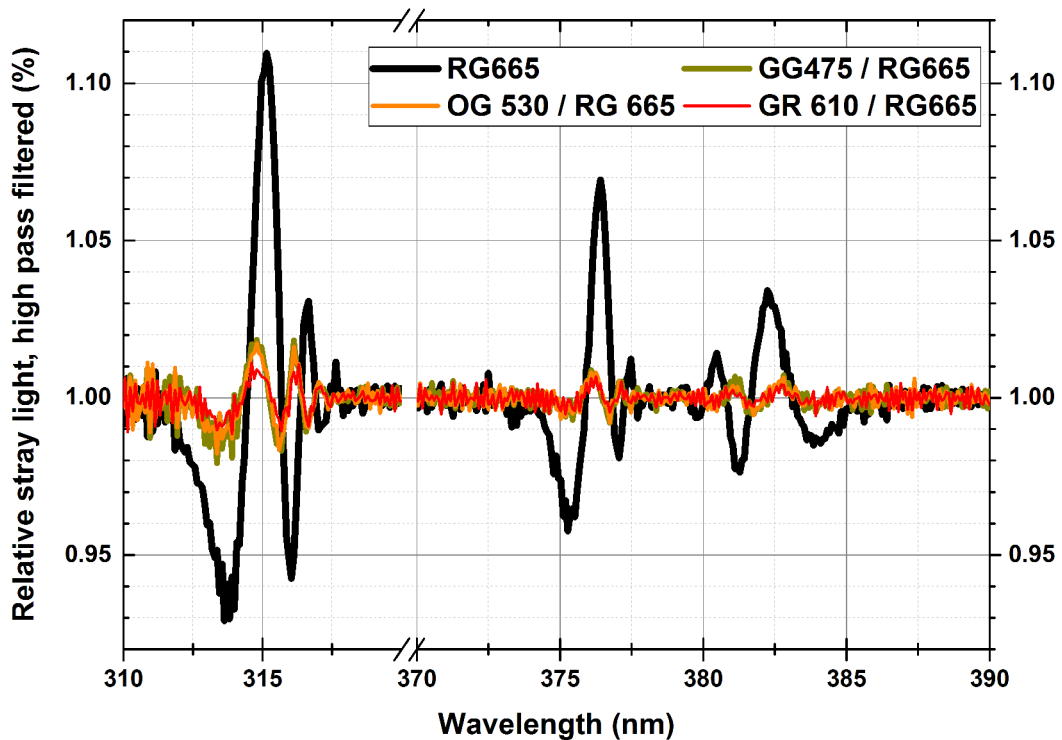
Fig. 5.8: The black line shows the high pass filtered (DOASIS high pass filter, 100 iterations)stray light spectrum measured with the RG655 filter using a tungsten lamp. The dark yellow, red and orange curve show the high pass filtered stray light spectra measured with filters GG475, OG 530 and RG610 divided by the black curve. This indicates that the differential structures at 315 nm and 380 nm originated mainly from light in the red and IR wavelength range. Note: The differential structures may have another characteristic when using a different light source (e.g. LED or scattered sunlight).

Conclusion of IDSL measurements

Stray light experiments were performed using a tungsten light source. It could be show that the stray light contribution for compact Avantes spectrometer (Type AvaBench-75 (ULS2048x64-U2)) with a wave length range of 300 nm to 460 nm can be up to 1.9 % of the true measured light signal when using this experimental setup. The stray light signal has differential features at 380 nm and below 320 nm. By using multiple color glass filters it could be shown that up to 25 %

of the total IDSL signal originate from light in the range of 500 nm to 650 nm. The rest of the IDSL as well as its differential features are mainly caused by light in the red and infra red region above 650 nm. Since the tungsten lamp has a significant light output above 650 nm this results may overestimate the IDSL contribution (especially its differential part) when measuring scattered sunlight during MAX-DOAS measurements. However, a lower limit of IDSL can be estimated by comparing the intensity in the UV spectrometer with the intensity of the vis spectrometer (see figure 5.9 upper plot).

During the experiments with the tungsten lamp an intensity ratio of 8.5 between 550 nm and 400 nm lead to an additional IDSL contribution of 0.4 % in the range of the UV spectrometer. The lower plot in figure 5.9 shows spectra of scattered sunlight recorded with the EnviMeS MAX-DOAS during the Dead Sea field campaign in 2014 under a telescope elevation angle of 90° (zenith). To account for different meteorological situations, a spectrum during clear sky (blue) and cloudy sky (gray) is displayed. The 550 nm to 400 nm ratio varies between 1 and 2.25 for clouds. Assuming a linear correlation of this ratio to the IDSL originating from the range of 500 nm to 650 nm this leads to a lower IDSL limit of 0.047 % and 0.11 % for clear sky and cloudy sky respectively. Section 5.1.5 will show that not only the amount of IDSL is critical for the DOAS analysis but more the difference of IDSL of spectra taken under different elevation angles. The contribution of red and IR light is probably in the order of 1 % of the total measured intensity and cannot be quantified from the measurements. Nevertheless, the ratio of UV and visible intensity (spectral color index, see section 5.1.5) can be used as a proxy for the strength of IDSL during MAX-DOAS measurements.
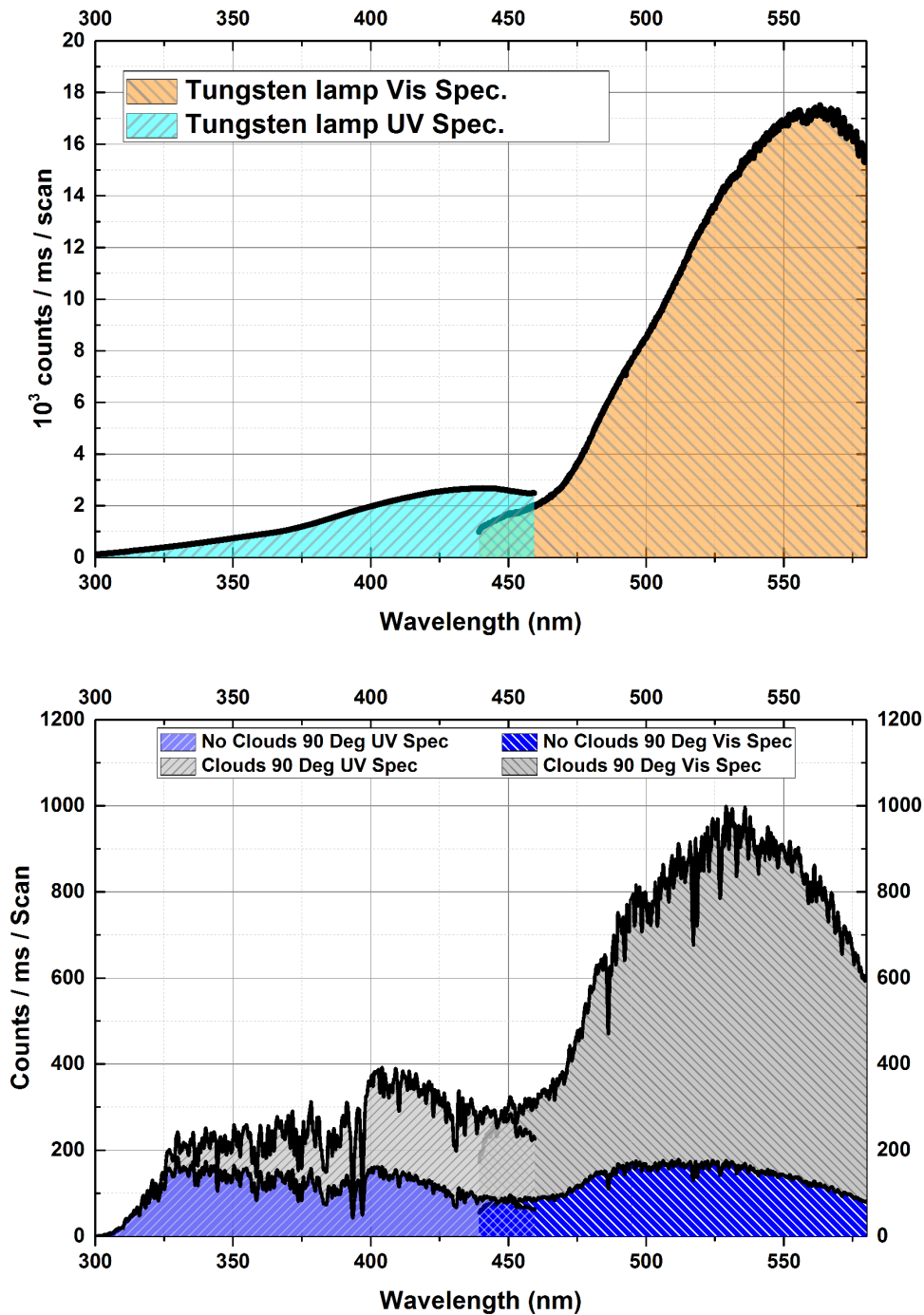
Fig. 5.9: **Top:** *Tungsten lamp spectrum measured with the UV and vis spectrometer of the EnviMeS MAX-DOAS instrument. Note that the fiber configuration is different for the two spectrometers. The UV spectrometer has 6 fibers while the vis spectrometer has only 1 fiber. Nevertheless, by comparing the shown curve with the curve of scattered sunlight* **Bottom:** *one can estimate the representativeness of the laboratory measurements for field measurements.*

5.1.3 Data acquisition

For the acquisition of all MAX-DOAS data the software MS-DOAS (U. Frieß pers. comm.) was used. Elevation angles, time resolution and sensor saturation of all MAX-DOAS instruments is summarized in Table 5.5. In case of the instrument at Ein Bokek 80° was chosen as reference elevation since the field of view at 90° was blocked by a balcony. For all other instruments, the reference spectra were taken at 90° elevation angle. The exposure time for single spectra was optimized to ensure a constant saturation. By adjusting the number of averaged single scans a constant time resolution was achieved. All parameters of the acquisition are summarized in table 5.5. Dark current and offset spectra were taken manually by blocking the telescope entrance or automatically during nights. Also, spectra of mercury emission lamps, needed for wavelength to pixel mapping and convolution of reference cross sections (see section 5.1.4), were taken manually during the campaigns.

Measurement site (year)	Time res. [sec]	Sat. [%]	Elev. angles [°]
Ein Bokek 2012	60	50	80, 20, 10, 5, 2, 1, 0, -5
Masada top 2012	20	50	90, 10, 5, 2, 1, 0, -1, -2, -5, -10, -28
Masada bottom 2014	60	60	90, 20, 10, 5, 2, 1, 0
Neve Zohar, Ein Gedi 2014	60	60	90, 20, 10, 5, 2, 1, 0
Car borne 2014	2	60	20, 2 or 10, 5

Table 5.5: Data acquisition settings for MAX-DOAS instruments.

5.1.4 DOAS analysis

The data of all MAX-DOAS instruments was analyzed with the same setup in terms of fit ranges and used reference cross sections, and temporal averaging of spectral data to maintain consistency. However, the mobile MAX-DOAS measurements were analyzed with a different temporal averaging. The analysis was done using an algorithm realized in JScript/DOASIS (Kraus [2006]). The used algorithm was originally written by Udo Frieß (pers. comm.) and was modified

for this thesis. Among minor changes, spectral averaging, IDSL correction, accounting for drifts in wave length to pixel mapping and features for the evaluation of data sets measured on mobile platforms were added.

Offset and dark current correction

Prior to any operation performed on the spectral data, all spectra are corrected for offset and dark current signal. Therefore an offset spectrum with minimal exposure time and typically 10.000 cans was recorded. A dark current spectrum was recorded with a rather high exposure time of 10 to 30 seconds (depending on the instrument) and one scan per spectrum. After correcting the offset of the dark current spectrum, all measured spectra were corrected with respect to the number of scans and exposure time.

Wavelength calibration and convolution of literature cross sections

To get the correct wavelength to pixel mapping spectra of a mercury lamp were recorded once the spectrometers temperature was stable. Applying the wavelengths of the dominant mercury emission lines from literature, the spectrometer can the be calibrated. Since the true width of the lines is in the sub-picometer range (see figure 5.10 taken from Sansonetti et al. [1996]) and cannot be resolved by the used spectrometer, the measured emission lines can be approximated as the instrument response function with sufficient accuracy. Five lines, labeled in figure 5.11, were used for the calibration.
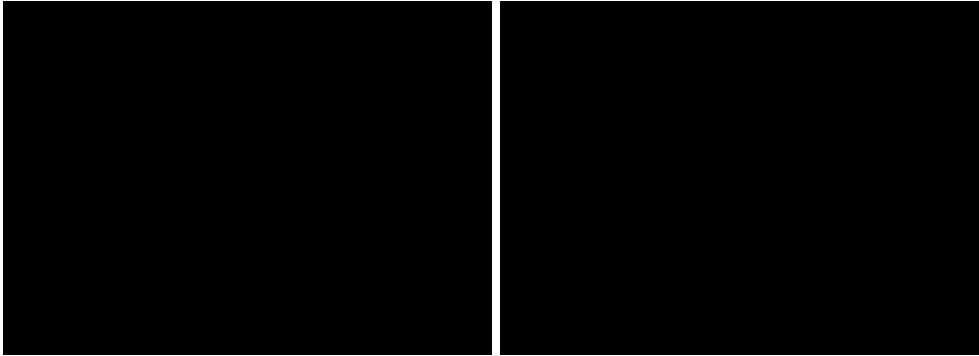
Fig. 5.10: **Left:** *Mercury line recorded with a resolution of 0.5 pm.* **Right:** *The same spectrum with resolution of 0.016 nm. Adapted from Sansonetti et al.* *[1996].*

The center pixel of the emission lines were determined by fitting a Gaussian curve. A polynomial of the order of three was fitted on the collection of emission line pixels to retrieve a continuous dispersion relation over the whole spectral range of the respective spectrometer. Further, an additional calibration was performed using the high resolution solar reference spectrum by Chance and Kurucz [2010]. For details about this method see Lampel [2014].The solar reference spectrum was convolved with the measured mercury line at 435.9 nm and fitted in small wavelength windows to a dedicated spectrum which was measured under a telescope elevation angle of 90° during the corresponding field campaign. A Ring spectrum and Ring$\cdot\lambda^4$ spectrum of the convoluted solar spectrum was included in the fit as well as NO_2, O_3, O_4 and H_2O absorption cross sections (Table 5.6). The fit ranges had an extend of approx. 20 nm and was shifted along the spectral range of the spectrometer from 330 nm to 440 nm with an increment of 0.7 nm. Using the DOASIS software, a polynomial was fitted to the shifts from the fits of every single fit window. The resulting polynomial represents a correction of the initial pixel to wavelength mapping by adding it to the initial polynomial gained from the mercury lines.

To adapt the high resolution literature cross section to the spectral resolution of the instrument a convolution with the measured mercury lines was performed.

For fit scenarios in the wavelength range below 400 nm, the 334 nm mercury line was used for the convolution. For fit scenarios in the range above 400 nm the 435 nm mercury line was used. Thus, a possible effect of a wavelength dependency of the slit function is minimized.
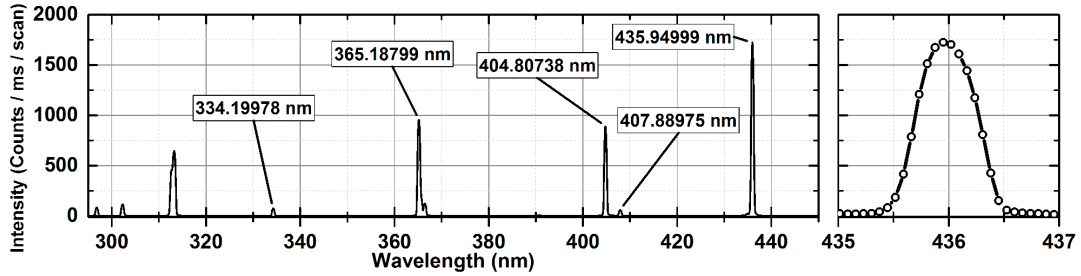
Fig. 5.11: **Left:** *Spectrum of a mercury emission lamp recorded with the UV spectrometer of the EnviMeS MAX-DOAS during the 2014 Dead Sea field campaign.* **Right:** *Zoomed in on the 435.95 nm line. The white dots represent the channels of the spectrometer showing that the line is sufficiently sampled. FWHMis approximately 0.56 nm.*

Spectral averaging

To increase the sensitivity to trace gas concentrations, the spectral data of the stationary MAX-DOAS measurements within one hour were averaged in order to maintaining a reasonable time resolution to sample the dynamics. A running mean filter was applied. This corresponds to an average of six to seven recorded spectra (equal to 2000 - 4000 single scans) for each telescope elevation angle. In the following the time stamps of the shown data points are defined by the center time of the averaged spectrum (see figure 5.12 for visualization). Even though different solar geometries (solar zenith angles, air mass factors) are averaged, the running mean filter had no negative effect on the quality of the profile retrieval which is described in section 5.1.7.
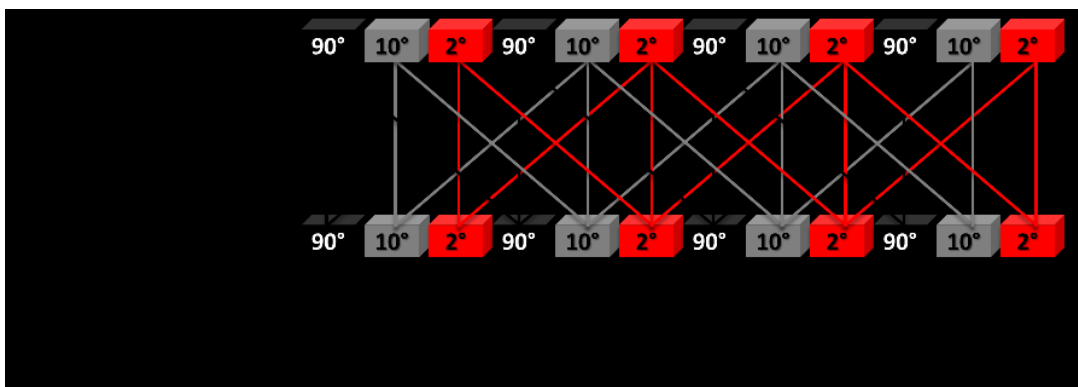
Fig. 5.12: Exemplary visualization of the spectral averaging prior to the DOAS analysis. A running mean is performed over equidistant spectra of the same elevation angle. For simplicity, only three elevation angles are shown (90°, 10°, 2°). The measurements were averaged over a time span of one hour corresponding to 6-7 recorded spectra.

Temperature dependency of the Ring spectrum

Figure 5.13 shows the difference in Ring spectra which are calculated with DOA-SIS (Bussemer [1993], Kraus [2006]) using different temperatures. Ring spectra calculated at 213 K and 273 K can have a difference by up to 5 % which is strongly differential with respect to the wavelength especially below 400 nm and potentially affecting the DOAS analysis of BrO and HCHO. To account for this effect, the temperature dependence of the Ring spectrum was linearized by using the difference of two Ring spectra calculated at 213 K and 273 K (J. Lampel, pers. comm.). For the analysis of all MAX-DOAS data in this thesis, the difference spectrum of the current Ring spectra was included in the fit.
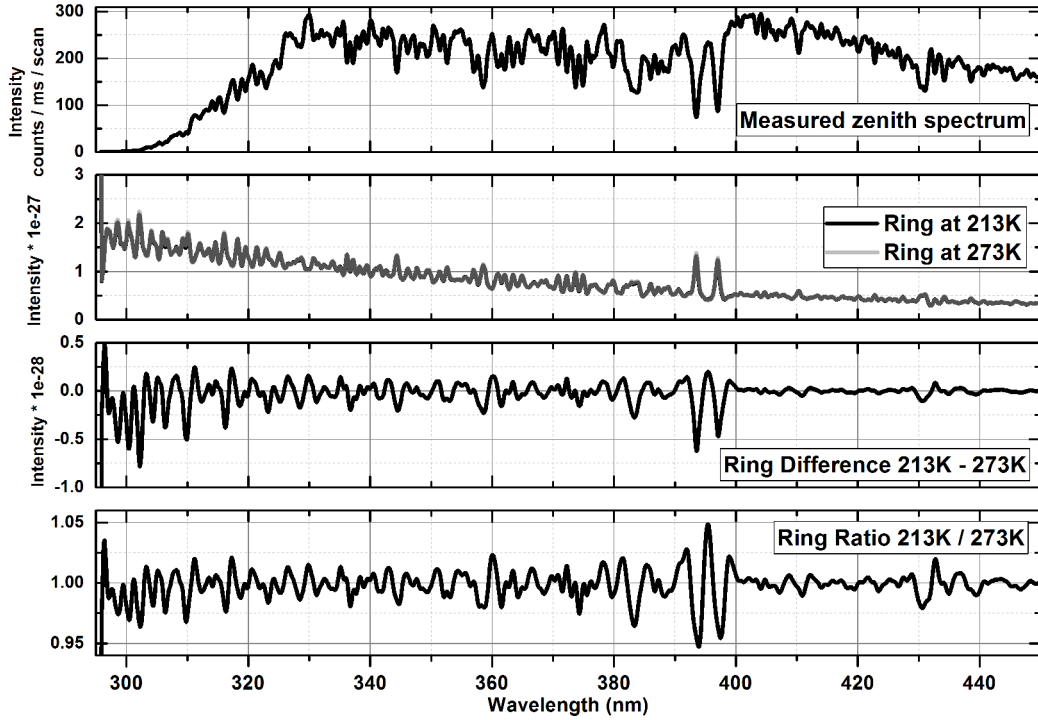
Fig. 5.13: Effect of different temperatures on the calculation of the Ring spectrum using DOASIS. **Top:** *Spectrum recorded by the EnviMeS MAX-DOAS instrument on Nov 5 2014 09:21 UTC during the Dead Sea campaign. Telescope elevation angle: 90°. SZA = 47.02.* **2nd from top:** *Ring spectra at 213 K and 273 K calculated from the measured zenith spectra using DOASIS.* **3rd from top:** *Difference spectrum of Ring spectra at 213k and 273K, which is included in the fit scenarios MX1 to MX4.* **Bottom:** *Ratio of Ring spectra at 213 k and 273 K.*

DOAS fit settings

Tables 5.6 and 5.7 give an overview of the reference cross sections and fit scenarios used for the analysis of the MAX-DOAS data. The choice of reference cross sections and fit ranges is based on the findings from Lampel [2014]:

- Using the O_4 literature cross section by Greenblatt et al. [1990] reduces spectral interference of O_4, BrO, and HCHO in the wavelength range of 332 nm to 358 nm.

- Correction of the water vapor cross section by Rothman et al. [2010] as supported by ship based MAX-DOAS measurements (see also Lampel et al. [2014]), optimizes the IO analysis with respect to the absorption of water vapor.

- Calculation of additional pseudo absorbers to account for vibrational Raman scattered sunlight of N_2 and O_2 molecules within the DOAS analysis which lead to reduced residuals and, hence, to an increase in the sensitivity for IO of up to 30 %.

All spectra were evaluated against a current zenith reference recorded with a telescope elevation angle of 90°. Due to the wavelength calibration with the high resolution solar spectrum and the temperature stabilization of the Avantes spectrometers, squeezing could be disabled in the spectral evaluation (i.e. squeeze was fixed to 1). Further the fit coefficient of the zenith spectrum was fixed to -1. To account for instrument driven stray light (IDSL, see section5.1.5) the reciprocal spectrum and the squared reciprocal spectrum of the current measurement spectrum was included in all fit scenarios. The parameters for shift of the zenith spectrum and the IDSL correction were unconstrained. The result were shift values close to zero. However, the residual structures were slightly lower compared to fixing the shift fixed to zero which is probably due to numerical inaccuracy caused by the interpolation made during the wavelength to pixel calibration via polynomial.The Ring spectra are calculated from the measured spectra. Therefore, the shifts of all the Ring were linked to the current reference.

The shifts of all other fit constituents (except for O_4, see below) were linked to each other but otherwise unconstrained. In this way, all references which carry the calibration of the solar calibrated mercury line spectrum, were shifted in the same manner if needed (e.g. drift of spectrometer temperature followed by a change in the wavelength to pixel mapping).

The shift of O_4 was set free. Especially for fit scenario MX4, large residual structures occurred if the shift of O_4 was linked to those of the other trace gases. Recent findings by Lampel et al. [2014] and J. Lampel (pers. comm.) revealed that a shift of the O_4 cross section in the wavelength range of 350 nm to 370

nm could compensate for an absorption band of water vapor which has yet been neglected in line data bases like HITRAN Rothman et al. [2013] or HITEMP Rothman et al. [2010]. This has to be considered for the interpretation of the following example fits.

Further, a DOAS polynomial of the was applied to the fit scenarios (order of three for MX1 to MX3 and MX5, oredr of one for MX4). For fit ranges and fit constituents of the fit scenarios refer to Tables 5.6 and 5.7.

Gas species	Index	Reference
BrO	1	Fleischmann et al. [2004]
$C_2H_2O_2$	2	Volkamer et al. [2005]
H_2O	3	HITEMP, Rothman et al. [2010]
		Lampel et al. [2014]
HCHO	4	Meller and Moortgat [2000]
HONO	5	Stutz et al. [2000]
IO	6	Spietz et al. [2005]
NO_2	7	Vandaele et al. [1998]
O_3 (293K)	8	Bogumil et al. [2003]
O_3 (223K)	9	Bogumil et al. [2003]
O_4	10	Greenblatt et al. [1990]
OClO	11	Bogumil et al. [2003]
SO_2	12	Bogumil et al. [2003]
Current Ring spectrum	13	Bussemer [1993], Kraus [2006]
Current Ring spectrum$\cdot\lambda^4$	14	Bussemer [1993], Kraus [2006]
Difference spectrum of Ring at 273 K and 213 K	15	Bussemer [1993],Kraus [2006]
		J. Lampel (pers. comm.)
VRS N_2	16	Lampel [2014]
VRS O_2	17	Lampel [2014]
reciprocal measurement spectrum	18	IDSL correction
reciprocal measurement spectrum squared	19	IDSL correction
Current zenith reference spectrum	20	from measurement

Table 5.6: Literature cross sections used for the spectral analysis of MAX-DOAS data.

Fitscenario Index	Wavelength intervall [nm]	Retrieved trace gas	Reference included (see Table 5.6)	DOAS Poly. Order
MX1	332-358	**BrO, HCHO**	1,4,5,7,8,9,10,12,13,14,15,16,17,18,19,20	3
MX2	348.5-373	**O$_4$, HONO**	1,4,5,7,8,9,10,12,13,14,15,16,17,18,19,20	3
MX3	418-441.9	**IO, NO$_2$**	3,6,7,13,14,15,16,17,18,19,20	3
MX4	439.5-457.9	**H$_2$O, C$_2$H$_2$O$_2$**	2,3,6,7,8,9,10,13,14,15,16,17,18,19,20	1
MX5	332.8-364.2	**OClO**	1,4,5,7,8,9,10,11,12,13,14,15,16,17,18,19,20	3

Table 5.7: Specifications of the fit scenarios used for the spectral analysis of the MAX-DOAS data. The numbers in column "Reference included" refer to Table 5.6.

Temperature variations of the spectrometer of the Ein Bokek MAX-DOAS and its treatment in the data evaluation

During the campaign in May 2012, the spectrometer housing of the MAX-DOAS instrument at Ein Bokek suffered from temperature drifts which lead to a variation of the wavelength to pixel mapping in the range of +/- 0.5 nm. Due to the strong shift variations, the DOAS fit was usually not able to converge to the right minimum. Especially at high column densities of one of the fit constituents (e.g. NO$_2$ after sunrise) negative column densities of the corresponding constituent were fitted implicating high residual structures. Since the difference between the initial wavelength calibration and the current calibration was large, the DOAS fit may converge to another, unphysical minimum of its cost function which implied a smaller shift relative to the initial wavelength calibration.

To treat this problem, the data set of the Ein Bokek MAX-DOAS was analyzed using a dynamic initial default shift value of the appropriate constituents in the fit scenarios (see flow chart in figure 5.14). Therefore, three iterations of the DOAS fit were performed with each fit scenario. Within each iteration, the default shift value (or shift starting condition) of the constituents (except the current reference spectrum, Ring spectra and IDSL corrections) is incremented. In the case of the Ein Bokek instrument, best choice for the increment was -0.5 nm starting with a starting value of the default shift of 0 nm. The RMS values of the three iterations with default shift values of 0 nm, -0.5 nm and -1 nm,

respectively, are compared and the fit result with the lowest RMS value is chosen. After the optimization of the default shift value, the algorithm checks if the current column density of NO_2 is above a threshold of six times the corresponding fit error. If this is the case, the squeeze of the fit constituents (again without the squeeze of the current reference spectrum, Ring spectra and IDSL corrections, all squeezes are linked) as set free. If this fit leads to better results (lower RMS) it was declared to be the final result, otherwise the fit with fixed squeeze is final. The high column density of NO_2 keeps the fit stable though having an additional free parameter.
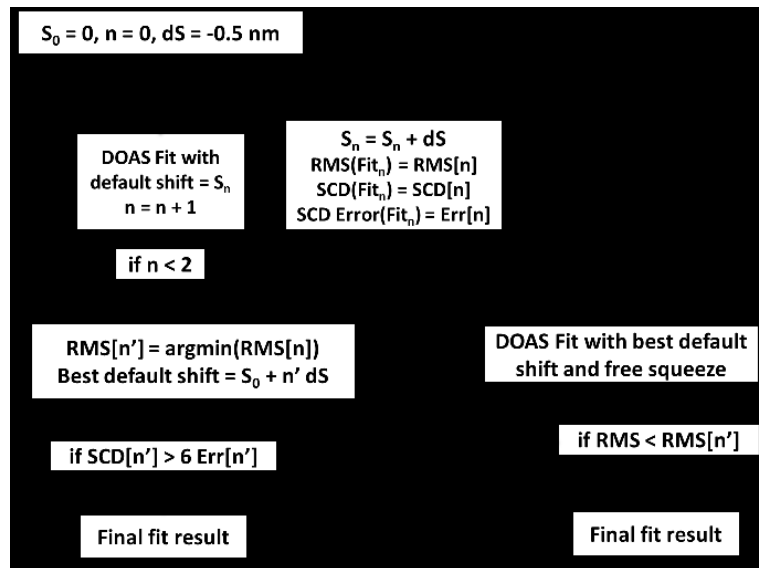
Fig. 5.14: Flow chart of the optimization of the default shift value (in nm) for the DOAS fit. This algorithm prevents false results in the case of strong variations in the wavelength to pixel mapping e.g. caused by strong temperature shifts of the spectrometer housing.

5.1.5 Impact of instrument driven stray light (IDSL) on the DOAS analysis

This chapter will describe how IDSL can affect the DOAS analysis and what can be done to minimize these effects. Chapter 5.1.2 revealed that the IDSL signal of the used spectrometers is free of differential structures in the wavelength where the DOAS fits are performed. Therefore, the following text only covers the correction of constant stray light (IDSL Type A) and neglects differential structures (IDSL Type B).

Theoretical consideration of IDSL within the DOAS analysis

Let $I_0(\lambda)$ be the spectrum measured under a telescope elevation angle of 90° and $I(\lambda)$ the spectrum measured under 0°. In the following the instrument driven stray light is assumed to be constant over the spectral range of the measured signal $I_0(\lambda)$ and $I(\lambda)$ and is defined by c_0 and c, respectively. The optical density D with respect to IDSL is given by equation 5.3.

$$D = -\ln\left[\frac{I(\lambda) + c}{I_0(\lambda) + c_0}\right] = -\ln(I(\lambda) + c) + \ln(I_0(\lambda) + c_0) \qquad (5.3)$$

Using the taylor expansion of $\ln(I(\lambda) + c)$ in c:

$$\ln(I(\lambda) + c) \approx \ln I(\lambda) + \frac{c}{I(\lambda)} - \frac{c^2}{2\,I^2(\lambda)} + O\left[\frac{1}{I^n}\right] \qquad (5.4)$$

one can rewrite equation 5.3 leading to

$$-D \approx \ln I(\lambda) - \ln I_0(\lambda) + \underbrace{\frac{c\,I_0(\lambda) - c_0\,I(\lambda)}{I(\lambda)\,I_0(\lambda)} - \frac{c^2\,I_0^2(\lambda) + c_0^2\,I^2(\lambda)}{2\,I^2(\lambda)\,I_0^2(\lambda)}}_{IDSL} + \dots \qquad (5.5)$$

The last term of equation 5.5 represents a coarse approximation of a constant stray light (free of differential structures) in terms of optical density (typically ≈ 2 % and $\approx 2*10^{-4}$ for the first and second term respectively, compare with chapter 5.1.2). It also shows that if both measurements $I_0(\lambda)$ and $I(\lambda)$ have the same amount of stray light and their intensities are similar, the stray light term is minimized. That means that the stray light problem for DOAS measurements originates not only from the fact that an instrument suffers from instrumental driven stray light. The difference of IDSL signals in $I(\lambda)$ and $I_0(\lambda)$ (measurement and reference) seems to potentially affect the DOAS evaluation. In the case of a non-constant, wavelength dependent stray light, the different terms of equation 5.4 have to be modulated with a wavelength dependent polynomial.

Definition of the spectral color index

As described in section 5.1.2 the IDSL signal in the range of 300 nm to 460 nm is mainly caused by light in the red to IR region and therefore proportional to the ratio of the intensities in UV and visible wavelength region. In the following the ratio of intensities at 330 nm and 400 nm is defined as the "color index". The color index can be used as a rough indication for the amount of IDSL since it is proportional to the ratio of intensities of the light of interest and the light which is causing IDSL. Further, the color index is correlated to clouds which enhance the measured ratio of visible to UV light. Figure 5.15 visualizes the definition of the color index. The spectra were recorded under clear sky (blue) and cloudiness (gray) with a telescope elevation of 90° (zenith) while solar azimuth and zenith angle were similar. In this example the color index of clear sky and clouds are roughly 1.4 and 0.9 respectively.

The color index is also influenced by the strength of total atmospheric scattering and thus by different solar zenith angles (SZA). At high SZAs (sun close to horizon), air mass factors are large and a significant part of the UV radiation is reduced due absorption caused by ozone and Rayleigh scattering. At low SZAs (sun close to zenith) air mass factors are smaller and thus UV radiation is less attenuated. Figure 5.16 shows the correlation of the zenith color index

and the color index under lower telescope elevations measured by the EnviMeS MAX-DOAS and the SZA at particular clear weather conditions during the 2014 campaign at the Dead Sea. The color index varies strongly with the telescope elevation angle. At low telescope elevation angles, the light is affected by scattering in the lower part of the atmosphere were the air number density and the abundance of aerosols is usually higher compared to the atmosphere which is observed under larger telescope elevation angles (e.g. at 20°). This additionally decreases the color index leading to different color indexes for small and large telescope elevations.
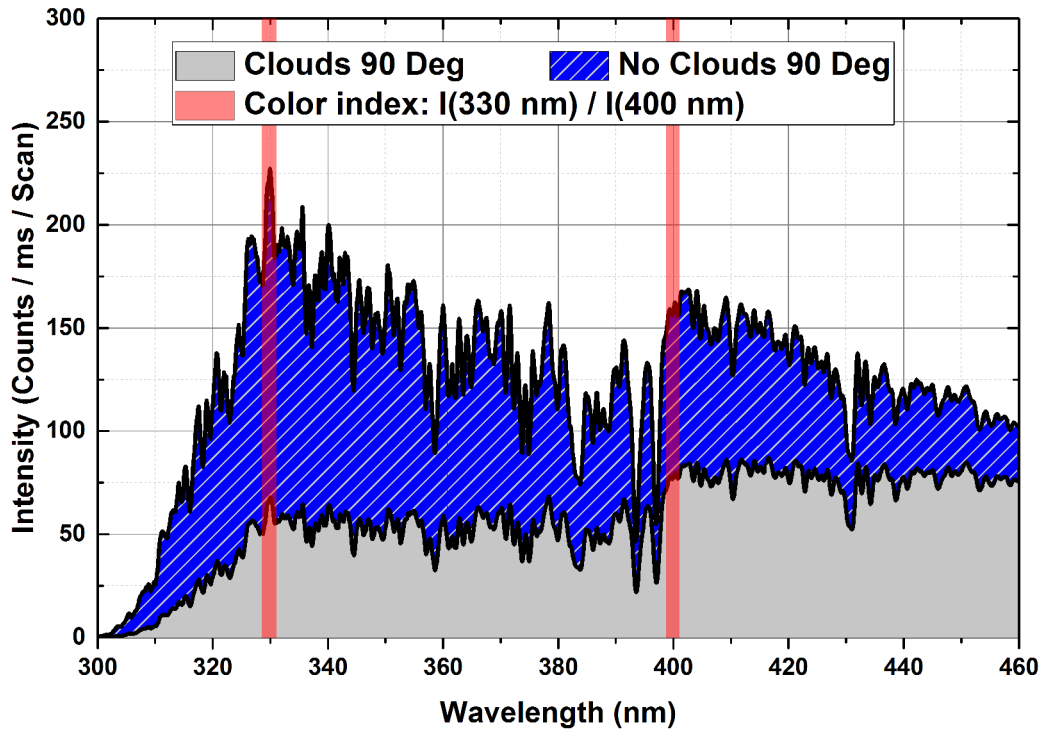
Fig. 5.15: **Top:** *Zenith spectra taken by the ISA MAX-DOAS instrument during the Dead Sea campaign in 2014. Both spectra were taken under similar geometric conditions (solar azimuth and solar zenith angle) but with different meteorologic conditions. The blue spectrum was recorded during clear sky while the gray spectrum was recorded during cloudiness. The red bars mark the wavelengths which are used to define the color index.* **Bottom:** *Meteorological conditions during which the spectra where taken (taken by KIT sky camera near the position of the MAX-DOAS instrument).*
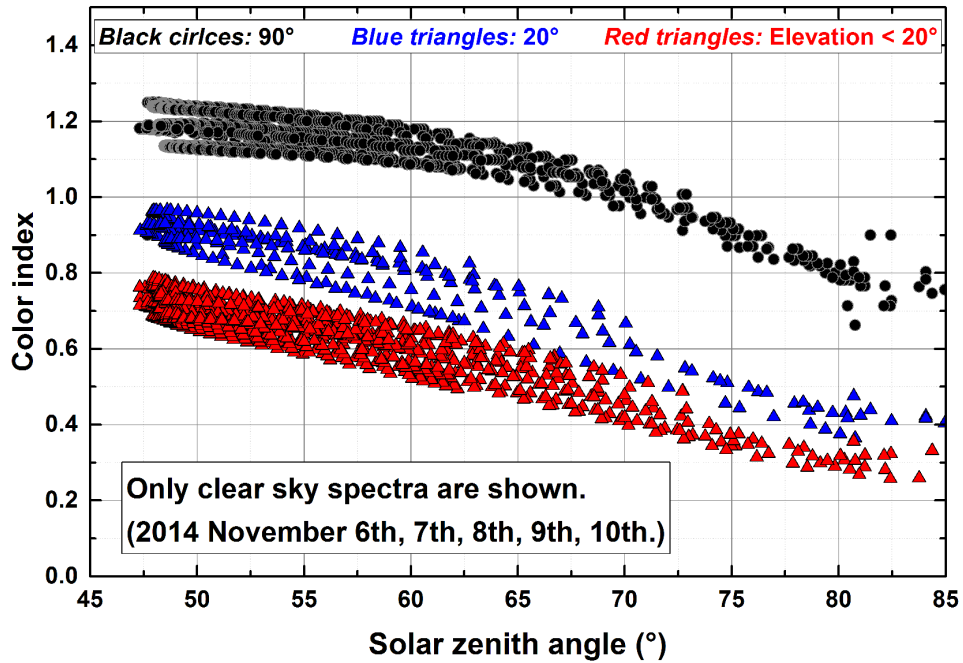
(a) The plot shows the correlation between the color index at different telescope elevation angles (**black circles:** 90°; **blue triangles** 20°; **red triangles** 10°, 5°, 2°, 1° and 0°) and the solar zenith angle during clear sky conditions and low aerosol load. The data was recorded by the EnviMeS MAX-DOAS on the days of 6th, 7th, 8th, 9th and 10th November during the Dead Sea campaign in 2014.
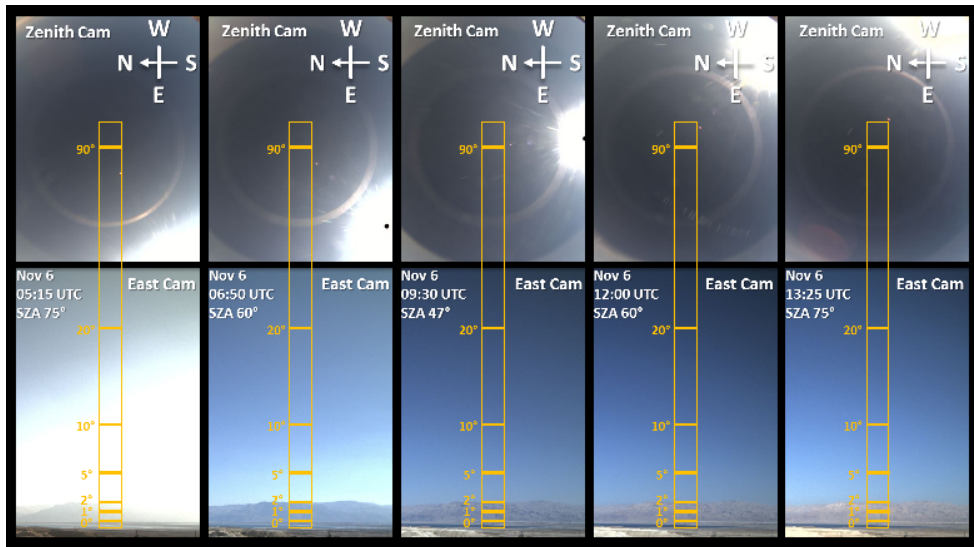
(b) Web cam pictures taken on the 6th of November 2014 during clear sky conditions at different SZAs. The yellow frame indicates the field of view of the telescope of the EnviMeS MAX-DOAS instrument, approximated from a simple geometric Ansatz using the altitude of the instruments and of the edge of the mountains. The distance to the mountains on the other side of the Dead Sea Valley is about 18 km.

Fig. 5.16

Increased RMS values during clear sky conditions

The DOAS analysis of the spectra recorded by both MAX-DOAS instruments during the Dead Sea campaign in November 2014 showed unusual high residual structures especially in the spectral range of the IO analysis. The residual structures correlate to clear sky conditions and therefore to the color index of the corresponding 90° zenith reference spectrum. In figure 5.17, a time series of RMS values of the IO fit of both MAX-DOAS instruments is displayed for Nov 25th 2014, where cloud conditions changed within a few hours. Both instruments show increased RMS values at high solar radiation. Once clouds are above the instruments (starting at 10:00 UTC) RMS values get significantly better especially in case of the ISA MAX-DOAS. Figure 5.18 (left plots, red) shows the correlation between the ratio of the color index in zenith direction and under lower telescope elevation angles and the strength of the residual structures (RMS). The middle and right plots (blue and black) show the effect of IDSL correction on the correlation of color index ratio and RMS. The plots show only data of spectra with sufficient high intensity (counts per exposure time per scans) to avoid high RMS values caused by low light during cloudiness (due to domination by photon noise). The residual structures could be minimized by including the reciprocal and the reciprocal squared, $I(\lambda)^{-1}$ and $I(\lambda)^{-2}$ of the spectra taken under low elevation angles in the fit, according to equation 5.4. Figure 5.18 (blue and black dots, middle and right plots) show how the correction reduces to total RMS values as well as weakens the correlation between RMS and zenith color index, when applying different corrections. As expected, the IDSL correction has a huge impact on the RMS values during clear sky while its impact is only low during cloudiness (compare red, blue and black dots at high solar radiation in figure 5.17). Further, it is noticeable that the ISA MAX-DOAS is more sensitive to IDSL in the spectral range of IO (418 nm to 441.9 nm) while the EnviMeS is more sensitive in the spectral range of BrO (332 nm to 358 nm). Having the same type of spectrometer, the different characteristics may be caused by the build-in BG3 filter but also by differences in the optical setup of the instruments (spectrometer wavelength range, fiber configuration).
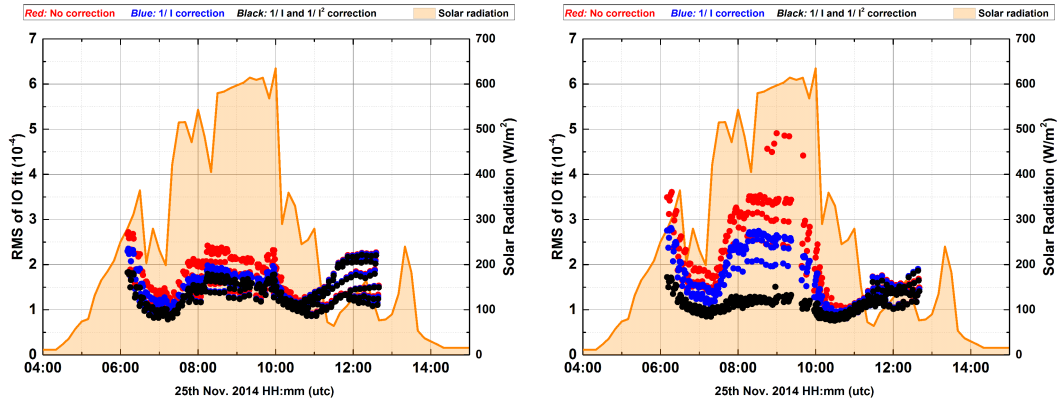
(a) EnviMeS MAX-DOAS RMS in IO fit range.

(b) ISA MAX-DOAS RMS in IO fit range.
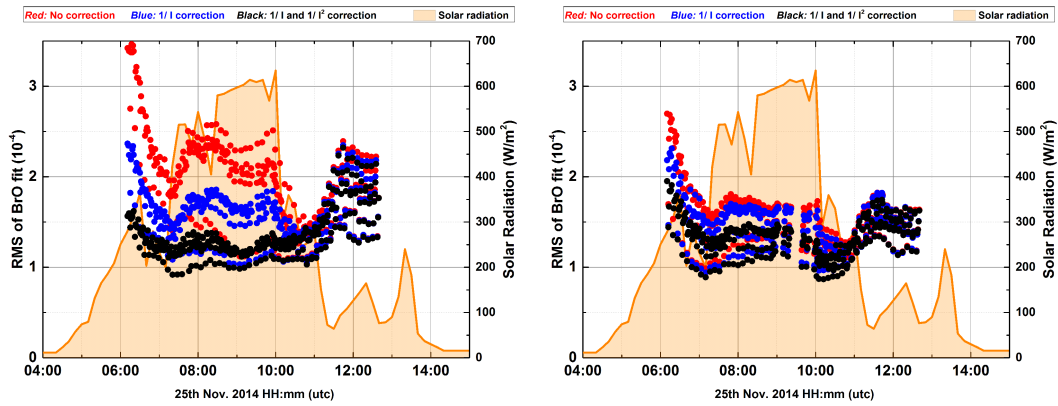
(c) EnviMeS MAX-DOAS RMS in BrO fit range.

(d) ISA MAX-DOAS RMS in BrO fit range.

(e) KIT Cube sky cam. 09:00 utc   (f) KIT Cube sky cam. 10:30 utc

Fig. 5.17: The upper and middle plot show the time series of RMS values from the IO fit and BrO fit of both the EnviMeS (build-in BG3 filter), plots (a) and (c)) and the ISA MAX-DOAS (no BG3 filter), plots (b) and (d). RMS values of all telescope elevations evaluated against the current 90° spectrum are show. 9 spectra of each elevation were averaged leading to a running mean of +/- 30 min. Red dots represent no correction, blue $I(\lambda)^{-1}$ correction and black $I(\lambda)^{-1}$ and $I(\lambda)^{-2}$ correction. Solar radiation (orange curve) was recorded by KIT weather station positioned next to the MAX-DOAS instruments). (e) and (f) show pictures of the sky cam supporting the interpretation of the solar radiation data.
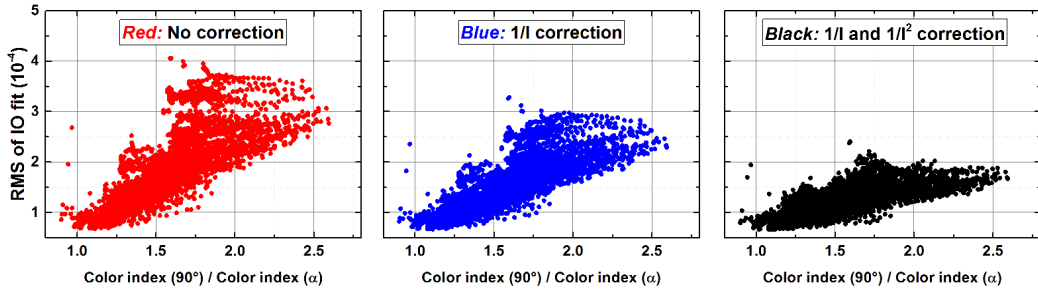
(a) EnviMeS MAX-DOAS - Zenith color index vs. RMS in IO fit range.
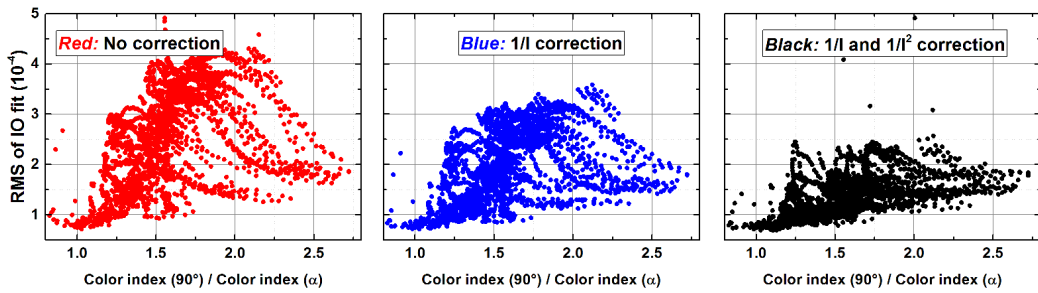
(b) ISA MAX-DOAS - Zenith color index vs. RMS in IO fit range.
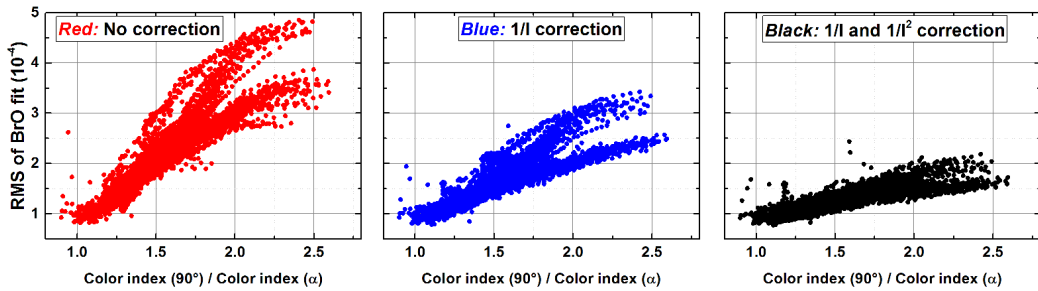
(c) EnviMeS MAX-DOAS - Zenith color index vs. RMS in BrO fit range.
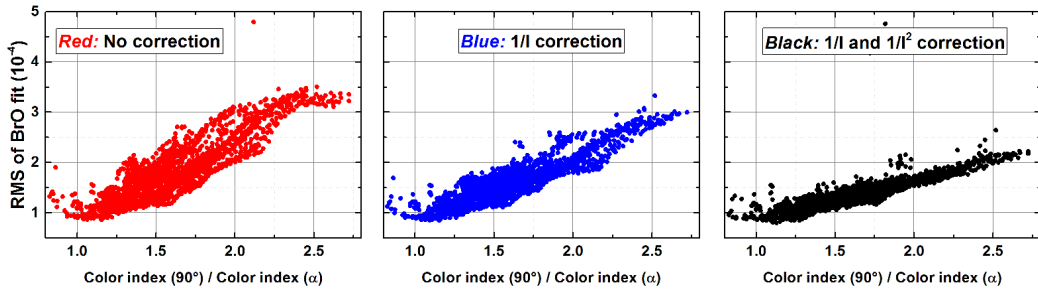
(d) ISA MAX-DOAS - Zenith color index vs. RMS in BrO fit range.

*Fig. 5.18: Correlation of the color index of the zenith spectrum and the RMS values of the DOAS analysis in the range of IO (**(a)** and **(b)**) and BrO (**(c)** and **(d)**) for different IDSL corrections: No correction (red, left), $I(\lambda)^{-1}$ correction (blue, middle); $I(\lambda)^{-1}$ and $I(\lambda)^{-2}$ correction (black, right). Only spectra with **intensity above 20000 counts per scan per second exposure time** at an **SZA greater than 70°** are shown to exclude low light conditions where RMS could be dominated by photon noise.*
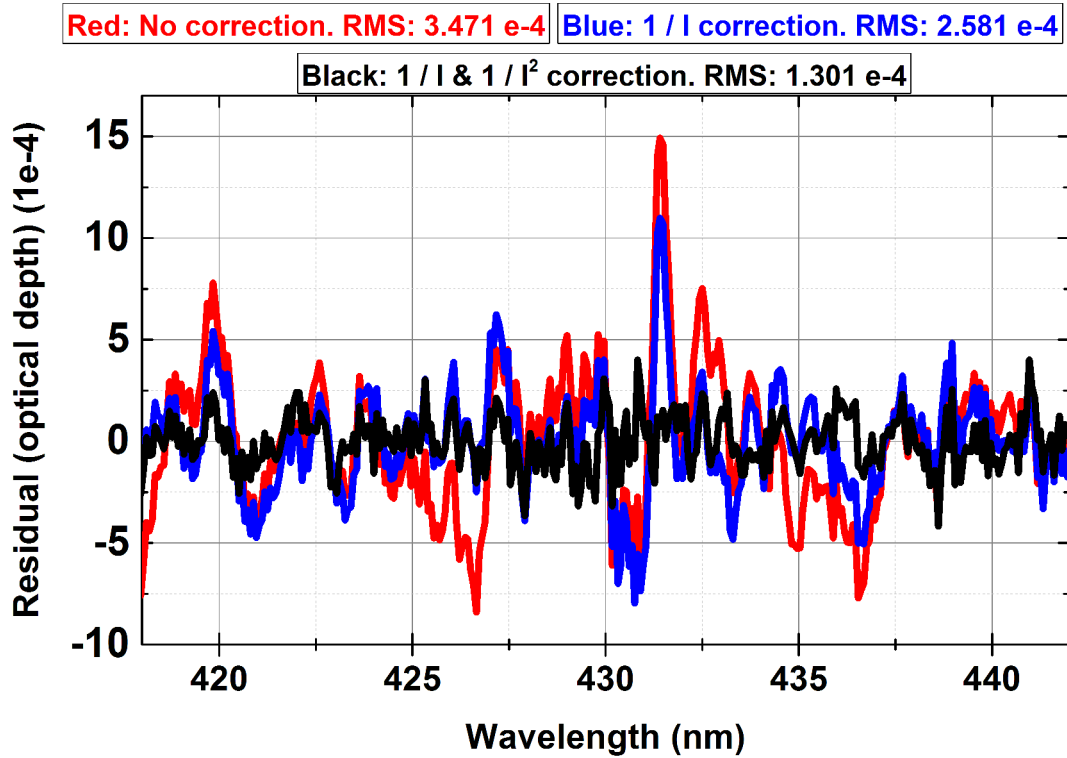
Fig. 5.19: Residual spectrum of an exemplary fit of ISA MAX-DOAS data during clear sky conditions on 25th 2014, 08:59 UTC using the IO fit scenario MX3 (see Table 5.7. The red line shows a residual spectrum with out IDSL correction while the blue and black lines show the residuals when including $I(\lambda)^{-1}$ or the combination of $I(\lambda)^{-1}$ and $I(\lambda)^{-2}$ in the fit.

Conclusions

The data of both MAX-DOAS instruments used during the campaign in November 2014 showed increased residual structures in the fit range of IO and BrO which could be correlated to clear sky conditions. Using the results from the stray light characterizations in chapter 5.1.2 the color index of a measured spectrum can be used as a rough indication for the amount of instrument driven stray light (IDSL) which is added on top of the "true" measured intensity. Using the Taylor expansion of the optical density 5.5 shows that a correction is needed not only if the spectra are contaminated with IDSL. The correction becomes more relevant if the reference spectrum, typically taken under a telescope elevation an-

gle of 90°, and the spectrum taken under lower elevation have different amounts of IDSL. Since the spectrum at low elevation angle has usually a lower color index ("more white, less blue light", ratio of UV to visible light intensity) and is therefore expected to have a higher IDSL signal, a correction term based on the reciprocal and reciprocal squared of the spectrum itself was used in the DOAS analysis. RMS values and detection limits for IO and BrO could be significantly improved (see figures 5.20 and 5.21). Especially in the case of the spectral range of the IO analysis (418 nm to 441.9 nm), where SCDs are usually low and close to the detection limit, the correction enhanced the amount of significant data points within the data set of the campaign in 2014 by decreasing the RMS values by up to $2 \cdot 10^{-4}$. In the case of the ISA MAX-DOAS, which found to have a high sensitivity for IDSL, the correction lead to slightly lower but more distinct IO SCDs. The impact on the spectral range of the BrO analysis (332 nm to 358 nm) was less than on the IO analysis but still the correction decreased the RMS values of up to $1 \cdot 10^{-4}$. A correction for differential IDSL signals was not applied since the differential IDSL structures were found to be outside of the wavelengths intervals which were used for the DOAS analysis (see figure 5.8 and Table 5.7).
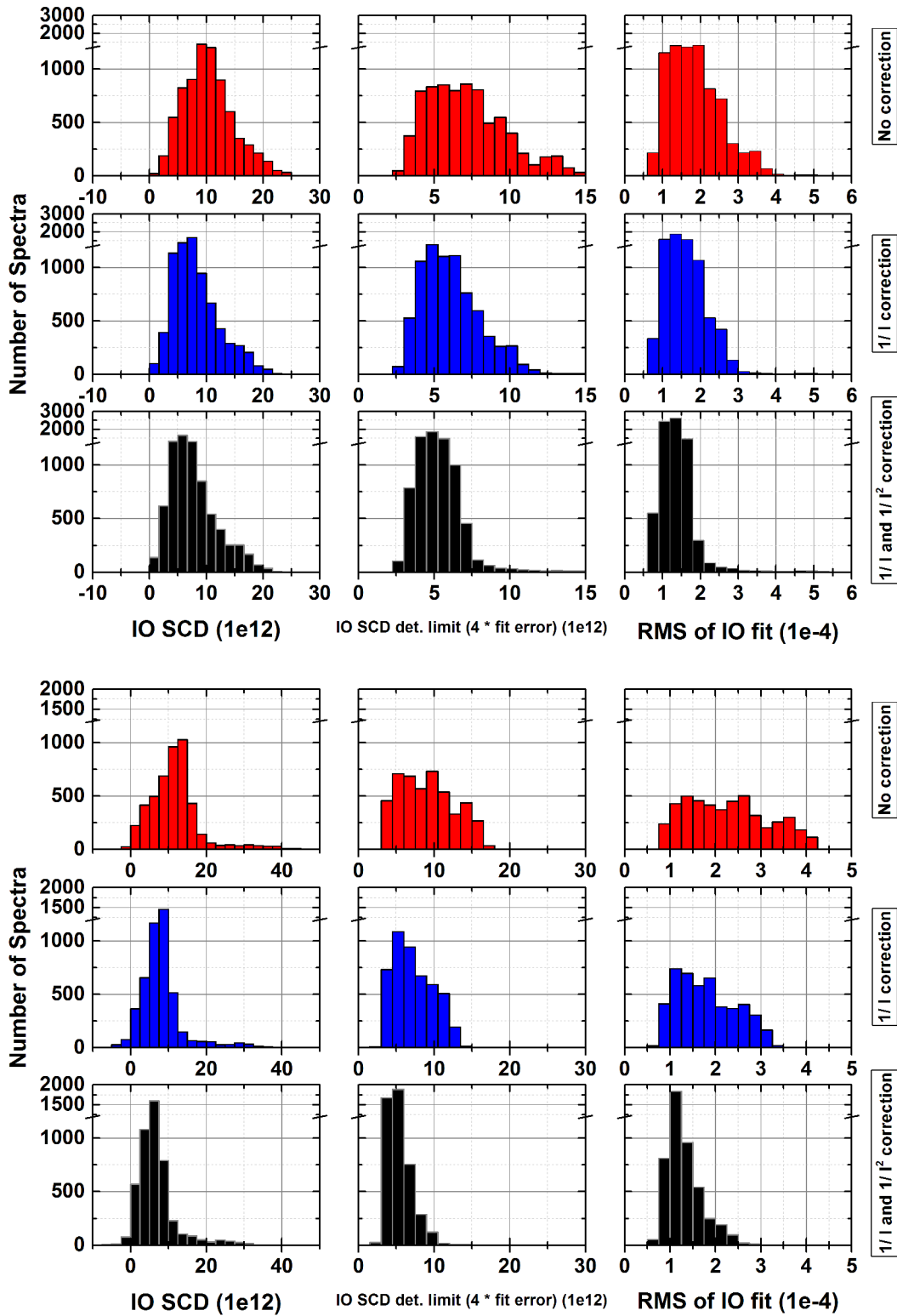
Fig. 5.20: The histograms show the impact of the IDSL correction on IO SCDs, IO detection limits and RMS values for both MAX-DOAS instruments (**top:** EnviMeS, **bottom:** ISA) during the time span of the campaign at the Dead Sea Valley in November 2014. **Upper plots, red:** No IDSL correction. **Middle plots, blue:** $I(\lambda)^{-1}$ correction. **Lower plots, black:** $I(\lambda)^{-1}$ and $I(\lambda)^{-2}$.
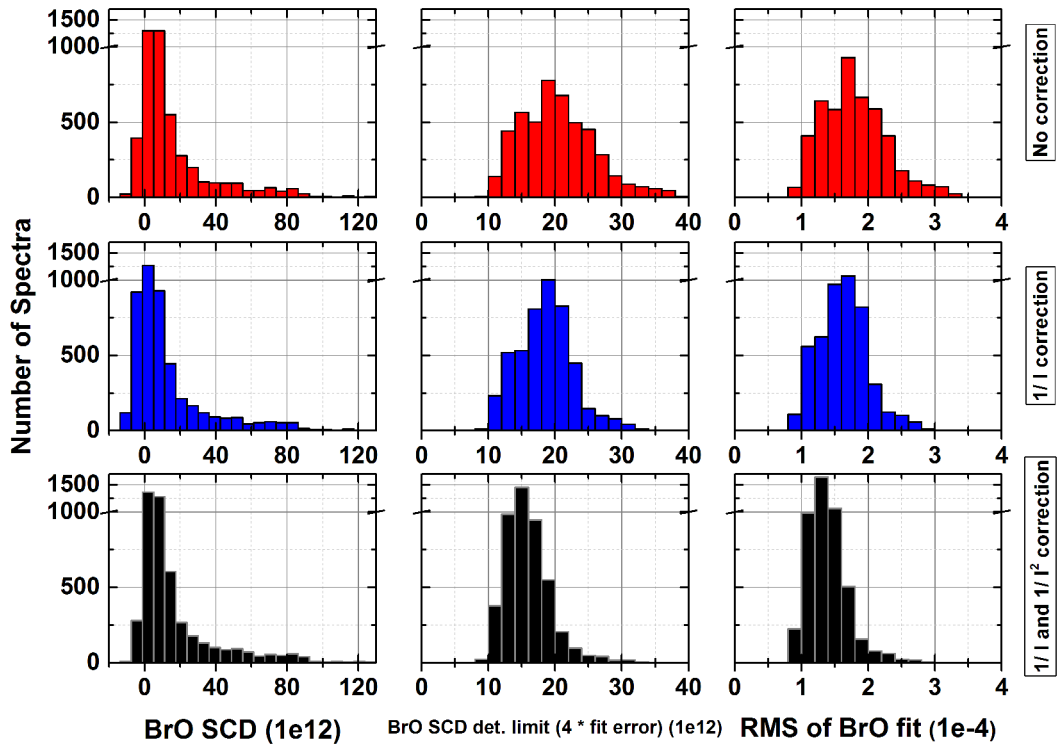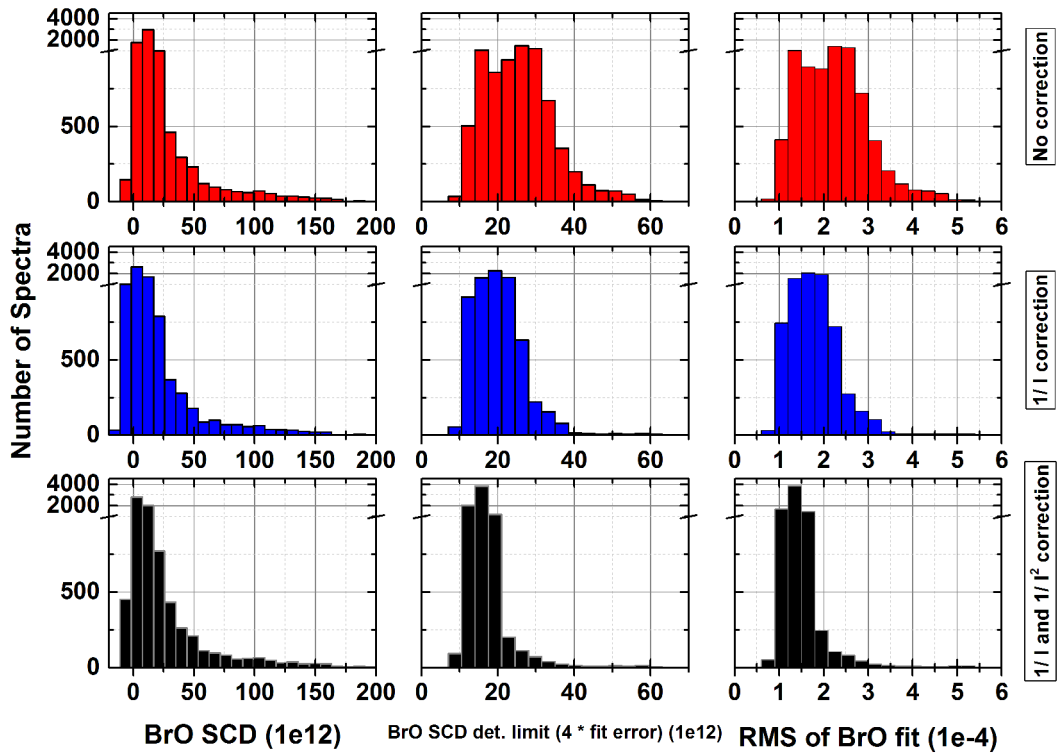
Fig. 5.21: Same as figure 5.20 but for BrO.

5.1.6 Quality of the MAX-DOAS analysis

Histograms of root mean square (RMS) values of the residual spectra are shown for every fit scenario and every MAX-DOAS instrument. The RMS values indicate how well the composition of the fit scenario accounts for the effects of scattering and absorption between the viewing geometries of reference spectrum (zenith) and low elevation angles as well as if there is sufficient signal to noise in terms of collected photons by the spectrometers sensor. RMS should be minimized and ideally more or less constant over the whole measurement period. At higher at high solar zenith angles (sunrise and sunset), RMS is dominated by photon noise due to low intensity of scattered sunlight.

Besides the RMS values, exemplary fit results are used to estimated the quality of the spectral evaluation. The elevation angle of the fit examples is 1°, which is the lowest elevation angle being used in the profile retrieval. The plots do not show secondary fit constituents for the sake of clarity. The errors of the slant column densities given in the figures are defined by the errors of the fit algorithm.

For the Ein Bokek MAX-DOAS, two example fits of IO at different elevation angles are shown. Despite being at 20 m above the water surface the instrument also recorded spectra under an telescope elevation angle of -5°. For that angle, extraordinary high slant column densities of IO were measured compared to the positive elevation angles.

The Masada top instrument of the campaign in 2012 had a different elevation sequence. It measured also at several negative elevation angles supporting the profile retrieval. Thus the example fits show data taken at an elevation angle of -2°.

Ein Bokek MAX-DOAS
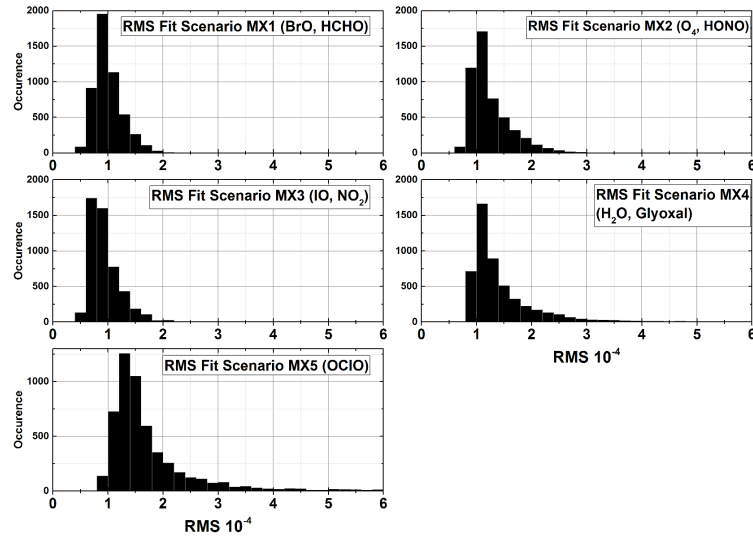
Fig. 5.22: Root mean square (RMS) values of the residual spectra from the data set acquired by the Ein Bokek MAX-DOAS in May 2012.
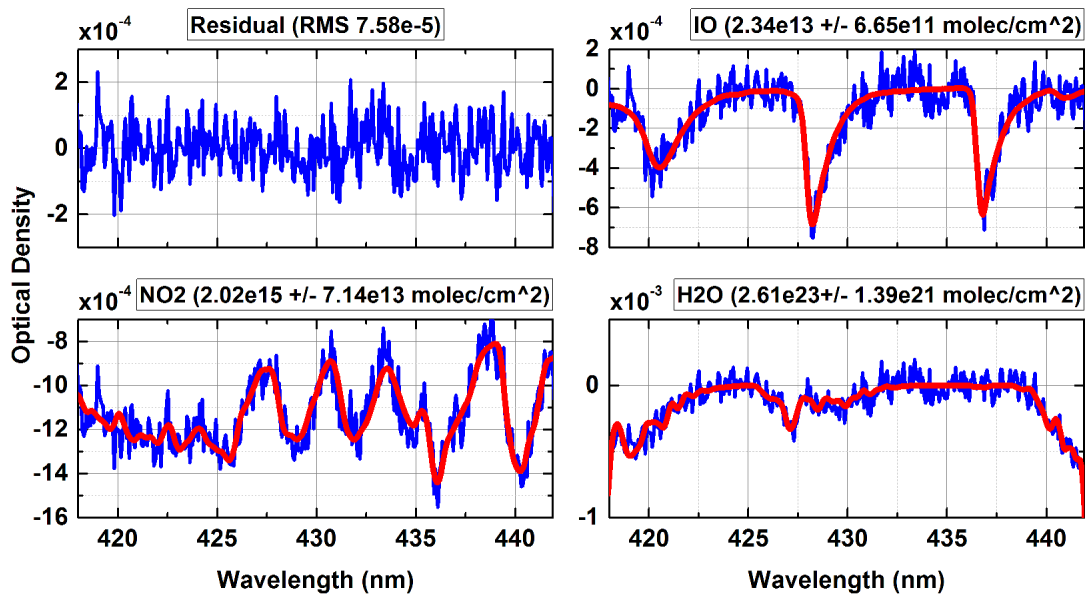
Fig. 5.23: Fit results of **fit scenario MX3** used for the retrieval of IO and NO_2. Spectrum 7325, 2012 May 12, 11:09 UTC, SZA 24.9°. Telescope elevation angle = -5°.
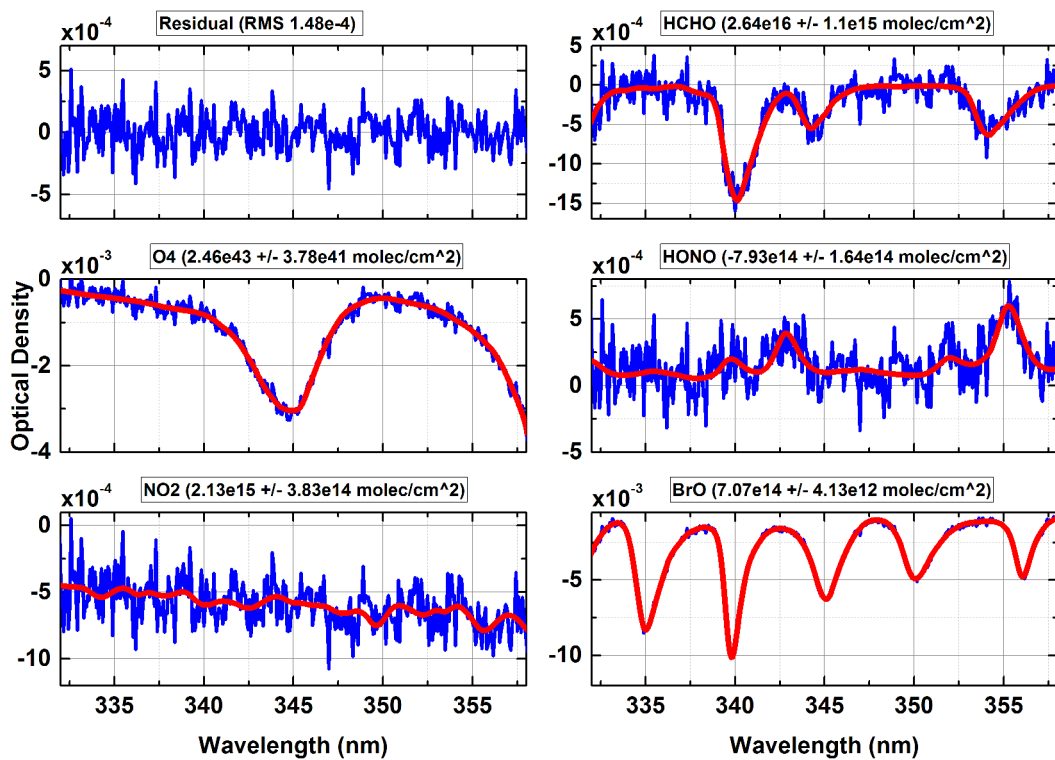
(a) Fit results of **fit scenario MX1** used for the retrieval of BrO and HCHO. Spectrum 5724, 2012 May 10, 14:20 UTC, SZA 65.26°. Telescope elevation angle = 1°.
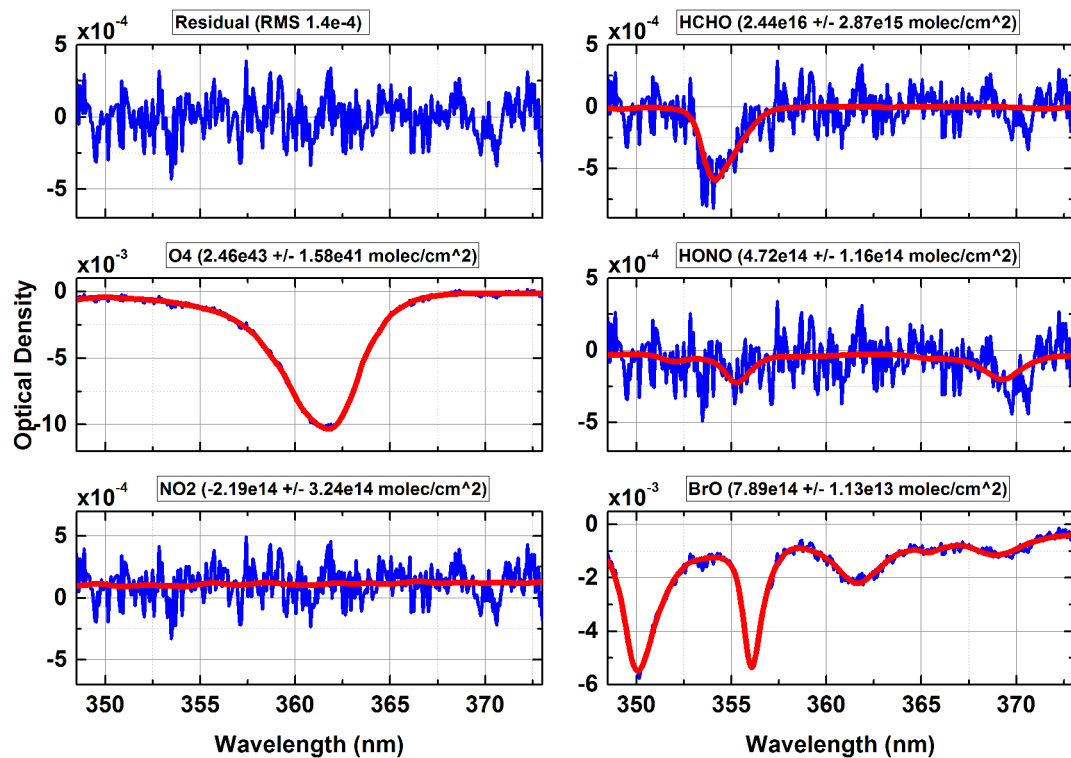
(b) Fit results of **fit scenario MX2** used for the retrieval of O_4 and HONO. Spectrum 5724, 2012 May 10, 14:20 UTC, SZA 65.26°. Telescope elevation angle = 1°.

Fig. 5.24: Example fits Ein Bokek MAX-DOAS.
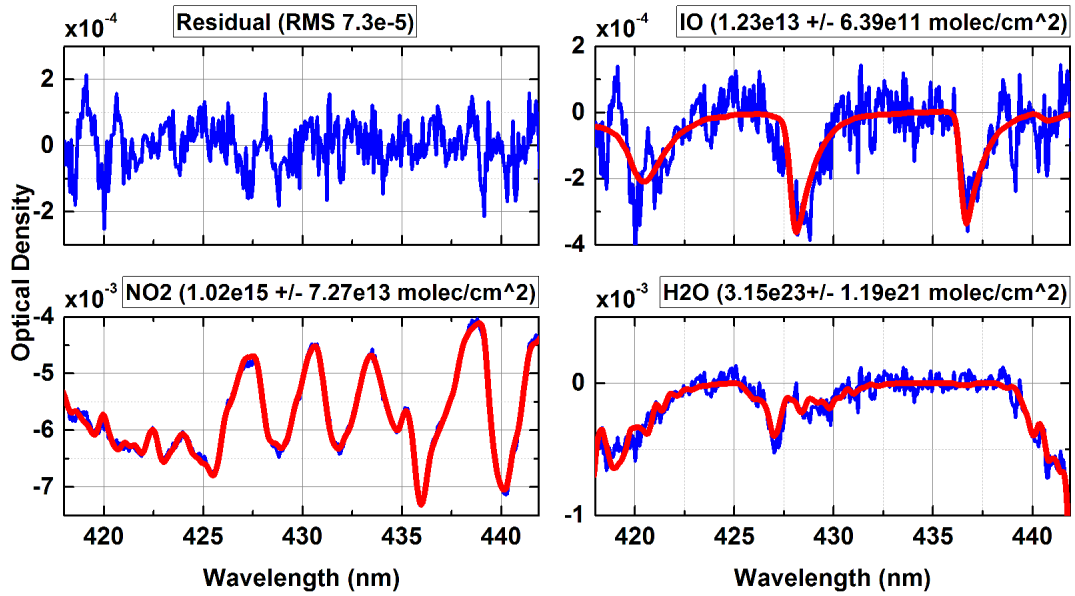
(a) Fit results of **fit scenario MX3** used for the retrieval of IO and NO$_2$. Spectrum 8612, 2012 May 14, 07:15 UTC, SZA 33.7°. Telescope elevation angle = 1°.
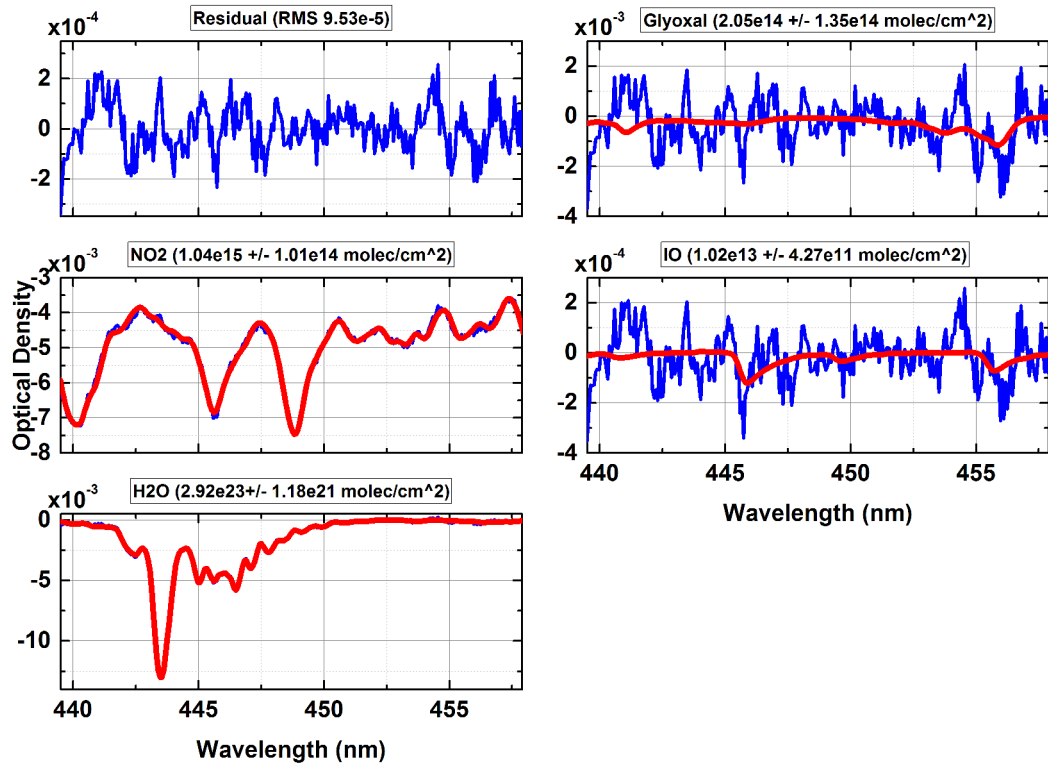
(b) Fit results of **fit scenario MX4** used for the retrieval of H$_2$O and Glyoxal. Spectrum 8612, 2012 May 14, 07:15 UTC, SZA 33.7°. Telescope elevation angle = 1°.

Fig. 5.25: Example fits Ein Bokek MAX-DOAS.
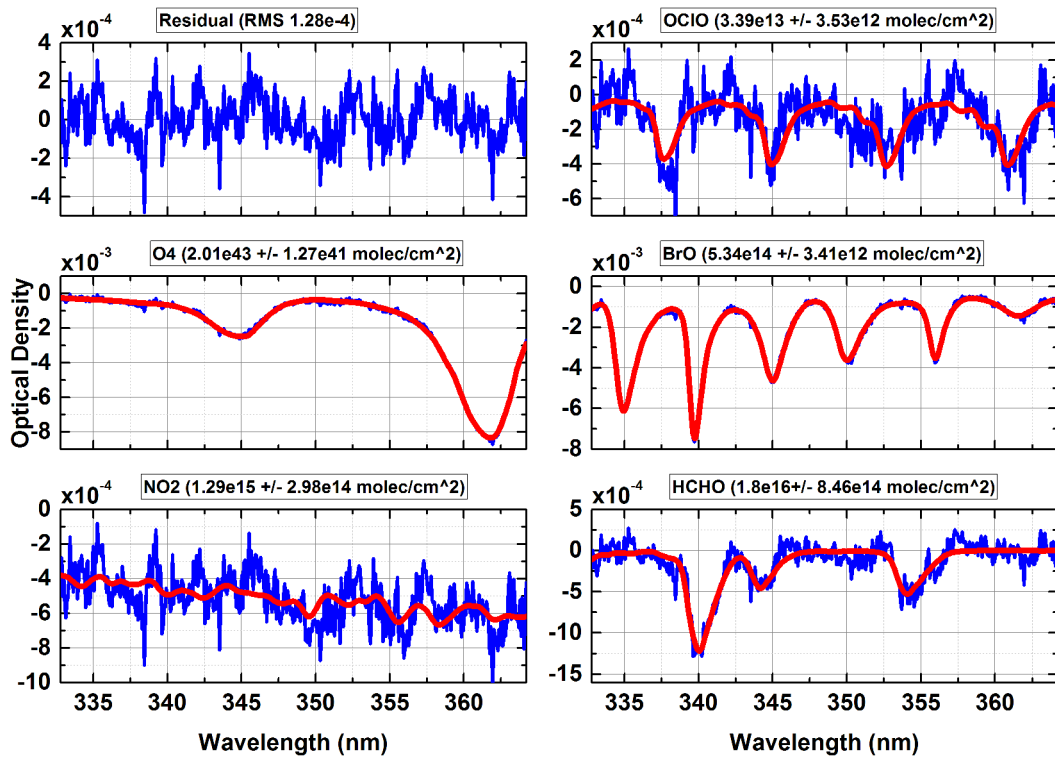
Fig. 5.26: Fit results of **fit scenario MX5** used for the retrieval of OClO. Spectrum 5580, 2012 May 10, 11:56 UTC, SZA 34.6°. Telescope elevation angle = 1°.

Masada top MAX-DOAS

Due to the setup of the spectrometer, residuals were too large to detect Glyoxal with the Masada top instrument in 2012. However, the corresponding fit scenario could be used for the retrieval of H_2O slant column densities (see figure 5.29).
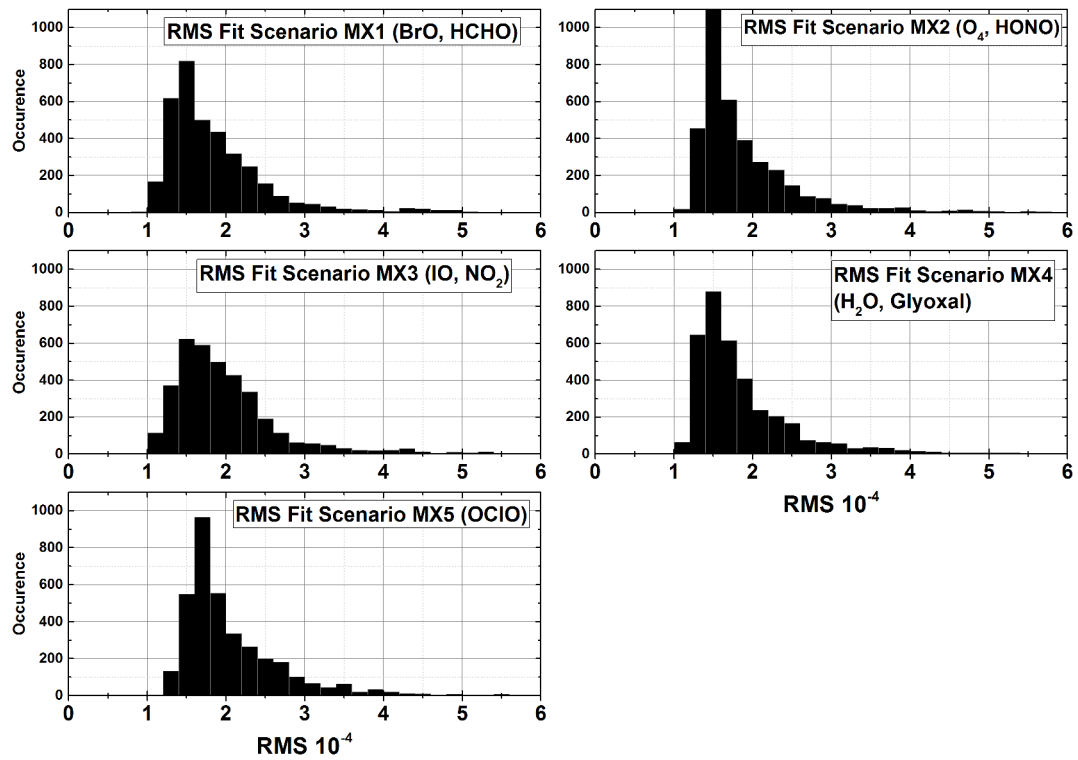
Fig. 5.27: Root mean square (RMS) values of the residual spectra from the data set acquired by the Masada top MAX-DOAS in May 2012.
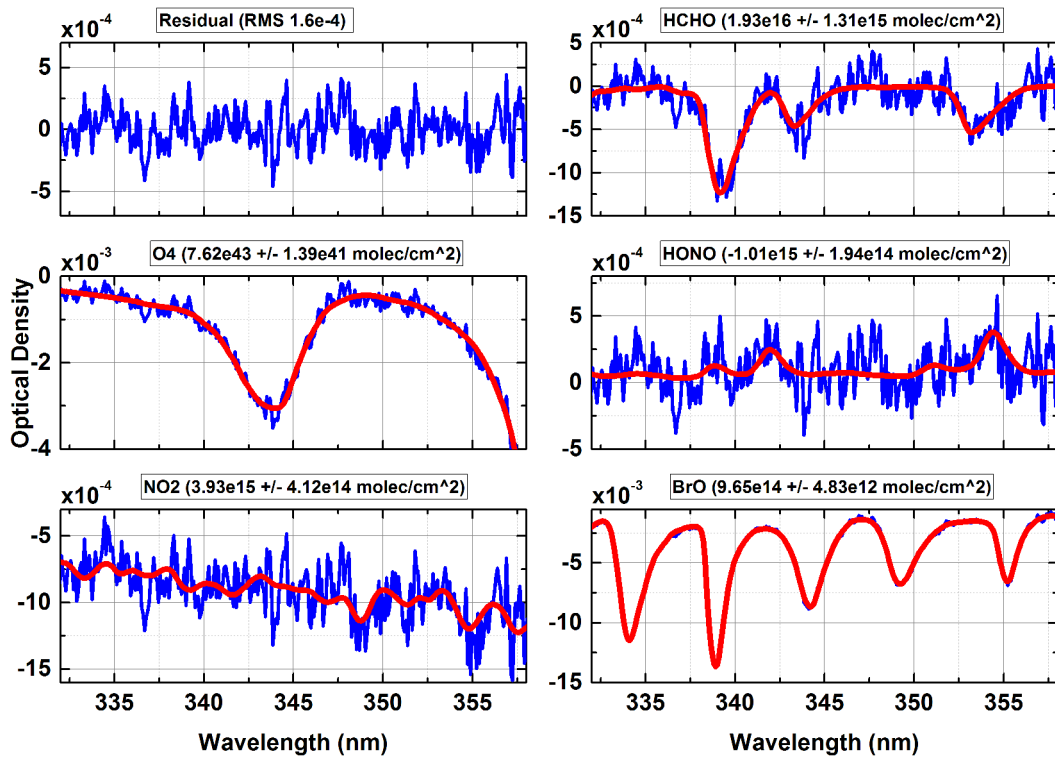
(a) Fit results of **fit scenario MX1** used for the retrieval of BrO and HCHO. Spectrum 3393, 2012 May 12, 10:45 UTC, SZA 20.5°. Telescope elevation angle = -2°.
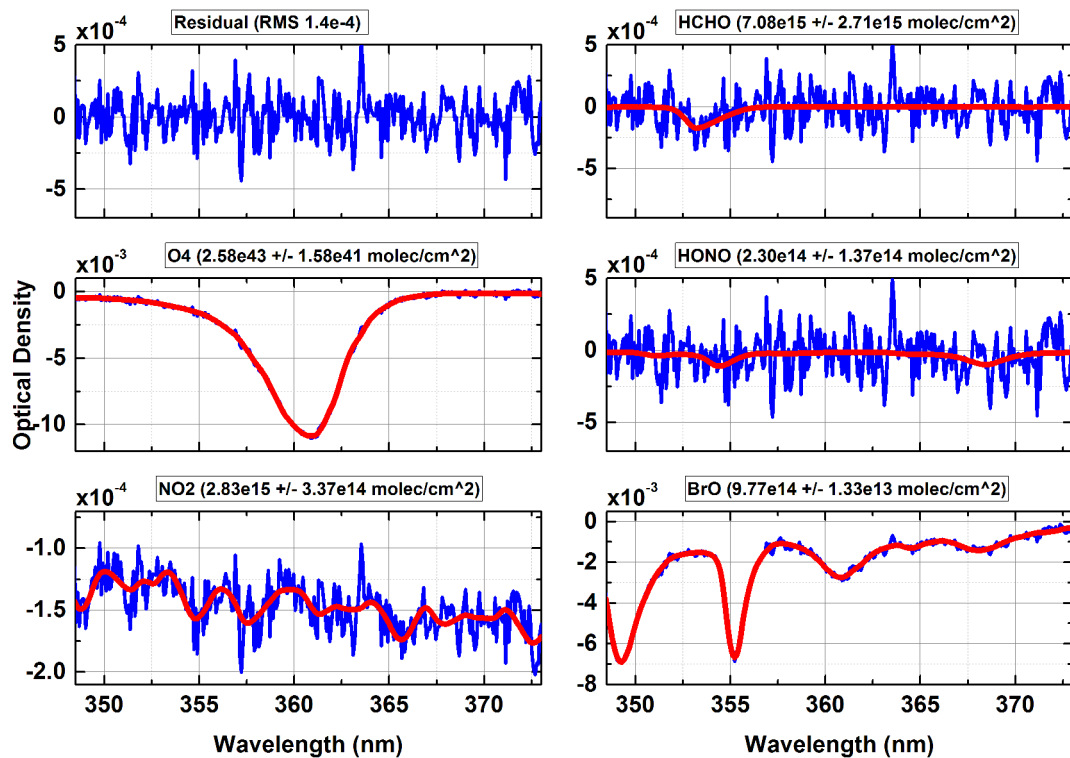
(b) Fit results of **fit scenario MX2** used for the retrieval of O₄ and HONO. Spectrum 3393, 2012 May 12, 10:45 UTC, SZA 20.5°. Telescope elevation angle = -2°.

Fig. 5.28: Example fits Masada top MAX-DOAS.
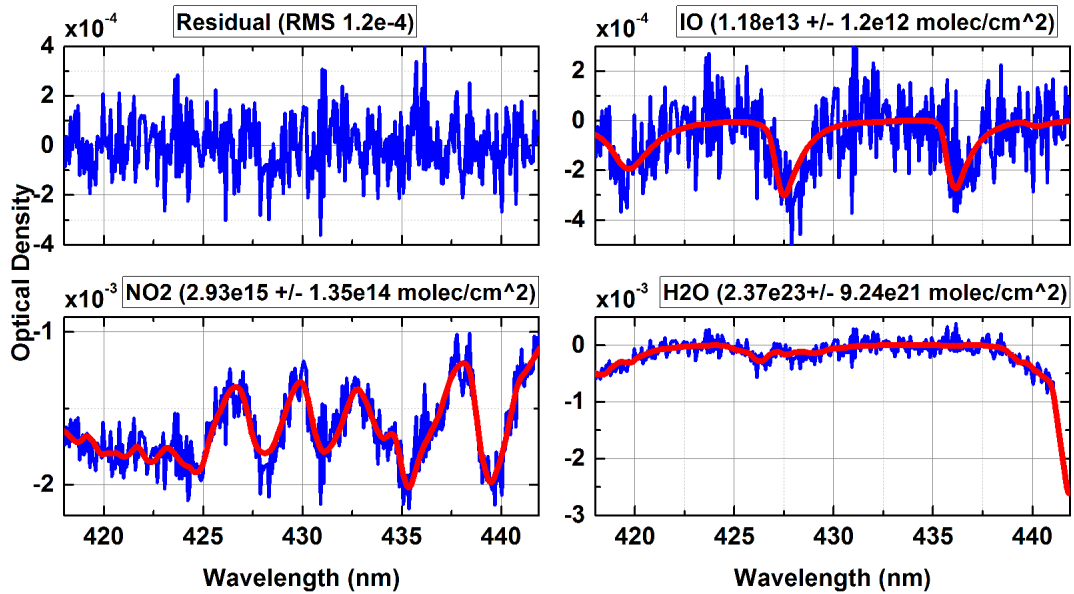
(a) Fit results of **fit scenario MX3** used for the retrieval of IO and NO$_2$. Spectrum 2341, 2012 May 10, 08:31 UTC, SZA 19.8°. Telescope elevation angle = -2°.
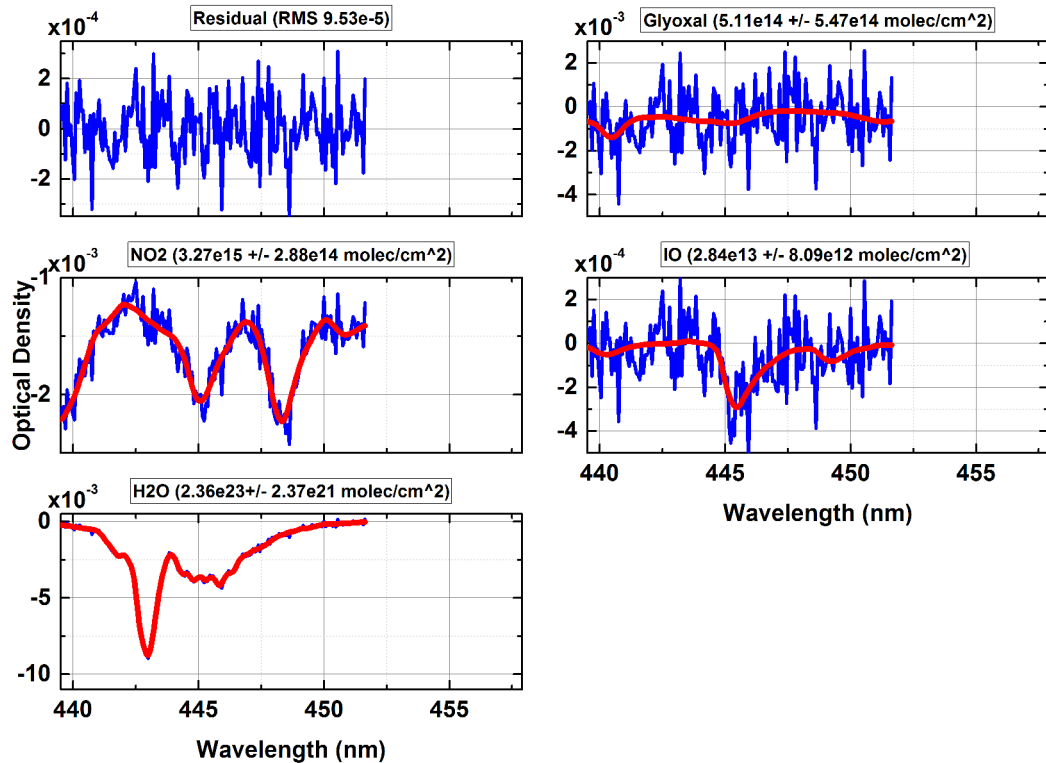
(b) Fit results of **fit scenario MX4** used for the retrieval of H$_2$O and Glyoxal. Spectrum 2341, 2012 May 10, 08:31 UTC, SZA 19.8°. Telescope elevation angle = -2°.

Fig. 5.29: Note that the spectrometer configuration of the instrument did not cover the full range of fit scenario MX4. However, for the sake of comparability, the same lower fit limit like with the other MAX-DOAS instruments was chosen to retrieve slant column densities of H$_2$O.
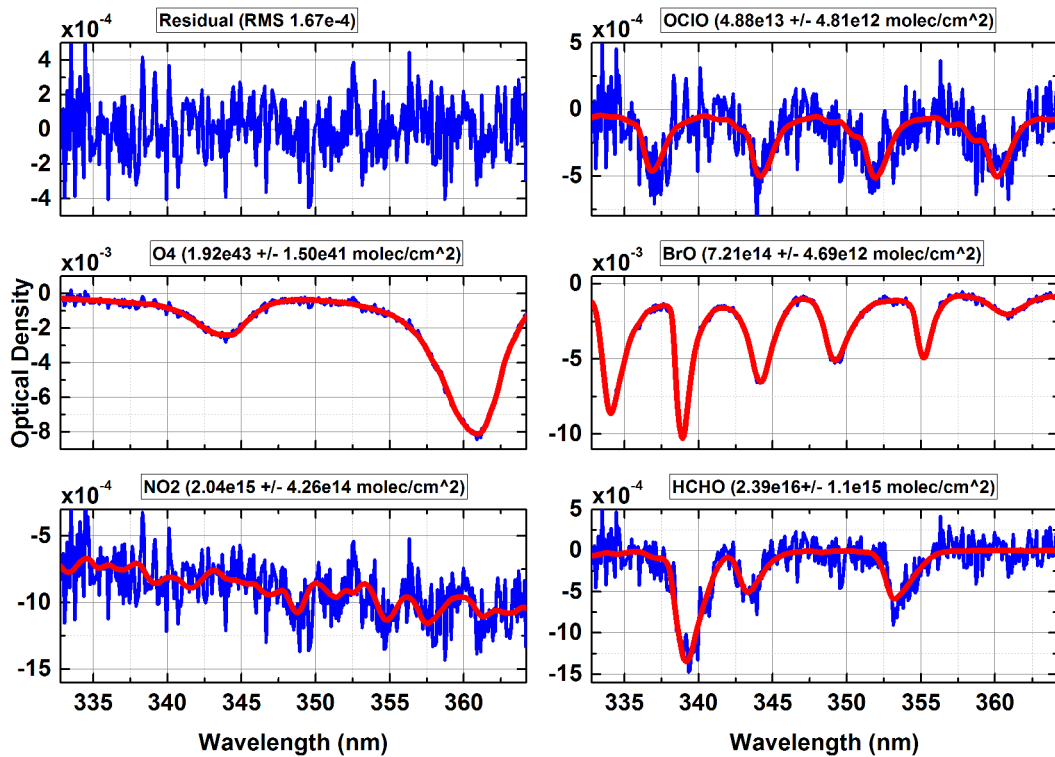
Fig. 5.30: Fit results of **fit scenario MX5** used for the retrieval of OClO. Spectrum 2517, 2012 May 10, 12:07 UTC, SZA 36.9°. Telescope elevation angle = -2°.

EnviMeS MAX-DOAS
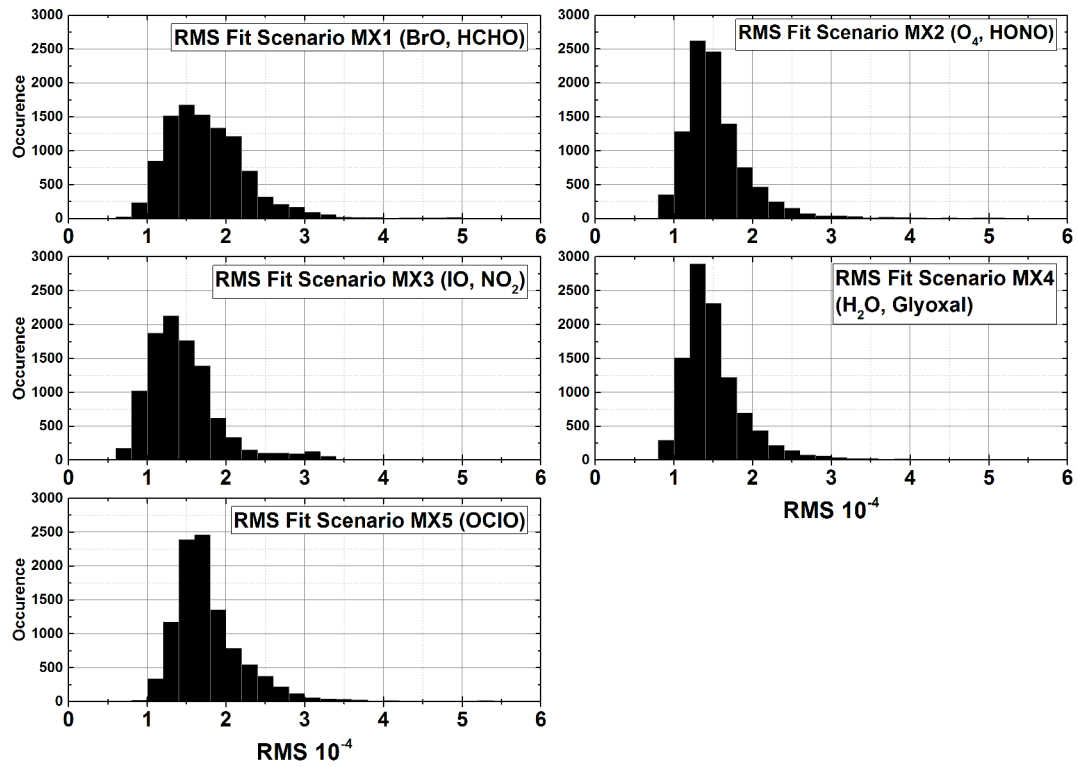
Fig. 5.31: Root mean square (RMS) values of the residual spectra from the data set acquired by the Masada bottom MAX-DOAS in November 2014.
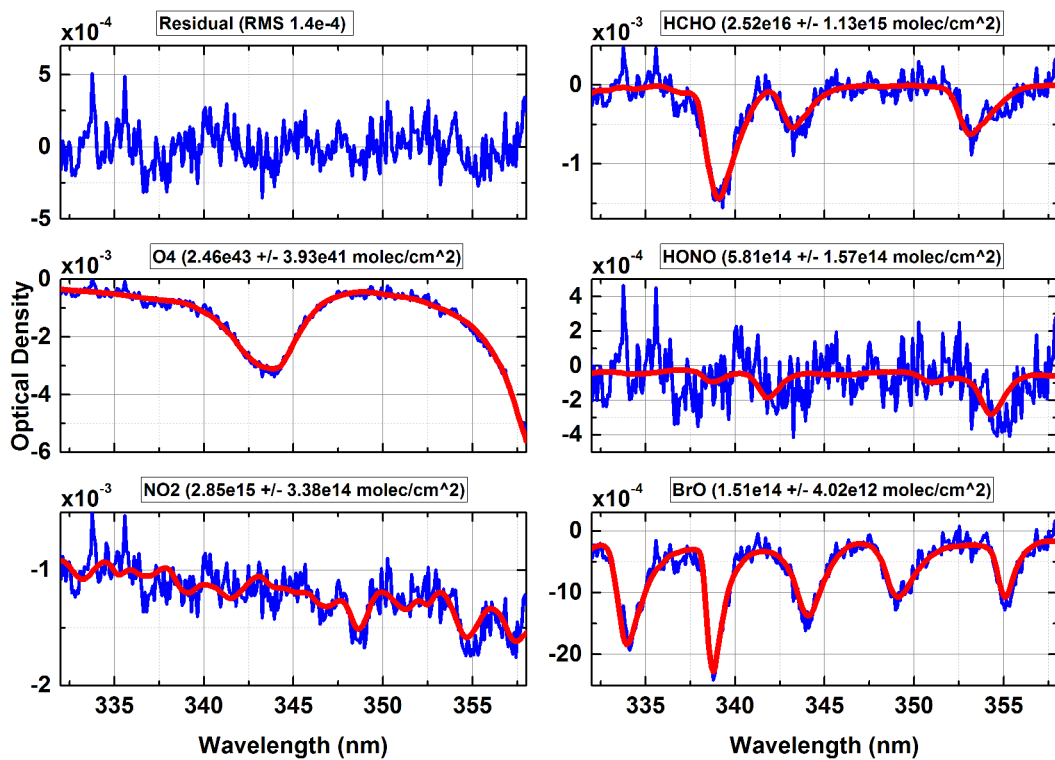
(a) Fit results of **fit scenario MX1** used for the retrieval of BrO and HCHO. Spectrum 13661, 2014 Nov 28, 08:21 UTC, SZA 51.9°. Telescope elevation angle = 1°.
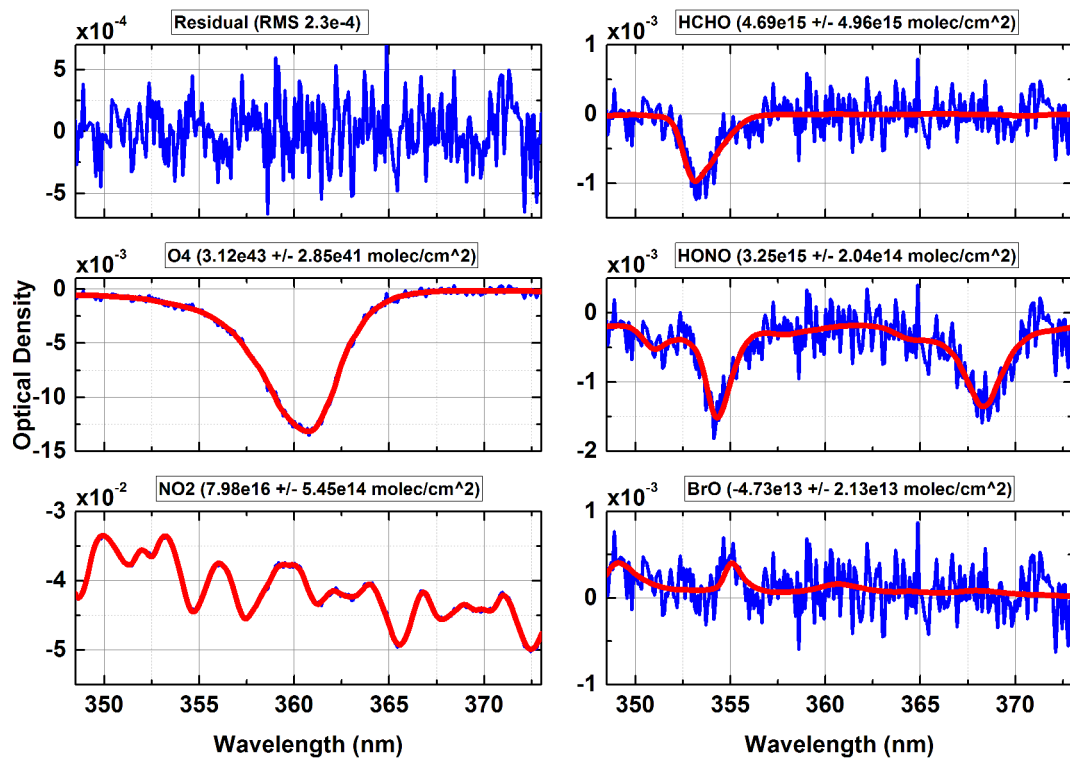
(b) Fit results of **fit scenario MX2** used for the retrieval of O$_4$ and HONO. Spectrum 4281, 2014 Nov 12, 04:59 UTC, SZA 79.9°. Telescope elevation angle = 1°.

Fig. 5.32: Example fits EnviMeS MAX-DOAS.
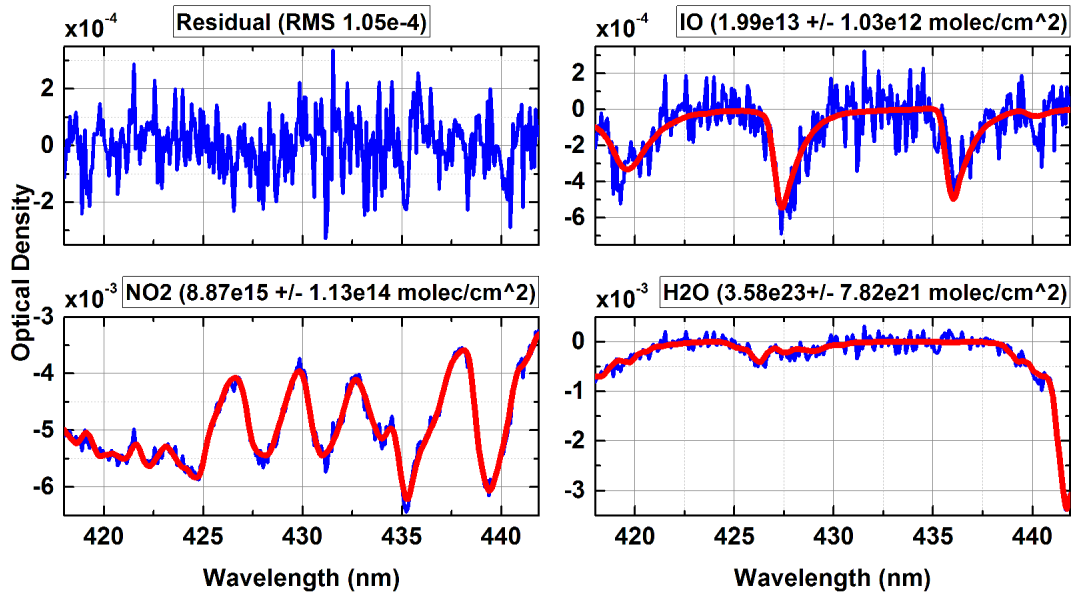
(a) Fit results of **fit scenario MX3** used for the retrieval of IO and NO_2. Spectrum 10837, 2014 Nov 23, 10:01 UTC, SZA 52.4°. Telescope elevation angle = 1°.
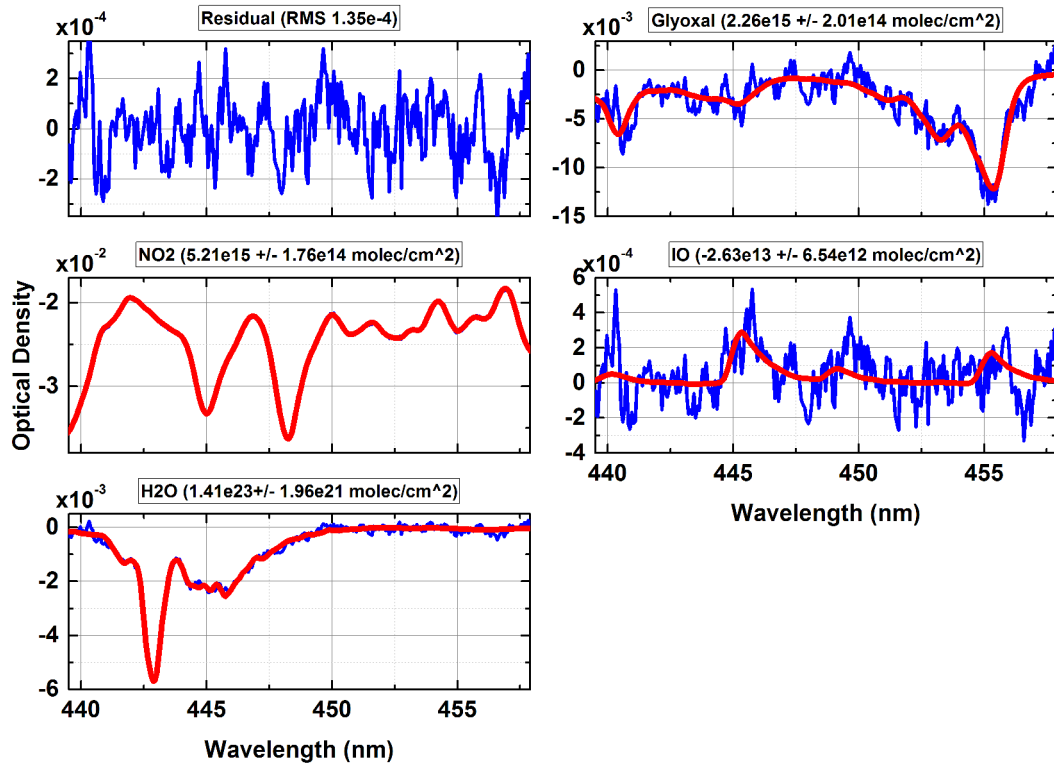
(b) Fit results of **fit scenario MX4** used for the retrieval of Glyoxal and H_2O. Spectrum 4477, 2014 Nov 12, 08:18 UTC, SZA 51.4°. Telescope elevation angle = 1°.

Fig. 5.33: Example fits EnviMeS MAX-DOAS.
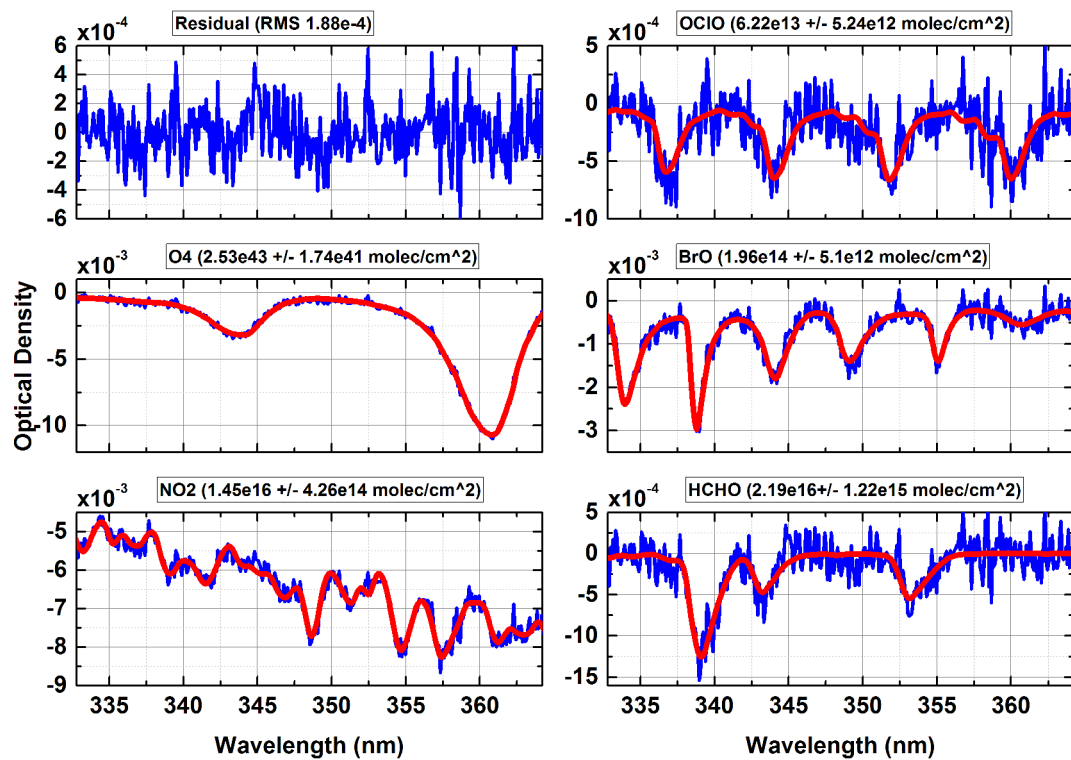
Fig. 5.34: Fit results of **fit scenario MX5** used for the retrieval of OClO. Spectrum 7071, 2012 Nov 17, 05:54 UTC, SZA 71.05°. Telescope elevation angle = 1°.

ISA MAX-DOAS stationary measurements
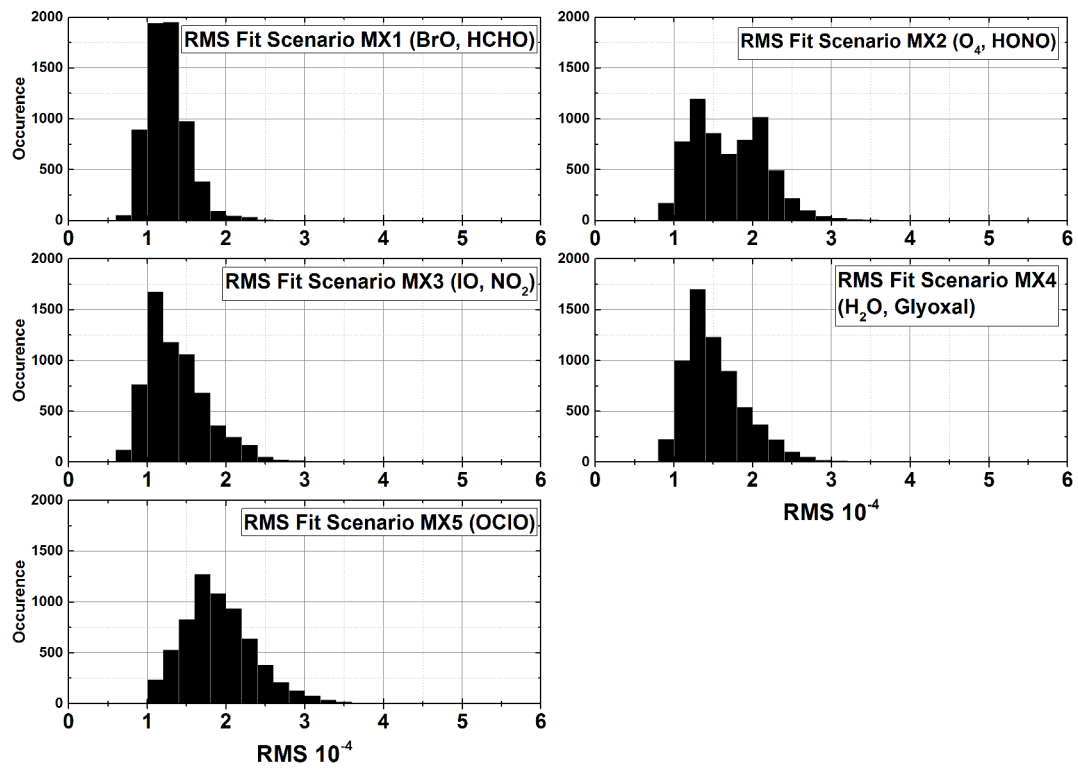
Fig. 5.35: Root mean square (RMS) values of the residual spectra from the data set acquired by the ISA MAX-DOAS in November 2014. Only stationary measurements are shown.
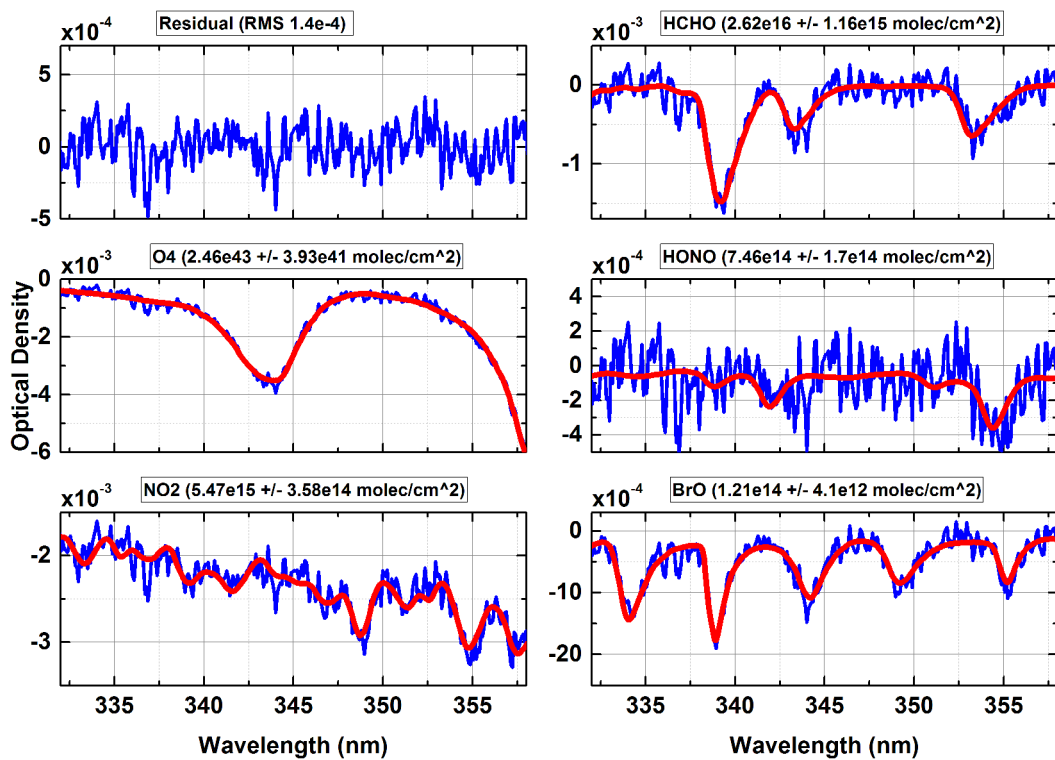
(a) Fit results of **fit scenario MX1** used for the retrieval of BrO and HCHO. Spectrum 18594, 2014 Nov 28, 08:18 UTC, SZA 54.3°. Telescope elevation angle = 1°.
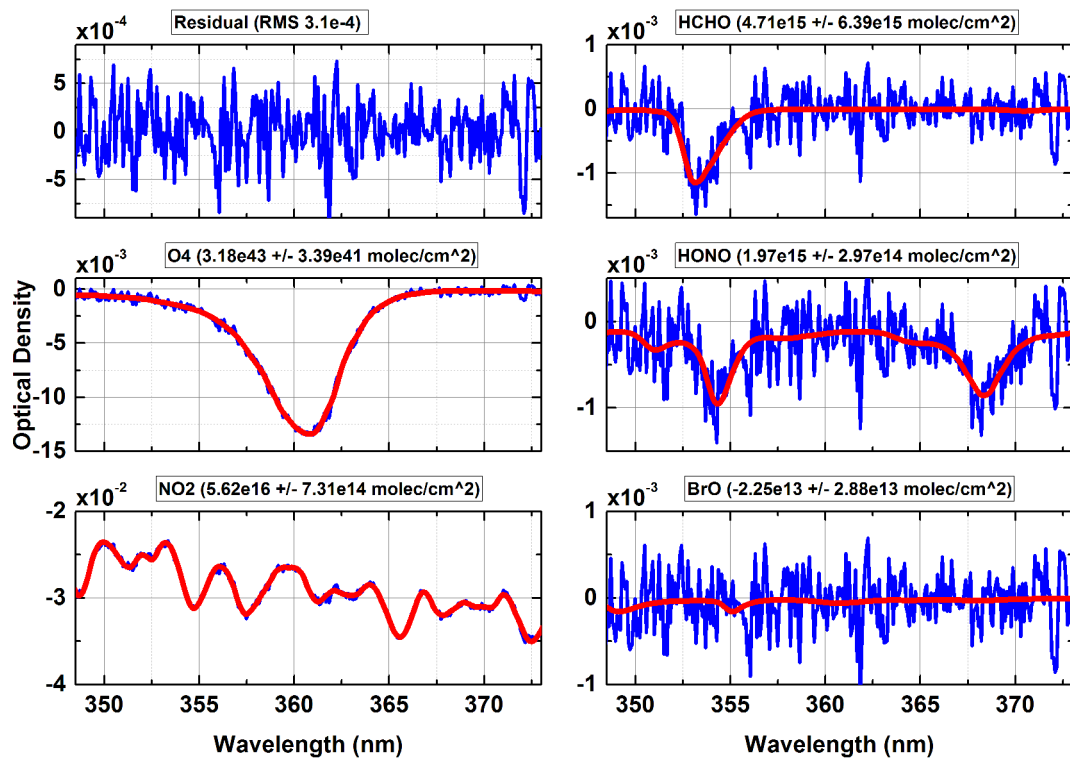
(b) Fit results of **fit scenario MX2** used for the retrieval of O_4 and HONO. Spectrum 3177, 2014 Nov 12, 04:59 UTC, SZA 79.9°. Telescope elevation angle = 1°.

Fig. 5.36: Example fits ISA MAX-DOAS. Only stationary measurements are shown.
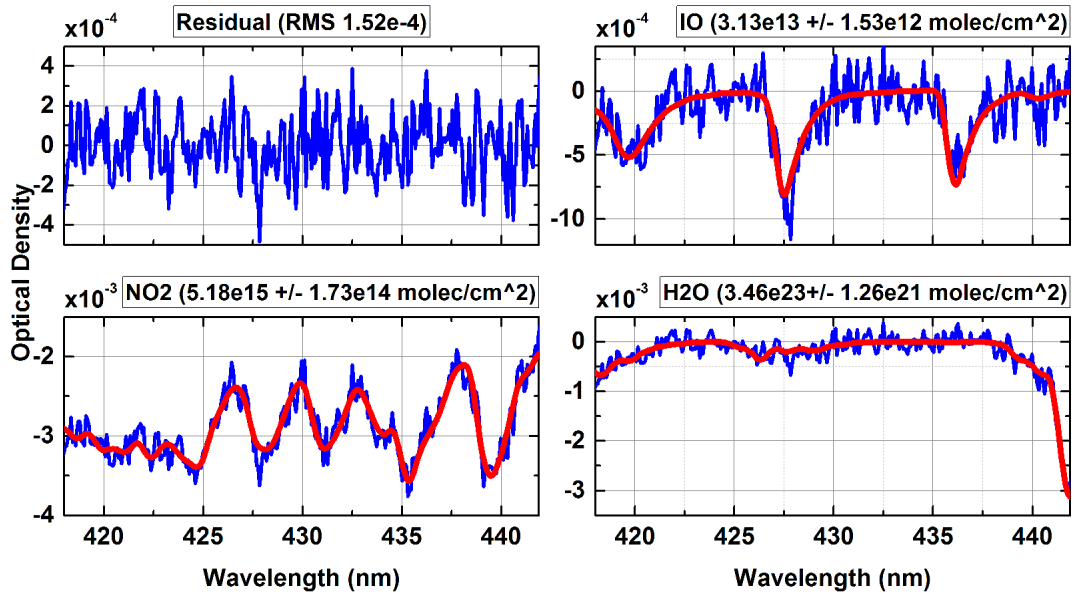
(a) Fit results of **fit scenario MX3** used for the retrieval of IO and NO_2. Spectrum 20290, 2014 Nov 28, 08:21 UTC, SZA 54.7°. Telescope elevation angle = 1°.
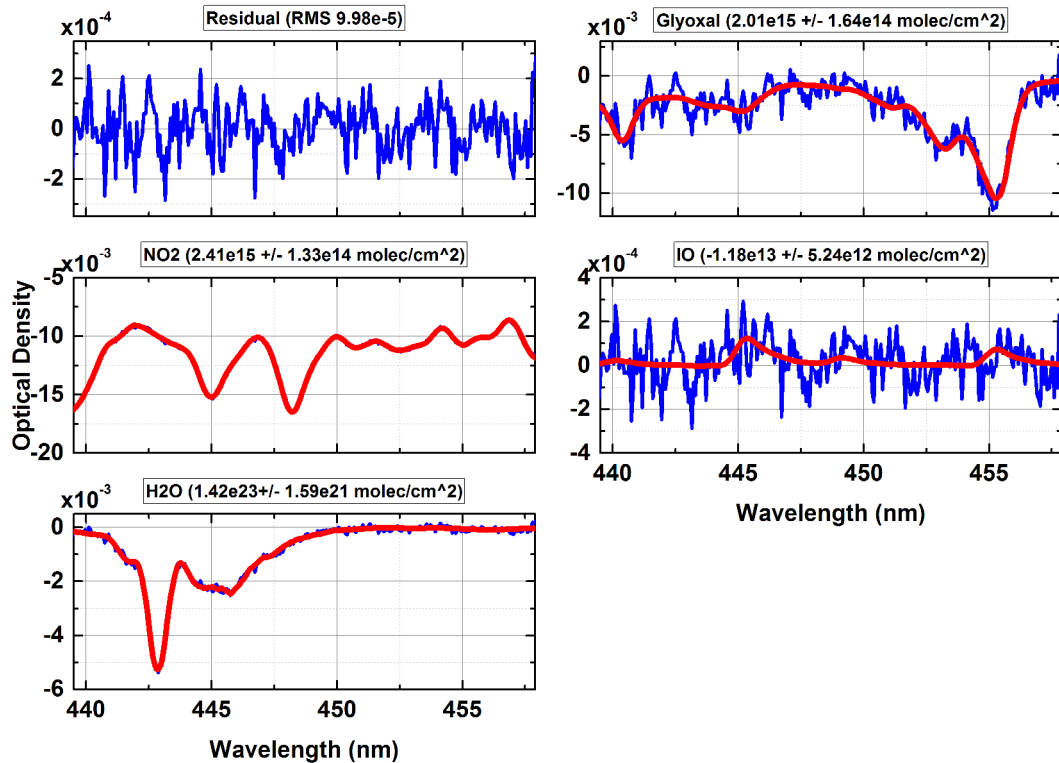
(b) Fit results of **fit scenario MX4** used for the retrieval of Glyoxal and H_2O. Spectrum 3448, 2014 Nov 12, 09:37 UTC, SZA 49°. Telescope elevation angle = 1°.

Fig. 5.37: Example fits ISA MAX-DOAS. Only stationary measurements are shown.

5.1.7 Retrieval of vertical profiles of aerosols and trace gases

The retrieval of aerosol extinction and trace gas concentrations from the measured slant column densities is carried out by applying the HEIPRO algorithm (Yilmaz [2012], see section 4.6). An exemplary application can be found in Frieß et al. [2011]. The settings for the retrieval are chosen with respect to the findings of Zielcke [2015], who performed extensive sensitivity studies to elaborated the influence of different retrieval parameters on the result. This was achieved by feeding simulated SCDs from synthetic profiles in the algorithm and comparing the retrieved profile with the initial, artificial profile.

Table 5.8 provides a summary of the HEIPRO retrieval parameters. For the sake of simplicity, the order of the table is adapted to the order of appearance in the HEIPRO configuration file, which is not necessarily intuitive. The setting for the a priori profiles are given in table 5.9.

During the campaign in 2014, an AERONET (Aerosol Robotic Network) sun photometer was deployed next to the MAX-DOAS near Masada. The AERONET data provided Angstroem coefficients, single scattering albedo and asymmetry parameters (Level 1.5 data, AERONET [2014]) which were fed into the MAX-DOAS retrieval algorithm.

Choice of elevation angles used for the retrieval

The sensitivity studies by Zielcke [2015] showed that the retrieved aerosol and trace gas profiles are extremely sensitive to the accuracy of the telescope elevation angles. Especially for elevation angles near the horizon ($1° > \alpha > -1°$), where the air mass factors vary strongly with α, a faulty elevation angle has a large influence on the result. Therefor, SCDs measured under $0°$ were not used for the inversion of aerosol and trace gas profiles. Further, the lowermost elevation angle of the MAX-DOAS instruments at Masada top (-28°) and Ein Bokek (-5°) were also excluded from the retrieval due to insufficient knowledge about the effects of ground albedo and reflections of the water surface at Ein Bokek.

Parameter	Value	Parameter	Value
Time resolution	15 min	Provide weight. func.	false
O_4 absorption band	360.8 nm	Delta x	0.1
Safe state	true	Ground albedo at 360.8 nm	$0.0342^{1)4)5)}$, $0.127^{2)3)}$
Number of iter. runs	2	Grip top	4.6 km
Adaptive a priori	false	Grid resolution	0.1 km, 0.05 km$^{2)}$
Iterative a priori	false	Aerosol/trace gas start level	0.01 km
Fix weighting func.	true	A priori error (relative)	2
Use intensity	false	Only variance	false
Reference elevation	$90°$, $80°^{4)}$	Correlation length	0.5km
Scale O_4 error	2	Fit Angstroem	false
(O_4) XS scale	1	Angstroem exponent	$1.36^{2)4)}$, AERONET$^{1)3)5)}$
Model (O_4) XS file	Hermans et al. [2002]	Fit SSA	false
Gamma	10^3	SSA 360	$0.93^{2)4)}$, AERONET$^{1)3)5)}$
Maximum gamma	10^8	Fit asymmetry	false
Scale gamma	1	Asymmetry 360	$0.69^{2)4)}$, AERONET$^{1)3)5)}$
Delta χ^2	10^{-3}	Wavelength correlation	true
Iteration steps	8		

Table 5.8: Parameters of the HEIPRO inversion algorithm used for the MAX-DOAS retrieval in this thesis. Some parameters depend on the condition at the corresponding location and are labeled with superscript numbers indication the location. $^{1)}$Ein Gedi, $^{2)}$Masada top, $^{3)}$Masada bottom, $^{4)}$Ein Bokek, $^{5)}$Neve Zohar

Parameter	O_4	BrO	IO	OClO	NO_2	HONO	HCHO	Glyoxal
Shape	exp.	exp.	exp.	exp.	exp.	exp.	exp.	exp.
Param1	0.2 km^{-1}	1 pptv 40 pptv$^{2)}$	1 pptv	1 pptv	1 ppbv	100 pptv	1 ppbv	100 pptv
Param2 (km)	1.5	1.5	1.5	1.5	1.5	1.5	1.5	1.5

Table 5.9: A priori settings for the retrieval of aerosol extinctions and trace gas concentrations. Locations are indicated by superscript numbers. For all retrievals, an exponentially decreasing a priori profile is chosen. Parameter 1 describes the ground value of the a priori. Parameter 2 describes scale height (1/e) of the a priori. Note the different ground value for the BrO a priori at Masada top, marked with$^{2)}$.

Figure 5.38 shows exemplary averaging kernels from the retrieval of MAX-DOAS data from the instruments used in this thesis. The averaging kernels describe the sensitivity of sensitivity of the retrieval result for the true state of the atmosphere. It can clearly be seen, that the averaging kernels for altitudes close to the instrument altitude (0 m asl for Masada top, 500 m below sea level else) are larger than above the corresponding instrument. This is due to the measurement geometry and the fact that the gain in information about vertical gradients is best for small elevation angles near the horizon.
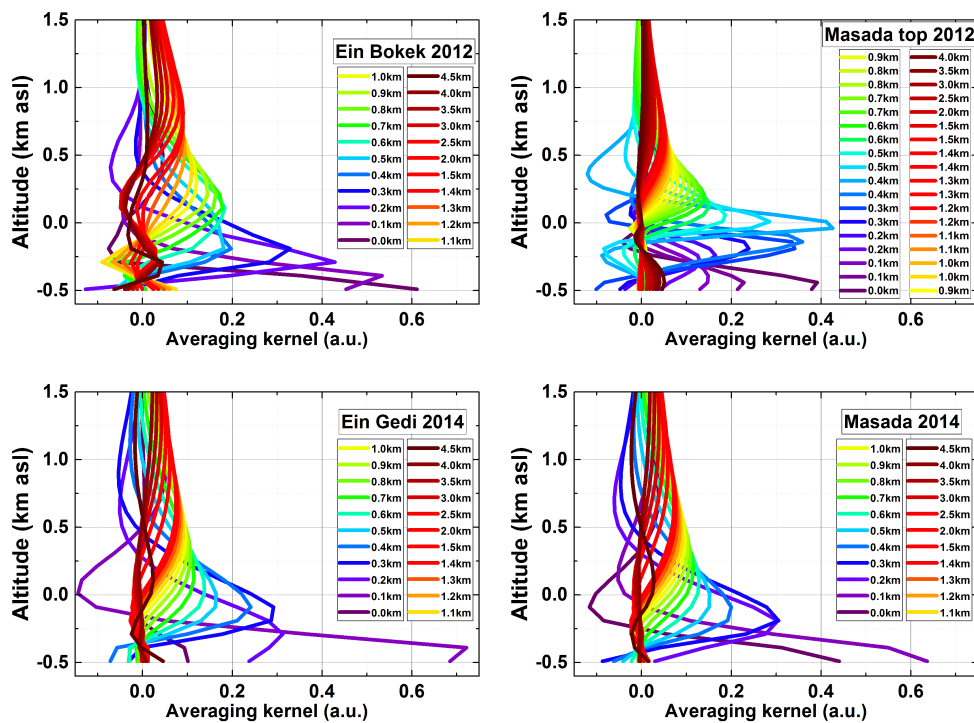
Fig. 5.38: Typical examples of averaging kernels from the retrieval of MAX-DOAS data on May 12 2012 10:38 UTC (upper plots) and Nov. 28 2014 10:08 UTC (lower plots). For the sake of clarity, only altitudes up to 2 km above ground level are shown.

5.2 LP-DOAS instrument 2012

5.2.1 Hardware

The LP-DOAS instrument which was used for the measurements at Ein Bokek is described by Pöhler [2010]. The telescope unit consists of a single spherical mirror and an Y-fiber bundle. The method of the fiber based telescope setup is described by Merten [2008]. A simplified scheme is shown in figure 4.3.

The main hardware components are listed in table 5.10. The light of a xenon arc lamp filtered by one of several color glass filters, depending on the current wavelength interval of the measurement. The filtered light is focused on a single optical fiber with a diameter of 800 μm using a fused silica lens. All optical fibers are also made of fused silica and have a sufficient transmission for light from the ultra-violet to visible range. The single fiber is coupled to a multi fiber bundle consisting of 6 single fibers with 200 μm diameter each arranged in a circular way. The coupling between the fibers leads to radial mode mixing which homogenizes possible inhomogeneities in the spatial and spectral distribution of the light emitted from the plasma spot of the xenon arc lamp. For the impact of mode mixing on spectral residual structures and thus on the measurement quality see Stutz and Platt [1997] or, more recent Eger [2014]. The multi fiber bundle guides the light to the telescopes mirror where it is parallelized and send out through the atmosphere on a retro reflector array. The reflector array is positioned 5 km away from the telescope and consists of 24 single reflectors made of fused silica. The light is reflected back to the telescopes mirror and focused on a single 200 μm fiber at the center of the multi fiber bundle. The center fiber guides the light to the spectrometer where its information is digitized and then sent to a PC for data storage and processing.

Component	Description
Light source	OSRAM XBO-75 (non-ozone free (OFR))
Color glass filters	Schott UG5, HOYA B390, Schott OG515 and Schott RG610
Optical fiber configuration	800 μm mono fiber coupled to 6:7:1 200 μm bundle
Telescope mirror	Diameter 30 cm, Focal length 150 cm
Lamp reference plate	sandblasted aluminum scatterer
Retro reflector array	24 single fused silica reflectors
Spectrometer optical bench	Acton Spectra 300i temperature stabilized at 36°C. Focal length 300mm, f-number f/4. Grating w. 600 grooves per mm. Blaze wavelength 300 nm. Spectral resolution 0.53 nm. Spectral width 80 nm / grating position.
Spectrometer camera	Roper Scientific 10:2KBUV cooled to -30°C 2048 x 512 pix CCD back-illuminated.
Data aquisition software	COS Mettendorf [2005] and Pöhler [2010]

Table 5.10: List of hardware specifications of the LP-DOAS instrument used during the campaign in 2012 at the Dead Sea.

5.2.2 Data acquisition

The LP-DOAS data was acquired using the software "Camera Operation Software" (COS) developed at the Institute for Environmental physics Heidelberg by Mettendorf [2005] and Pöhler [2010]. The software controls the shutters for background and lamp reference measurements as well as the stepper motors for the automatic adjustment and optimization of the telescope heading, the motors for the filter wheel and the motor for the grating of the spectrometer. Figure 5.39 shows a schematic of the measurement procedure. R_j are reference spectra, A_i are atmospheric spectra and R_B and A_B the corresponding background spectra. Within each wavelength interval, 5 lamp reference spectra and 4 atmospheric spectra were recorded in an interlaced way to minimize the difference of possible lamp variations during the time between the first and the last spectrum. This minimizes possible residual structures in the DOAS analysis when adding up spectra to enhance the signal to noise ratio (see section 5.2.3). At the end of this sequence the background spectra are recorded followed by an optimization of the telescope heading and thus light path alignment. Measurements were performed in 5 wavelength intervals with center wavelengths 280 nm, 330 nm, 430 nm, 560

nm and 640 nm with a width of 80 nm each. Since the 640 nm range was used to measure NO_3, which is rapidly dissociated during daylight, only night time measurements were performed in this wavelength region to enhance to measurement time in other wavelength intervals instead.

This was achieved by turning the spectrometer grating using a stepper motor. For each wavelength interval, an appropriated color glass filter (see table 5.10) was used to reduce IDSL inside the spectrometer (see Eger [2014]), except for 280 nm where the signal to noise is dominated by photon noise rather than residual structures caused by IDSL. A 2048x512 pixel CCD (Roper Scientific 10:2KBUV) mounted onto an Acton 300i optical bench was used. The pixel of the CCD were vertically binned to groups of 8 and a region of interest of 50 lines was used. The exposure time of every spectrum was optimized to get a constant saturation of about 10% (10.000 counts) per single line resulting in a saturation of the readout register of about 30%. However the maximum exposure time was limited to 1 sec. The number of scans per spectrum was fixed to 25. Thus the duration of one sequence including atmospheric, reference and background spectra was limited to about 4.5 minutes but usually between 1 to 2 minutes depending on light attenuation due to dust or haze.
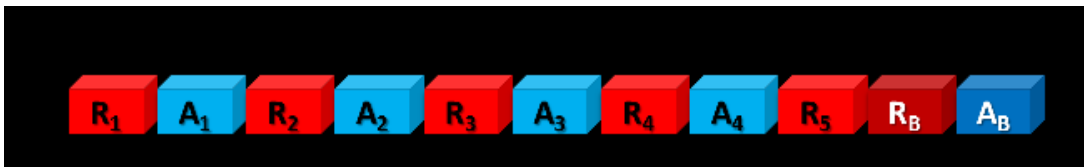
Fig. 5.39: The figure shows a scheme of the measurement routine of the LP-DOAS instrument during the campaign at the Dead Sea in 2012. The center wavelengths of the different wavelength ranges were 280nm, 330nm, 430nm, 560nm and 640nm.

5.2.3 Data Analysis

The spectral data acquired with the LP-DOAS instrument was analyzed using the software DOASIS (Kraus [2006]) with an algorithm written in JScript by D.

Pöhler (pers. comm.). Different fit scenarios were used to retrieve concentrations of a variety of trace gas species in the wavelength range from 240 nm to 680 nm. The species and the literature cross sections used for the analysis are listed in table 5.11. Table 5.12 shows the specifications of all fit scenarios including wavelength intervals, fit constituents and order of DOAS polynomial.

Wavelength calibration and convolution of literature cross sections

All literature cross sections of the trace gases were convolved using emission lines of a mercury (in the UV range up to 470 nm) and a neon lamp (visible range 520 nm to 680 nm) to adapt to the spectral resolution of the LP-DOAS spectrometer. Figure 5.40 shows the recorded spectra of the lamps. The spectra were calibrated with known wavelengths from the literature. Additionally, the spectra were calibrated with a daylight background spectrum taken during the measurements at the Dead Sea. Though being reflected by the soil behind the retro reflector, the background spectrum still contains the differential features of the solar spectrum and can be used for a fine tuning of the wavelength to pixel mapping (similar that what has been done for the MAX-DOAS analysis, section 5.1.4). The lines which were used for the convolution of the high resolution literature spectra of the trace gas absorptions are indicated by the colors cyan and red, for the mercury lamp and neon lamp respectively. The small plots in the right side show the convolution kernels in detail to demonstrates a sufficient sampling by the spectrometer of the LP-DOAS instrument. The spectral resolution (FWHM of the convolution kernels) was about 0.53 nm.
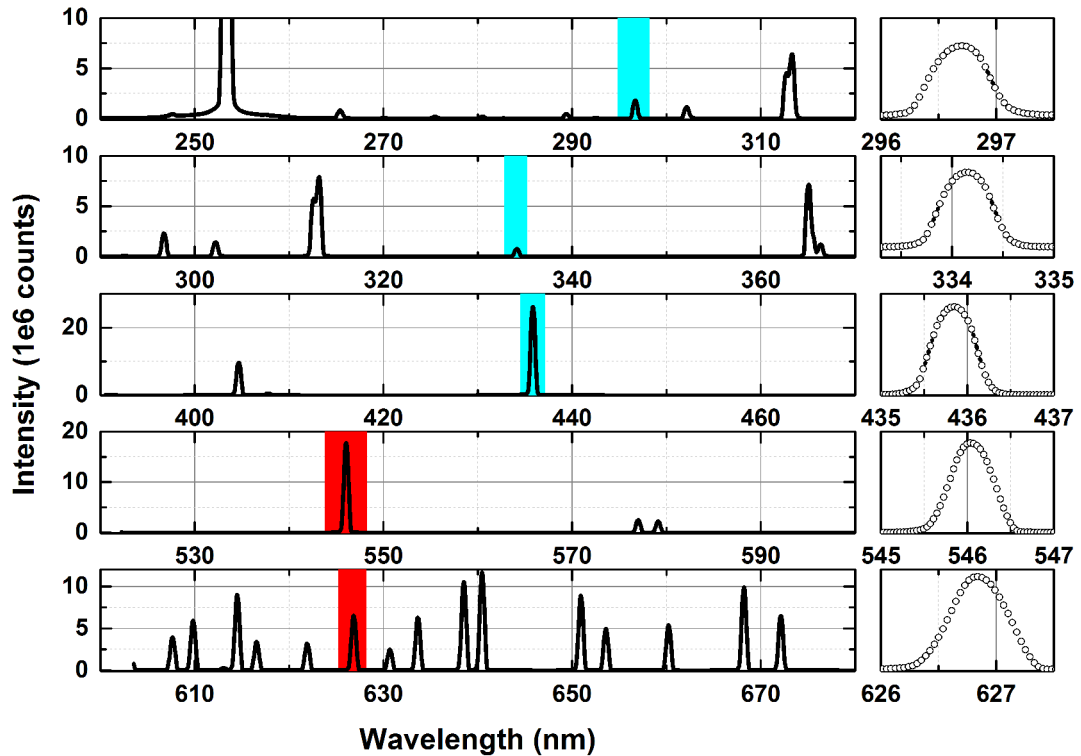
*Fig. 5.40: Spectra of a mercury lamp (240 nm to 470 nm) and a neon lamp (520 nm to 680 nm) recorded with the LP-DOAS instrument during the Dead Sea campaign 2012. The highlighted lines at 296 nm, 334 nm, 435 nm, 547 nm and 627 nm (**cyan for the mercury lamp and red for the neon lamp**) were used for the convolution of the high resolved literature cross sections to adapt them to the instruments spectral resolution of $\approx$ 0.53 nm. The small plots on the right show the convolution kernels in detail (scaled to their maximum) to demonstrate sufficient sampling. White circles correspond to spectrometer pixels, respectively.*

Correction of dark current, offset and atmospheric background signal

The atmospheric spectra as well as the lamp reference spectra were corrected with their corresponding background spectra (light source blocked). Exposure time and number of scans of an atmospheric spectrum and its corresponding background spectrum were always identical. The same prevails for lamp reference and lamp reference background. Therefore, the background correction can be

done by simply subtracting the background spectrum. This also corrects for dark current and offset signal.

Spectral averaging

To enhance the signal to noise ratio, the spectra taken within one measurement loop at a specific wavelength (see also 5.39) are co-added. The background corrected atmospheric and reference spectra were merged into one atmospheric and one reference spectrum. Equation 5.6 illustrates how the single atmospheric spectra A_i, lamp reference spectra R_j and their backgrounds with index B are processed to generate an optical density spectrum D to which the fit scenarios listed in table 5.12 are applied. The array in brackets on the left site represents the chronological order of the recorded spectra.

$$[R_1; A_1; R_2; A_2; R_3; A_3; R_4; A_4; R_5; R_B; A_B] \Rightarrow \ln \frac{\sum_{i=0}^{4}(A_i - A_B)}{\sum_{j=0}^{5}(R_j - R_B)} = D \quad (5.6)$$

Conversion of fitted slant column densities into volume mixing ratios

To convert the slant column densities from the fit result to volume mixing ratios, current meteorological data for pressure and temperature from the KIT weather station at Dead Sea Works Pump Station P88 was used (31.329°N, 35.402°E). It should be noted that the station is 14 km north of the LP-DOAS. However, being on the same altitude, the spatial distance is not significant for temperature and pressure values. The total length of the light path was determined by GPS.

DOAS Fit settings

Ten fit scenarios were used to retrieve the slant column densities of trace gases along the light path and thus the volume mixing ratios. Since the measurements

were performed in a broad spectral range of 240 nm to 680 nm the composition of the fit scenarios is adapted for the equivalent wavelength range. Table 5.11 shows the reference cross section which were used for the DOAS analysis. The column "Index" is used in table 5.12 (column "Includes references") and indicates whether the corresponding constituent is included in the fit scenario. Besides absorption cross sections of trace gases, an atmospheric back ground spectrum and a reciprocal lamp spectrum is included in all fit scenarios. The spectra are always taken from the current measurement. The background spectrum in the fit scenario accounts for a fast change in background intensity. The shadow of a cloud, sunrise or sunset can quickly change the illumination of the area behind the retro reflector. This results in a different background signal between the time when the atmospheric spectra are recorded and the time where the actual background spectrum is recorded. In this case, the subtraction of the background spectrum from the atmospheric spectra may overcompensate or under-compensate the real background signal. The background spectrum in the fit scenario corrects for this effect.

A reciprocal lamp spectrum is also included in the fit scenarios, to account for instrument driven stray light (5.1.5). The "Atmospheric daytime reference" is used for the spectral retrieval of I_2 (see below).

Constituent	Index	Reference
BrO	1	Fleischmann et al. [2004]
$C_2H_2O_2$	2	Volkamer et al. [2005]
ClO	3	Simon et al. [1990]
H_2O	4	Rothman et al. [2010], Lampel et al. [2014]
HCHO	5	Meller and Moortgat [2000]
HONO	6	Stutz et al. [2000]
I_2	7	Spietz et al. [2006]
IO	8	Spietz et al. [2005]
NO_2	9	Vandaele et al. [1998]
NO_2	9b	Vandaele et al. [2002]
NO_3	10	Yokelson et al. [1994]
O_2	11	Rothman et al. [2013]
O_3	12	Serdyuchenko et al. [2014]
O_4	13	Thalman and Volkamer [2013]
OBrO	14	Fleischmann and Burrows [2002]
OClO	15	Bogumil et al. [2003]
OIO	16	Spietz et al. [2005]
SO_2	17	Bogumil et al. [2003]
Atmospheric background spectrum	18	measurement
Reciprocal lamp spectrum	19	calc. from measurement
Atmospheric daytime reference	20	measurement

Table 5.11: List of literature cross sections used for the spectral analysis of LP-DOAS data.

The wavelength ranges of the fit scenarios as well as their fit constituents are listed in table 5.12. A DOAS polynomial of the order of two or three was also included depending on the width of the fit range and differential character of the fit constituents. For the retrieval of SO_3 and O_3 (fit scenario LP2), all spectra were high pass filtered (high pass filter function of the analysis software DOASIS, 2000 iterations). The wavelength shifts for all trace gases in the fit scenario were linked to each other. Shifts of reciprocal lamp reference and background spectrum were fixed to zero.

Fitscen. Index	Wavelength interval [nm]	Retrieved trace gas	Includes references (see table 5.11)	DOAS Poly. order	RMS Threshold
LP1	291.3 - 301.5	**ClO**	1,3,9,13,17,18,19	3	-
LP2	297.9 - 325.2	**SO$_2$, O$_3$**	1,5,9,12,15,17,18,19	3+HP2000	2∗10e-3
LP3	336.3 - 370.3	**HONO, O$_4$**	1,5,6,9,13,15,18,19	3	2∗10e-3
LP4	324.7 - 355.4	**BrO, HCHO, OClO**	1,4,5,6,9,13,14,17,18,19	3	1∗10e-2
LP5	423.4 - 448.3	**IO, NO$_2$, H$_2$O**	2,4,8,9b,18,19	3	2∗10e-3
LP6	453.5 - 467.5	**C$_2$H$_2$O$_2$**	2,4,8,9b,18,19	3	2∗10e-3
LP7	565.7 - 578.7	**H$_2$O**	4,7,9b,10,18,19	2	2∗10e-3
LP8	530.6 - 561.2	**I$_2$**	7,9b,10,18,19,20	2	2∗10e-3
LP9	548.3 - 566.3	**OIO, OBrO**	4,7,9b,10,18,19	3	2∗10e-3
LP10	603.5 - 643.3 659.11 - 677.28	**NO$_3$, O$_2$**	4,9b,10,12,13,18,19	2	1∗10e-2

Table 5.12: Specifications of the fit scenarios used for the spectral analysis of the LP-DOAS data. In fit scenario LP4 a additional high pass filter with 2000 iterations was applied. In fit scenario LP10 two separated fit ranges are used to exclude strong water absorption.

Retrieval of I$_2$ using an atmospheric daytime reference spectrum

Due to its periodic spectral nature, the fitting of the absorption cross section of I$_2$ is often ambiguous. Systematical residual noise is likely to be interpreted as an artificial I$_2$ signal. Figure 5.41 shows an exemplary fit of I$_2$ using the fit scenario LP8 (see table 5.12). To enhance the stability of the fit, a broad fit range from 530 nm to 561 nm is used. The lifetime of I$_2$ with respect to photolysis is in the order of 5-10 seconds (see Saiz-Lopez et al. [2004]). Therefore, I$_2$ abundance can be assumed insignificant during daylight. This allows to add an atmospheric daylight reference spectrum in the fit scenario decreasing the residual structures by a few 10^{-4} by accounting for water absorption and other spectral structures which may originate from unknown absorbers or from instrumental effects. No additional water reference cross section was included in this particular fit scenario.

The daylight reference spectrum was chosen within a limited solar zenith angle interval of 60° to 80° and was recorded during every sunset. Assuming a daytime

I_2 mixing ratio below the detection limit, this criterion ensures the reference to be essentially void of I_2 absorption structures and temporally close to twilight measurements where the abundance of molecular iodine is expected. It will be shown in later that the dynamics of the I_2 signal is in the order of minutes. Therefore, spectral averaging is not a choice because too much temporal information would be lost.
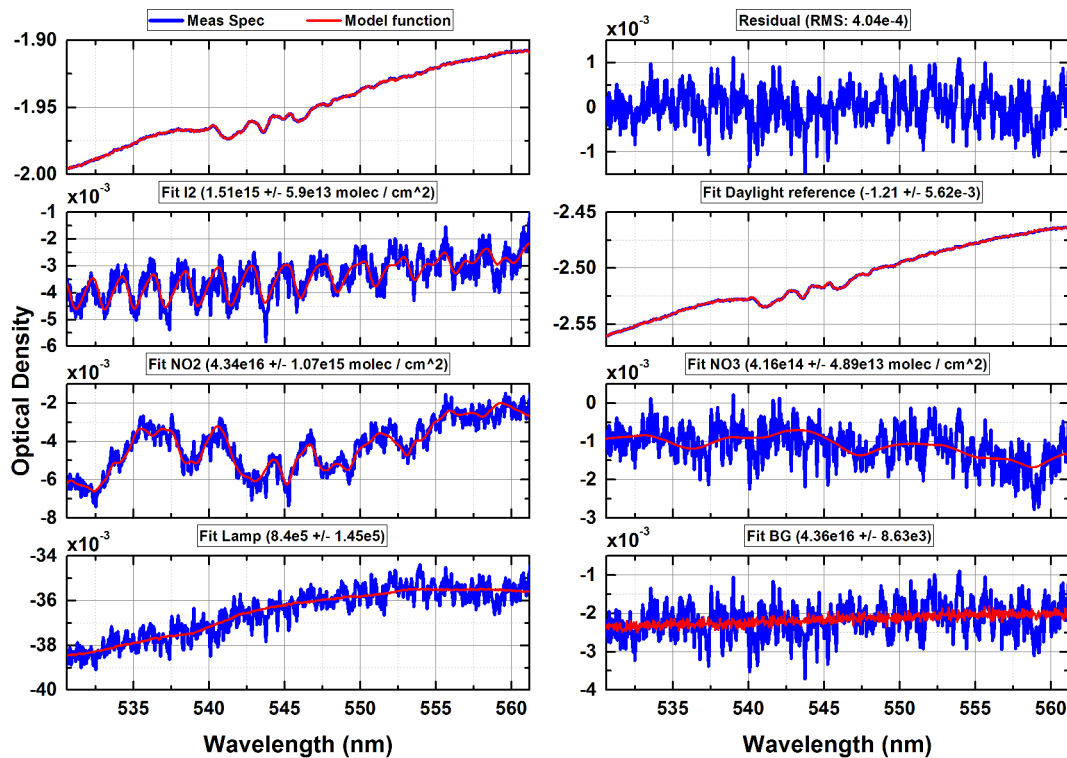
Fig. 5.41: Exemplary fit result of fit scenario LP8 applied on the spectrum recorded on May 12th 2012, 17:38 UTC, SZA 104°. The DOAS polynomial is not shown for the sake of clarity. The fitted slant column density of I_2 corresponds to a volume mixing ratio of about 60 pptv. The prominent absorption features in the daylight reference spectrum are caused by absorption of water vapor. The slant column density errors are defined by the errors of the fit algorithm.

5.2.4 Quality of the LP-DOAS data analysis

Several examples of spectral fits of the retrieved trace gases are shown in figures 5.42 to 5.48 in order to estimate the quality of the spectral evaluation. Secondary fit constituents (e.g. fit of background spectrum, polynomial, trace gases which are retrieved in other fit scenarios) are not shown in the fit examples for the sake of simplicity. Further, RMS histograms are shown in figure 5.49. In every fit scenario, an RMS threshold filter was used. The threshold corresponding to the different fit scenarios are listed in table 5.12. On the one hand, the RMS indicates how well the measured optical density is represented by the model function. On the other hand, the RMS of the residual spectra is dominated by photon noise (due to the high time resolution of the measurements) and other instrumental noise. Therefore, the RMS values can be used as a representation for the quality of the DOAS analysis. However, the histograms do not represent the best possible quality which can be achieved with the hardware of the instrument because only a limited number of spectra was averaged during the analysis. A compromise between sufficient accuracy and time resolution was made which is crucial when investigating the dynamics of high reactive trace gases on the scale of minutes.
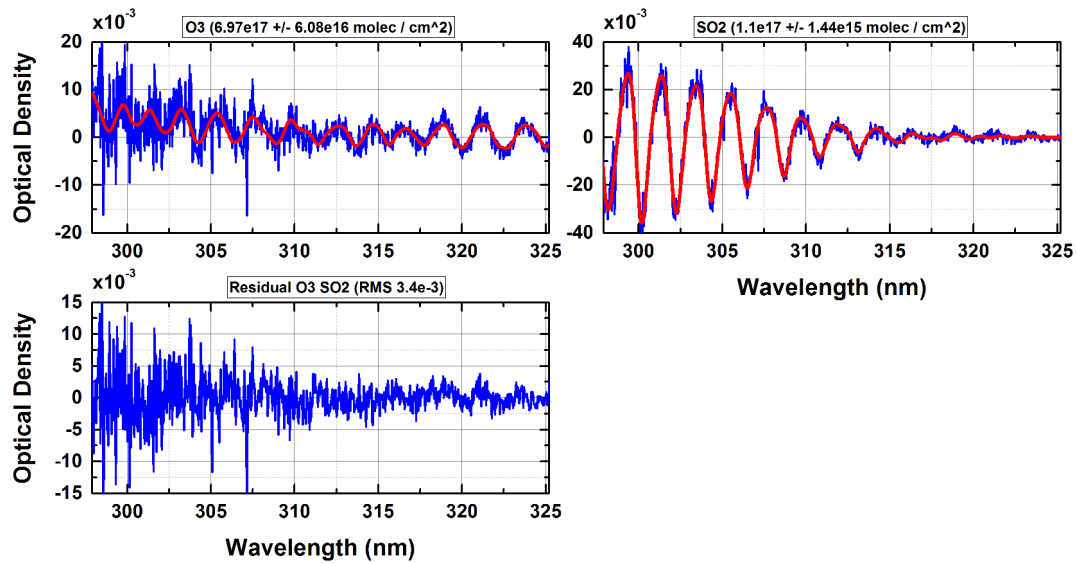
*Fig. 5.42: Fit result of spectrum number 2754 using **fit scenario LP2**. 2012 May 6, 20:00 UTC. SZA 126°. O_3 vmr: 27.8 +/- 4.9 ppbv. SO_2 vmr: 4.4 +/- 0.12 ppbv. Secondary fit constituents (refer to table 5.12) are not shown. The slant column density errors are defined by the errors of the fit algorithm.*
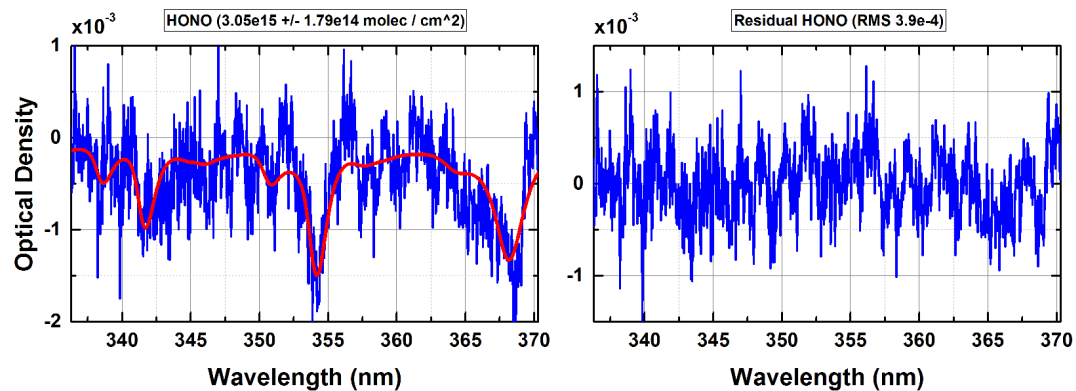
*Fig. 5.43: Fit result of spectrum number 5050 using **fit scenario LP3**. 2012 May 12, 07:24 UTC. SZA 118°. HONO vmr: 120 +/- 1.4 pptv. Secondary fit constituents (refer to table 5.12) are not shown. The slant column density errors are defined by the errors of the fit algorithm.*
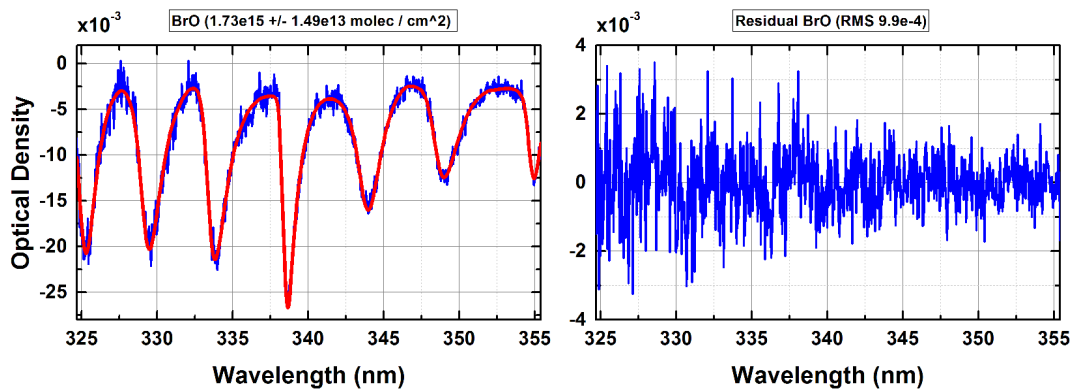
*Fig. 5.44: Fit result of spectrum number 2078 using **fit scenario LP4**. 2012 May 5, 14:11 UTC. SZA 63°. BrO vmr: 70 +/- 1 pptv. Secondary fit constituents (refer to table 5.12) are not shown. The slant column density errors are defined by the errors of the fit algorithm.*
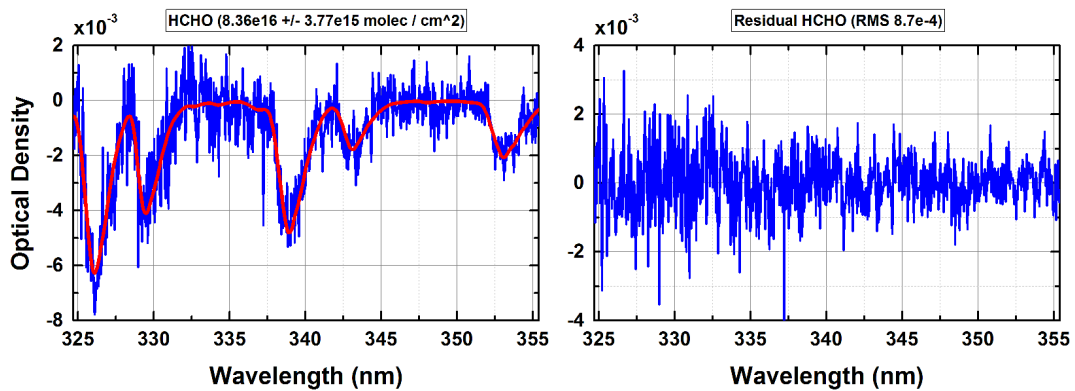
*Fig. 5.45: Fit result of spectrum number 1862 using **fit scenario LP4**. 2012 May 5, 07:49 UTC. SZA 28°. HCHO vmr: 3.3 +/- 0.3 ppbv. Secondary fit constituents (refer to table 5.12) are not shown. The slant column density errors are defined by the errors of the fit algorithm.*
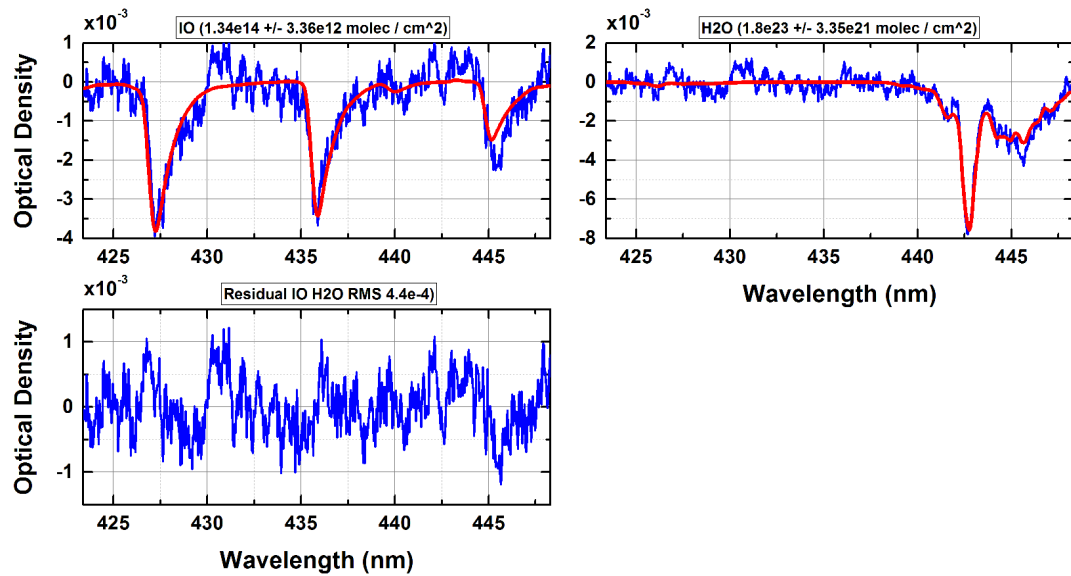
Fig. 5.46: Fit result of spectrum number 5294 using **fit scenario LP5**. 2012 May 12, 11:56 UTC. SZA 34°. IO vmr: 5.4 +/- 0.27 pptv. H_2O vmr: 0.7 +/- 0.03 %. Secondary fit constituents (refer to table 5.12) are not shown. The slant column density errors are defined by the errors of the fit algorithm.
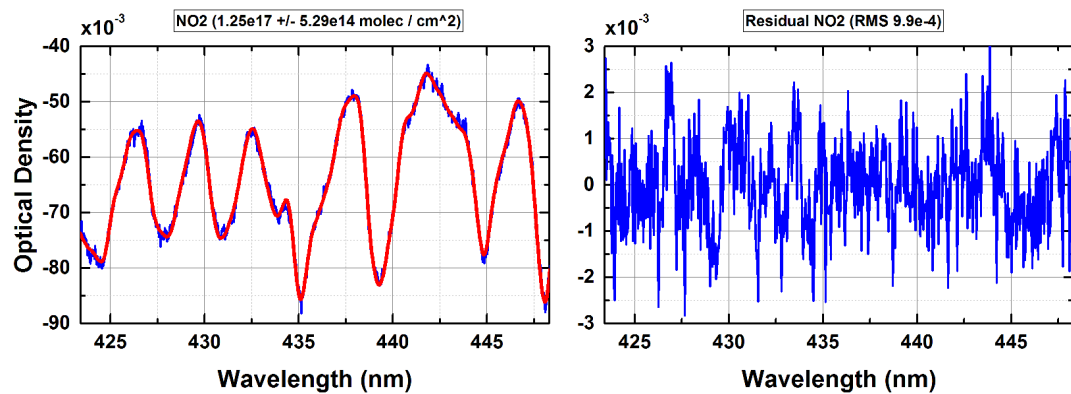
Fig. 5.47: Fit result of spectrum number 4666 using **fit scenario LP5**. 2012 May 11, 05:54 UTC. SZA 51°. NO_2 vmr: 5 +/- 0.03 ppbv. Secondary fit constituents (refer to table 5.12) are not shown. The slant column density errors are defined by the errors of the fit algorithm.
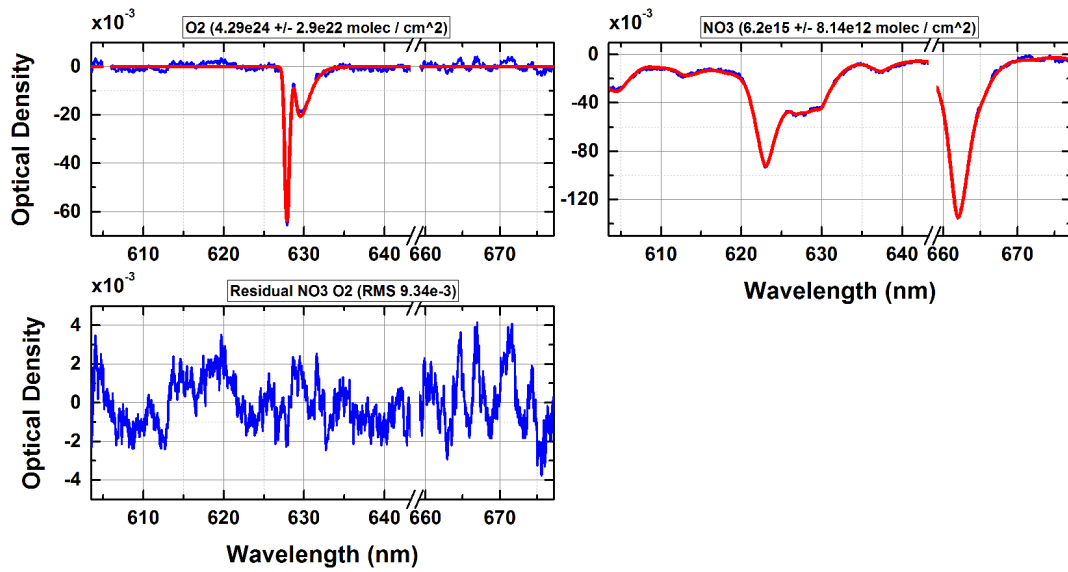
Fig. 5.48: Fit result of spectrum number 4686 using **fit scenario LP10**. *2012 May 11, 18:56 UTC. SZA 117°. O_2 vmr: 17.3 +/- 0.2 %. NO_3 vmr: 249 +/- 0.65 pptv. Secondary fit constituents (refer to table 5.12) are not shown. The slant column density errors are defined by the errors of the fit algorithm.*
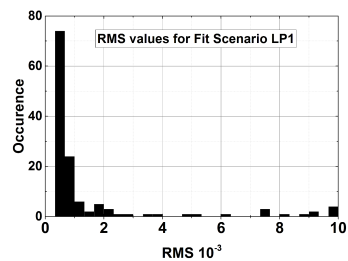
(a) Histogram of RMS values of fit scenario LP1 used for the retrieval of **ClO**.
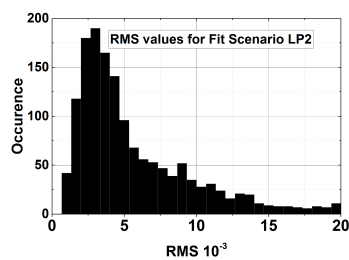
(b) Histogram of RMS values of fit scenario LP2 used for the retrieval of O_3 and SO_2.
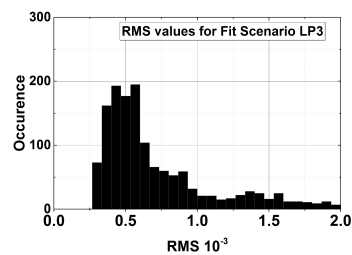
(c) Histogram of RMS values of fit scenario LP3 used for the retrieval of **HONO** and O_4.
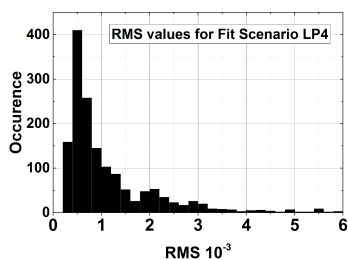
(d) Histogram of RMS values of fit scenario LP4 used for the retrieval of **BrO**, **HCHO** and **OClO**.
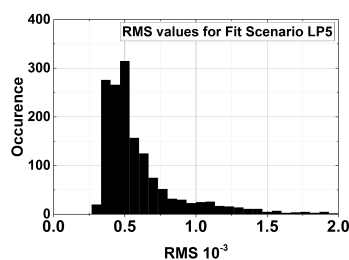
(e) Histogram of RMS values of fit scenario LP5 used for the retrieval of **IO**, NO_2 and H_2O.
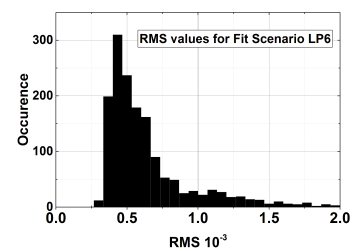
(f) Histogram of RMS values of fit scenario LP6 used for the retrieval of $C_2H_2O_2$.
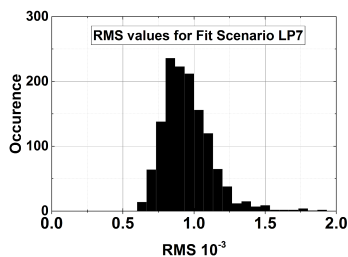
(g) Histogram of RMS values of fit scenario LP7 used for the retrieval of H_2O at 570 mn.
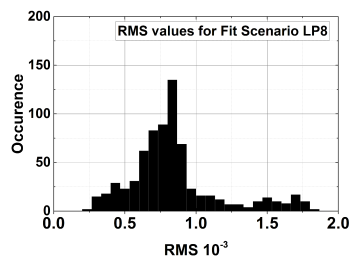
(h) Histogram of RMS values of fit scenario LP8 used for the retrieval of I_2.
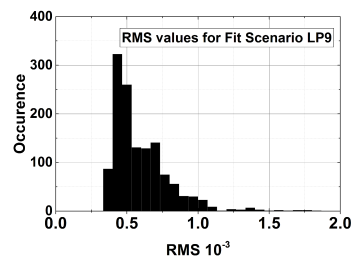
(i) Histogram of RMS values of fit scenario LP9 used for the retrieval of **OIO** and **OBrO**.
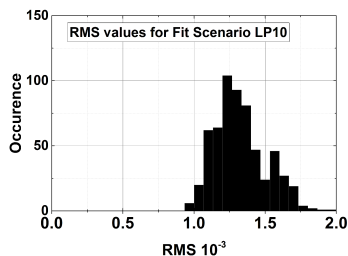
(j) Histogram of RMS values of fit scenario LP10 used for the retrieval of NO_3 and O_2.

Fig. 5.49: Histograms of residual root mean square values of the LP-DOAS analysis for all fitscenarios listed in table 5.12.

6

Measurement setup of Dead Sea Campaign 2012

In May 2012, an extensive field campaign was carried out at the Dead Sea within the framework of DFG research unit 763 "Natural Halogen Processes in the Environment - Atmosphere and Soil (HaloProc)". The goal was to get a better understanding of the sources and source strengths of reactive halogen species at the Dead Sea Valley. Figure 6.1 shows a map with the positions of the instruments.

A MAX-DOAS instrument was set up at the mesa of Masada. Another MAX-DOAS instrument was set up at a balcony of a hotel at Ein Bokek together with a LP-DOAS instrument, a particle counter and an aerosol sampler. The hotel was approximately 20 m away from the water surface. The retro reflector of the LP-DOAS was installed at a construction site of the Dead Sea Works company at the dam separating Israel from Jordan, resulting in the LP-DOAS measurement path being located entirely above water.

The particle counter and an aerosol sampler were operated by Katharina Kamilli (working group of Prof. Andreas Held from University of Bayreuth). The two MAX-DOAS instruments were operated by Robert Holla, who already presented parts of the data in his PhD thesis (see Holla [2013]). The LP-DOAS instrument was operated by the author of this thesis.

An overview of the positions and headings of the instruments is given in table 6.1.
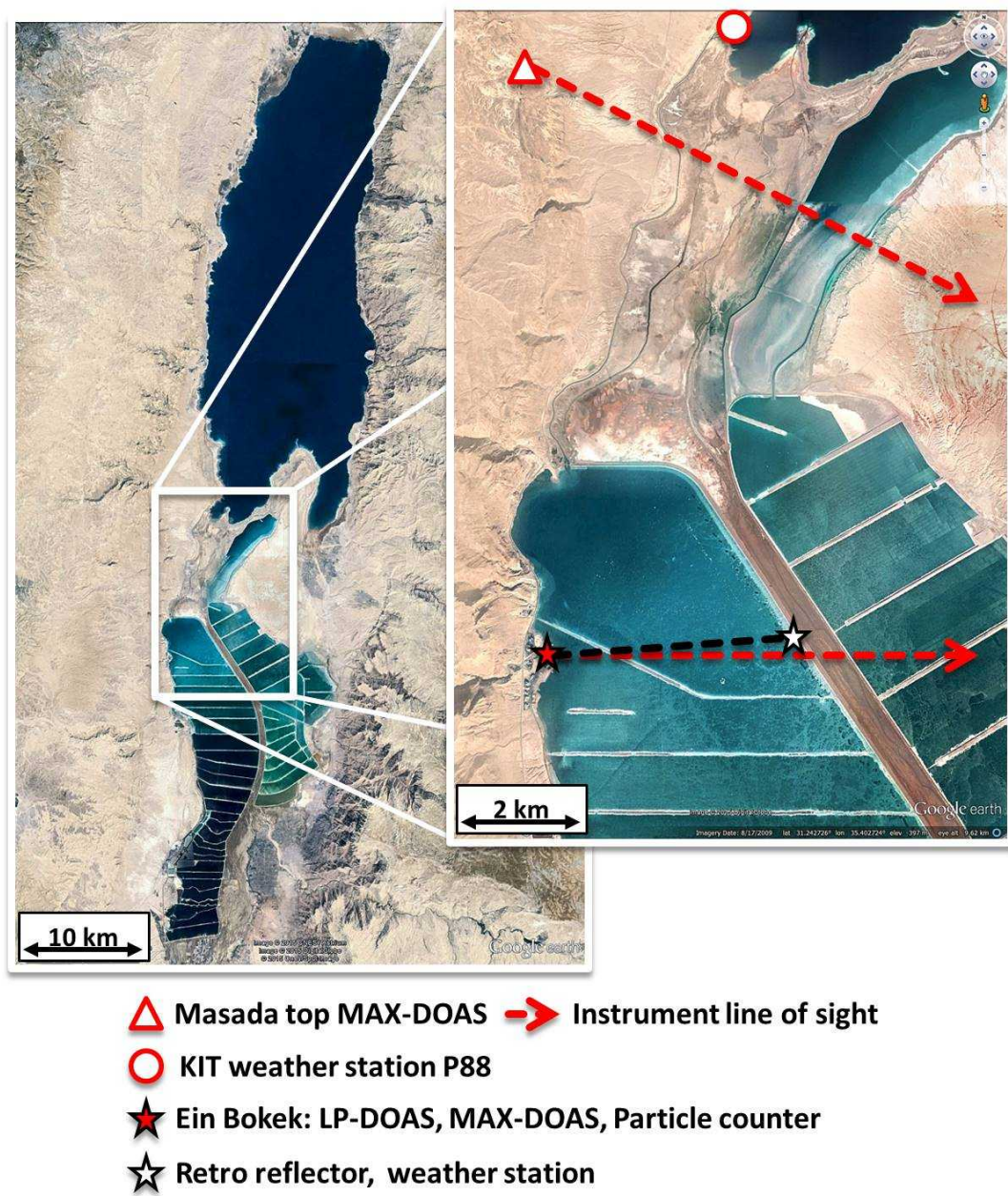
Fig. 6.1: Measurement setup of the Dead Sea campaign in 2012. Adapted from Google Earth. Images ©2015 CNES/Astrium, ©2015DigitalGlobe, ©2015 Cnes/Spot Image.

Instrument	Coordinates	Altitude above Dead Sea level in m	Heading
LP-DOAS telescope	31.1995°N 35.3648°E	20	83°
LP-DOAS reflector	31.2051°N 35.4159°E	2	-
MAX-DOAS Ein Bokek	31.1995°N 35.3648°E	20	90°
MAX-DOAS Masada top	31.3167°N 35.3546°E	435	118.5°
Particle counter	31.1995°N 35.3648°E	20	60° to 160°
Aerosol filter	31.1995°N 35.3648°E	20	60° to 160°
Masada weather station P88	31.3289°N 35.4009°E	20	-
Ein Bokek weather station	31.2051°N 35.4159°E	4	-

Table 6.1: Coordinates and headings of the instruments of the camapign in 2012.

6.1 Meteorology

Meteorological data was monitored by two weather stations. One station is permanently installed at Dead Sea Works pump station P88 which is located at the southern end of the northern basin where water is pumped to the evaporation ponds in the southern basin. The station is operated by the Institute for Meteorology Karlsruhe (IMK). A detailed description of the weather station can be found at IMK [2012]. The station has scientific grade sensors to measure wind speed, wind direction, solar radiation as well as temperature and humidity.

A second weather station (Type *Vantage Pro 2* by Davis Instruments) was temporarily deployed next to the LP-DOAS retro reflector on the dam between the Israeli and Jordanian evaporation ponds at the southern basin of the Dead Sea.

6.2 Water surface roughness from camera pictures

During the campaign, a web cam mounted on the balcony of the Hotel at Ein Bokek was continuously recording pictures with a time resolution of minutes. The viewing direction of the web cam was similar to the heading of the MAX-DOAS and LP-DOAS telescopes. Besides the monitoring of the cloudiness, these

pictures can be used to derive the water surface roughness which is influenced by wind speed. Figure 6.2 shows pictures of a passing wind front from northern direction. It can be clearly observed how the water reflection decreases instantly when the front-line of the wind front passes. The change in reflectivity and simultaneous decrease in apparent brightness of the water surface was used as an indicator to determine the surface roughness. The camera pictures of the measurement period were manually evaluated. In the following meteorological plots, the WSR will be displayed as a cyan area if surface roughness is detected in the camera pictures.

Besides giving information about wind speeds, which at least qualitatively substitutes the weather station at the reflector (in particular during times of weather station failure) the WSR provides another important influence factor. It indicates a fast change in meteorologic conditions, or more precise, a sudden swirl or turbulent mixing of air masses at the position of the LP-DOAS and MAX-DOAS measurements.

Fig. 6.2: Pictures of the web cam at Ein Bokek (viewing direction east). Between 13:17 UTC and 13:20 UTC on May 5th 2012, an increase in wind speed from northern direction caused small waves on the water surface thus increasing its roughness and decreasing its reflectivity (red arrow).

6.3 LP-DOAS measurements

The LP-DOAS instrument was sheltered inside a hotel room of "LOT Hotel" at Ein Bokek. The telescope was pointing through an permanently open balcony door (see pictures in figure 6.3). The height of the balcony was approximately 20 m above the water surface of the Dead Sea. The pictures in figure 6.4 show the view from the balcony to the reflector and vice versa. The reflector was placed on the dam which isolates the evaporation ponds of the Dead Sea Works company. The distance between the telescope and the reflector was 4910 m resulting in a total light path length of 9820 m. The height of the reflector was approximately 2 m above Dead Sea level.

(a) Retro reflector array consisting of 24 single reflectors (each 7 cm diameter).

(b) LP-DOAS telescope at LOT Hotel at Ein Bokek.

Fig. 6.3: Picture **(a)** shows the retro reflector array on a dam of the Dead Sea Works company. The reflector was about 2 m above water level. **(b)** shows the telescope in a room of LOT Hotel in Ein Bokek. Height above water level was about 20 m.

(a) View from telescope to retro reflector.   (b) View from retro reflector to telescope.
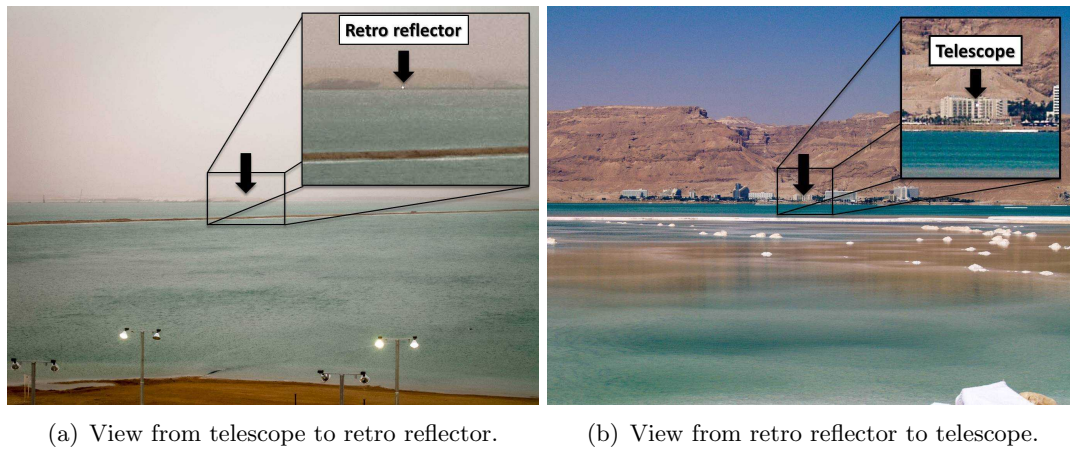
*Fig. 6.4: The Pictures **(a)** and **(b)** show the view from the telescope to the reflector and vice versa (on different days). The distance between telescope and reflector was about 5 km.*

6.4 Ein Bokek MAX-DOAS

The scanner unit of the MAX-DOAS at Ein Bokek was mounted on the railing of the hotel balcony. The heading was 90°. Besides the classical, positive elevation angles, spectra were also recorded at -5°. Figure 6.5 illustrates the resulting measurement geometry. A telescope elevation angle of 80° has been chosen as reference elevation since the light path with 90° viewing direction was blocked by the above balcony of the hotel. For details about the data acquisition see section 5.1.3. Figure 6.5 shows a cross section of the measurement geometry along the line of of the instrument. It is important to note that only positive elevation angles were used in the profile retrieval. This means that besides the vertical gradient, also the retrieved surface mixing ratios are affected by positive elevation angles alone which is sufficient for the box dimension of 100 m (and an instrument altitude of 20 m). Thus the difference between the retrieved surface mixing ratios and the measured mixing ratios from the LP-DOAS can be used to determine a more detailed gradient of the trace gases within the first 100 m above the water surface.

At -5°, the telescope is pointed at the water surface at a distance of approximately 230 m away from the scanner. If the reflectivity of the water surface is sufficiently high (as can be seen in the picture of figure 6.5), the light path in the box below the instrument doubles to approximately 460 m. This will be important for the comparison with the LP-DOAS data later.

6.5 Masada top MAX-DOAS

Another MAX-DOAS instrument was set up at the mesa of Masada at a balcony of a hut provided by the personal of the Masada National Park. The altitude of the instrument was approximately 435 m above the bottom of the valley (20 m absolute altitude). The heading of the telescope was 118.5°. Besides the classical elevation sequence, spectra under several negative elevation angles were also recorded (for details about the data acquisition, see section 5.1.3). Figure 6.6 shows a cross-section along the line of sight of the instrument. Using a simple geometric Ansatz, the position where the field of view of the telescope points at the ground are calculated and displayed in the figure.
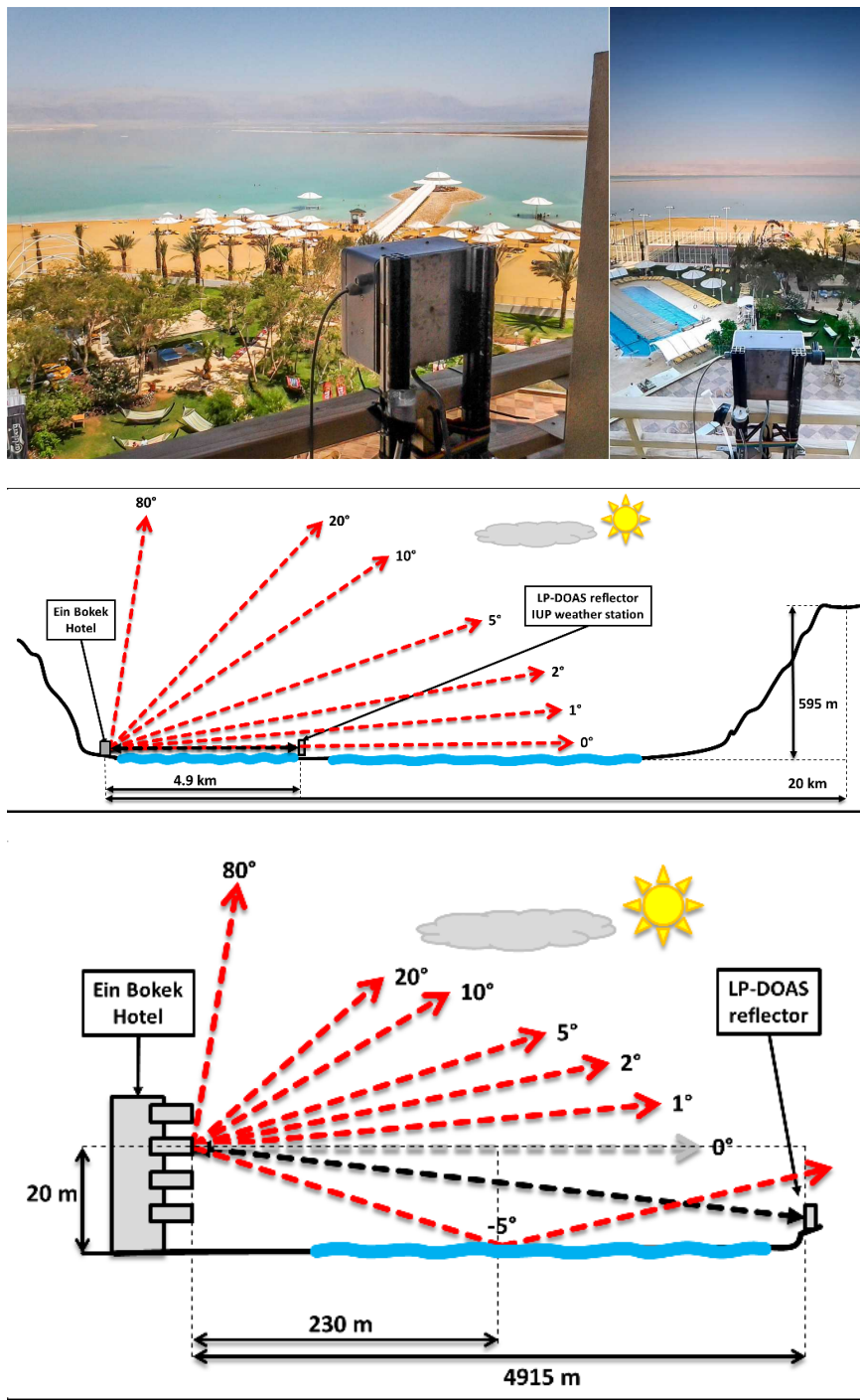
Fig. 6.5: **Top:** *MAX-DOAS scanner mounted at the balcony of the LOT Hotel at Ein Bokek 20 m above the water surface. Right pictures illustrates the telescope heading of 90° (east).* **Middle:** *Geological cross-section along the line of sight of the DOAS instruments at Ein Bokek. Height profile adapted from Google Earth. ©2015 Google, ©2015 ORION-ME, ©2015 Digital Globe, US Dept of State Geographer.* **Bottom:** *Detailed measurement geometry of the DOAS instruments at Ein Bokek.*
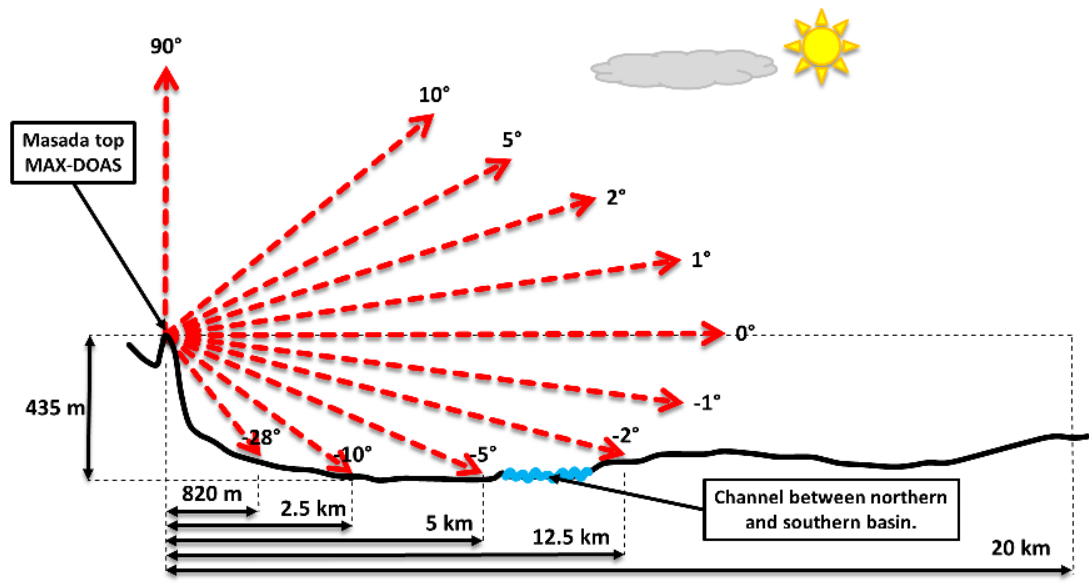
Fig. 6.6: **Top:** *MAX-DOAS installed at a hut at the mesa of Masada at 435 m above the water surface of the Dead Sea. Telescope heading was 118.5°.* **Bottom:** *Geological cross-section along the line of sight of the MAX-DOAS instrument at Masada top. Height profile adapted from Google Earth. ©2015 Google, ©2015 ORION-ME, ©2015 Digital Globe, US Dept of State Geographer.*

6.6 Particle counter

The particle counter, which was also applied in Ofner et al. [2013], was located in the same hotel room like the LP-DOAS and MAX-DOAS at Ein Bokek. The inlet of the instrument was mounted at the balcony in a distance of 2 m away from the walls of the building. The aerosol samplers were also mounted on the balcony of the hotel room. Due to the layout of the hotel building, the catchment area of both the sampler and the particle counter is restricted to wind coming from directions between 60° and 160° (see figure 6.7). The particle counter consisted of a Differential Mobility Analyzer (DMA) and a Condensation Particle Counter (CPC). Together, the units work as a Scanning Mobility Particle Sizer (SMPS). Due to technical failures the DMA was not operative during a short period from May 4th to May 6th and only CPC data is available, which means the total number of particles with diameters between 9 nm and 1000 nm without the size classification feature of the DMA. For the period between May 9th to 15th, particle numbers in the range of 10 nm to 150 nm were measured by the SMPS.
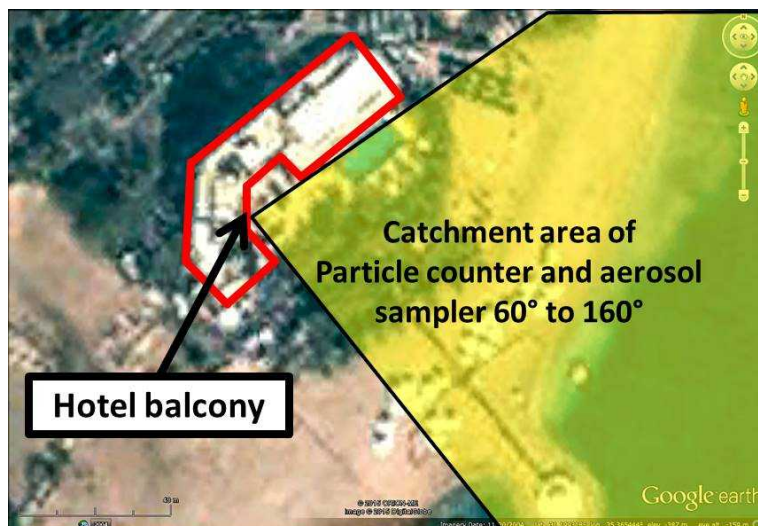
Fig. 6.7: LOT hotel at Ein Bokek. Besides the LP-DOAS and the MAX-DOAS, the particle counter and the aerosol samplers are mounted to the hotel balcony. The footprint of the hotel building is marked in red. The resulting catchment area for in-situ instruments is highlighted in yellow. Image taken from Google Earth. ©2015 ORION-ME, ©2015 Digital Globe.

7

Measurement setup of Dead Sea Campaign 2014

A second campaign was carried out between November 5th and 30th 2014. Based upon the findings of the campaign in May 2012, the main goal in 2014 was to get more insight in the vertical as well as horizontal distribution of trace gases, especially reactive halogen species. Further, it was aimed to investigate the impact of local meteorology on the observed trace gas dynamics. The measurements were integrated in an extensive meteorological field campaign by the Karlsruhe Institute for Technology (KIT). The KIT set up a wide range of instruments at the bottom of Masada to monitor multiple meteorological parameters. The composite of all meteorological instruments described as the "KIT Cube". Besides several self-sustaining weather stations which observed solar radiation, wind, temperature and humidity, the KIT Cube consists of two wind LIDARS, a SODAR, a ceilometer, a cloud radar and an AERONET sun photometer. In the following, data of the wind LIDAR (Leospehere Windcube), the weather stations and the ceilometer is shown (courtesy of KIT, Andreas Wieser, Jan Handwerker and Jutta Metzger, pers. comm.).

To investigate the gas phase chemistry at the Dead Sea Valley, two MAX-DOAS instrument were deployed with one being stationary at the KIT Cube (9heading of 80° for the whole time period while the other instrument was temporary set up at different sites and was used for car MAX-DOAS measurements on 5 days. The temporal locations were: 1) Neve Zohar, which is located at the shore of the southern evaporation ponds, azimuthal heading of 90°. 2) At the KIT Cube at Masada but with a azimuthal heading of 20°, different to the stationary

instrument. 3) At Ein Gedi, located at the northern, natural basin of the Dead Sea, heading 90°. A map in figure 7.1 shows the locations of the instruments. Coordinates of the potions of the instruments and their headings are summarized in table 7.1.
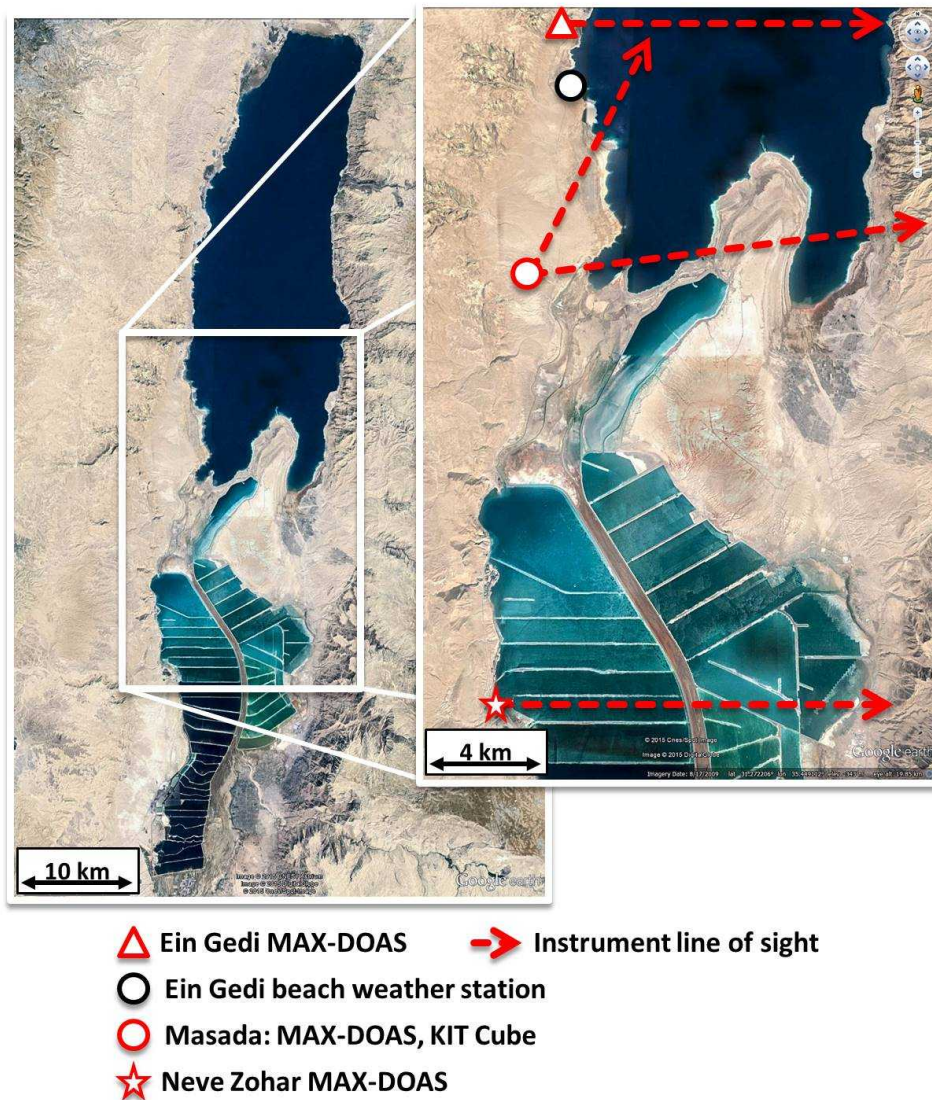
Fig. 7.1: Measurement setup of the Dead Sea campaign in 2014. Adapted from Google Earth. Images ©2015 CNES/Astrium, ©2015DigitalGlobe, ©2015 Cnes/Spot Image.

Instrument	Coordinates	Altitude above Dead Sea level in m	Heading
Neve Zohar MAX-DOAS	31.1995°N 35.3648°E	90	90°
Masada MAX-DOAS	31.3176°N 35.3725°E	57	80°
Masada ISA MAX-DOAS	31.3178°N 35.3730°E	57	20°
Ein Gedi MAX-DOAS	31.4698°N 35.3947°E	20	90°
Ein Gedi weather station	31.4163°N 35.3871°E	2	-

Table 7.1: Coordinates and headings of the instruments of the camapign in 2014.

7.1 Measurement setup

7.1.1 MAX-DOAS at Neve Zohar

During Nov. 8th and 13th, the ISA MAX-DOAS instrument was deployed at at Neve Zohar at a roof of a building (far right on the picture in figure 7.2). As indicated in figure 7.3, the telescopes field of view was located entirely over the water surface of the evaporation pond. The altitude of the instrument was approximately 30 m above water surface level.

Fig. 7.2: Picture of the evaporation ponds at Neve Zohar taken on Nov 8th 2014, viewing direction east.
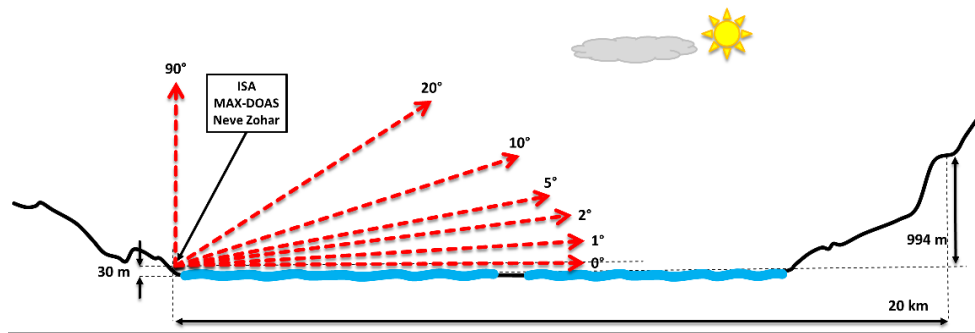
Fig. 7.3: Geological cross-section along the line of sight of the MAX-DOAS instruments at Masada. Height profile adapted from Google Earth. ©2015 Google, ©2015 ORION-ME, ©2015 Digital Globe, US Dept of State Geographer.

7.1.2 MAX-DOAS and KIT Cube at Masada

The measurement site at Masada in 2014 is described a "Masada bottom" to avoid confusion with the measurement site at Masada 2012, which was located at the mesa of Masada. The scanner unit of the EnviMeS MAX-DOAS was permanently mounted on top of the container of the KIT Cube's control room. The heading of the scanner unit was 80°. The spectrometer unit and the computer were located inside and connected via multi core cable and a mutli fiber bundle of 10 m length. The ceilometer, AERONET and wind LIDAR were located a few ten meters distant from the control room of the KIT Cube. The sketch of the measurement geometry in figure 7.4 shows, that the instruments field of view is located above water as well as land mass which is caused by the topography of the Dead Sea basins at that latitude. Especially the distance of approximately 3 km should be kept in mind for the interpretation of the data. The visibility in the wavelength of the MAX-DOAS instruments (300 nm to 450 nm) may vary between 10 and 40 km depending on aerosol load.

During Nov. 19th to 21th and 23th to 25th, the ISA MAX-DOAS was also deployed at the KIT Cube site to perform parallel measurements with a different azimuthal heading of 20°. Therefore, the instrument was placed on the platform of the Wind LIDAR next to the KIT Cube control room. the sketch of the viewing geometry

in figure 7.4 shows that the field of view is located above 8 km of land mass. Depending on visibility range, the trace gas content in air masses above land may dominate the measurements.
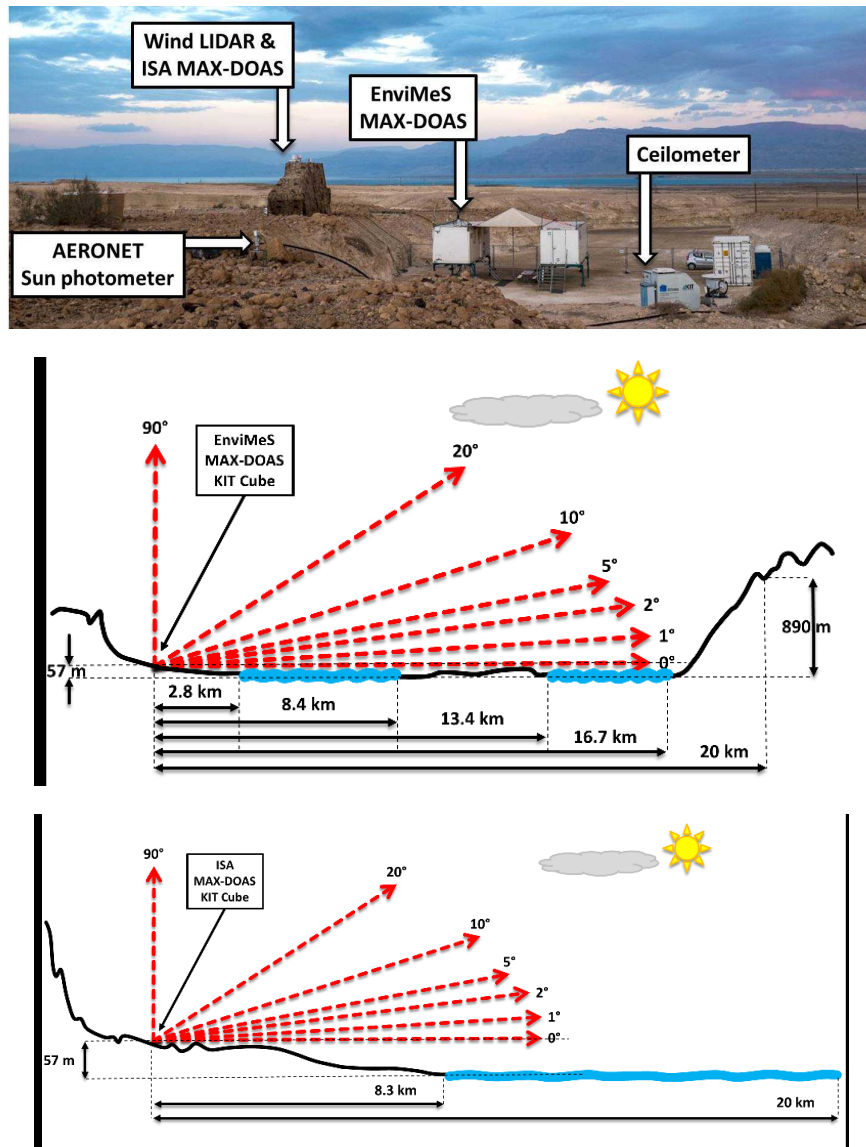
Fig. 7.4: **Top:** *Picture showing the measurement site at Masada on Nov 16th, viewing direction east.* **Bottom:** *Geological cross-section along the line of sight of the MAX-DOAS instruments at Masada. Height profile adapted from Google Earth. ©2015 Google, ©2015 ORION-ME, ©2015 Digital Globe, US Dept of State Geographer.*

7.1.3 MAX-DOAS at Ein Gedi

During Nov. 26th and 30th, the ISA MAX-DOAS was deployed at Ein Gedi to observe the natural, northern Dead Sea basin. The instrument was located at the roof of the Ein Gedi field school reception which is hostel in the Ein Gedi national park. The heading of the telescope was 90° with an altitude of 30 m above the water surface. The building is located on a steep flank of the valley. The distance to the shore is approximately 400 m.
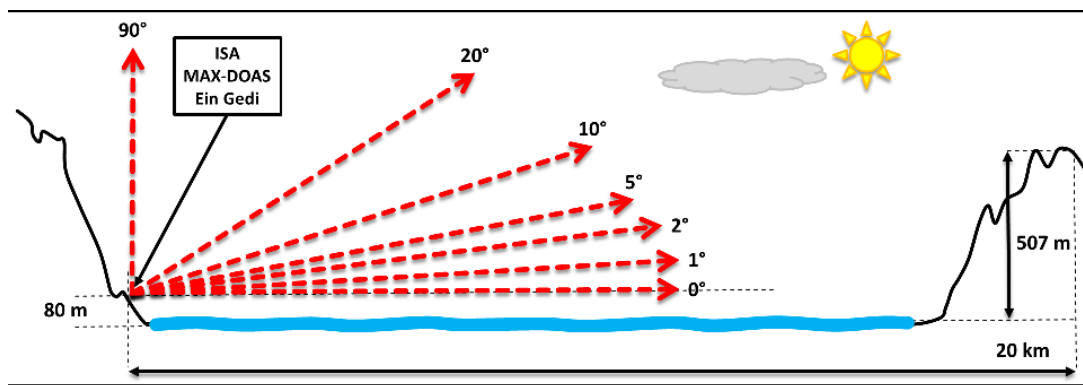
Fig. 7.5: **Top:** *Picture showing the instrumetn at Ein Gedi on Nov 26th, viewing direction 90°.* **Bottom:** *Geological cross-section along the line of sight of the MAX-DOAS instruments. Height profile adapted from Google Earth. ©2015 Google, ©2015 ORION-ME, ©2015 Digital Globe, US Dept of State Geographer.*

Part III

Field studies at the Dead Sea Valley

8

Results of Dead Sea Campaign May 2012

In this section, the results of the campaign performed in 2012 are presented. The first section considers meteorological data. In the following section, the results from trace gas measurements are presented by showing time series and vertical profiles (if available) of mixing ratios. Data of the station at Masada courtesy of KIT IMK, Jutta Zingler (pers. comm.).

8.1 Meteorology

Since the weather station located at the LP-DOAS reflector at Ein Bokek suffered from several failures due to overheating, data from both stations is only available for some days. Therefore, a comparison of the two stations should be done with caution. During nighttime, the wind direction at Ein Bokek is similar to Masada. At day time, wind coming from the northern direction dominates. In figure 8.1 the distributions of wind speed, temperature and relative humidity during day and night are displayed. Wind speed tend to be a few m/s higher during night than during day. Temperatures were ranging between a maximum of 37°C during daytime and 23°C during nighttime. Further a range of relative humidity between 10 and 60% was observed. There was no precipitation during the campaign. On clear conditions, peak solar radiation of 1000 W7m^2 were measured at the bottom of the valley. Figure 8.3 shows wind rose plots from the two weather stations at Masada (P88) and at the LP-DOAS reflector in Ein Bokek during day and during night time.

Figure 8.2 gives an overview of the time series of horizontal and vertical wind speed, wind direction and water surface roughness (WSR) retrieved from camera pictures (see section 6.2. The WRS can only be retrieved during daytime. The data shows that whenever the meteorological conditions at the southern basin change (change in wind speed and / or direction measured by the weather station at the Ein Bokek, blue data), the water surface is clearly influenced (resulting in increased water roughness as indicated by a cyan shaded area in the data plot). Both stations show prevailing northerly to northwesterly winds during the night. At daytime, the Masada P88 station, located on the southern end of the northern basin showed, wind directions between north and east. Since the station is located at the western shore, the eastern winds can be attributed to sea breeze winds that are caused by upwelling air over land masses warmer than the water surface during day time. The upwelling air over land causes air from the direction of the water surface to be dragged towards the land. This leads to wind with directions approximately perpendicular to the alignment of the corresponding coastline.
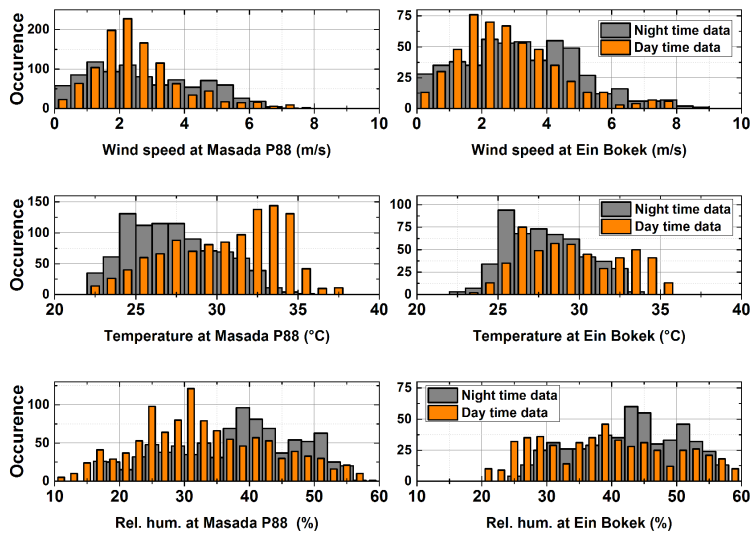
Fig. 8.1: Histogram of horizontal wind speeds, temperatures and relative humidity at the two stations separated in day time and night time data.
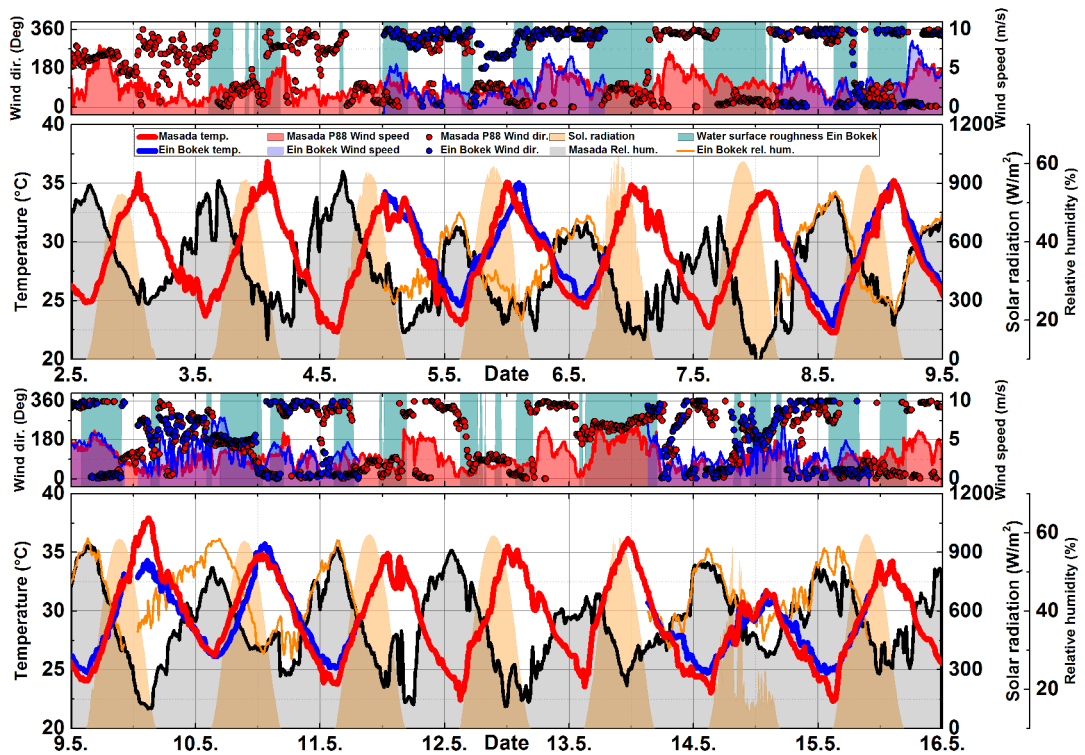
Fig. 8.2: Time series of wind data recorded by the weather stations P88 at Masada (red data) and at the LP-DOAS reflector at Ein Bokek (blue data). Further, relative humidity at Masada (grey area) and at Ein Bokek (orange line) as well as solar radition (orange area) is plotted. Cyan shaded areas indicate water surface roughness induced by wind. Ticks are at 00:00 and 12:00 UTC.
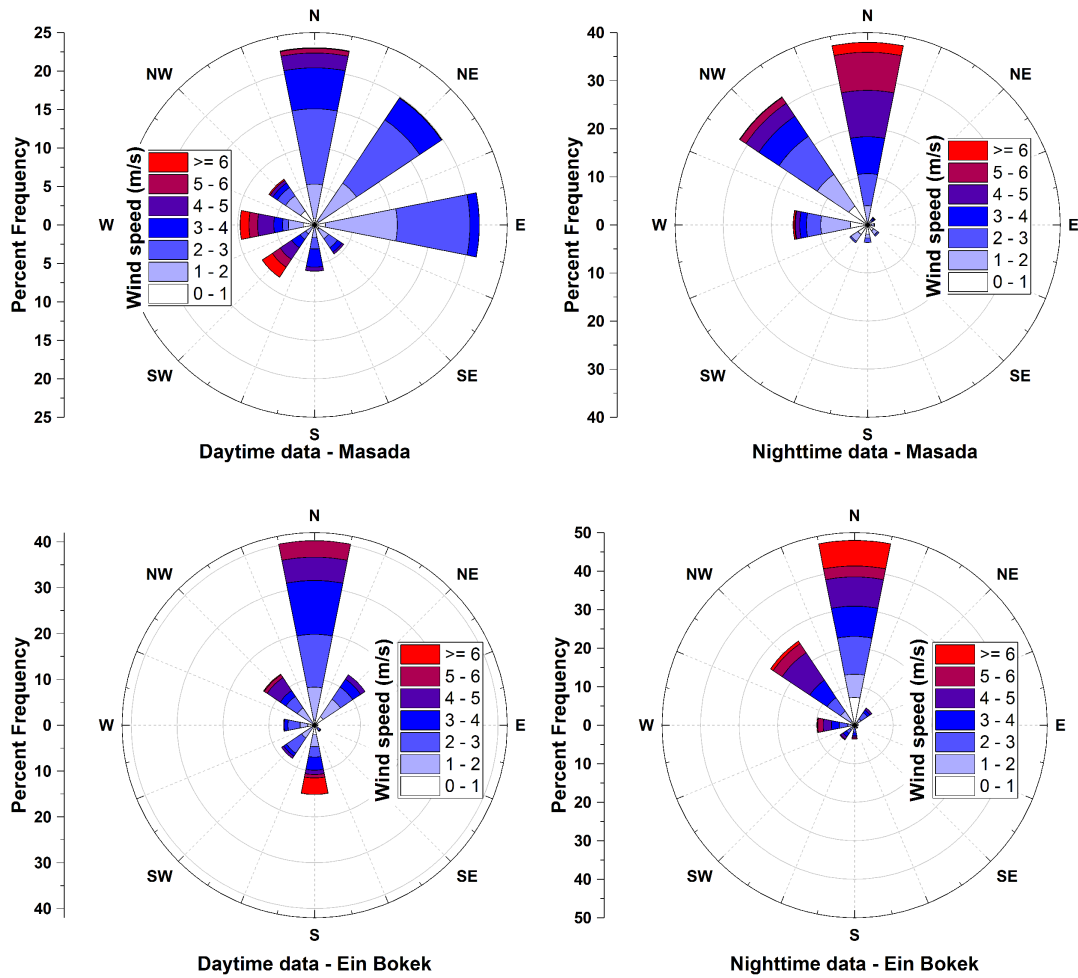
Fig. 8.3: Wind rose plots of horizontal wind speed at the weather stations at Masada and at Ein Bokeks. Note that, due to several failures, the data set of the weather station at the reflector covers only a small part of the total campaign time. Therefore, a comparison of wind roses from the two stations should be done with caution.

8.2 Aerosol optical depth

Aerosol optical depths (AOD) were retrieved from the slant column densities of the oxygen collision complex O_4 measured by MAX-DOAS at a wavelength of 360nm. It describes to what extent light at 360nm in the atmosphere is extincted by scattering caused by aerosols. Figure 8.4 shows the time series of the AODs at Masada and Ein Bokek. Additionally, the meteorological data from the two weather stations is displayed. At Ein Bokek, AODs tend to be higher compared to Masada. On several days a peak of around 0.8 was observed shortly after sun rise followed by a decrease to values of 0.5 towards afternoon. Largest AODs were observed on May 13th at Ein Bokek with values of 1.2.

Figures 8.5, 8.6 and 8.7 show retrieved the vertical profiles. The profiles show extinctions at the altitude of the corresponding retrieval box. The vertical extent of the boxes is 100 m and 50 m for the instrument Ein Bokek and Masada, respectively. At Ein Bokek, ground near aerosol is predominantly observed in teh morning around 06:00 UTC. During noon time, elevated aerosol layers are regularly observed (09:00 to 12:00 UTC). At Masada, the vertical distribution is more homogeneous with respect to altitude.

The retrieved AODs match the observations made by the cameras at Masada and Ein Bokek (see figure 8.8). However, the different wavelength ranges of the camera (visible) and the MAX-DOAS (UV, 360nm) should be considered when comparing the data in terms of visibility. The dust event on May 13th is clearly observable in both the vertical profiles and the camera pictures at both locations.
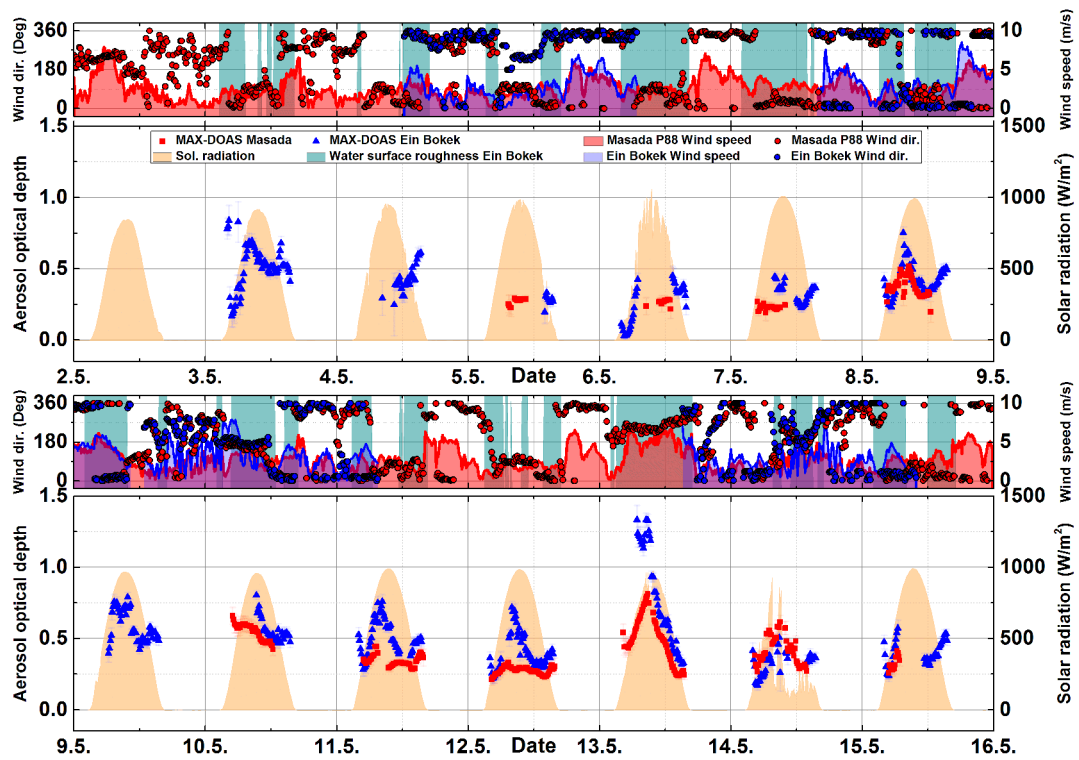
Fig. 8.4: Time series of aerosol optical depths measured by MAX-DOAS at Ein Bokek (red squares) and at Masada (blue triangles). Ticks are at 00:00 and 12:00 UTC. Errors are retrieval errors.
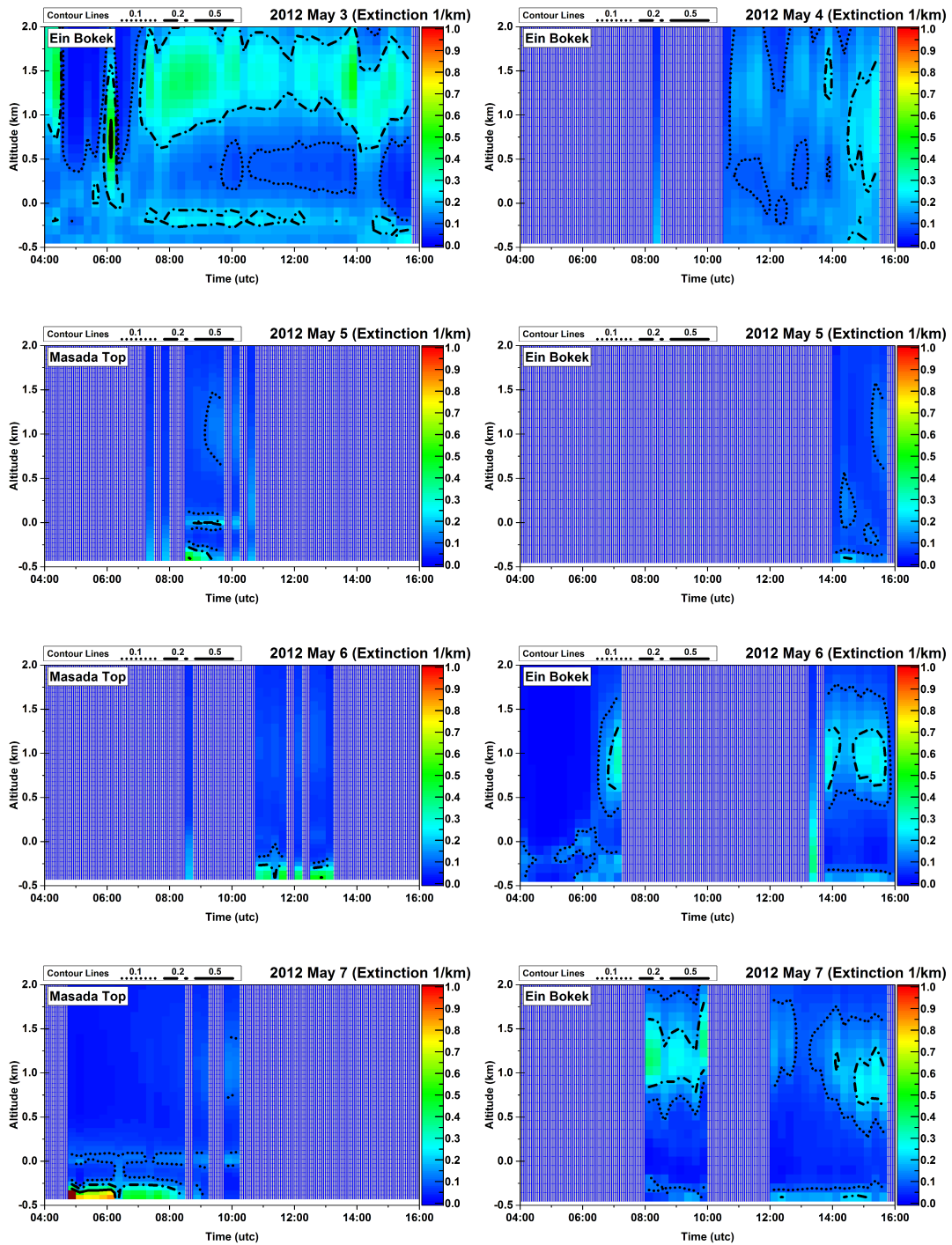
Fig. 8.5: Vertical profiles of aerosol optical depths retrieved from the data of the MAX-DOAS at Masada (left) and Ein Bokek (right). Note that the first plots show data of the MAX-DOAS at Ein Bokek on May 3rd and 4th 2012. Shaded areas indicate missing data.
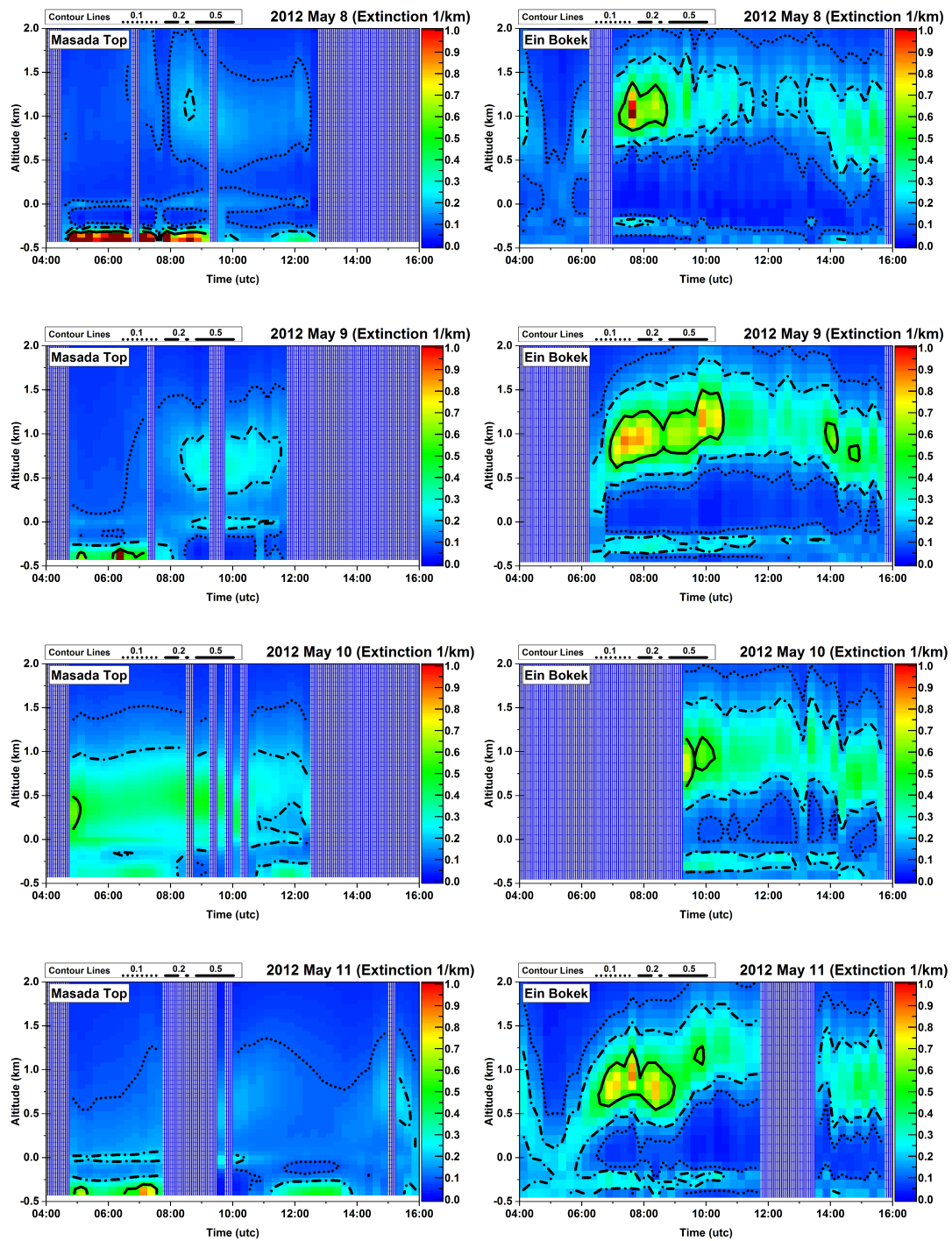
Fig. 8.6: Same description as for figure 8.6.
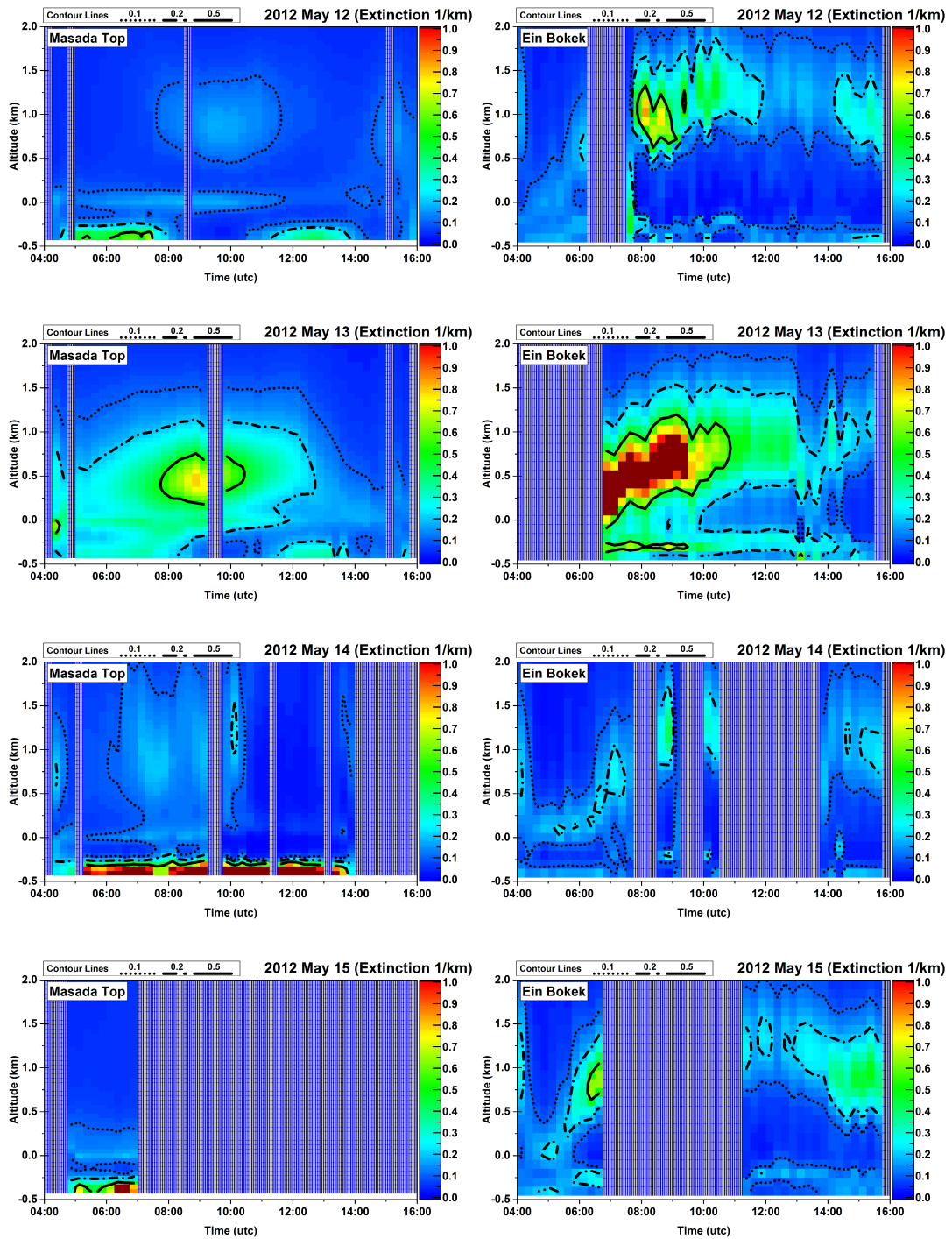
Fig. 8.7: Same description as for figure 8.6.
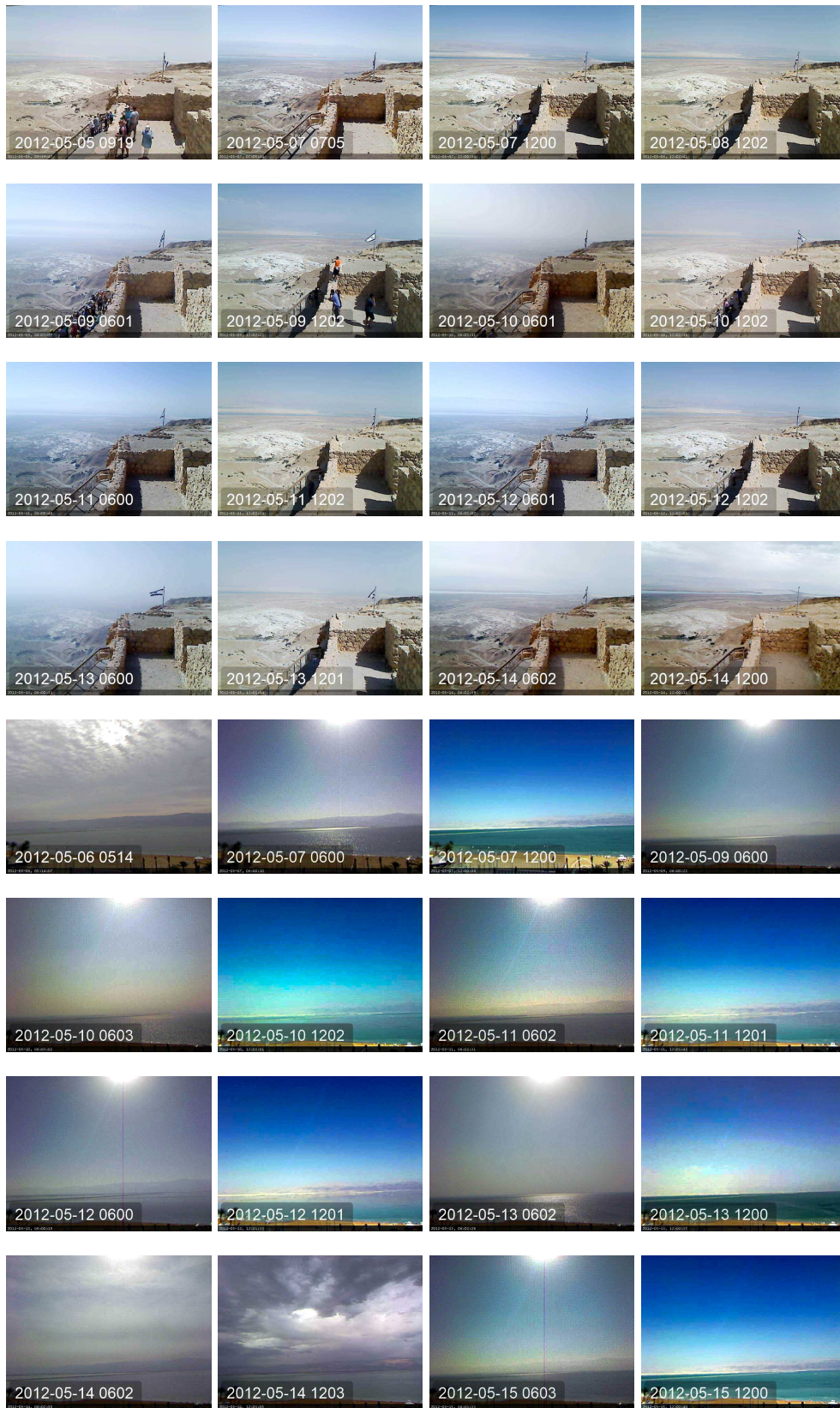
Fig. 8.8: Pictures taken by cameras near the MAX-DOAS instruments at Masada Top (upper 16 pictures) and Ein Bokek (lower 16 pictures). Time stamps are in UTC.

8.3 Bromine monoxide
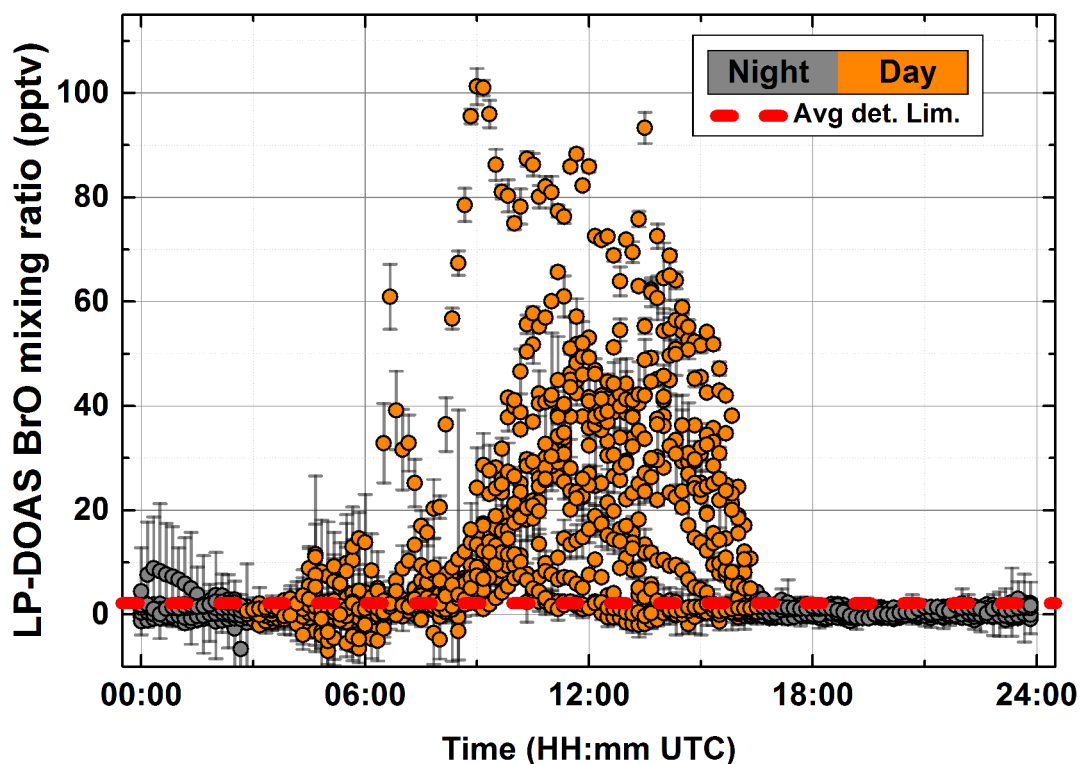
Fig. 8.9: BrO volume mixing ratios measured by LP-DOAS during the whole campaign plotted against time of day. Errors are 2 times fit error. The average detection limit is 3 pptv and is defined as 4 times the fit error. Color code represents day and night time (solar radiation above and below 10 W/m^2).

Significant abundances of Bromine monoxide (BrO) were regularly observed. Figure 8.9 shows all volume mixing ratios (vmrs) measured by the LP-DOAS during the campaign plotted against time of day. The measured BrO vmrs are ranging from below the total average LP-DOAS detection limit of 3 pptv up to 100 pptv. On most of the days, BrO starts to increase 2 to 3 hours after sunrise and strongly decrease with sunset indicating that its formation most likely depends on solar radiation. The peak mixing ratios are predominantly observed in the afternoon after 12:00 UTC. Significant BrO mixing ratios during sun rise were not observed.

The MAX-DOAS instruments observed slant column densities (SCDs) of up to 7 $\cdot 10^{14}$ molec/cm^2 and 11 $\cdot 10^{14}$ molec/cm^2 at Ein Bokek and Masada respectively with an detection limit below 1 $\cdot 10^{14}$ molec/cm^2. Histograms of SCDs are shown in figure 8.10.

The upper plot in figure 8.11 shows the time series BrO mixing ratios from data of all DOAS instruments as well as the meteorological data. Black dots are LP-DOAS data while red triangles and blue squares represent retrieved mixing ratios of the lower most box (0 to 100 m above ground for the Ein Bokek MAX-DOAS, 0 to 50 m above ground for the Masada MAX-DOAS) of the profile retrieval. Note that the negative elevation angle of the Ein Bokek MAX-DOAS was not included in the retrieval so only elevation angles pointing upwards account to the retrieved surface vmrs.

The lower plot in figure 8.11 shows time series of BrO vertical column densities (VCDs) for a direct comparison of the two MAX-DOAS instruments. Similar to the surface mixing ratios, the VCDs at Masada are larger than those at Ein Bokek with peak values of 18 $\cdot 10^{18}$ molec/cm^2 and 11 $\cdot 10^{18}$ molec/cm^2 respectively.
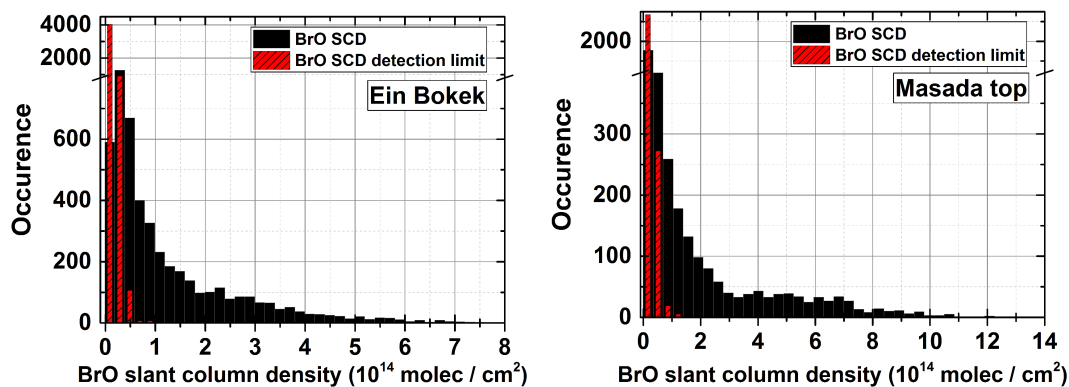
Fig. 8.10: BrO slant column densities measured by the MAX-DOAS instruments. Data of all elevation angles is shown. Red bars represent the distribution of the detection limits which are defined as 4 times the fit error. Note the different scales for the different locations.
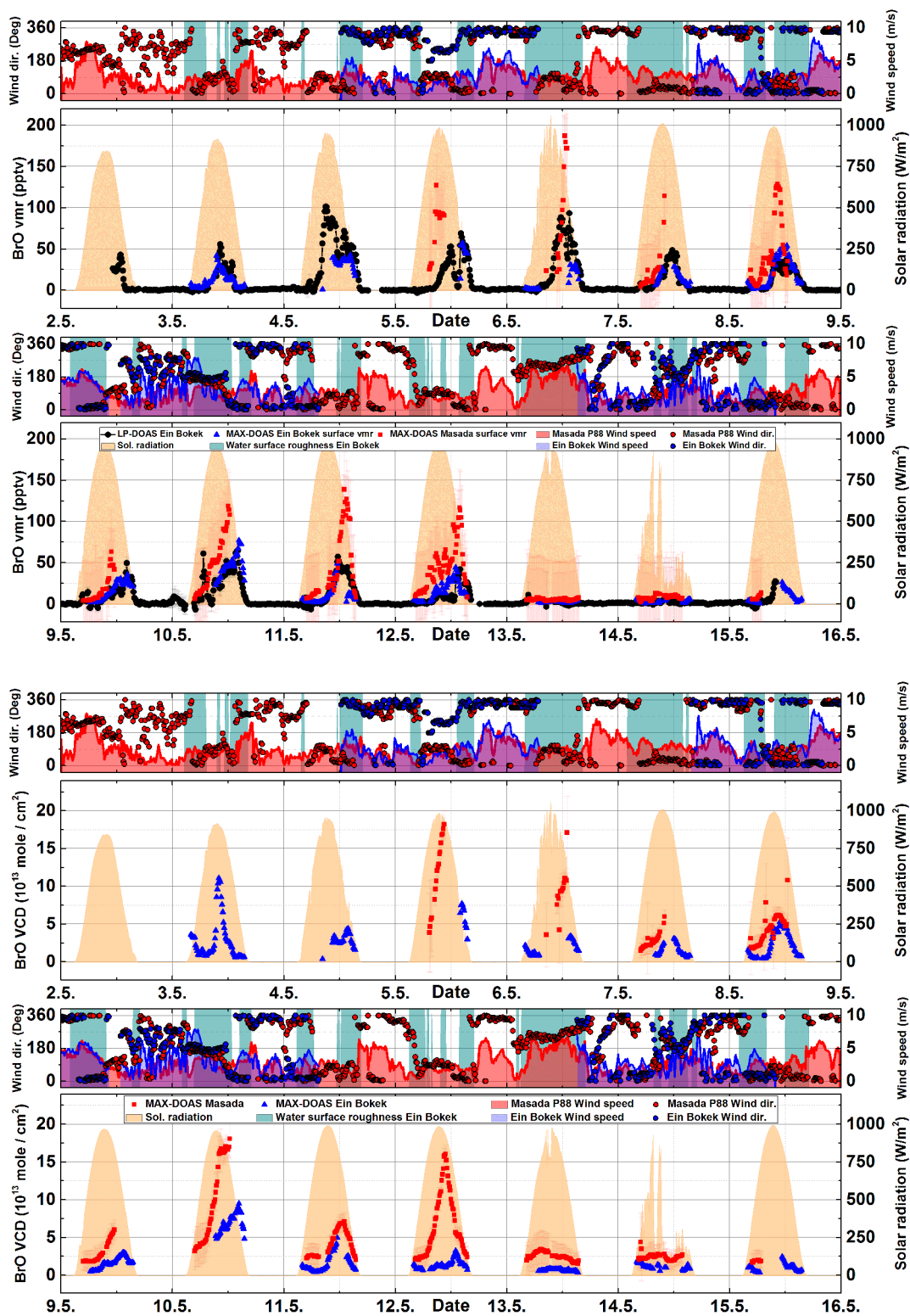
Fig. 8.11: **Top:** *Time series of BrO volume mixing ratios measured by LP-DOAS (black dots), MAX-DOAS at Ein Bokek (red squares) and Masada (blue triangles).* **Bottom:** *MAX-DOAs VCDs. Ticks are at 00:00 and 12:00 UTC. LP-DOAS errors are 2 times fit error. MAX-DOAS errors are total retrieval errors.*

Figures 8.12, 8.13 and 8.14 show the profiles of mixing ratios retrieved from the MAX-DOAS data. Note that profiles of May 13th to 15th are not shown since no significant BrO signal was observed (compare VCDs in figure 8.11). A profile height of 4 km was retrieved but only -500 m to 2000 m are shown since no significant BrO abundance was detected above 1km. As mentioned above, both instruments observed high BrO vmrs of several 10 pptv during most of the days of the campaign. However, BrO was not only detected near ground level. On several days the vertical extent of BrO reached up to 1.5 km above the ground (1 km absolute altitude) with mixing ratios between 5 and 20 pptv . Confined Elevated layers of 10 to 50 pptv of BrO are observed on May 8th at Ein Bokek and on 10th, 11th and 12th at Masada.
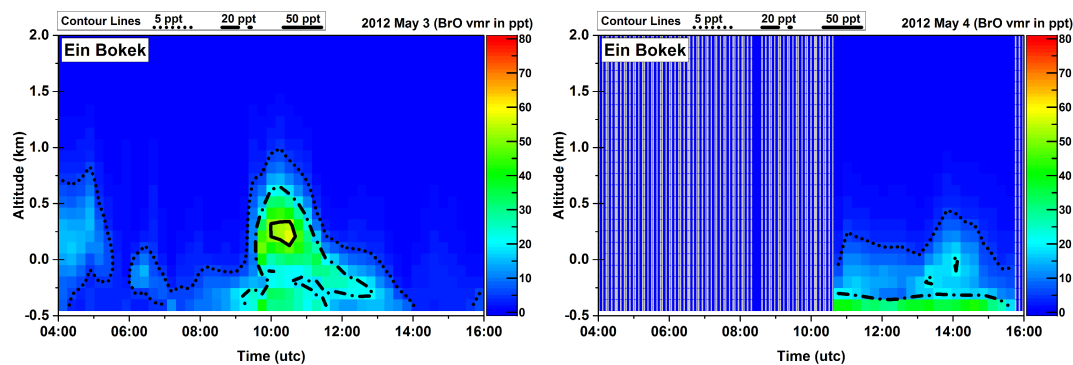
*Fig. 8.12: Vertical profiles of BrO retrieved from the data of the MAX-DOAS **at Ein Bokek** on May 3rd and 4th 2012. The location of the instrument is noted in the upper left corner. Date is in the upper right corner. Levels of contour lines are displayed above each profile plot. Shaded areas indicate missing data.*
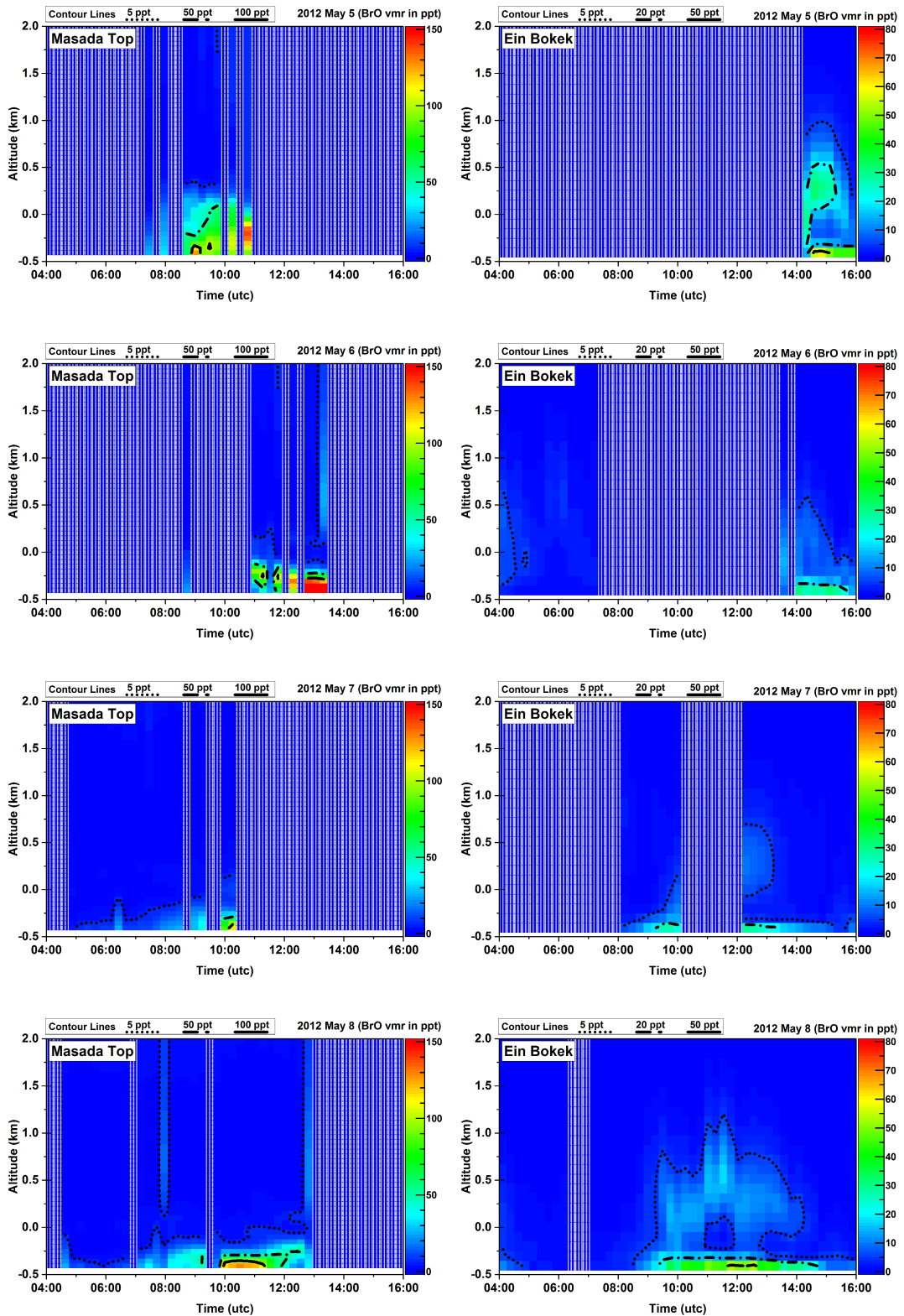
Fig. 8.13: Vertical profiles of BrO retrieved from the data of the MAX-DOAS at Masada (left) and Ein Bokek (right). Note the different color scales for the different locations. Shaded areas indicate missing data.
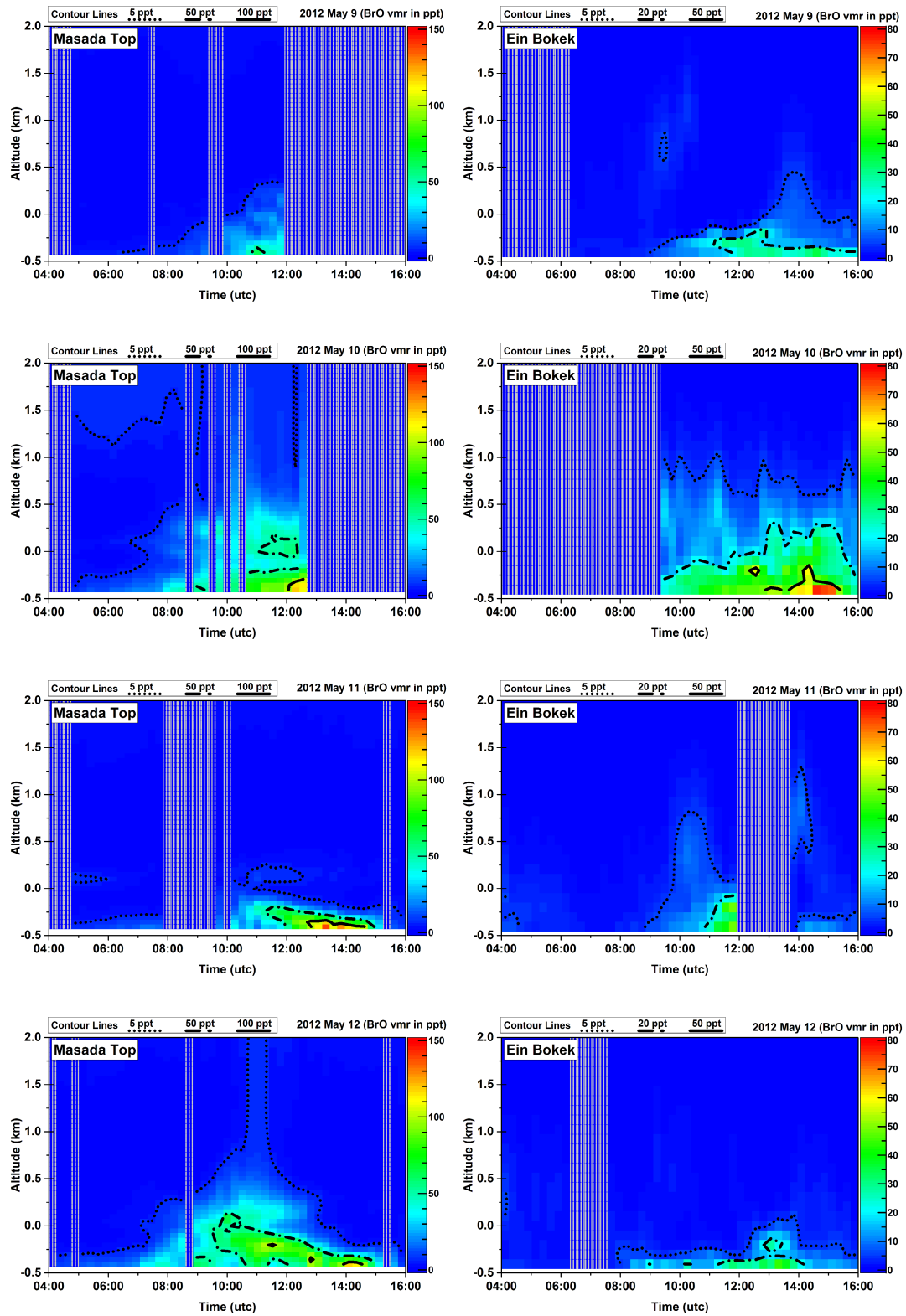
Fig. 8.14: Same description as for figure 8.13.

8.4 Iodine monoxide
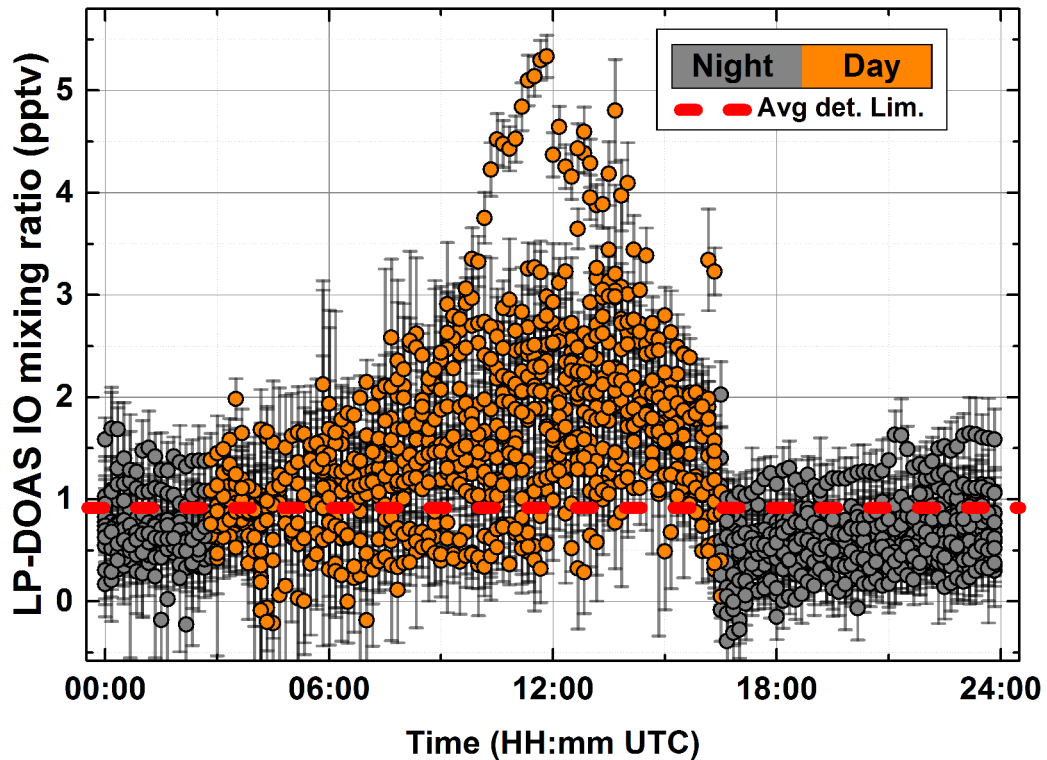
Fig. 8.15: IO volume mixing ratios measured by LP-DOAS during the whole campaign plotted against time of day. Errors are 2 times fit error. The average detection limit is 7pptv and is defined as 4 times the fit error. Color code represents day and night time (solar radiation above and below 10 W/m^2).

Significant amounts of iodine monoxide (IO) were observed by the LP-DOAS on nearly every day of the 2 weeks campaign. Figure 8.15 shows all IO mixing ratios measured by the LP-DOAS as function of UTC daytime. The time series of surface vmrs from MAX-DOAS and vmrs from LP-DOAS data as well as VCDs are shown in figure 8.16.

Figures 8.17, 8.18 and 8.19 show profiles retrieved by the SCDs of the MAX-DOAS instruments at Masada Top and Ein Bokek. On most days the vertical extent of IO is limited to the first 250 m above ground level with mixing ratios

between 0.5 pptv and 1 pptv. For the Masada instrument, where also negative elevation angles were included in the profile retrieval, mixing ratios of up to 1.5 pptv were observed on several days. On May 10th, the vertical extension of IO reached 1km above ground level (500 m absolute altitude). On May 13th, elevated layers of IO are observed at Masada. But with only 0.5pptv and SCDs close to the detection limit, this is quite doubtful. Mixing ratios of the instrument at Ein Bokek, where only positive elevation angles were used, did barely exceed 0.5 pptv.
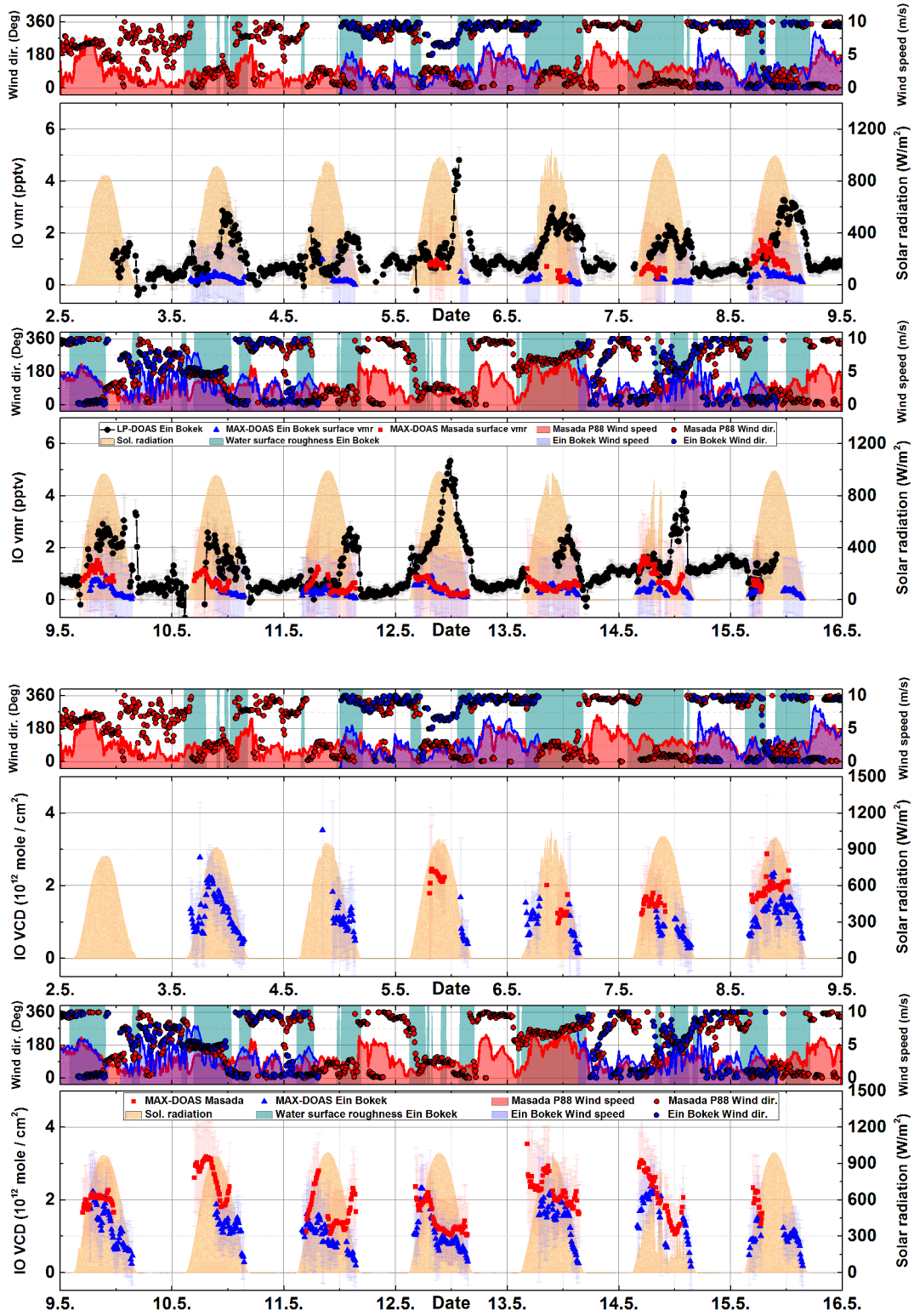
Fig. 8.16: Time series of IO volume mixing ratios measured by LP-DOAS (black dots), MAX-DOAS at Ein Bokek (red squares) and Masada (blue triangles). Lower plot shows MAX-DOAS VCDs. Ticks are at 00:00 and 12:00 UTC. LP-DOAS errors are 2 times fit error. MAX-DOAS errors are total retrieval errors.
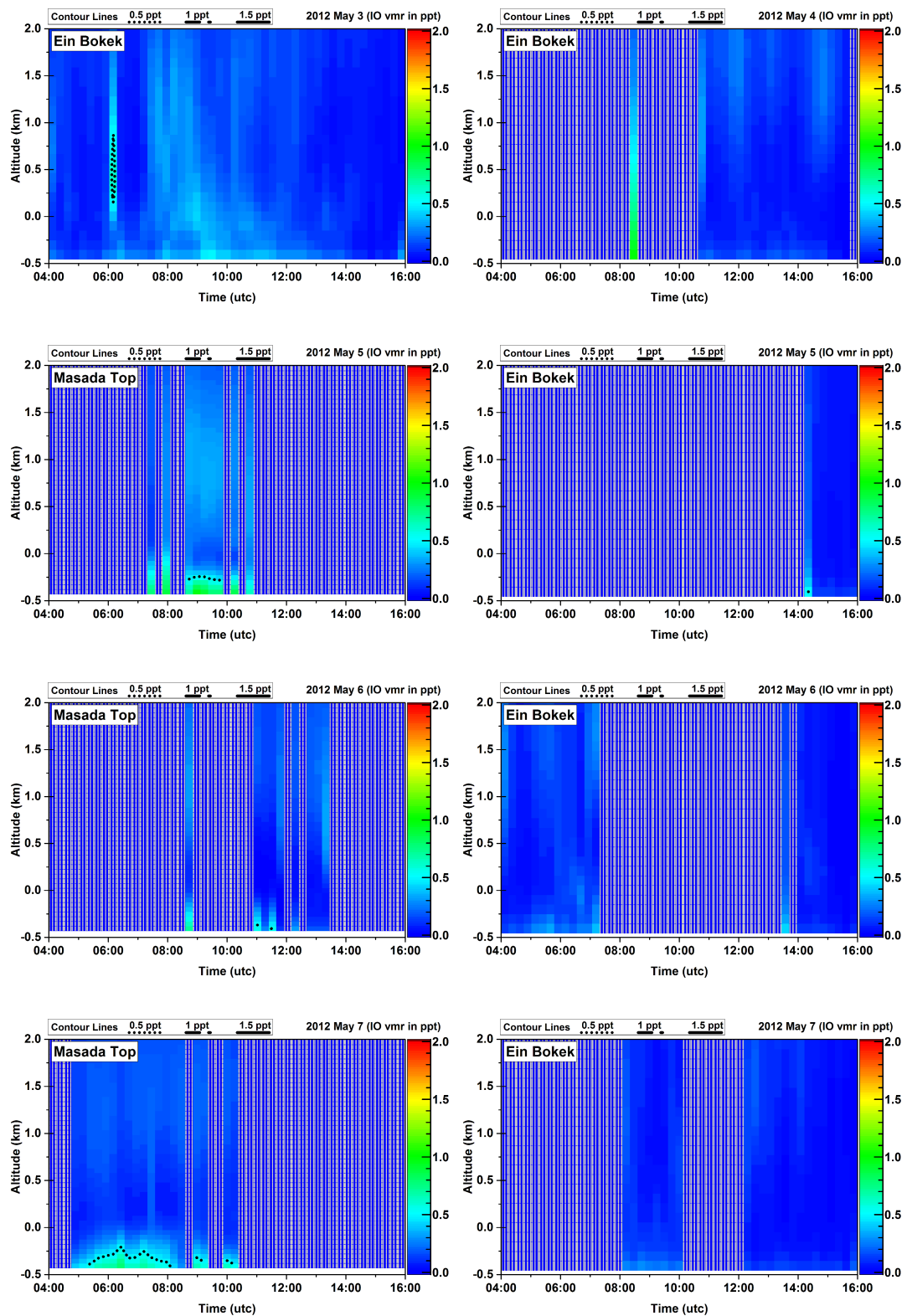
Fig. 8.17: Vertical profiles of IO retrieved from the data of the MAX-DOAS at Masada (left) and Ein Bokek (right). Note that the first plots show data of the MAX-DOAS at Ein Bokek on May 3rd and 4th 2012. Shaded areas indicate missing data.
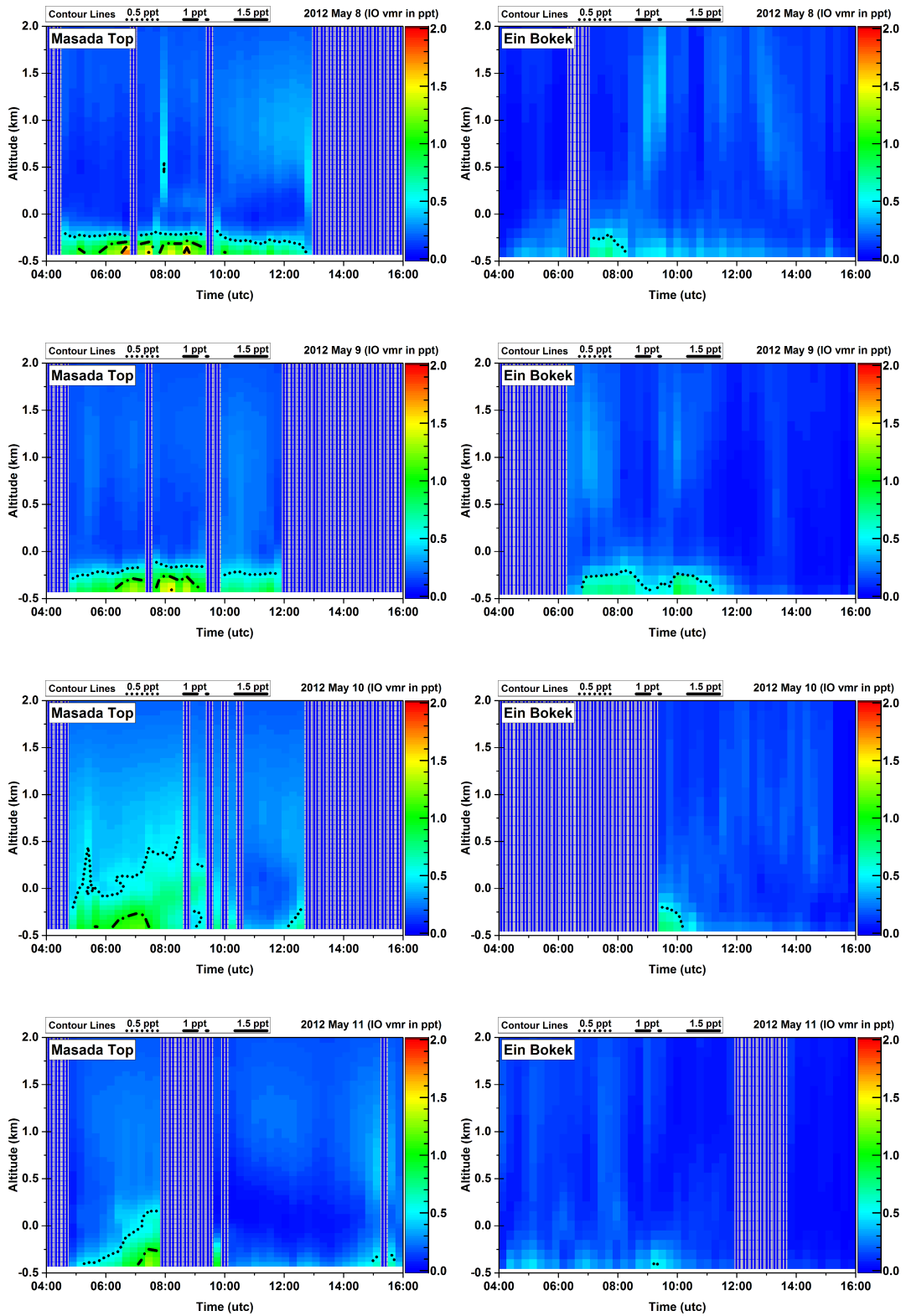
Fig. 8.18: Same description as for figure 8.18.
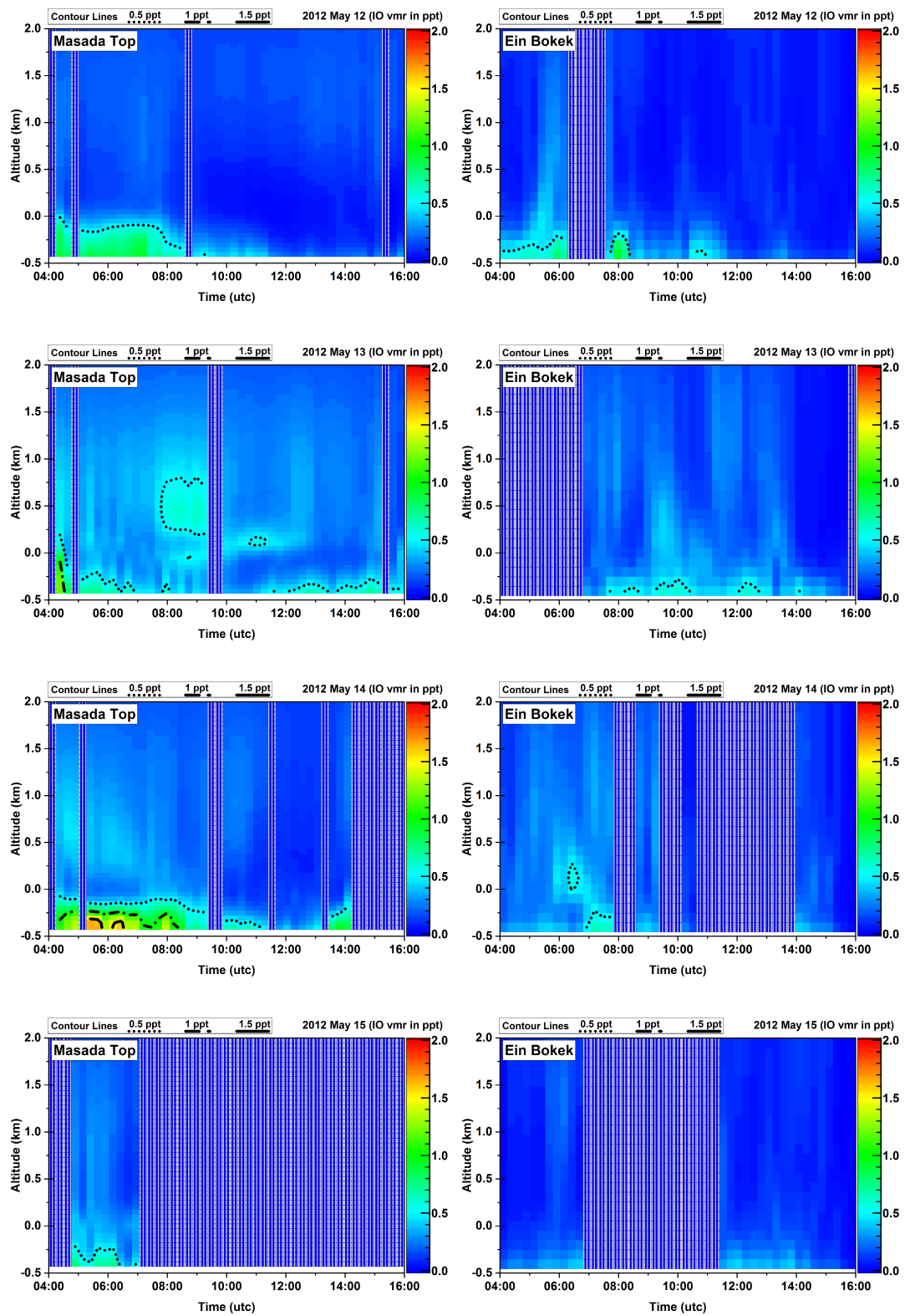
Fig. 8.19: Same description as for figure 8.18.

8.5 Molecular iodine
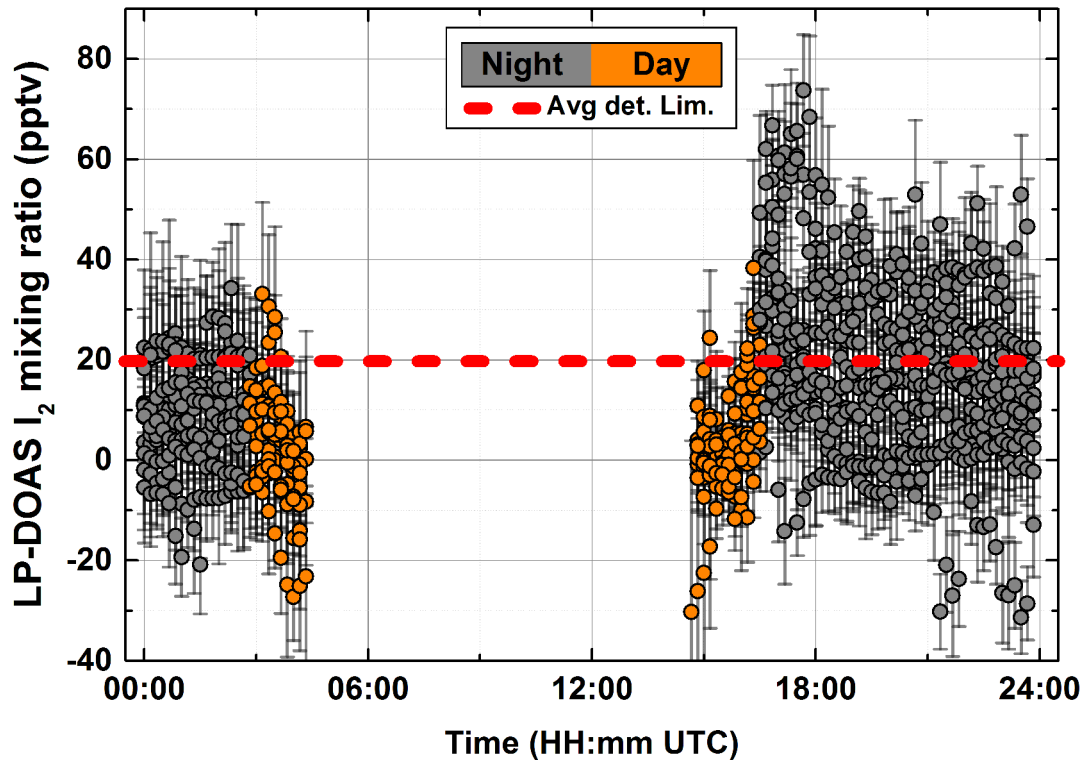
Fig. 8.20: I_2 volume mixing ratios measured by LP-DOAS during the whole campaign plotted against time of day. Errors are 2 times fit error. The average detection limit is 20 pptv and is defined as 4 times the fit error. Color code represents day and night time (solar radiation above and below 10 W/m^2).

Besides iodine monoxide, also molecular iodine was observed by the LP-DOAS after sunset on most days of the campaign. Figure 8.20 shows all I_2 mixing ratios plotted against time of day. Since a day reference spectrum was used for the spectral analysis mixing ratios of iodine are retrieved only during night and twilight. For details of the analysis, see section 5.2.3.

In figure 8.21, the time series of iodine mixing ratios from LP-DOAS data are displayed. The I_2 detection limit is shown in red. Additionally the IO time series is plotted. Significant vmrs of I_2 were observed only shortly after sunset increas-

ing strongly with rates up to 50 pptv/h (from detection limit of 20 to 70 pptv). On most days, mixing ratios dropped with decay rates similar to those of the increases shortly after reaching the peak value. In this cases the temporal extent of the I_2 peaks was approximately one hour.
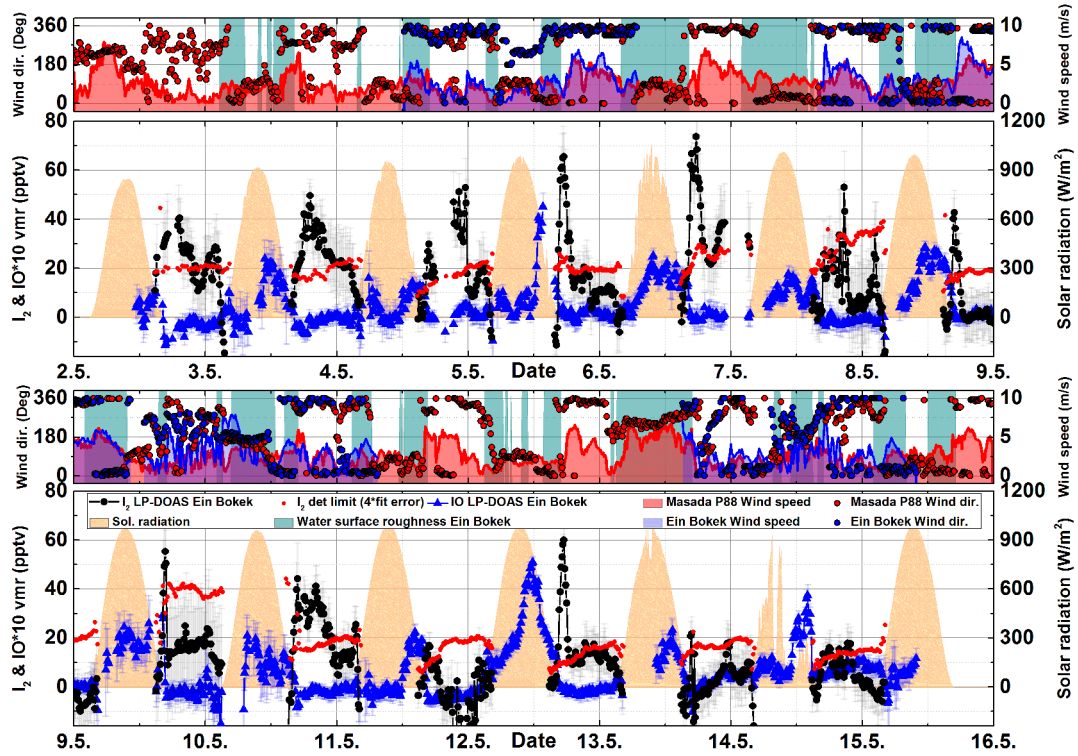
Fig. 8.21: Time series of I_2 (blackdots) and IO (blue triangles) volume mixing ratios measured by LP-DOAS at Ein Bokek. Ticks are at 00:00 and 12:00 UTC. LP-DOAS errors are 2 times fit error. Additionally, the detection limit of I_2 is displayed in red, defined as 4 times fit error.

8.6 Chlorine dioxide
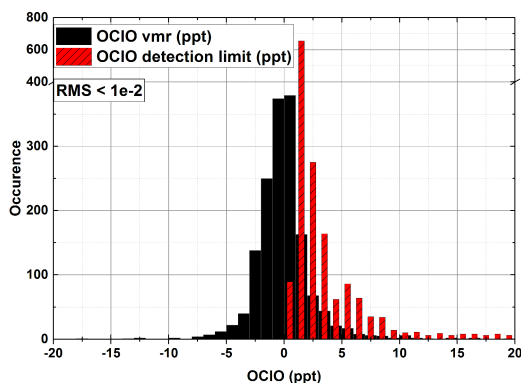
Fig. 8.22: Histogram of mixing ratios with corresponding detection limits from LP-DOAS data. Average detection limit 3.7 pptv.

The LP-DOAS instrument observed no significant abundance of chlorine dioxide (average detection limit of 3.7 pptv). Figure 8.22 shows a histogram of all vmrs and corresponding detection limits. In figure 8.23, histograms of OClO SCDs of both MAX-DOAS instruments during the measurement period are displayed indicating that a large part of measured OClO SCDs are below the detection limit. However, on a single day (May 10th), the MAX-DOAS instruments could observe OClO slant column densities of up to $5.5 \cdot 10^{13}$ molec/cm^2 at Masada top at an elevation angle of -1° and $4.7 \cdot 10^{13}$ molec/cm^2 at Ein Bokek at 0°. On that particular day, the aerosol optical depth, and hence, the visibility was reduced (see also section 8.2). Thus, the sensitivity of the LP-DOAS was reduced leading to a detection limit for OClO of approximately 20 pptv. This has to be considered for the interpretation.

Time series of surface volume mixing ratios and vertical column densities from the retrieved from the MAX-DOAS data acquired on May 10th are displayed in figure 8.25. At Masada surface vmrs are slowly rising after sunrise to peak values of 2 pptv. Unfortunately, the instrument had a failure at around 12:00 UTC so data after wards is missing. At Ein Bokek, data was available from 09:00 UTC

on. Surface vmrs reached values of 5 pptv followed by leveling off at 3 pptv until sunset.

Figure 8.24 shows the corresponding vertical profiles. At Masada the highest volume mixing ratios of 5 pptv are observed at absolute altitudes of -100 m to 100 m (which corersponds to 300 m to 500 m above ground level). At Ein Bokek, the maximum of the vertical distribution of OClO is located near the surface (0 to 100 m above ground) and corresponds to the mixing ratios shown in figure 8.25. After 12:00 UTC, OClO is homogeneously distributed between absolute altitudes of -400 m and 100 m with mixing ratios of 3 pptv.
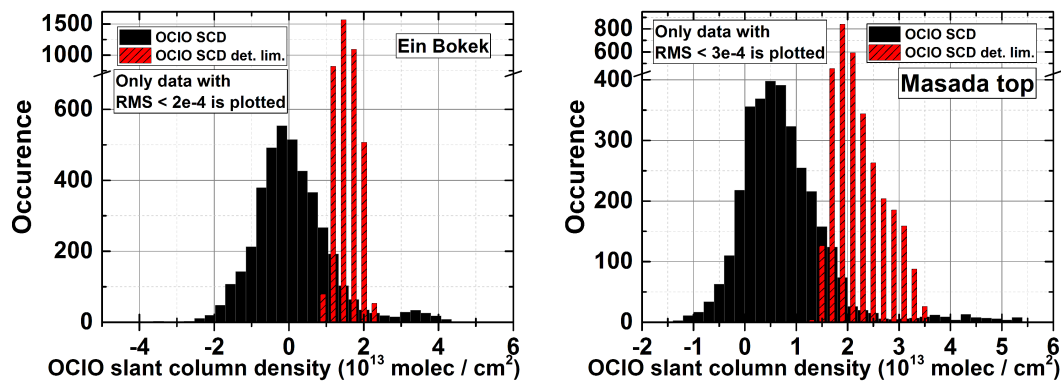
Fig. 8.23: Histogram of slant column densities under all measured elevation angles with corresponding detection limits from MAX-DOAS data. **Left:** *Ein Bokek.* **Right:** *Masada top. Note that the data is filtered for RMS according to the label in the plots.*
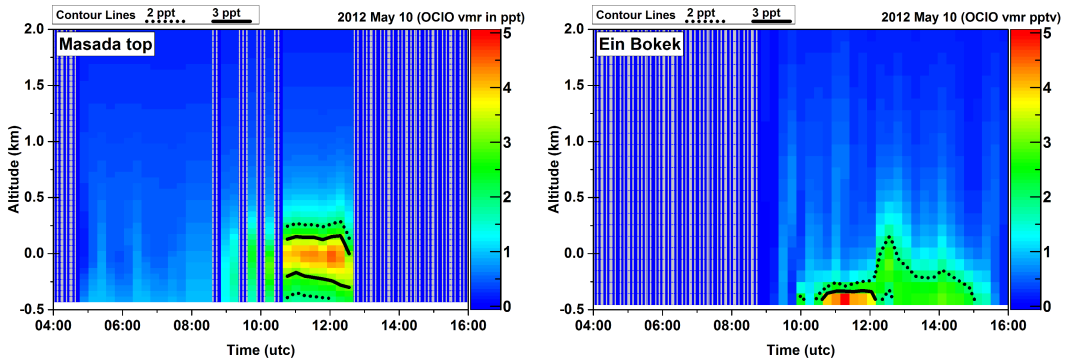
*Fig. 8.24: Vertical profiles of IO retrieved from the data of the MAX-DOAS at Masada (**left**) and Ein Bokek (**right**). Shaded areas indicate missing data.*
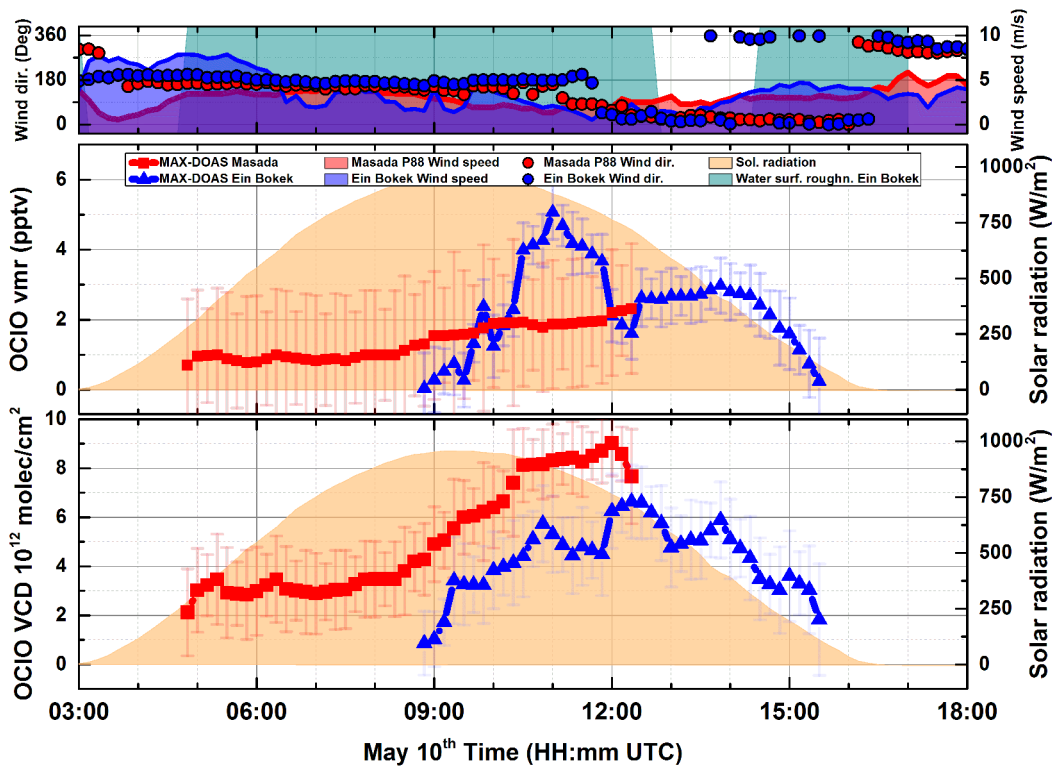
*Fig. 8.25: Time series of meteorology (**top**), OClO surface mixing ratios (**middle**) and OClO vertical column densities (**bottom**) from MAX-DOAS data in Ein Bokek (blue triangles) and Masada (red squares). Errors are total retrieval errors.*

8.7 Ozone
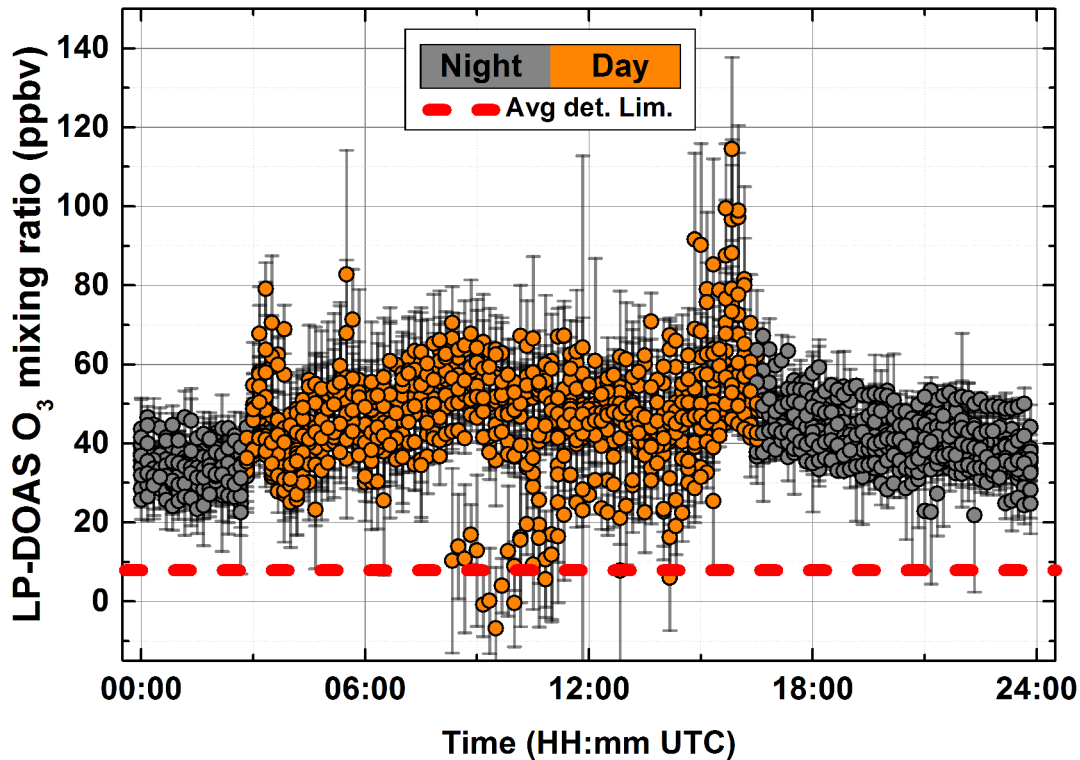
Fig. 8.26: O_3 volume mixing ratios measured by LP-DOAS during the whole campaign plotted against time of day. Errors are 2 times fit error. The average detection limit is 13ppbv and is defined as 4 times the fit error. Color code represents day and night time (solar radiation above and below 10 W/m^2).

Ozone volume mixing ratios observed by the LP-DOAS instrument are displayed in figure 8.26. A time series of the data is given in figure 8.27. Daytime mixing ratios range from 100 ppbv down to below the detection limit of 13 ppbv (during noon on May 4th and 6th). During nighttime an ozone decrease from values of 60 pbbv down to 20 ppbv during sunset and sunrise is observed. Since the spectral analysis of ozone is done in the deep uv (298 to 325 nm, compare table 5.12), the quality of the data is strongly influenced by the visibility. On May 10th and 13th high aerosol load increased the signal to noise ratio and therefore significance of the ozone data. Hence the data was filtered and not shown in the time series.
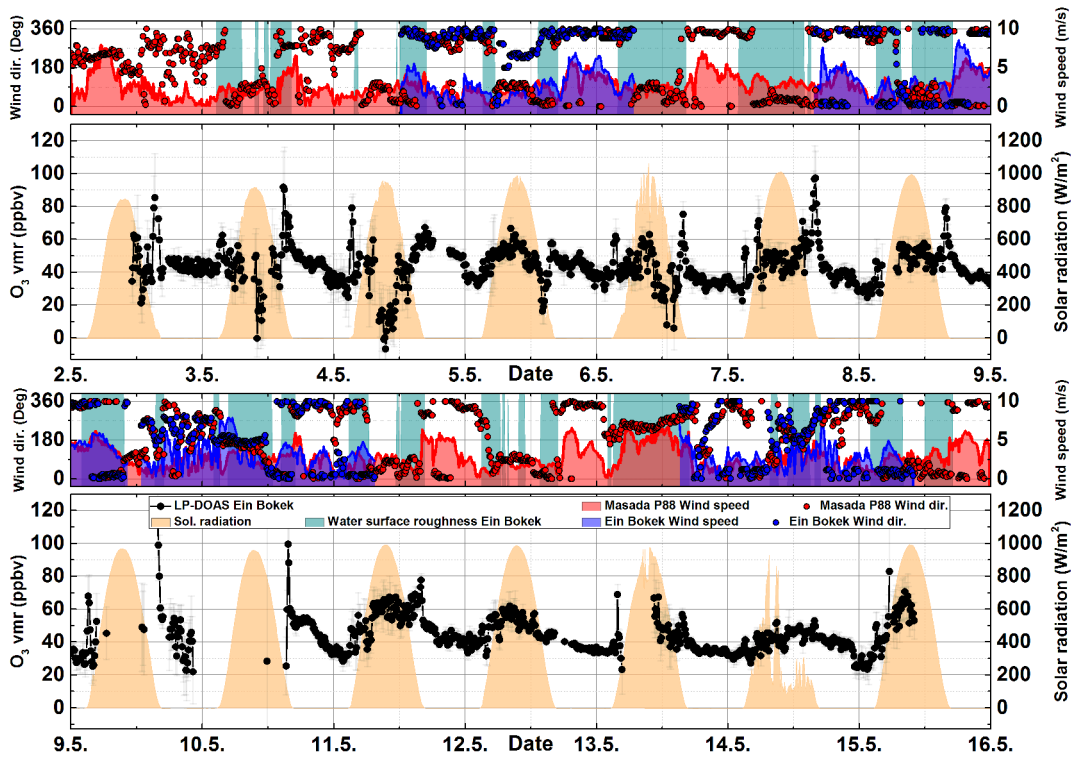
Fig. 8.27: Time series of O_3 volume mixing ratios measured by LP-DOAS at Ein Bokek. Ticks are at 00:00 and 12:00 UTC. LP-DOAS errors are 2 times fit error.

8.8 Nitrogen dioxide
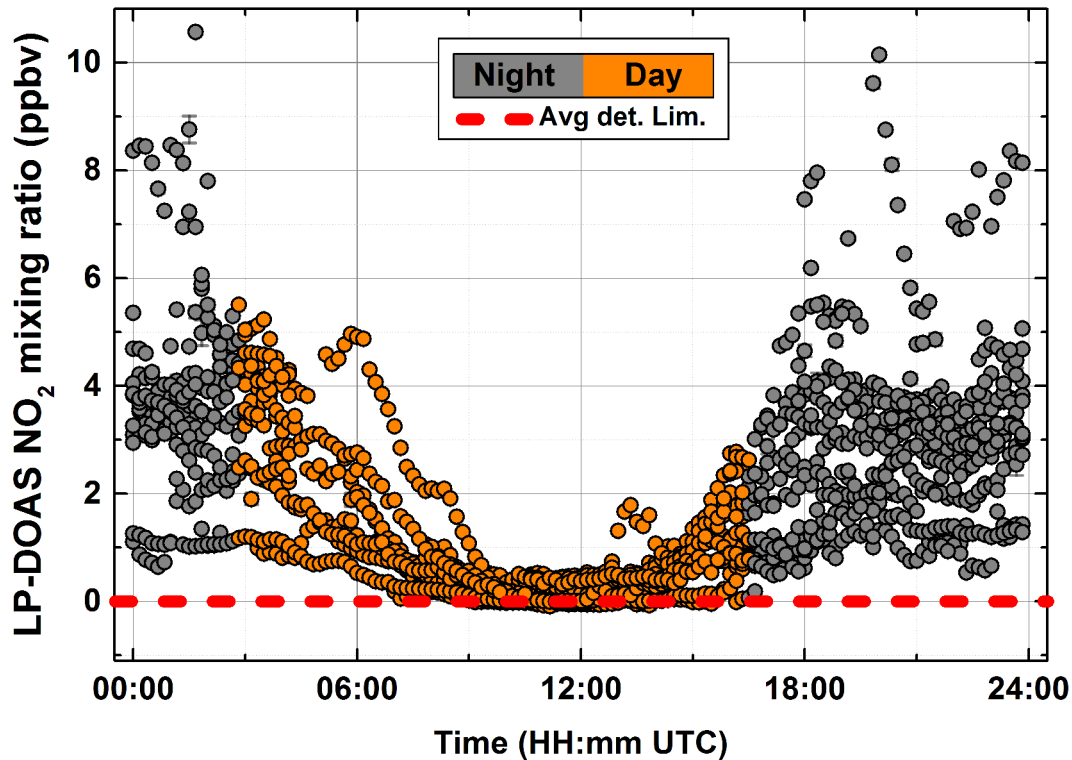
Fig. 8.28: NO$_2$ volume mixing ratios measured by LP-DOAS during the whole campaign plotted against time of day. Errors are 2 times fit error, however errors are smaller than the extension of the data points. The average detection limit is 50pptv and is defined as 4 times the fit error. Color code represents day and night time (solar radiation above and below 10 W/m^2).

Nitrogen dioxide volume mixing ratios showed significantly different variations during night and daytime. Figure 8.28 displays the NO$_2$ mixing ratios retrieved from LP-DOAS data plotted against time of day. During nighttime, values between 1 and 5 ppbv were regularly observed with occasional short peaks reaching up to 11 ppbv. At sunrise, vmrs decrease with rates of up to 3 ppbv/h down to values between 500 pptv and below the detection limit of 50 pptv. In the afternoon, NO$_2$ mixing ratios rise again with decreasing solar radiation (usually starting at 14:00 to 15:00 UTC) up to nighttime values.

The time series of NO_2 surface vmrs from LP-DOAS and MAX-DOAS at Ein Bokek and Masada (figure 8.29, upper plot) are comparable in terms of amplitude and dynamics. Similar to the behavior of the surface vmrs, the time series of vertical column densities in figure 8.29, lower plot, also show strong decreases starting at sunrise with decay rates of up to 10^{15} molec/cm^2/h. The short rises in NO_2 VCDs at Ein Bokek on May 3rd and 9th can be attributed to the vertical NO_2 distribution displayed in figures 8.30, 8.31 and 8.32. On those particular days, the instrument at Ein Bokek observed a rise in nitrogen dioxide in high altitudes between 0 and 2 km absolute altitude before noon. On all other days, NO_2 at all altitudes is usually decaying after sunrise. At Masada, two separate layers of nitrogen dioxide with a minimum at the altitude of the instrument (approximately 20 m absolute which also defines the upper rim of the valley on the western side) are regularly observed (e.g. May 9th). After noon time (past 10:00 UTC) NO_2 tends to increase at absolute altitudes around 1 to 2 km. At Ein Bokek, this is followed by an apparent descent of elevated NO_2 mixing ratios down to the ground (strongest example occurred on May 7th).
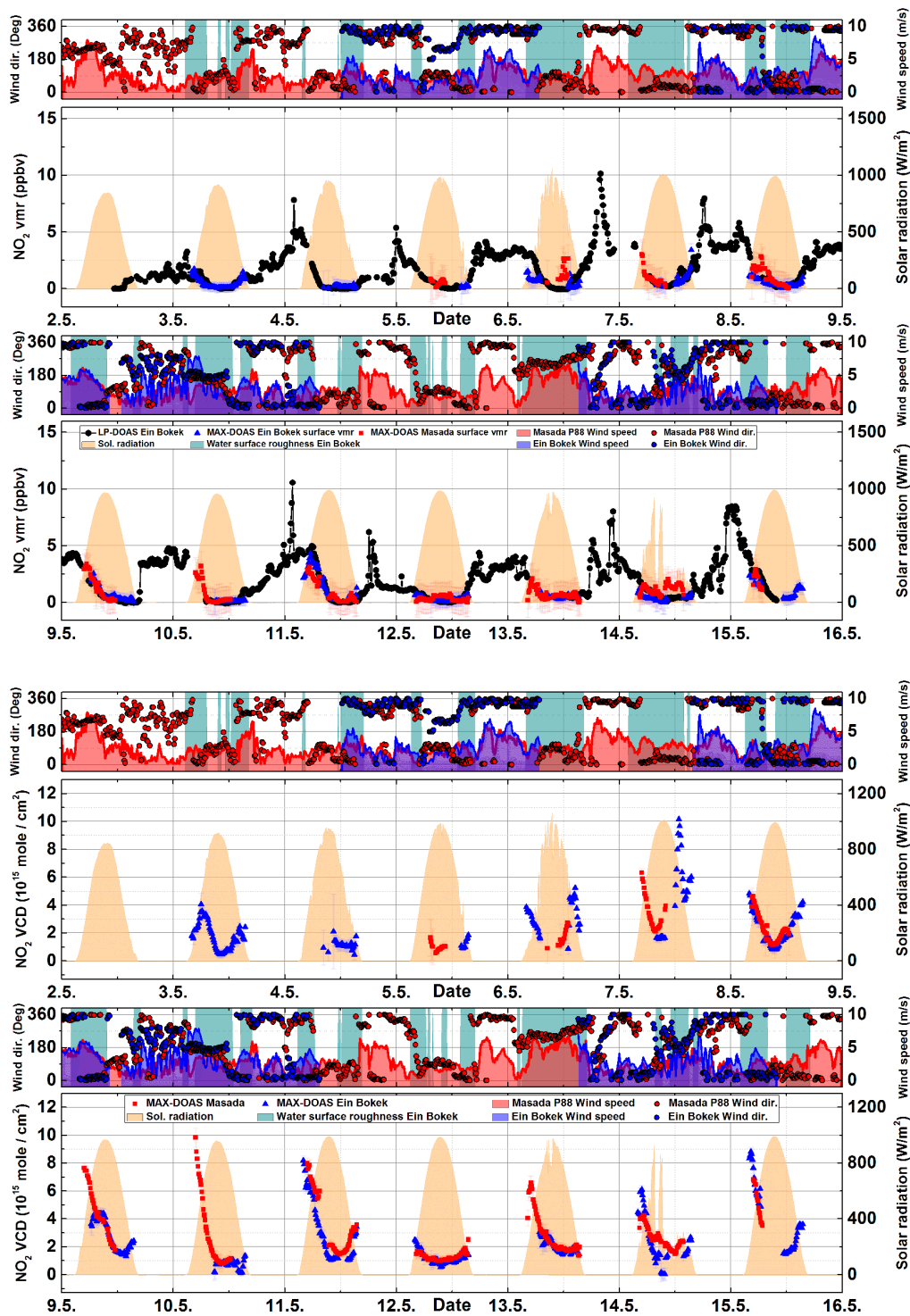
Fig. 8.29: Time series of NO$_2$ volume mixing ratios measured by LP-DOAS (black dots), MAX-DOAS at Ein Bokek (red squares) and Masada (blue triangles). Ticks are at 00:00 and 12:00 UTC. LP-DOAS errors are 2 times fit error. However, error bars are smaller than the extent of the data points in this plot. MAX-DOAS errors are total retrieval errors.
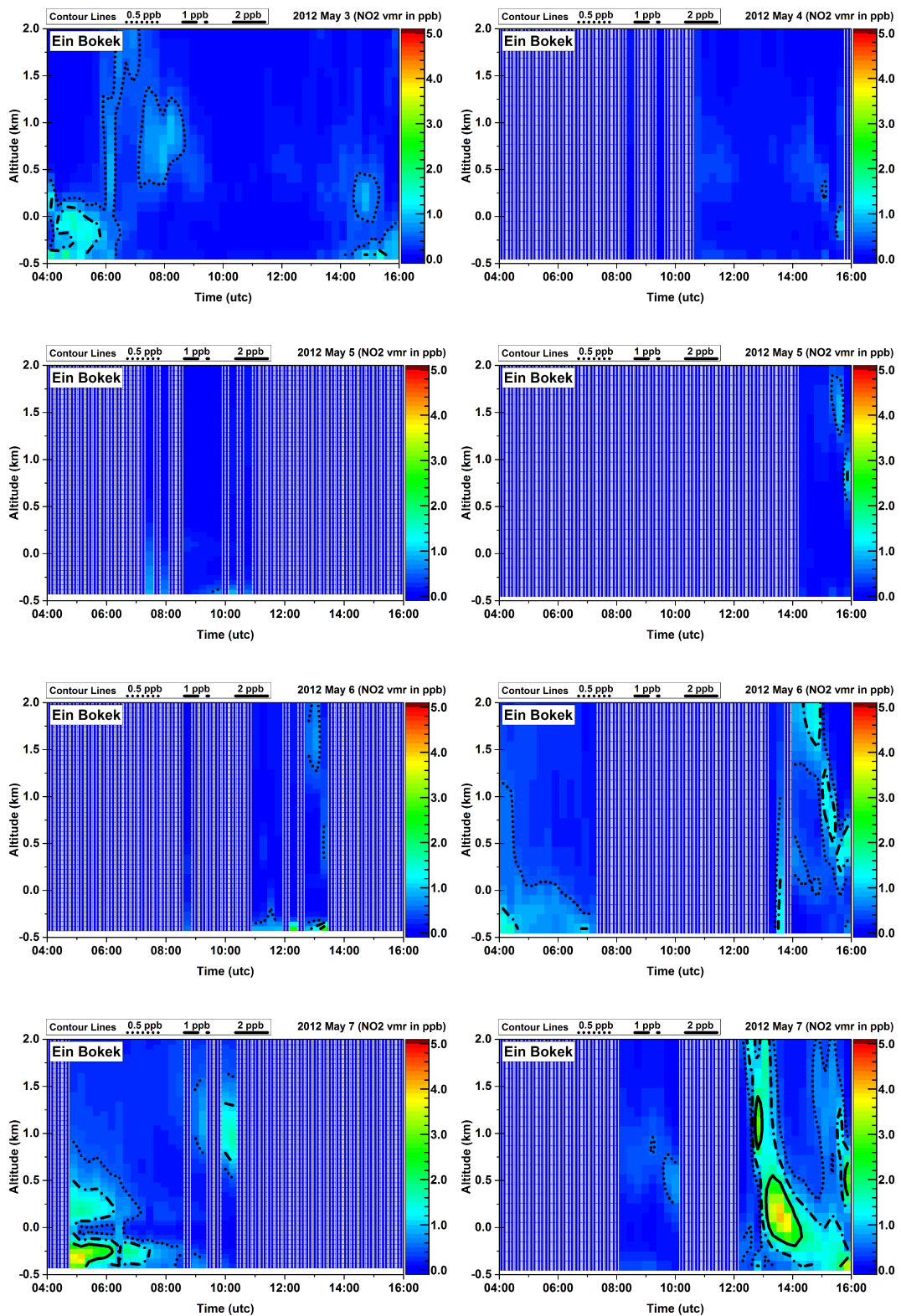
Fig. 8.30: Vertical profiles of NO₂ retrieved from the data of the MAX-DOAS at Masada (left) and Ein Bokek (right). Note that the first plots show data of the MAX-DOAS at Ein Bokek on May 3ʳᵈ and 4ᵗʰ 2012. Shaded areas indicate missing data.
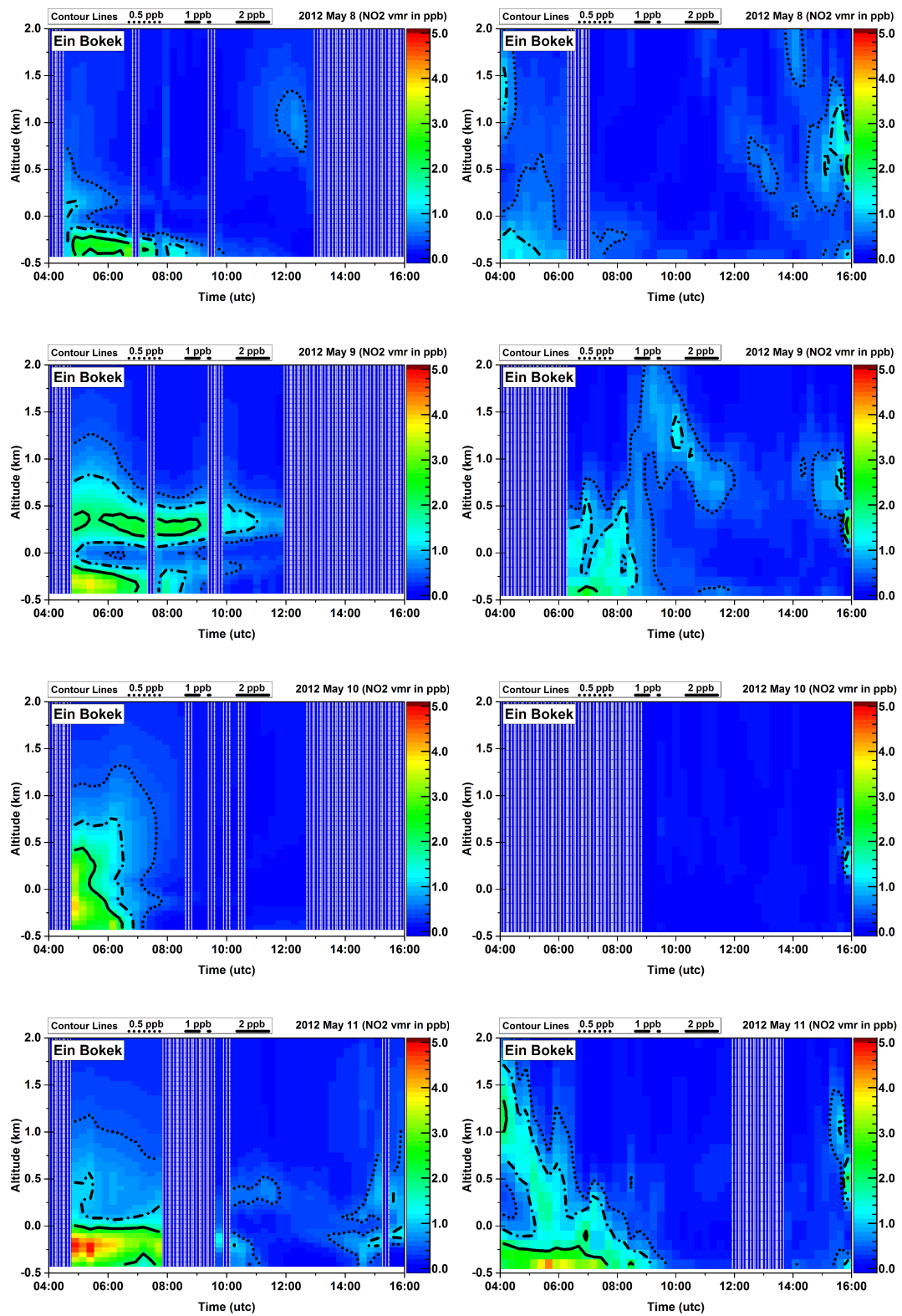
Fig. 8.31: Same description as for figure 8.31.
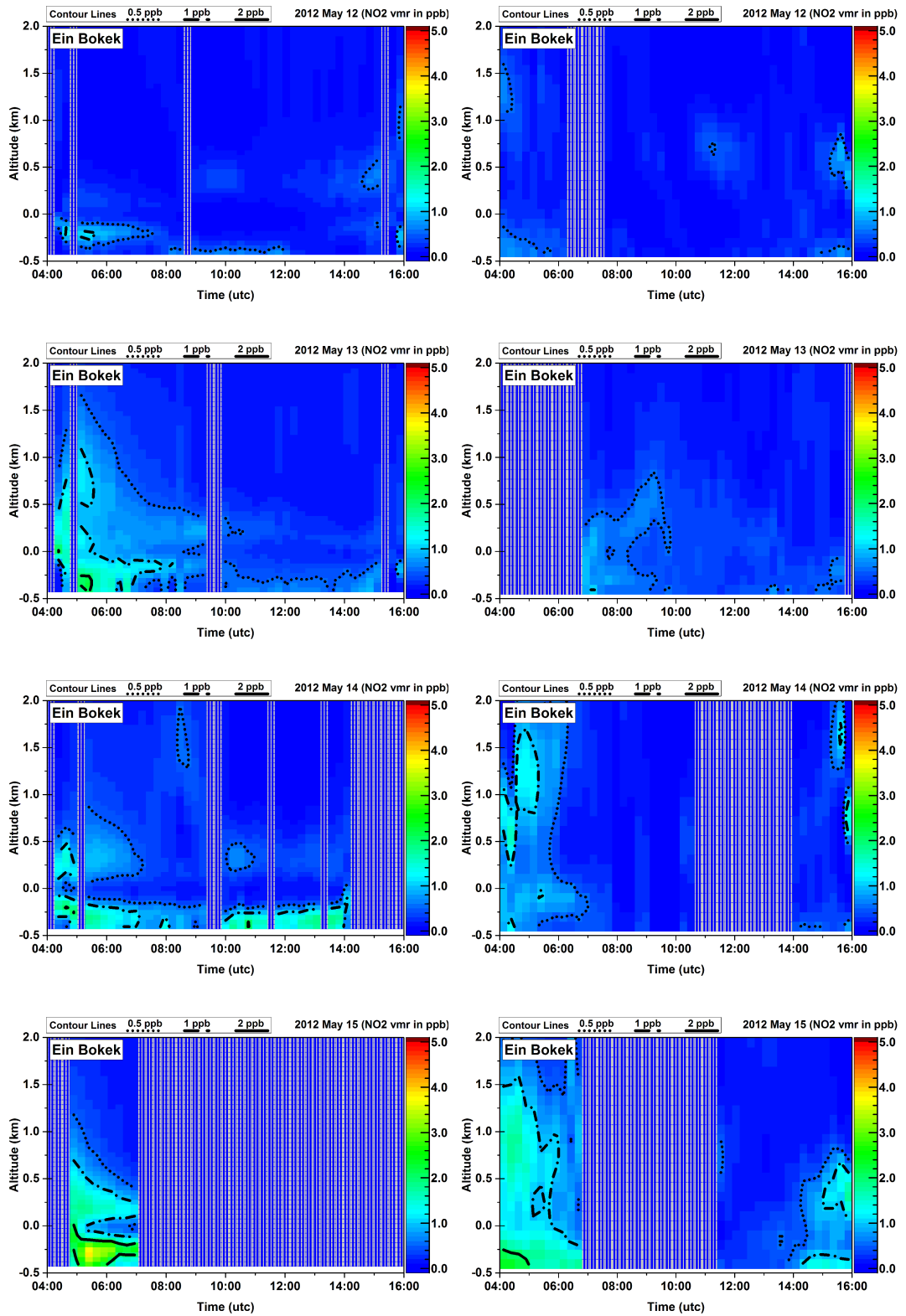
Fig. 8.32: Same description as for figure 8.31.

8.9 Nitrate
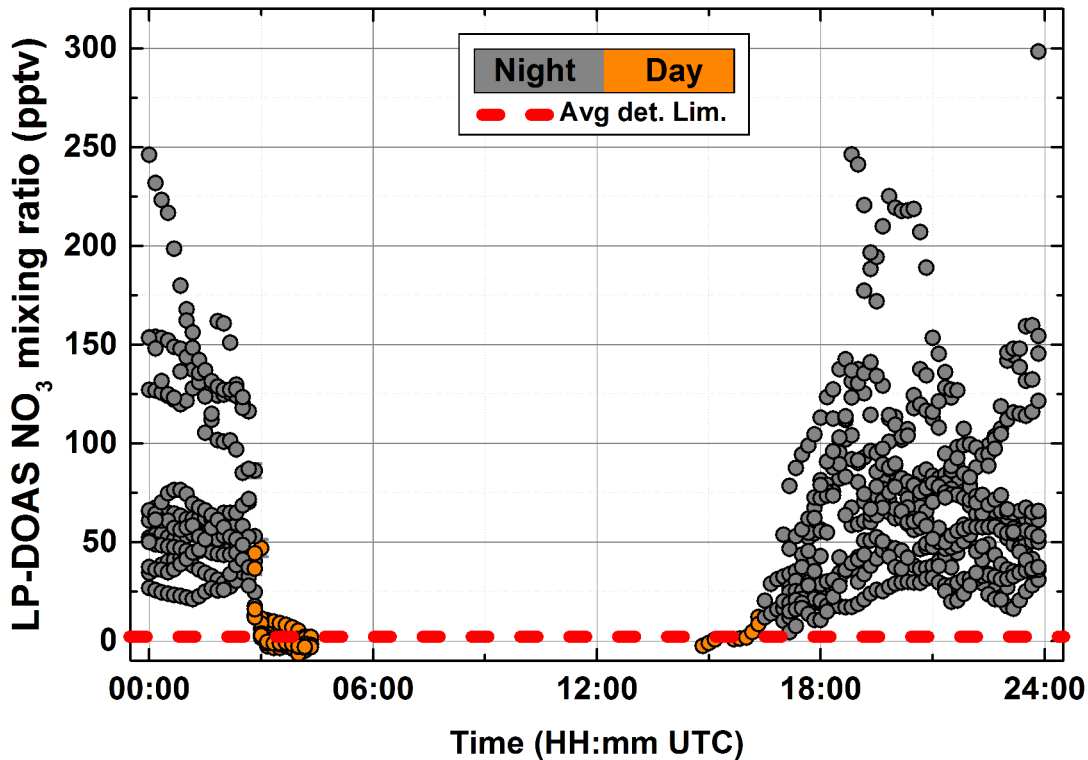
Fig. 8.33: NO₃ volume mixing ratios measured by LP-DOAS during the whole campaign plotted against time of day. Errors are 2 times fit error. However, error bars are smaller than the extent of the data points in this plot. The average detection limit is 1.5 pptv and is defined as 4 times the fit error. Color code represents day and night time (solar radiation above and below 10 W/m²).

During nighttime, the LP-DOAS instrument was able to observe nitrate with mixing ratios between 5 and 300 pptv (see figure 8.33 for all vmrs plotted as a function of daytime). During sunrise and sunset, mixing ratios were near the average detection limit of 1.5 pptv. The average mixing ratio during nighttime was 60 pptv with peaks of significantly higher NO₃ shortly after sunset on may 5th and 11th. Figure 8.34 provides a time series of nitrate mixing ratios during the campaign period.
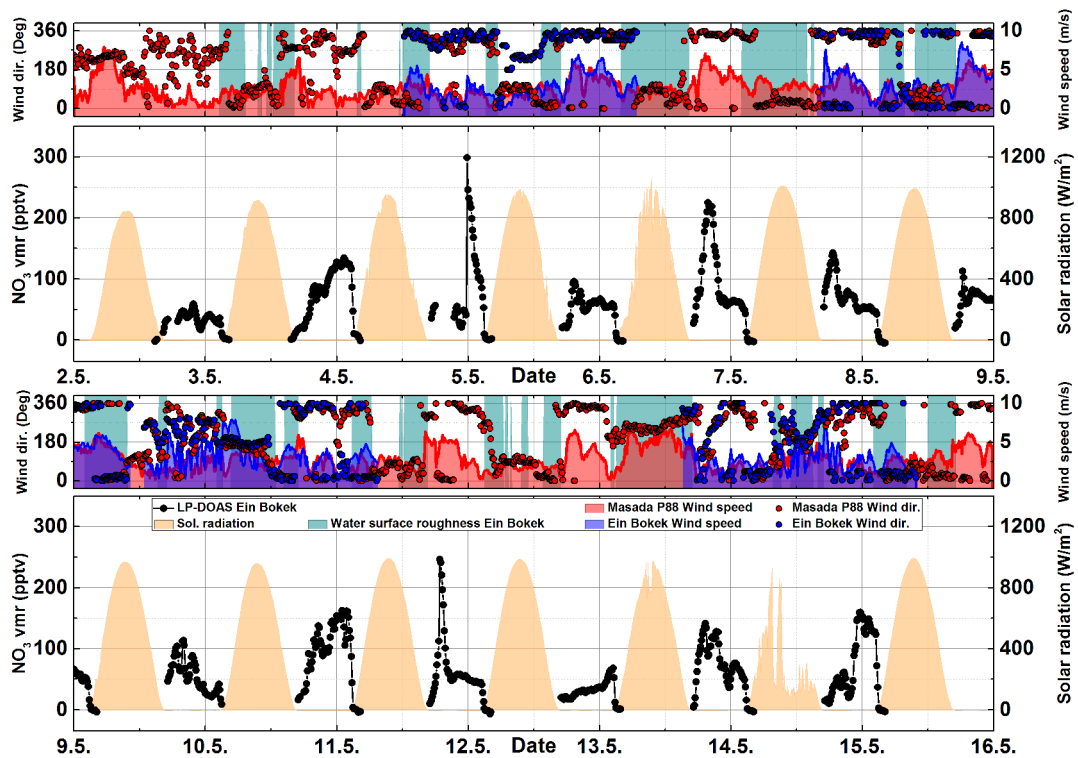
Fig. 8.34: Time series of NO₃ volume mixing ratios measured by LP-DOAS at Ein Bokek. Ticks are at 00:00 and 12:00 UTC. LP-DOAS errors are 2 times fit error. However, error bars are smaller than the extent of the data points in this plot.

8.10 Nitrous acid
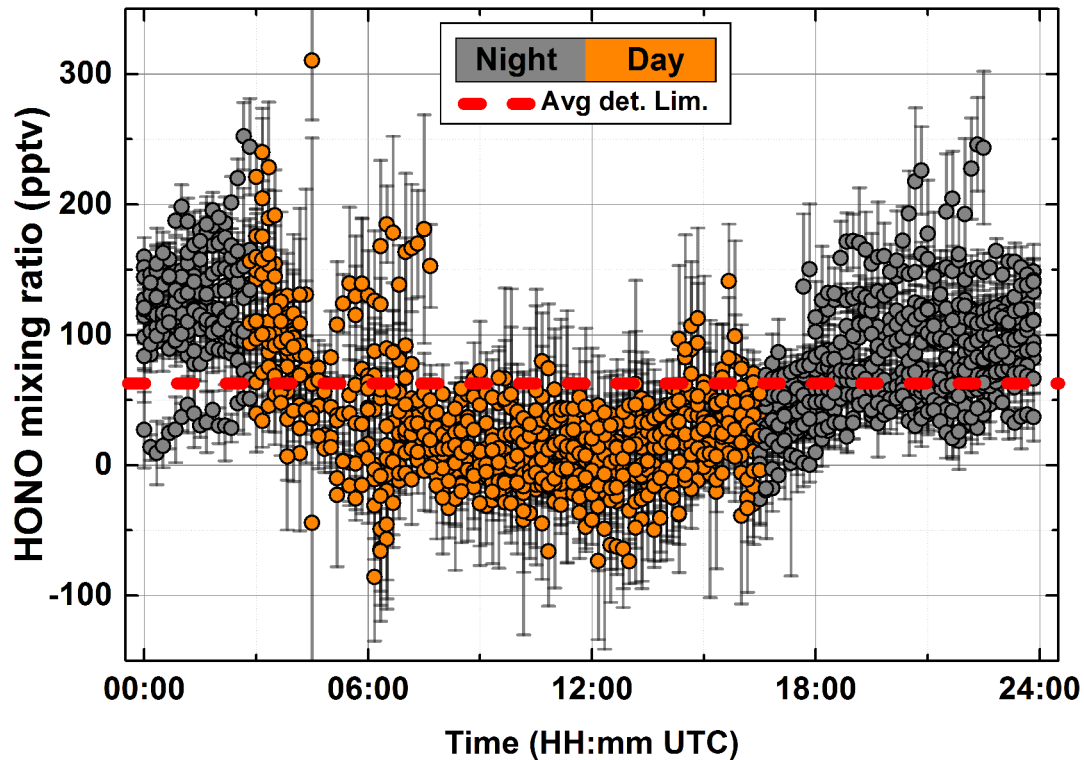
Fig. 8.35: HONO volume mixing ratios measured by LP-DOAS during the whole campaign plotted against time of day. Errors are 2 times fit error. The average detection limit is 50 pptv and is defined as 4 times the fit error. Color code represents day and night time (solar radiation above and below 10 W/m².).

Significant amounts of nitrous acid (HONO) were observed by the LP-DOAS instrument during nighttime with volume mixing ratios of up to 250 pptv at an average detection limit of 50 pptv (see figure 8.35 for all vmrs plotted against time of day). The time series in figure 8.36 shows that the typical diurnal variations. HONO starts to rise after sunset with rates of approximately 15 pptv/h. In figure 8.35, some data points show elevated HONO vmrs during daytime. However, considering the increased errors of these data points, the values are most likely not significant. No significant amounts of HONO were detected by the MAX-DOAS instruments.
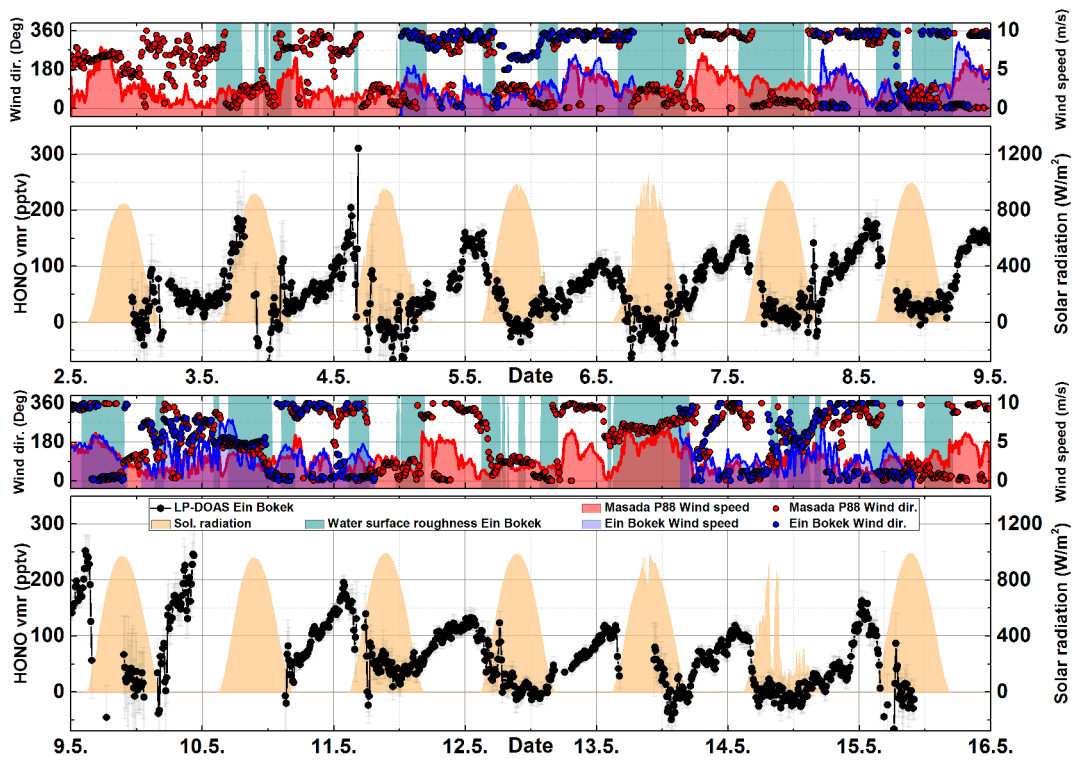
Fig. 8.36: Time series of HONO volume mixing ratios measured by LP-DOAS at Ein Bokek. Ticks are at 00:00 and 12:00 UTC. LP-DOAS errors are 2 times fit error.

8.11 Formaldehyde
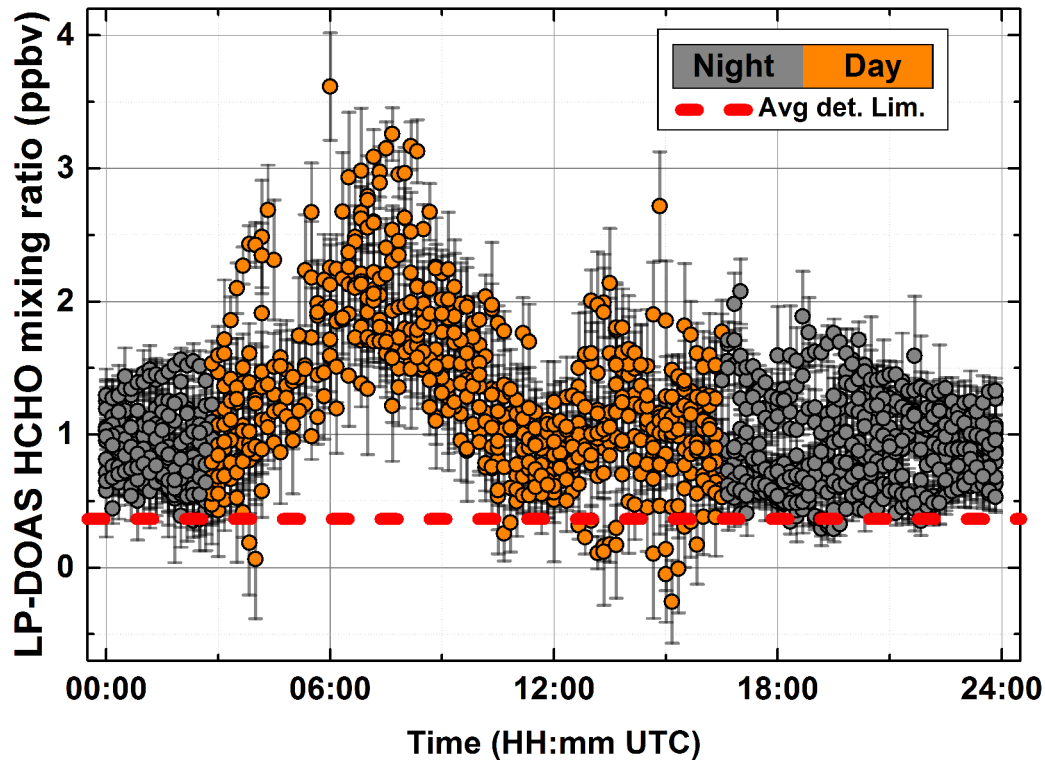
Fig. 8.37: HCHO volume mixing ratios measured by LP-DOAS during the whole campaign plotted against time of day. The plot shows only data with errors smaller than 0.5 ppbv. Error bars are 2 times fit error. The average detection limit is 0.4 ppbv and is defined as 4 times the fit error. Color code represents day and night time (solar radiation above and below 10 W/m^2).

The LP-DOAS observed mixing ratios of formaldehyde (HCHO) in the range of the average detection limit of 0.8 ppbv to peak values of 6 ppbv. Visibility had a strong impact on the measurement sensitivity because the spectral range of the HCHO retrieval is in the UV at 330 nm. This results in larger errors on several days of the measurement period. For the sake of clarity, only data points with errors smaller than 0.5 ppbv are shown in figure 8.37. The time series in the upper plot in figure 8.38 involves all data points with out filtering. Especially data on May 9 [th] and 10 [th], the sensitivity was low resulting in larger errors.

Therefore, this data should be considered with caution. The HCHO retrieval from MAX-DOAS data was less influenced by visibility (usage of sunlight comapred to the artificial light source of the LP-DOAS) resulting in a better the sensitivity compared to the LP-DOAS on these particular days. On the other days, HCHO vmrs retrieved by the data of the DOAS instruments are in good agreement. HCHO tends to rise after sunset from nighttime mixing ratios between 0.5 ppbv and 1.5 ppbv to 3 ppbv during daytime. The peak values are followed by a decrease of approximately 0.5 ppbv/h towards the afternoon.

The time series of vertical column densities retrieved from MAX-DOAS data (figure 8.38, lower plot) also shows rising slopes in the morning. Decays towards the afternoon are not regularly observed. On some days, HCHO VCDs are constantly increasing during the day (e.g. May 8th, 11 th and 12 th) indicating a different dynamics in different altitudes. Indeed, the vertical profiles of HCHO (figures 8.39 , 8.40 and 8.41) show strong vertical gradients with mixing ratios larger than 4 ppbv at an absolute altitude of 1 km while having 1 pbbv at ground level (Ein Bokek MAX-DOAS on May 3rd and 8th). While the vertical gradients at Ein Bokek are very distinct and dynamic in terms of time, at Masada HCHO seems to be more homogeneously distributed both spatially and temporally. On both locations, the dominating part of HCHO tends to be at altitudes between 100 m and 1.5 km above ground (absolutes altitudes of -300 m to 500 m). Surface mixing ratios seem not to be representative for the total amount of HCHO in the Dead Sea Valley.
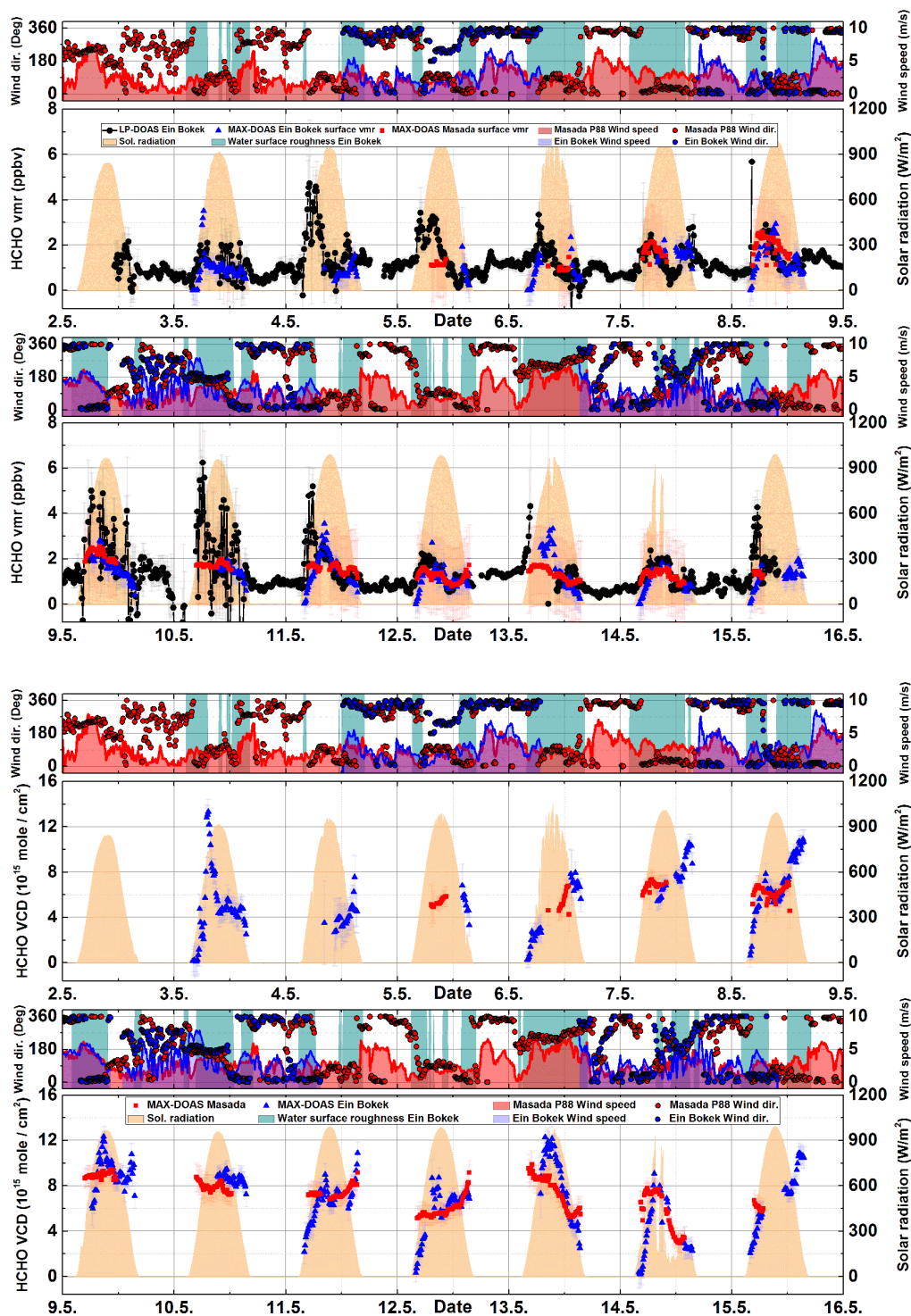
Fig. 8.38: Time series of HCHO volume mixing ratios measured by LP-DOAS (black dots), MAX-DOAS at Ein Bokek (red squares) and Masada (blue triangles) and VCDs from MAX-DOAS. Ticks are at 00:00 and 12:00 UTC. LP-DOAS errors are 2 times fit error. MAX-DOAS errors are retrieval errors.
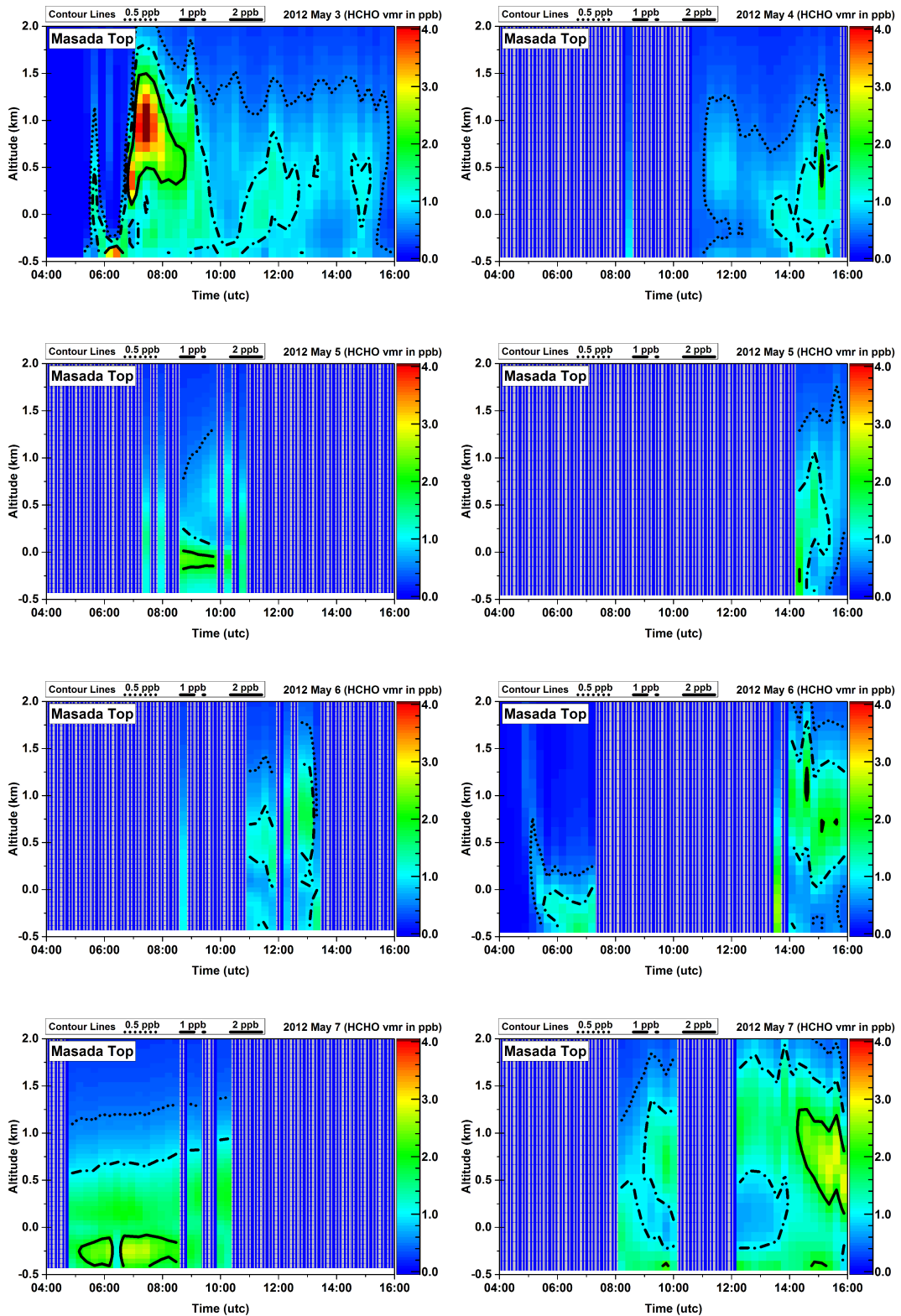
Fig. 8.39: Vertical profiles of HCHO retrieved from the data of the MAX-DOAS at Masada (left) and Ein Bokek (right). Note that the first plots show data of the MAX-DOAS at Ein Bokek on May 3rd and 4th 2012. Shaded areas indicate missing data.
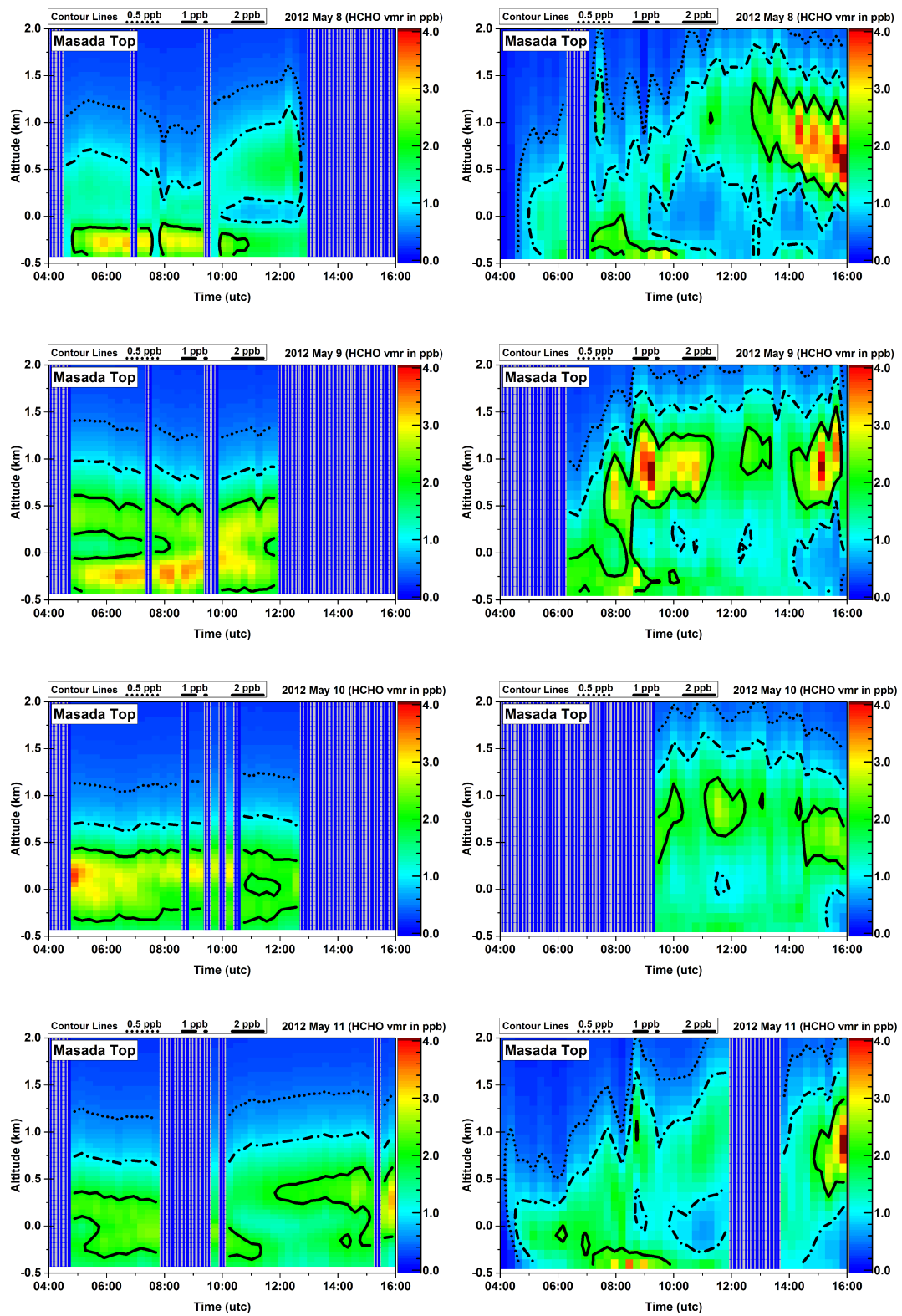
Fig. 8.40: Same description as for figure 8.40.
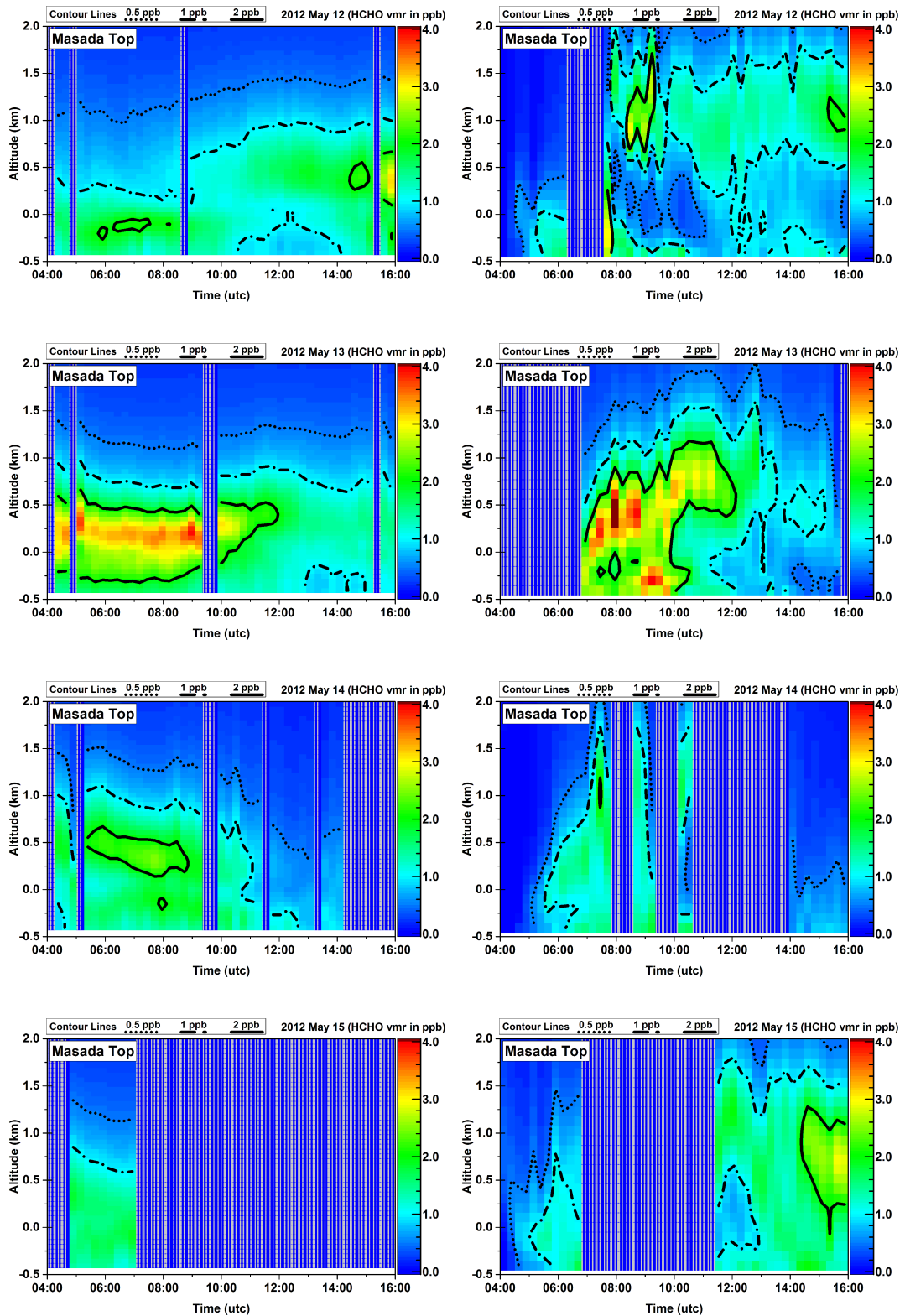
Fig. 8.41: Same description as for figure 8.40.

8.12 Sulfur dioxide
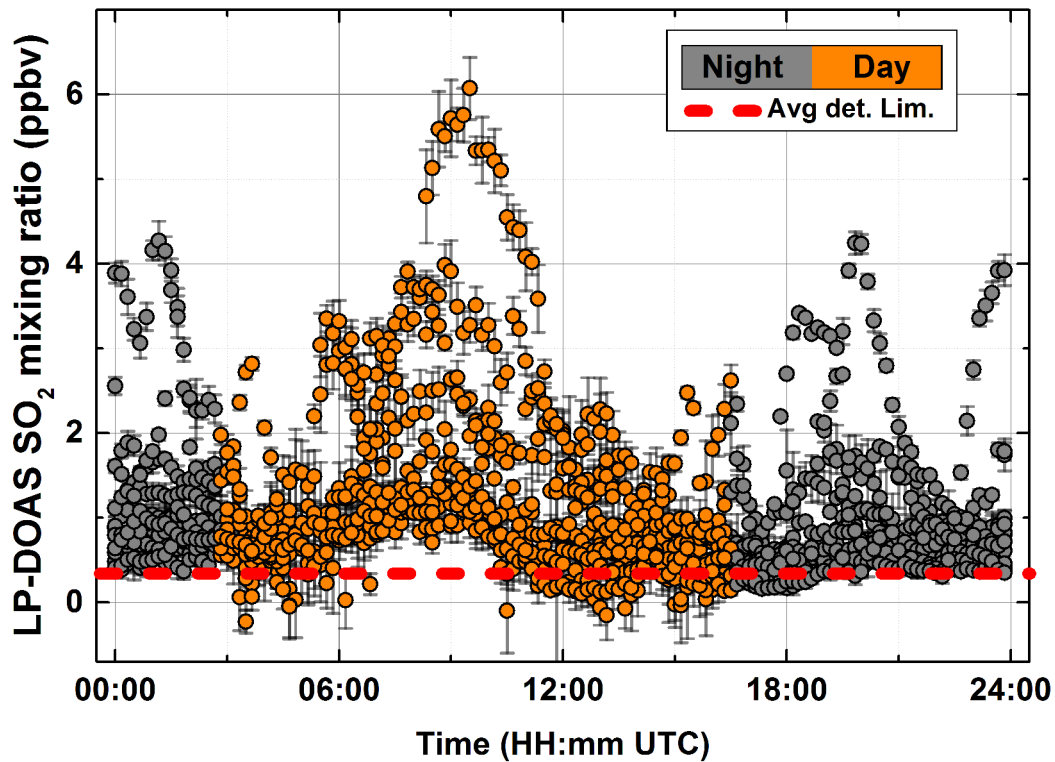
Fig. 8.42: SO_2 volume mixing ratios measured by LP-DOAS during the whole campaign plotted against time of day. Errors are 2 times fit error. The average detection limit is 300 pptv and is defined as 4 times the fit error. Color code represents day and night time (solar radiation above and below 10 W/m^2).

Figure 8.42 shows the mixing ratios of sulfur dioxide (SO_2) measured by LP-DOAS with respect to daytime. With an average detection limit of 300 pptv, the LP-DOAS observed mixing ratios of up to 6 ppbv. Dominant peaks with a temporal extension of 1 to 2 hours could be observed occasionally during night and daytime. Further, mixing ratios were almost constantly above 500 pptv. Despite several peaks, not repetitively pattern of the diurnal variation of SO_2 is observed. The dynamics is most likely driven by the local construction sites by the Dead Sea Works company which were located on the dam of the evaporation ponds near Ein Bokek.
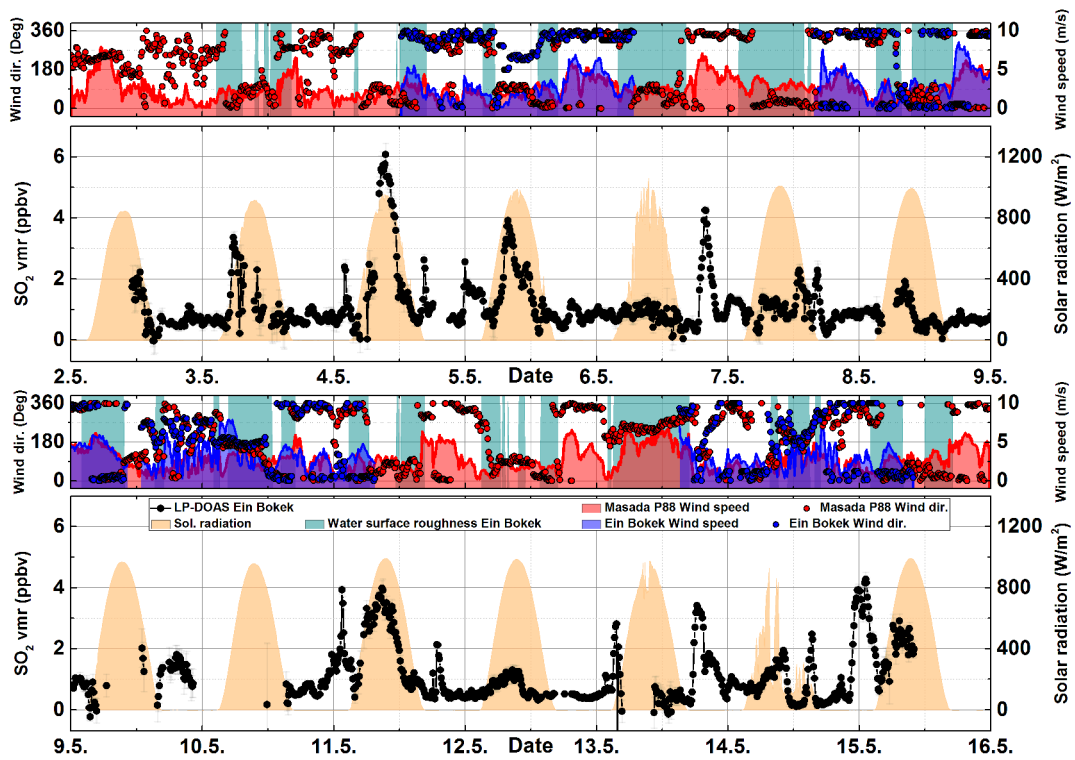
Fig. 8.43: Time series of SO$_2$ volume mixing ratios measured by LP-DOAS at Ein Bokek. Ticks are at 00:00 and 12:00 UTC. LP-DOAS errors are 2 times fit error.

8.13 Particle Counter
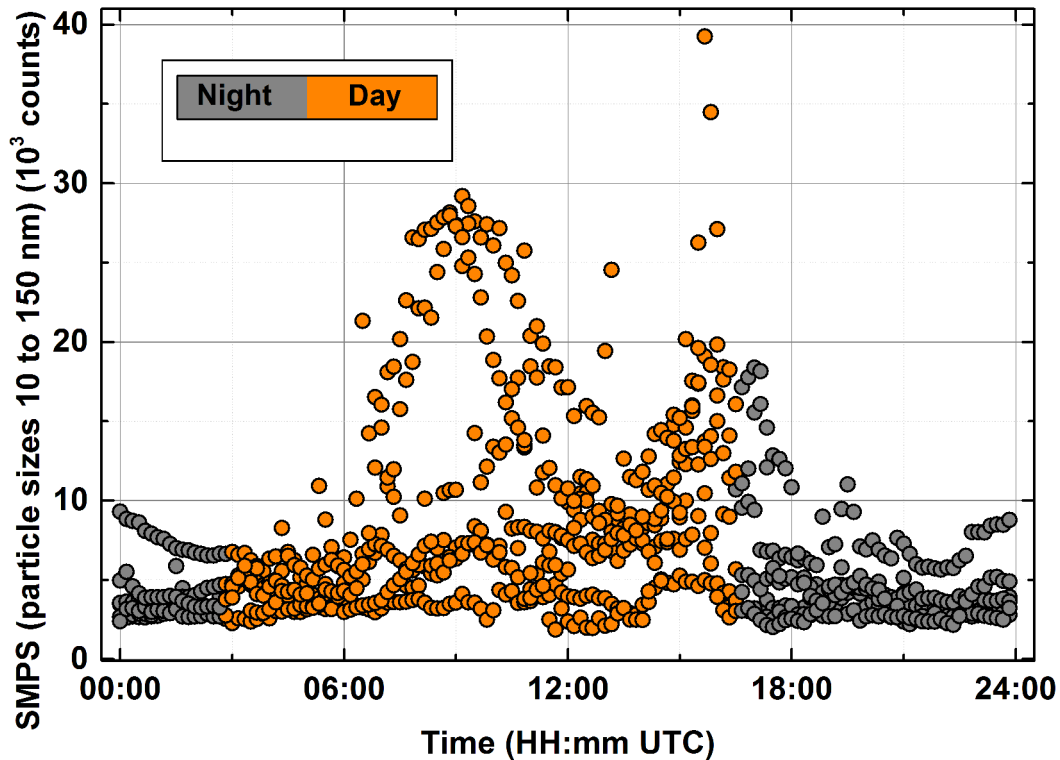
Fig. 8.44: Numbers of particles with diameters between 10 and 150 nm measured by SMPS at Ein Bokek plotted against time of day. Color code represents day and night time (solar radiation above and below 10 W/m^2).

As described in section 6.6 on May 4th and 5th only the CPC unit was operative so the total number of particles in the diameter range between 9nm and 1000nm was measured. The DMA unit of the SMPS, which measured particles with diameters between 10 and 150 nm, only worked during May 9th and 15th. Figure 8.44 shows only the SMPS data with operative DMA plotted against time of day. The time series in figure 8.45 shows all data. Highest particle numbers were measured during daytime where values were about a factor of three higher than during nighttime. The time series shows a strong dynamical behavior of the SMPS data on several days.
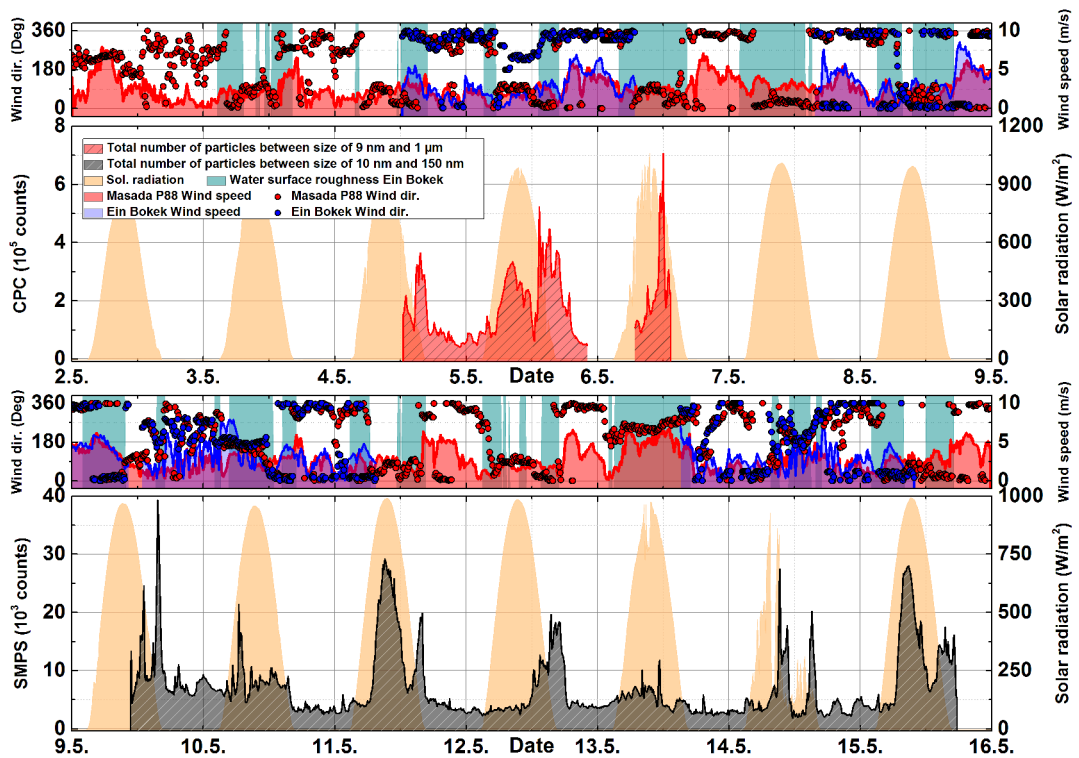
Fig. 8.45: Time series of particles. During May 4th and 5th, only the CPC unit (indicated by red area, shaded) was operative measuring the total number of particles with diameters between 9 nm and 1000 nm.

8.14 Bromine dioxide and iodine dioxide
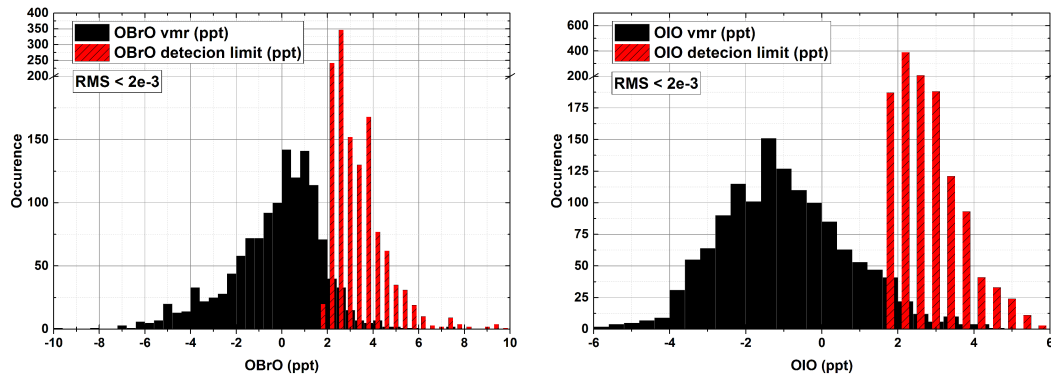
Fig. 8.46: Average detection limits:OBrO 3.3pptv, OIO 2.9pptv, OClO 3.7 pptv

No significant mixing ratios of bromine dioxide (OBrO) and iodine dioxides (OIO) were observed by the LP-DOAS instrument. Average detection limits were 3.3 pptv (OBrO), 2.8 pptv (OIO). Figure 8.46 shows histograms of measured volume mixing ratios and the corresponding detection limit.

9

Results of Dead Sea Campaign November 2014

Within the following section, the result from the measurement campaign in November 2014 are presented. Meteorology, aerosol optical depth and trace gas species are discussed within a dedicated subsection each. The results of the mobile MAX-DOAS measurements will be presented in the discussion section to support the interpretation of the data from stationary measurements

9.1 Meteorology

Two weather stations at Ein Gedi and at the KIT Cube at Masada recorded meteorological data (courtesy of KIT IMK, Andreas Wieser and Jutta Metzger, pers. comm.). Figure 9.1 shows histograms of various meteorological data. Temperatures were ranging between almost 30°C during daytime down to 17°C during night time. Relative humidity ranged from values below 20 % (during the first week of the campaign) up to almost 80%. Wind speeds during daytime were slightly higher than during nighttime. Wind speed peak values of above 12 m/s were measured on a few days shortly before and during sunrise (e.g. November 16th, 17th and 22th). Twelve of the twenty-six days of the measurement period had significant cloud coverage. On cloud free days, solar radiation reached peak values of approximately 700 W/m^2. Further, on some days precipitation of 0.8 mm and 1.8 mm were observed on Nov 17th and 24th. On 26th a sandstorm event occurred between 09:30 and 15:00 UTC, having significant impact on visibility.

Between Nov 5th and 10th, a decrease in relative humidity is observed with minimum values of 20 % on Nov 8th followed by an daily increase up to values between 30 % and 60 %. Also, the difference between daytime and nighttime temperatures in the period of Nov 5th to 10th is significantly larger than on the following days of the measurement period. Looking at the wind speeds, one can assume that the meteorology in the first days of the campaign in dominantly driven by air masses with low humidity brought to the Dead Sea valley by prevailing northerly winds at increased speeds between 5 m/s and 10 m/s. From Nov. 9th on, wind speed decreased to 2 m/s, relative humidity and cloud coverage increased, as indicated by solar radiation data.

Wind rose plots in figure 9.1 indicate prevailing northerly and southerly winds at moderate to high wind speeds during daytime at both locations. At nighttime, besides northerly and southerly winds, also south-westerly and north-westerly directions were observed at Ein Gedi and Masada, respectively, although at low wind speeds.
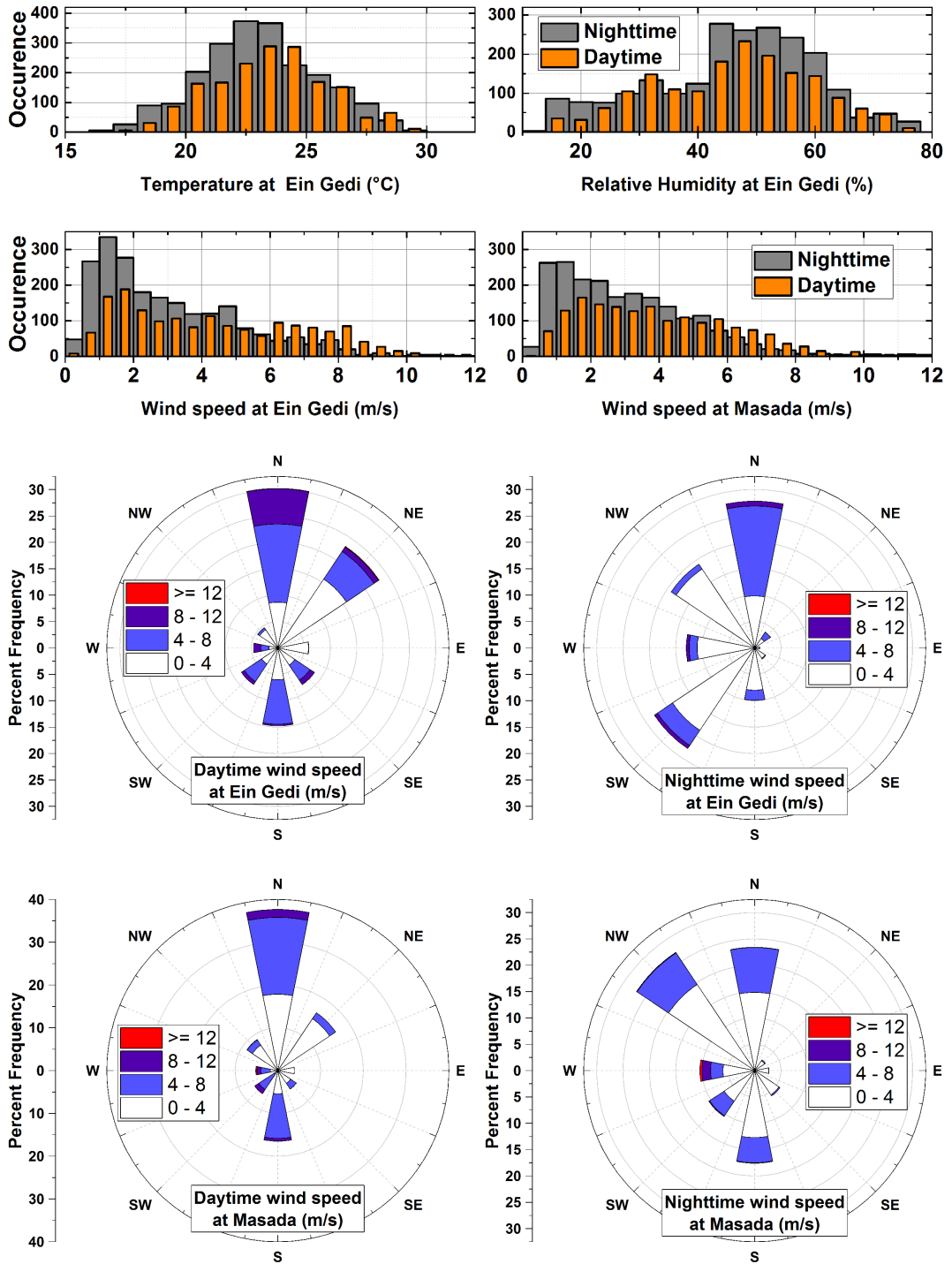
Fig. 9.1: Histograms of temperature and relative humidity measured at Ein Gedi as well as wind speed measured at Ein Gedi (left) and Masada (right). Orange and gray bars represent day time and night time data, respectively. Wind rose plots show distributions of horizontal wind speed and wind directions at the weather stations at Ein Gedi and at Masada.
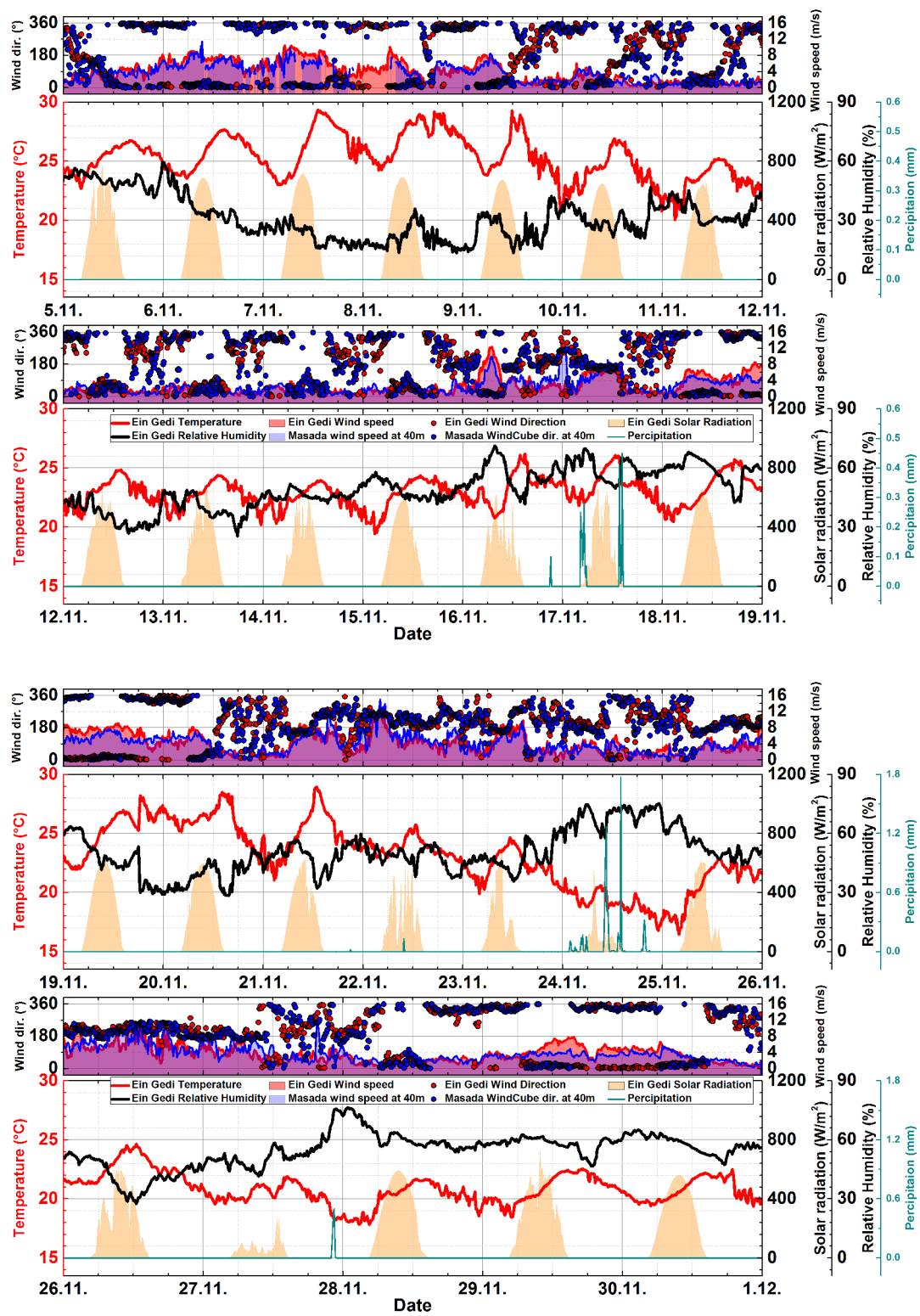
Fig. 9.2: Time series of wind data, temperature, relative humidity and solar radiation from weather stations at Ein Gedi and at Masada. Ticks are at 00:00 and 12:00 UTC.

(a) Clear

(b) Clouds

(c) Rain

(d) Sandstorm
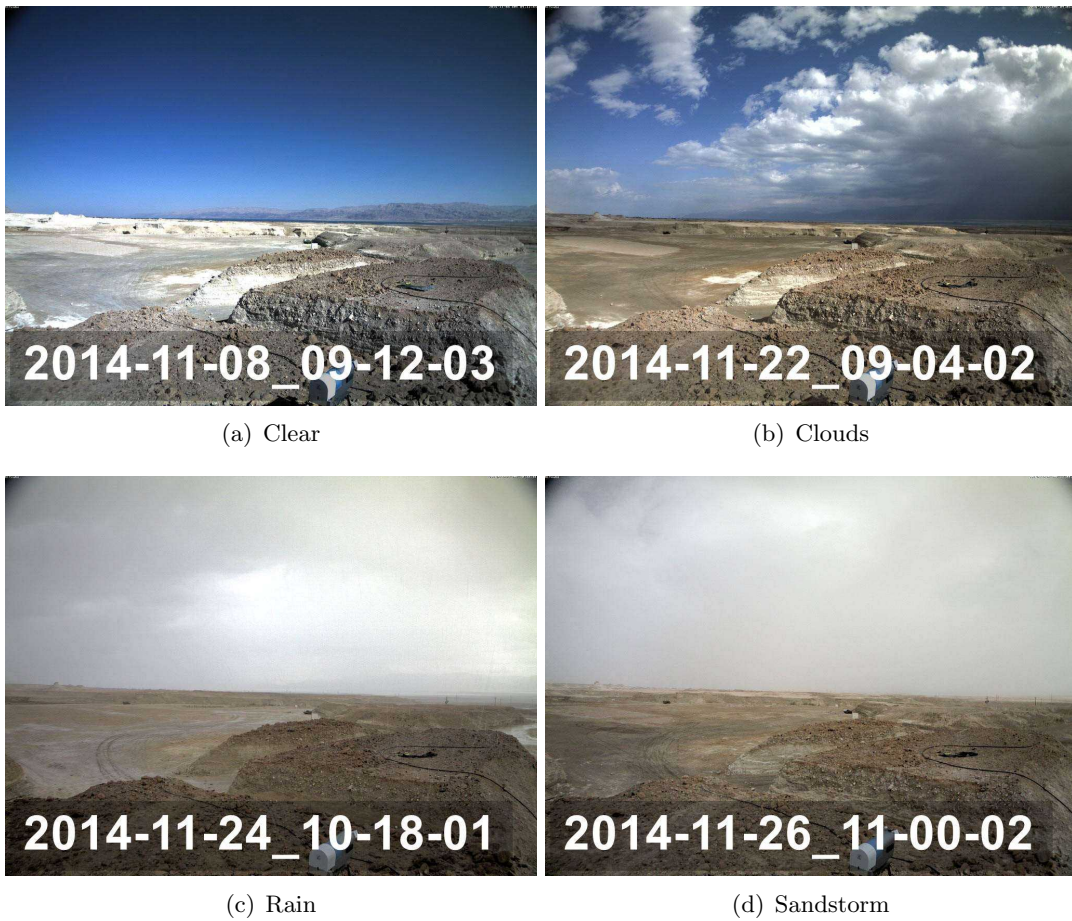
Fig. 9.3: Example pictures of different meteorological situations recorded by KIT Cube camera, viewing direction east (90°). Courtesy of KIT IMK. Andreas Wieser and Jutta Metzger, pers. comm..

9.2 Aerosol optical depth

Figure 9.4 shows the time series of aerosol optical depths (AODs) retrieved from data of the two MAX-DOAS instruments as well as meteorological data. AODs from different instruments at different locations (Neve Zohar, Masada, Ein Gedi) is distinguishable by different symbols and colors (see plot caption and legends). Note that, since peak values of above 20 were observed on some days, the y-axis in the figures has a breaks which allows to display a wide range of AODs. The weather station at Ein Gedi featured a pyranometer to measure solar radiation. Hence, a wide wavelength range ranging from the near UV to near infra red is used. Clouds cause decreases in measured solar radiation and can therefore be easily identified in the time series (orange area in figure 9.4).

Note that the aerosol optical depth from MAX-DOAS data is retrieved in the wavelength range of 350 nm to 370 nm. Therefore, AODs and solar radation measured by the weather station must not necessarily correlate. Due to the observed wavelength range and measurement geometry, the MAX-DOAS instruments are more sensitive to haze or precipitation near the ground surface than to clouds in higher altitudes above 1km. Between Nov 5th and 10th, where meteorological conditions were clear and relative humidity as decreasing (compare section 9.1 above), constantly decreasing AOD were observed day by day with a minimum of 0.01 on Nov. 7th afternoon. From Nov. 8th on, AODs increased with every day with a rate of about 0.1 per day until leveling off at 0.2 on Nov. 10th. During the following days AODs around 0.4 were measured during cloudy days. Precipitation events caused optical depths of 3 (e.g. Nov. 17th in the morning and afternoon). During a sandstorm event on Nov. 26th, AODs of up to 1.2 were observed.
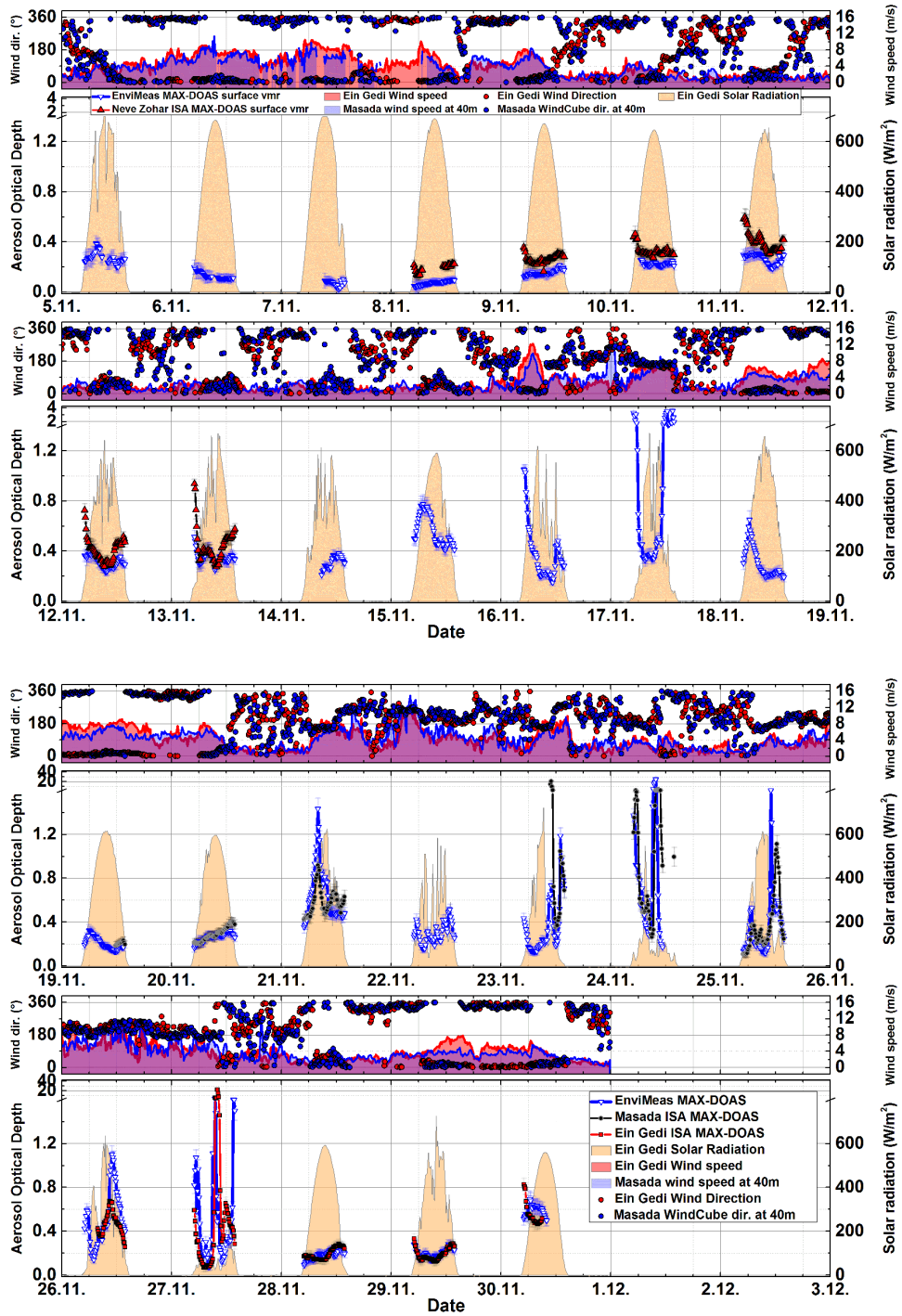
Fig. 9.4: Time series of aerosol optical depths retrieved from MAX-DOAS data. Solar radiation (orange area), data of the ISA MAX-DOAS at Neve Zohar (red triangles), at Masada (black circles) and at Ein Gedi (red squares) as well as data of the EnviMeS MAX-DOAS at Masada (blue triangles) is shown. Plots above the AOD time series show wind data from weather stations at Ein Gedi (red area and dots) and Masada (blue area and dots). Note the breaks in the y-axis to display the wide range of observed AODs. Major ticks are at 00:00 UTC.

Figures 9.5 to 9.9 show vertical profiles of aerosol extinction retrieved from MAX-DOAS data as well as back scatter signal measured by a laser zenith ceilometer, operating at 1064 nm, located next to the MAX-DOAS instrument at the KIT Cube site near Masada ceilometer data courtesy of KIT IMK, Andreas Wieser, Jan Handwerker pers. comm.). The ceilometer consists of a LIDAR (Light Detecting And Ranging) unit which is pointing in zenith direction. It allows to retrieve the altitude of atmospheric scatters by measuring the time between emitted light and back scattered signal. The first 200 m of the ceilometer profiles show no data. This is due to filtering of data points with a specific signal to noise ratio. The evaluation of the raw data, the profile retrieval and filtering was done performed by the operators of the KIT Cube (KIT IMK, Jan Handwerker, pers. comm.)

For the comparison of ceilometer and MAX-DOAS data, it should be noted that, both instruments measure under different geometries (only zenith direction for the ceilometer, up to 20 km forward looking for the MAX-DOAS). Further, note that in the plots, the scale for back scatter scale is logarithmic while the scale for MAX-DOAS AODs is linear.

Events of precipitation and the sand storm on Nov. 26th are qualitatively visible in both the ceilometer data and also in the MAX-DOAS data. Further both instrument types show an increase in signal on Nov. 10th compared to the previous days.
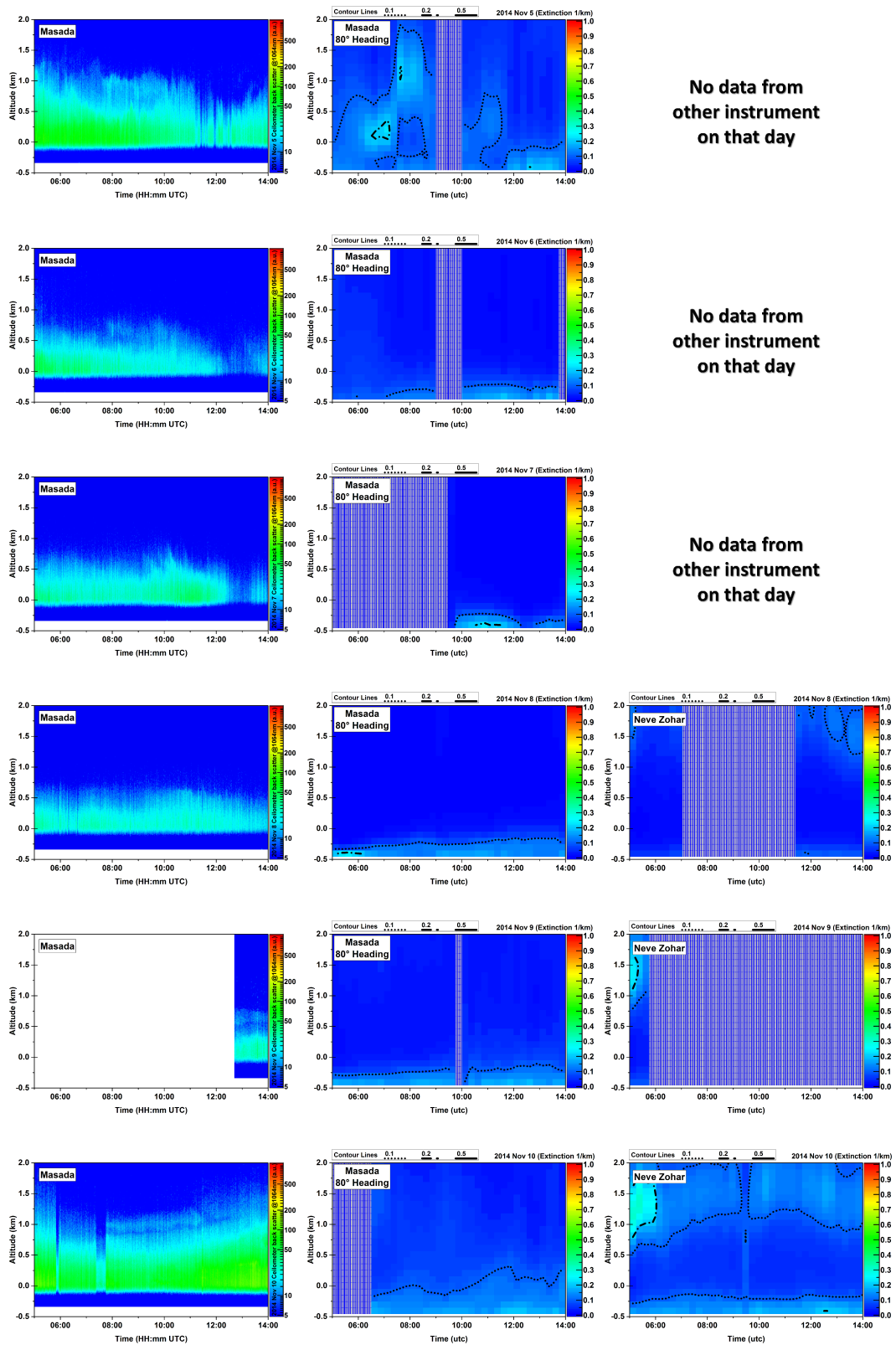
Fig. 9.5: Vertical profiles back scatter signal from the ceilometer at Masada (left plots) and of aerosol extinction from the data of MAX-DOAS at Masada (middle column) and the ISA MAX-DOAS (right column, see plot label for different locations). Data of the same day is displayed in each row. Color code of MAX-DOAS plots ranges from 0 to 1 km^{-1} with contour lines at 0.1, 0.2 and 0.5 km^{-1}..
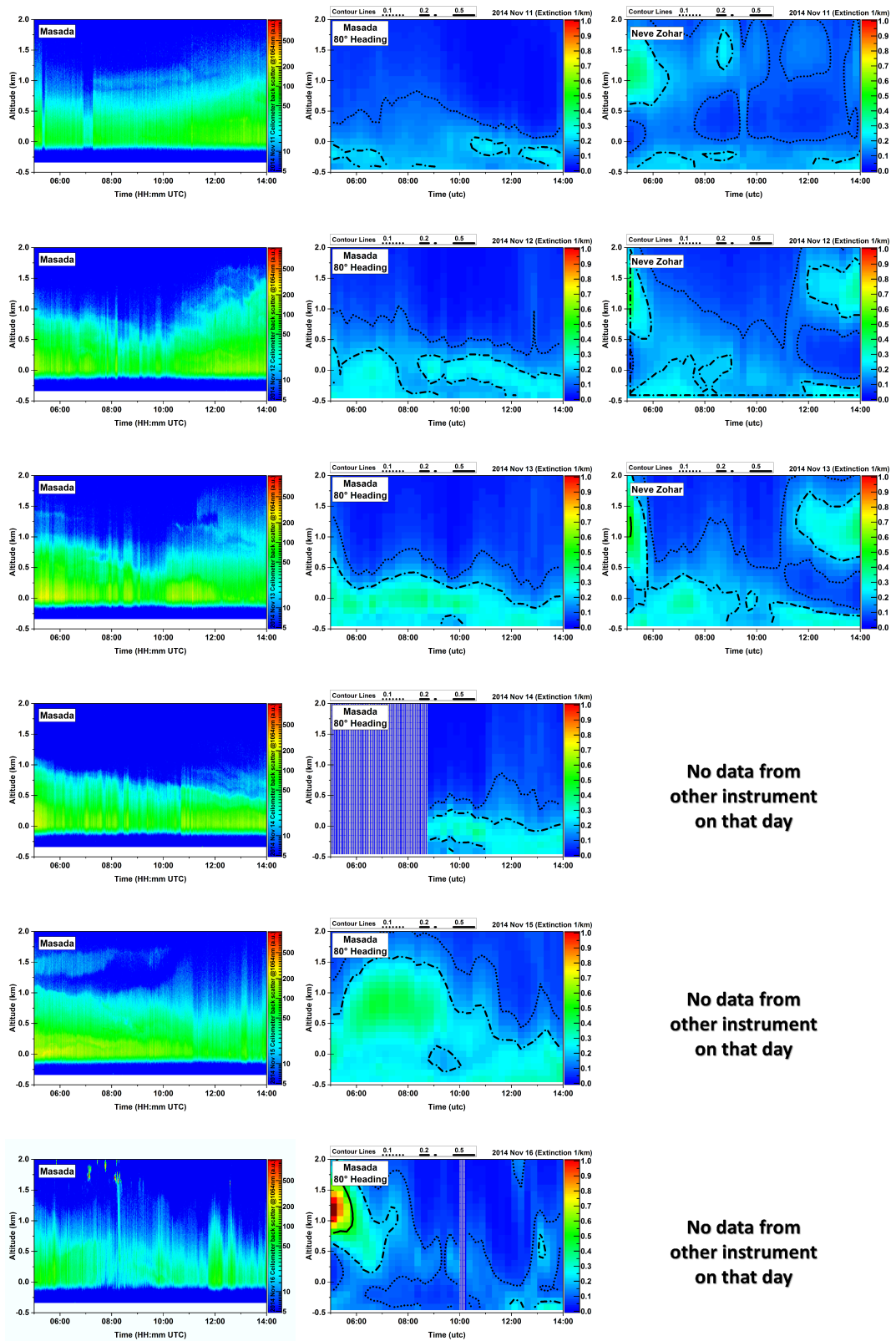
Fig. 9.6: Same as figure 9.5 but for subsequent days.
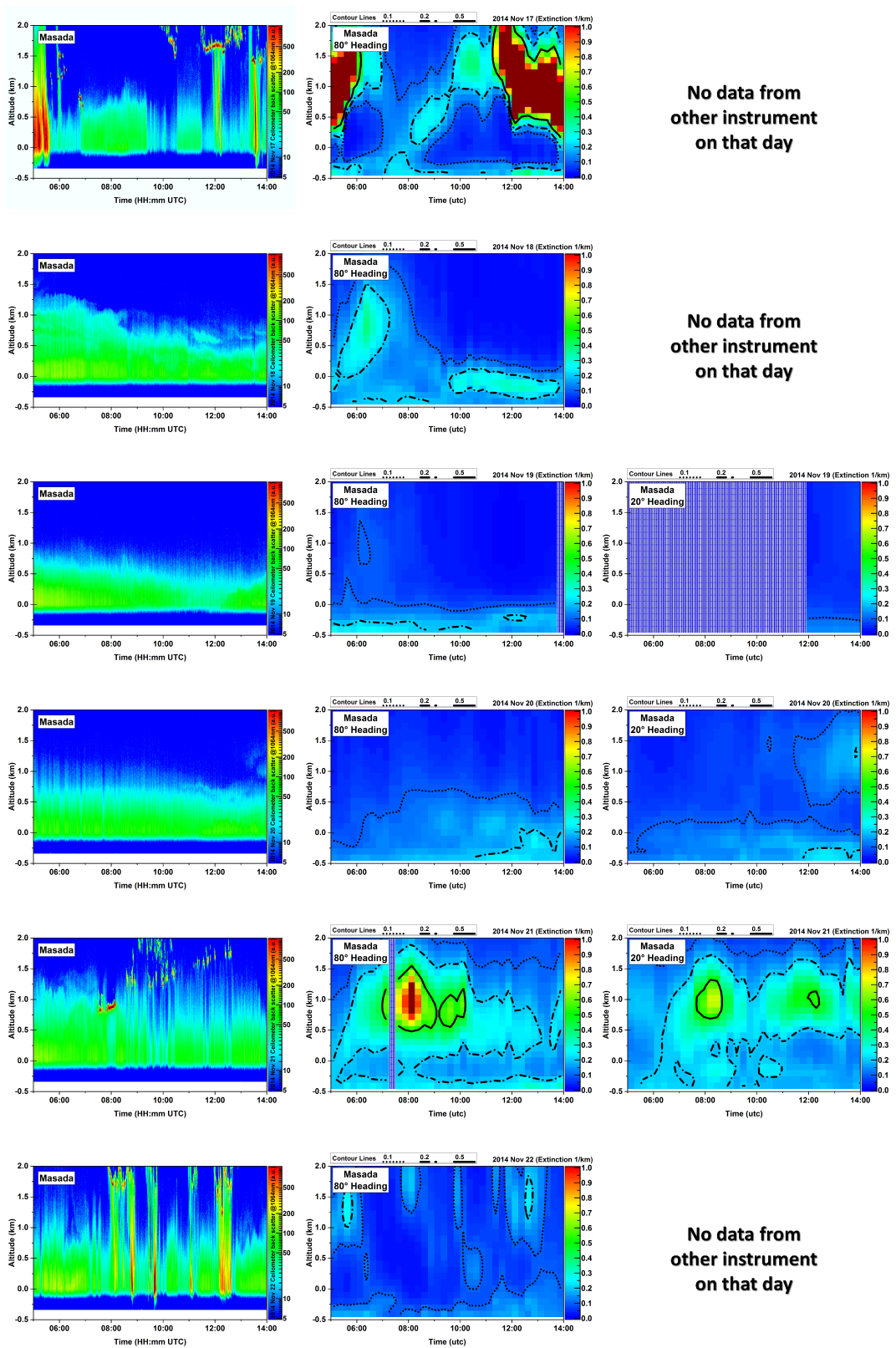
Fig. 9.7: Same as figure 9.5 but for subsequent days.
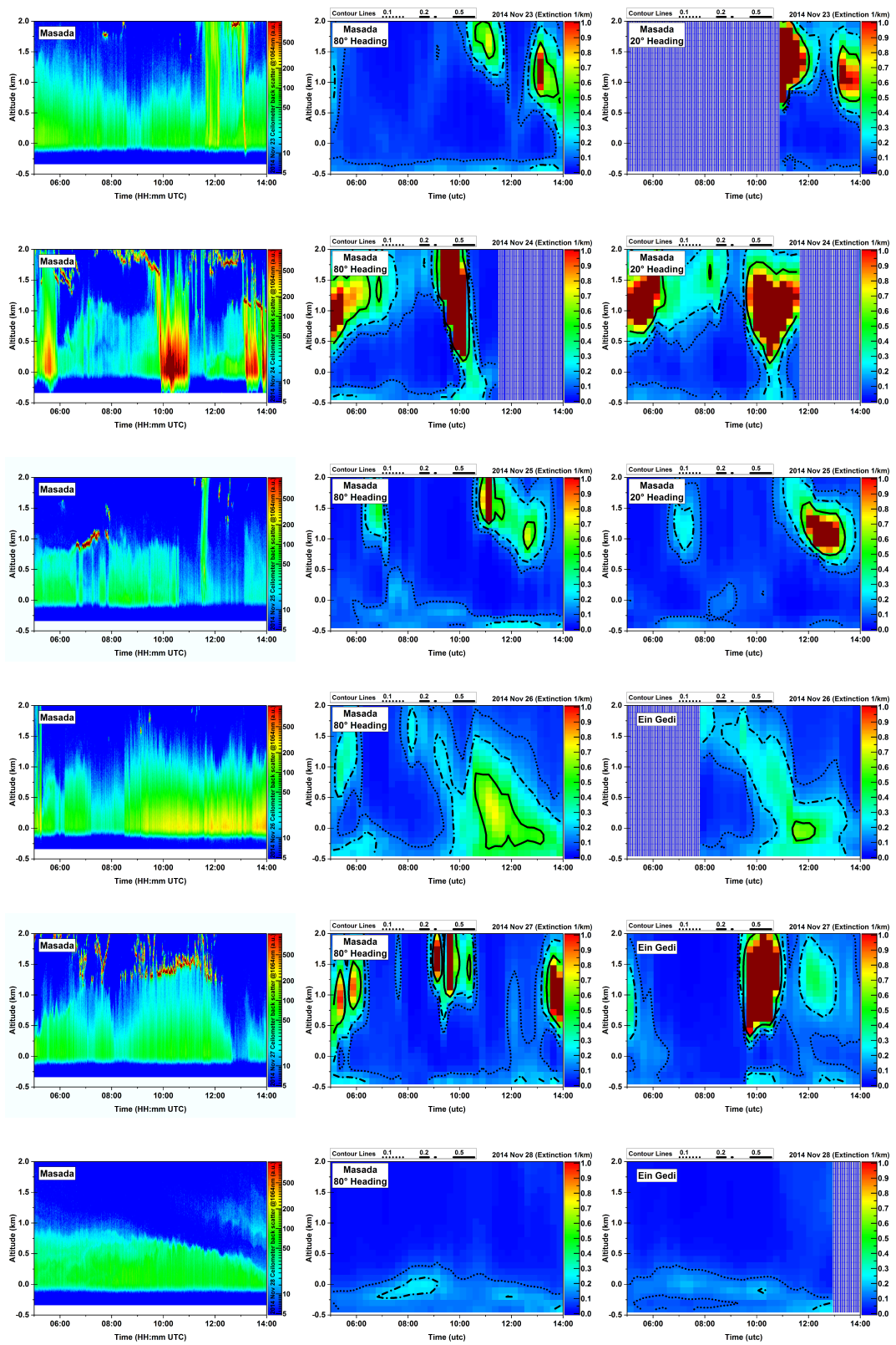
Fig. 9.8: Same as figure 9.5 but for subsequent days.
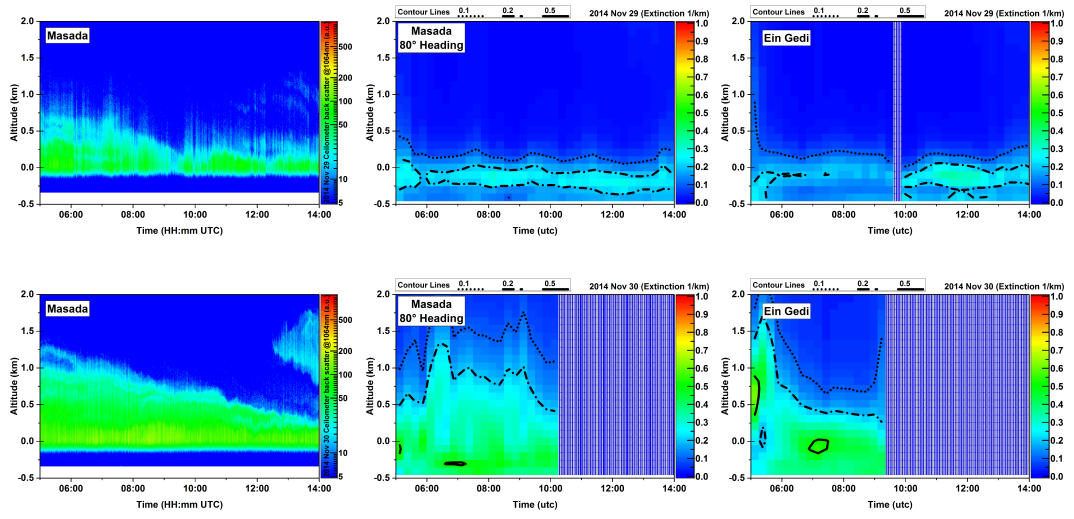
Fig. 9.9: Same as figure 9.5 but for subsequent days.

9.3 Bromine monoxide

Significant amounts of bromine monoxide were detected by the MAX-DOAS instruments on fourteen of the twenty-six days of the measurement period. Figure 9.10 shows the time series of surface mixing ratios and vertical column densities. Mixing ratios were ranging between 1 pptv and 6 pptv on most of the days with significant BrO abundance. On Nov. 8th and 17th comparatively high values of 20 pptv and 40 pptv, repectively, were observed at Masada. At Neve Zohar, where the MAX-DOAS instrument measures above an evaporation pond, peak vmrs of 4 pptv were detected on Nov 4th. At Ein Gedi, a maximum of 5 pptv was observed on Nov. 28th. The temporal dynamics of the surface vmrs and the vertical column densities shows strong gradients of 10 pptv/h (on Nov. 15th). On the morning of Nov. 17th BrO increased even by 30 pptv within half an hour. However, also rather smooth increases of BrO were observed on Nov 8th. The variations in the observed BrO seem to correlate with solar radiation and, hence, dynamics of the cloud coverage.

Figure 9.11 shows vertical profiles of BrO retrieved from the MAX-DOAS data. Only days with significant BrO abundance are shown. Pairs of neighboring plots show data of different instruments from the same day. Missing parallel data is indicated accordingly. While on most days, BrO is located near the surface with mixing ratios of up to 10 pptv, the data from Nov. 17th, 21th, 25th and 28th show distinct layers of BrO several hundred meters above the ground containing mixing ratios between 10 and 30 pptv.
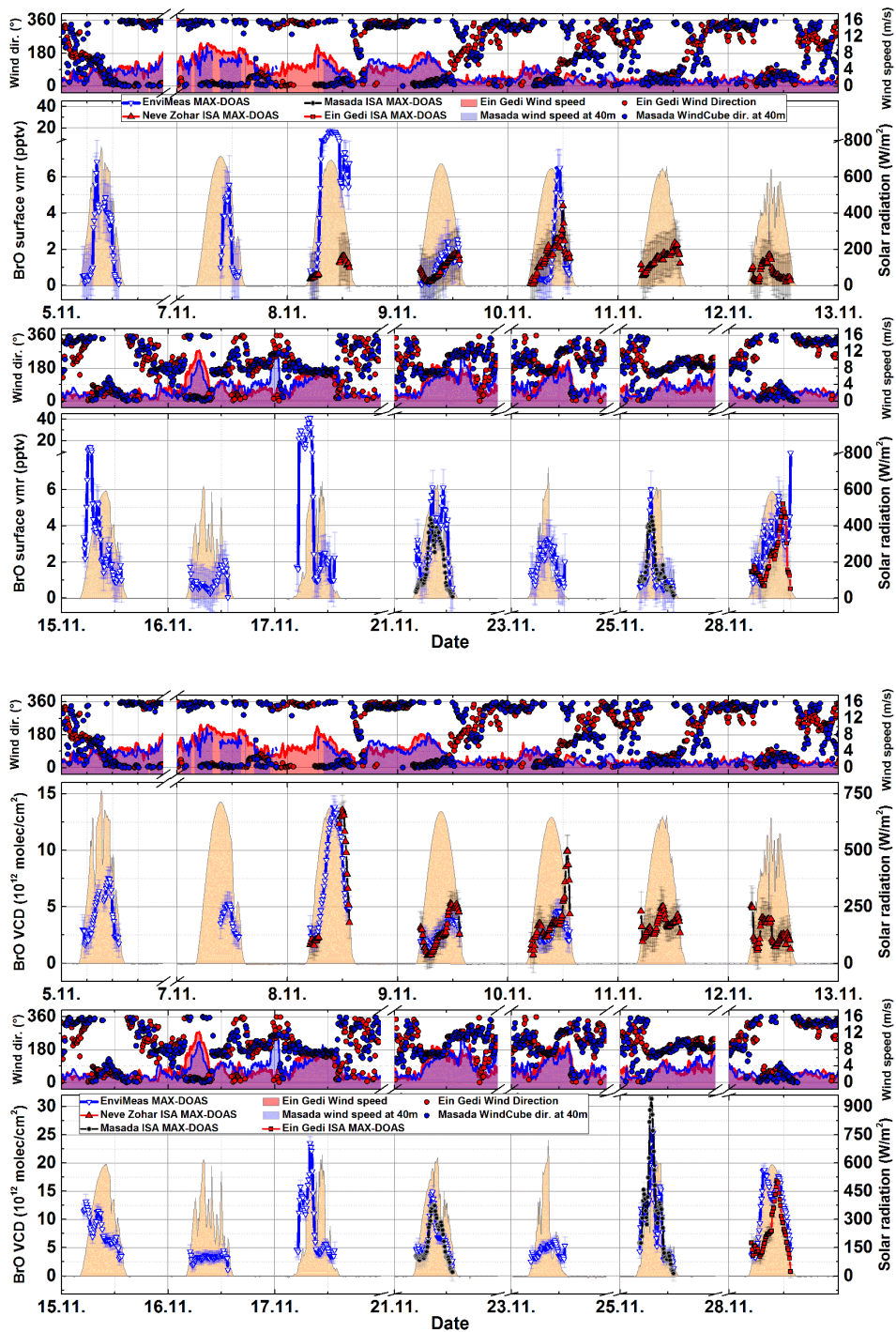
Fig. 9.10: Time series of BrO surface mixing ratios and VCDs retrieved from MAX-DOAS data. Solar radiation (orange area), data of the ISA MAX-DOAS at Neve Zohar (red triangles), at Masada (black circles) and at Ein Gedi (red squares) as well as data of the EnviMeS MAX-DOAS at Masada (blue triangles) is shown. Plots above the BrO time series show wind data from weather stations at Ein Gedi (red area and dots) and Masada (blue area and dots). Major ticks are at 00:00 UTC. Note the breaks in the y-axis to display the large range of BrO vmrs. Errors are total retrieval errors.
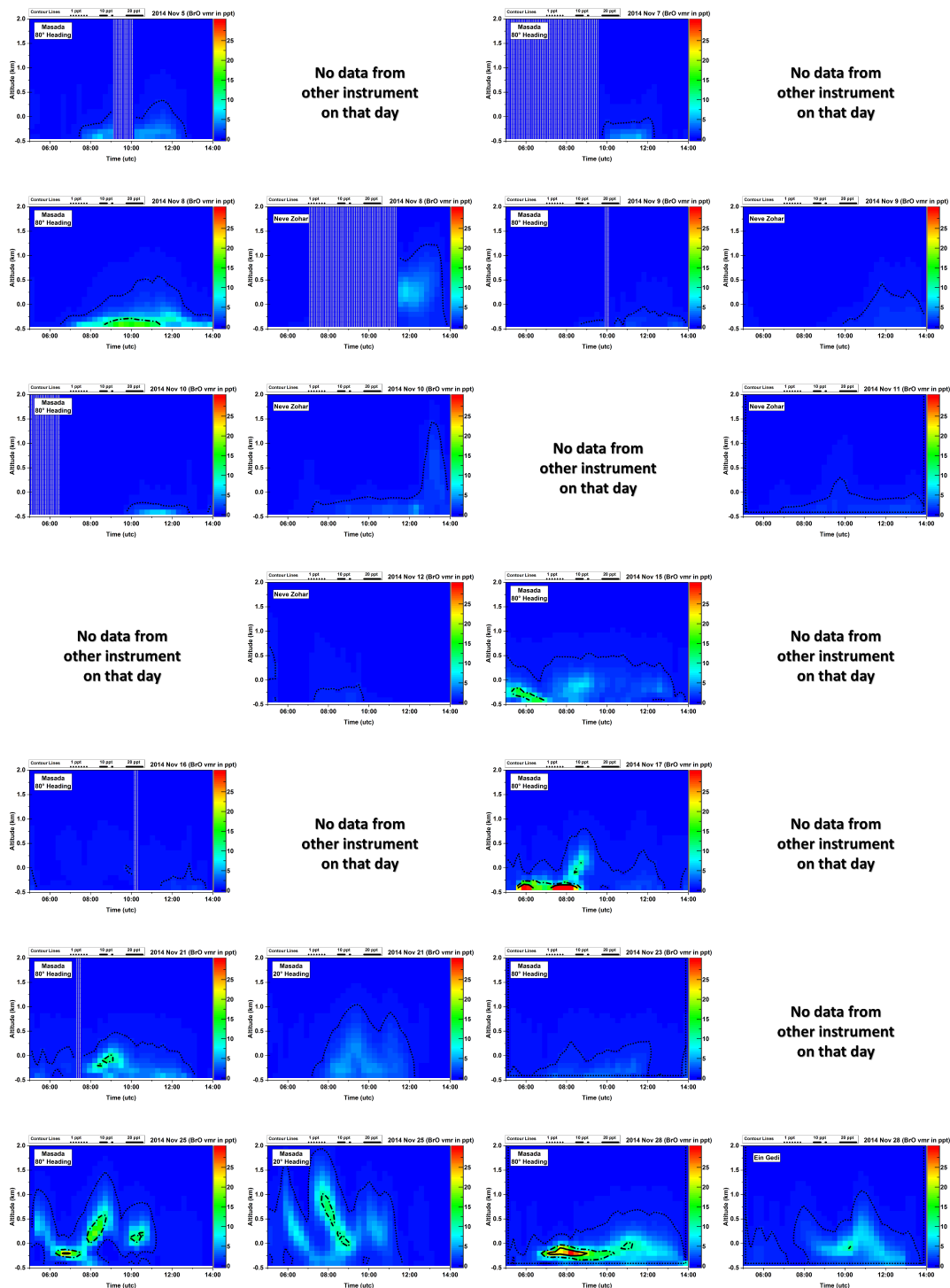
Fig. 9.11: Vertical profiles of BrO volume mixing ratios retrieved from the data of MAX-DOAS at Masada and the ISA MAX-DOAS (see plot label for details). Neighboring plots from first and second column as well as from third and forth column are from the same day. X-axis displays times from 05:00 to 14:00 UTC. Y-axis represents absolute altitude from -0.5 km to 2 km. Color code is from 0 to 30 pptv with contour lines at 1 pptv, 10 pptv and 20 pptv.

9.4 Iodine monoxide

Figure 9.12 shows the time series of days with IO surface mixing ratios and vertical column densities respectively. Only data of days with significant slant column densities were retrieved. Maximum mixing ratios of 1.3 pptv were observed on Nov. 5th and 18th at Masada and on Nov. 28th at Ein Gedi. At the evaporation ponds at Neve Zohar, surface IO barely exceeded 0.5 pptv.

Vertical profiles in figure 9.13 show IO of 0.5 pptv at elevated altitudes between 500 m and 2 km above ground. At other locations, IO is predominantly located near the surface with concentrations of 1 to 1.3 pptv.
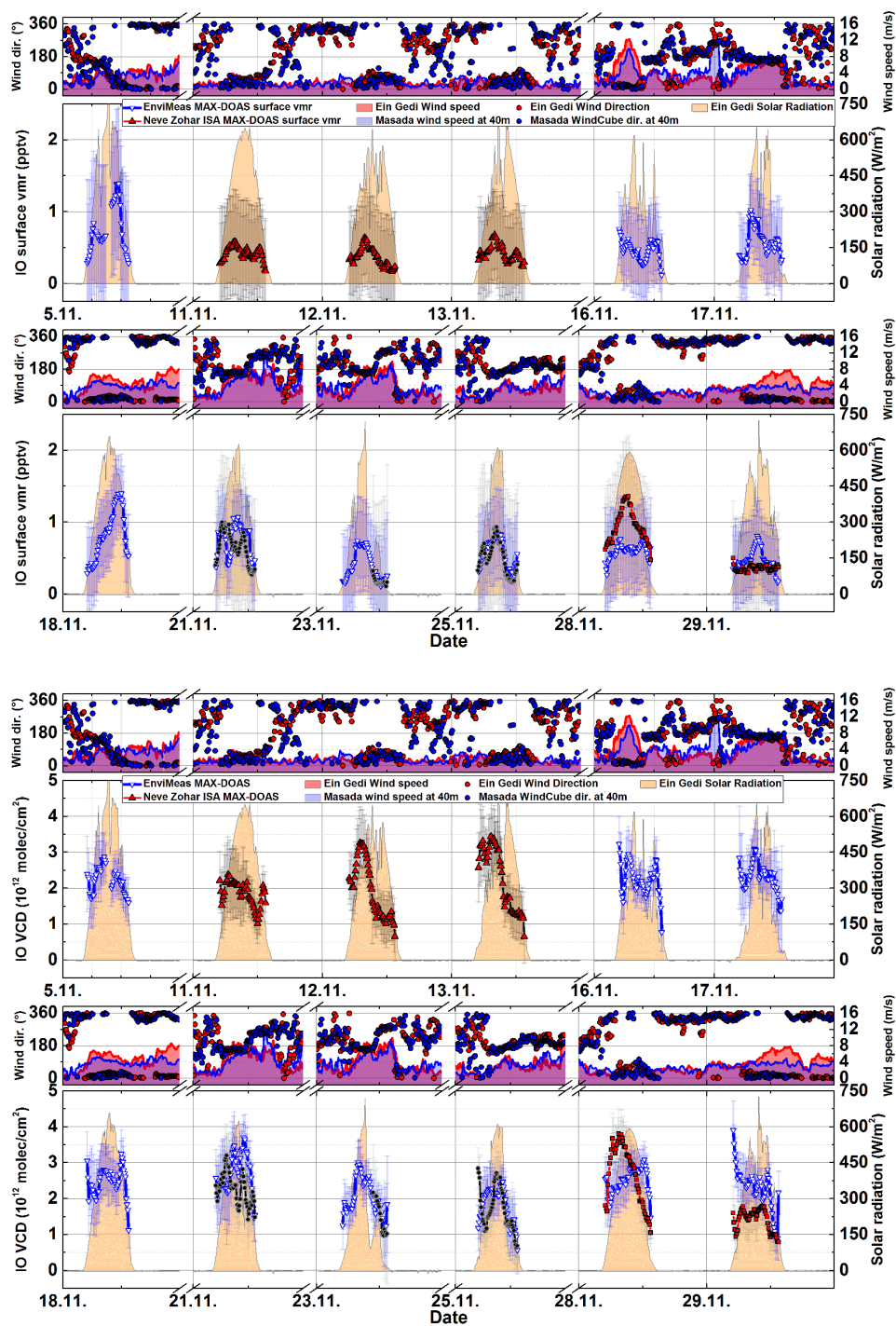
Fig. 9.12: Time series of IO surface mixing ratios and VCDs retrieved from MAX-DOAS data. Solar radiation (orange area), data of the ISA MAX-DOAS at Neve Zohar (red triangles), at Masada (black circles) and at Ein Gedi (red squares) as well as data of the EnviMeS MAX-DOAS at Masada (blue triangles) is shown. Plots above the IO time series show wind data from weather stations at Ein Gedi (red area and dots) and Masada (blue area and dots). Major ticks are at 00:00 UTC. Note the breaks in the y-axis to display the large range of IO vmrs. Errors are total retrieval errors.
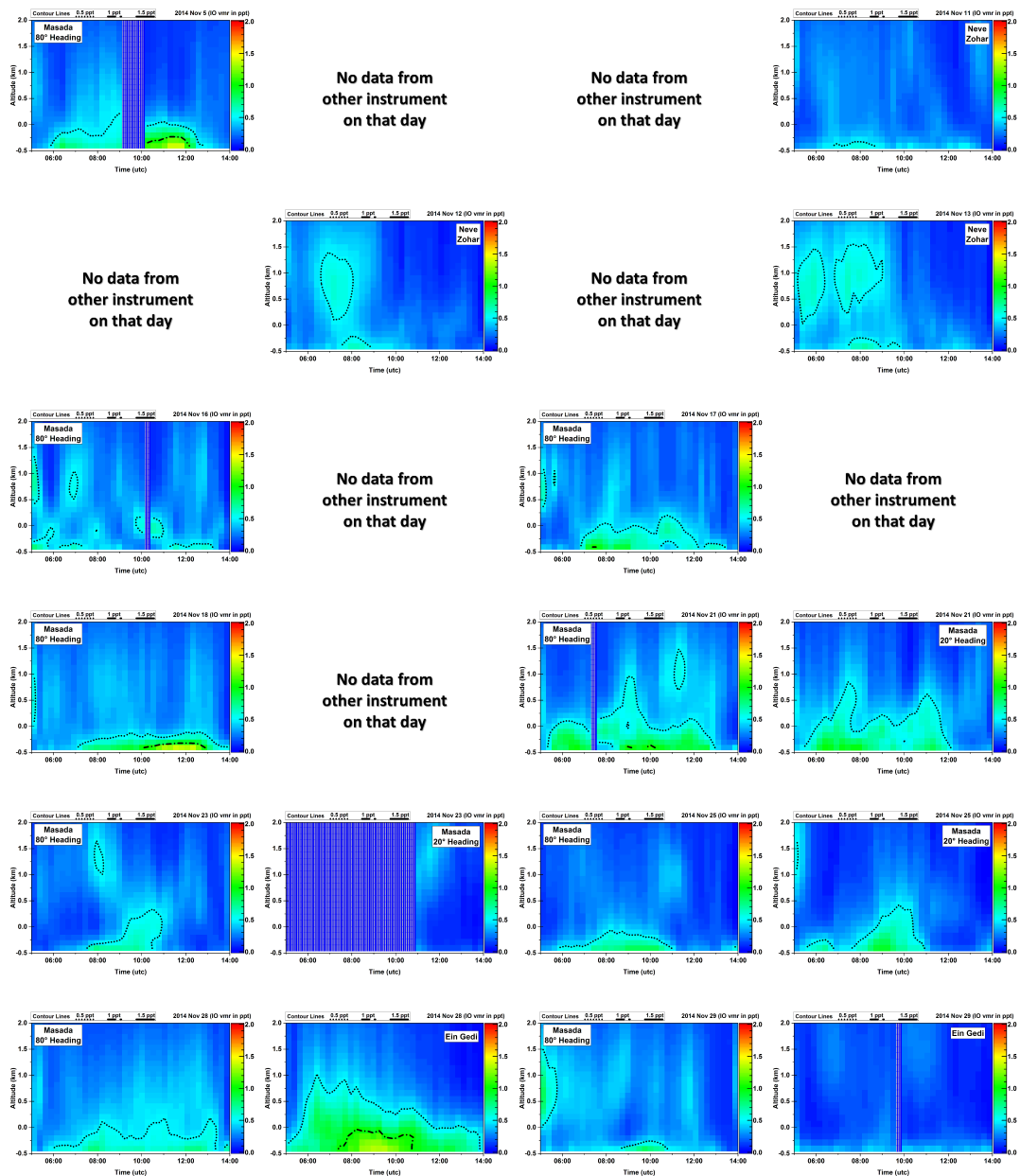
Fig. 9.13: Vertical profiles of IO volume mixing ratios retrieved from the data of MAX-DOAS at Masada and the ISA MAX-DOAS (see plot label for details). Neighboring plots from first and second column as well as from third and forth column are from the same day. X-axis displays times from 05:00 to 14:00 UTC. Y-axis represents absolute altitude from -0.5 km to 2 km. Color code is from 0 to 2 pptv with contour lines at 0.5 pptv, 1 pptv and 1.5 pptv.

9.5 Chlorine dioxide
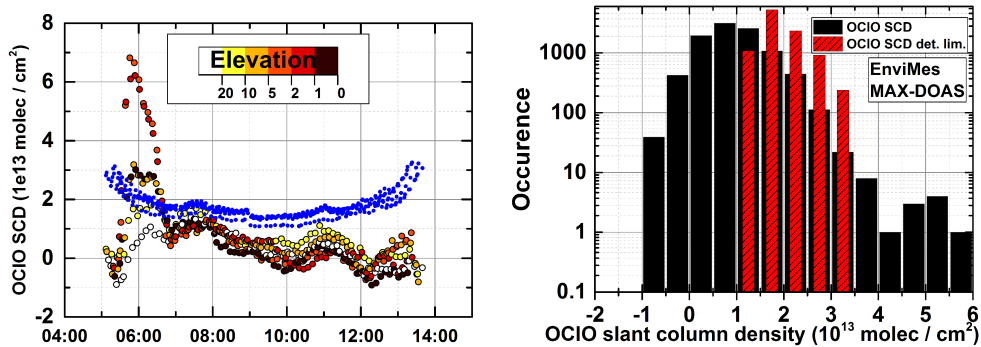
Fig. 9.14: **Left:** *OClO slant column densities measured by the MAX-DOAs at Masada on Nov. 17th 2014. Color represents elevation angle. Blue dots represent detection limit of four times fit error.* **Right:** *Histogram of all SCDs (black) and detection limits (red). For the sake of clarity, a logarithmic scale is chosen.*

Significant amounts of chlorine dioxide were detected by the Masada instrument on exclusively on Nov. 17th. Figure 9.14 shows the time series of measured slant column densities and detection limits from Nov. 17th and a histogram of all SCDs. A short rain event occurred between 05:00 and 06:00 UTC (see also extinction profiles and ceilometer data in figure 9.7). At 07:00 cloud passed and revealed mostly clear sky and, hence, increased solar radiation. Camera pictures in figure 9.15 illustrate the meteorological situation on that morning.

Fig. 9.15: Camera pictures taken between 04:00 and 09:00 UTC. Viewing direction same as MAX-DOAS instrument (east).

Figure 9.16 shows the time series of surface mixing ratios and vertical column density. OClO shows a strong increase at 05:30 UTC rising from below 1 pptv up to a peak value 6.5 pptv within twenty minutes followed by a decay over 90 minutes down to below 1 pptv. The vertical column densities shows a similar but smoother increase. The retrieved vertical profiles in figure 9.16, lower plot, indicate that OClO is distributed near the surface and tends to extend vertically within several minutes. The ISA MAX-DOAS instrument was deployed for mobile measurements on that day but no OClO could be detected.
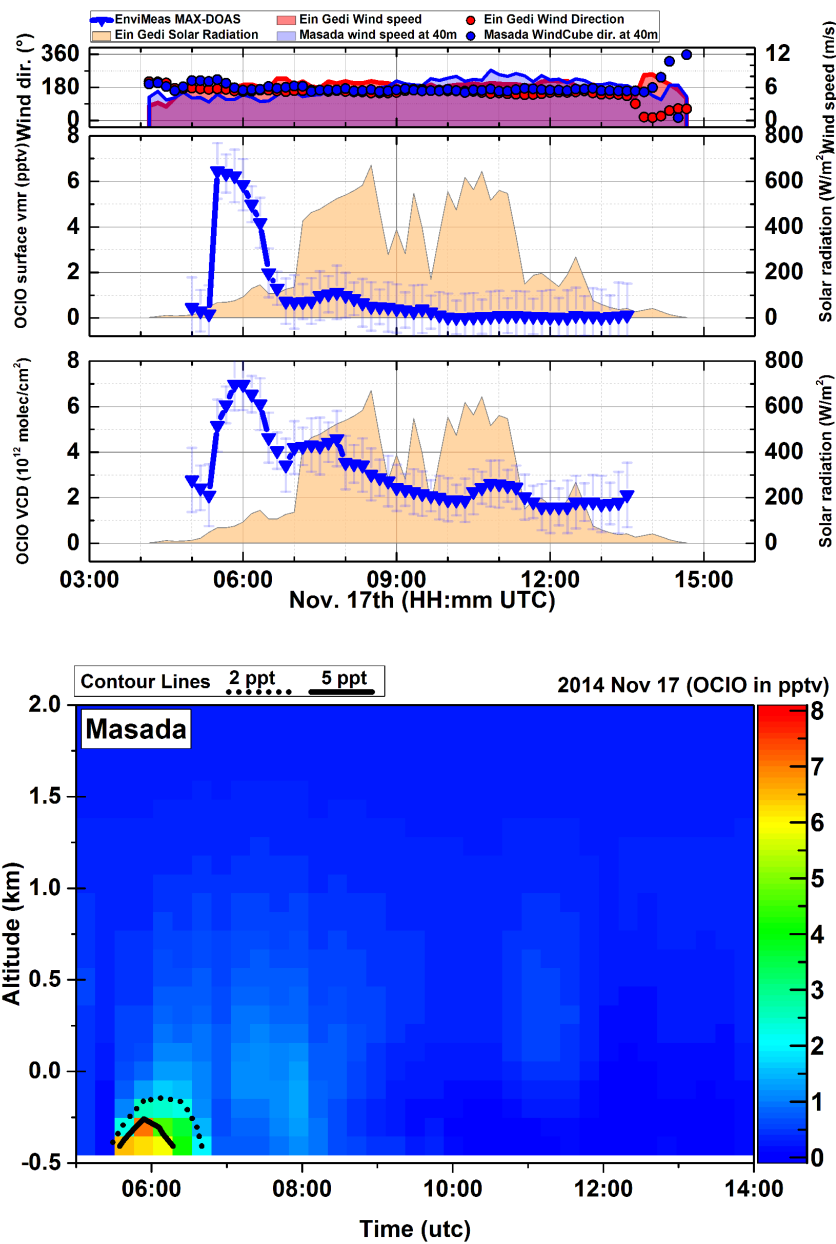
Fig. 9.16: Time series of surface mixing ratios and vertical column densities (top) and vertical profiles of OClO retrieved from MAX-DOAS data at Masada. Plots above the OClO time series show wind data from weather stations at Ein Gedi (red area and dots) and Masada (blue area and dots). Major ticks are at 00:00 UTC. Errors are total retrieval errors.

9.6 Nitrogen dioxide

Nitrogen dioxide (NO_2) was detected at surface mixing ratios in the range from below 100 pptv (e.g. Nov. 28th) up to 6 ppbv (Nov. 5th). Typical diurnal variations show a decay of NO_2 in the morning and a slight increase in the afternoon, whereas the dynamics at Neve Zohar Masada and Ein Gedi were similar. However, daily minimum values range from 100 pptv to 1 ppbv. For time series of surface mixing ratios and vertical column densities see figure 9.17. The discrepancy in the dynamics of surface volume mixing ratios and the vertical column densities can be explained by strong vertical gradients of NO_2 (see figure 9.19 and 9.20). On several days (e.g. Nov. 12th and 13th), the observed NO_2 distribution seems to be depleted from above towards the ground. At 12:00 UTC, apparently descending NO_2 is observed in higher altitudes. Yet other days show very low NO_2 over a wide range of altitude (e.g. Nov. 21th, 25th and 28th). Also profiles with a dominant maximum at 1 km above ground could be observed on Nov. 29th and 30th.
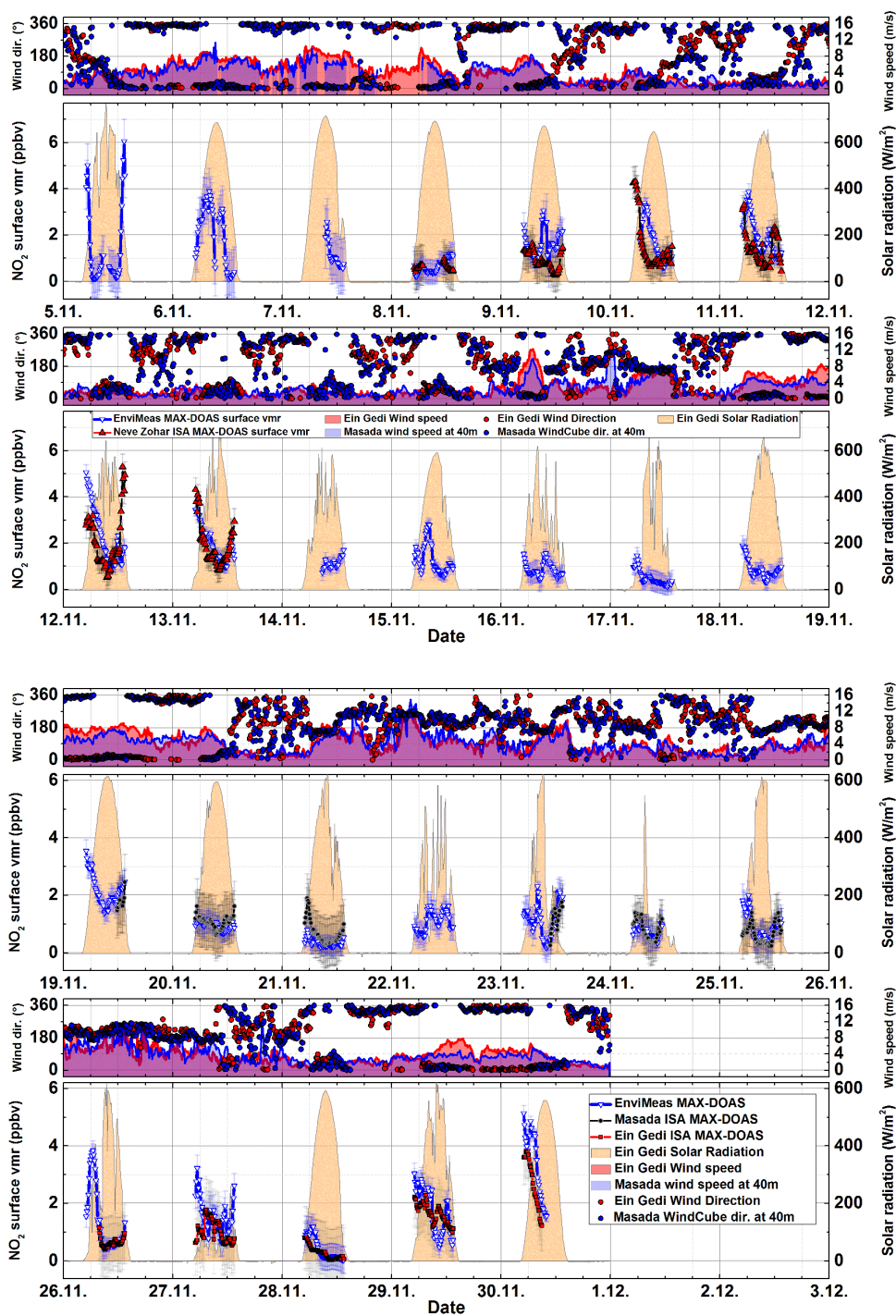
Fig. 9.17: Time series of NO$_2$ surface mixing ratios retrieved from MAX-DOAS data. Solar radiation (orange area), data of the ISA MAX-DOAS at Neve Zohar (red triangles), at Masada (black circles) and at Ein Gedi (red squares) as well as data of the EnviMeS MAX-DOAS at Masada (blue triangles) is shown. Plots above the NO$_2$ time series show wind data from weather stations at Ein Gedi (red area and dots) and Masada (blue area and dots). Major ticks are at 00:00 UTC. Errors are total retrieval errors.
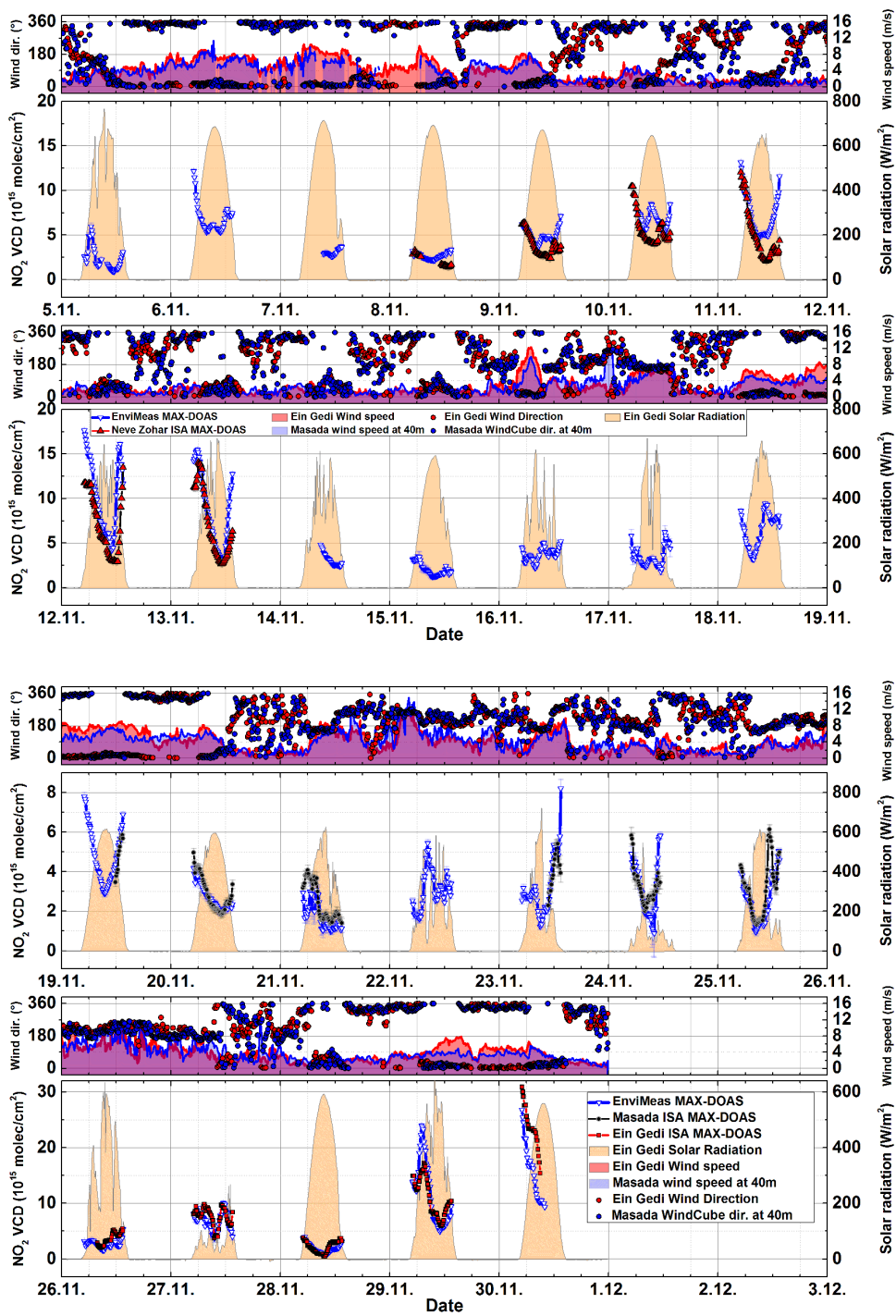
Fig. 9.18: Same as figure 9.17 but for VCDs.
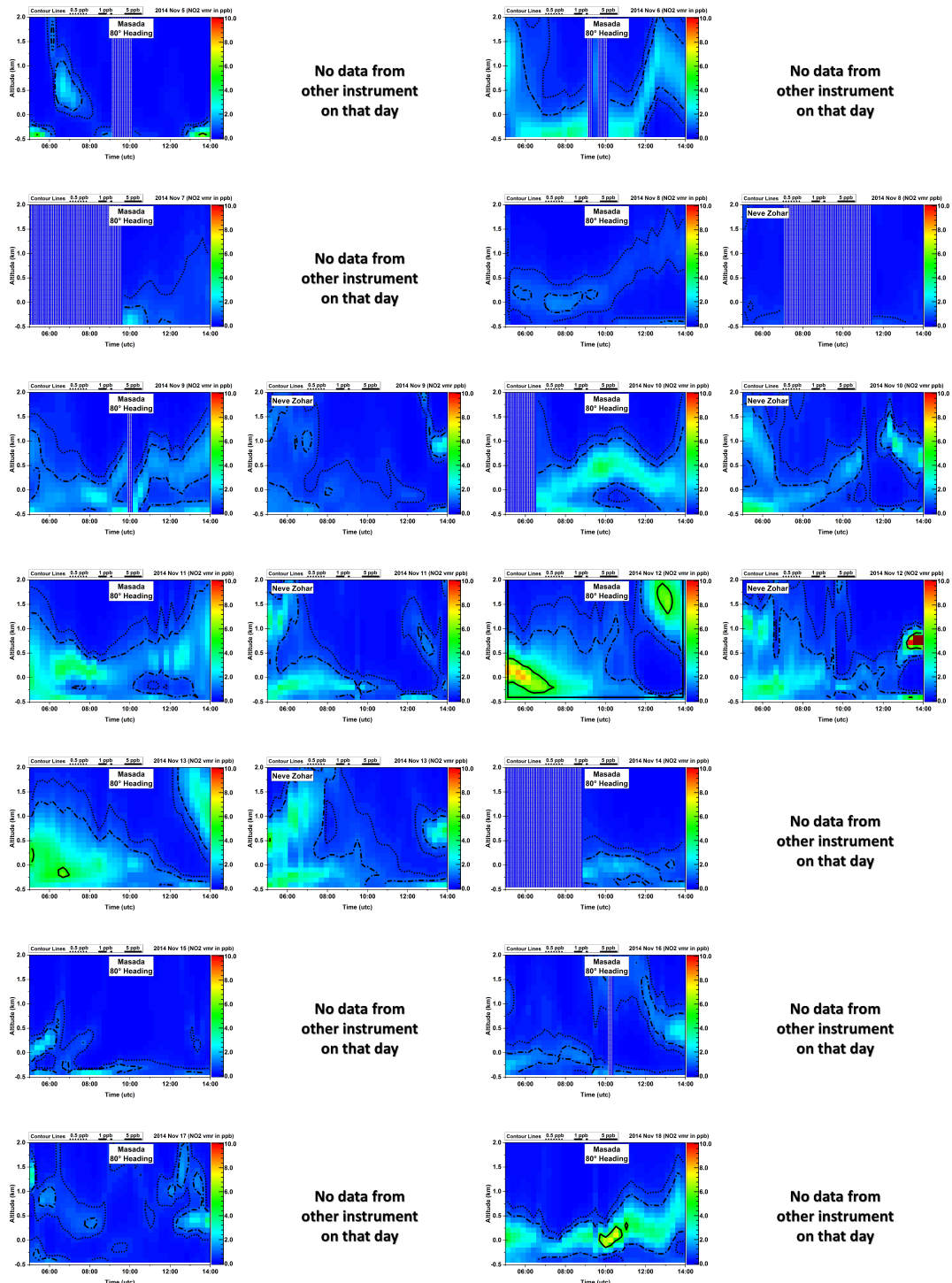
Fig. 9.19: Vertical profiles of NO₂ volume mixing ratios retrieved from the data of MAX-DOAS at Masada and the ISA MAX-DOAS (see plot label for details). Neighboring plots from first and second column as well as from third and forth column are from the same day. X-axis displays times from 05:00 to 14:00 UTC. Y-axis represents absolute altitude from -0.5 km to 2 km. Color code is from 0 to 10 ppbv with contour lines at 0.5 ppbv, 1 ppbv and 5 ppbv.
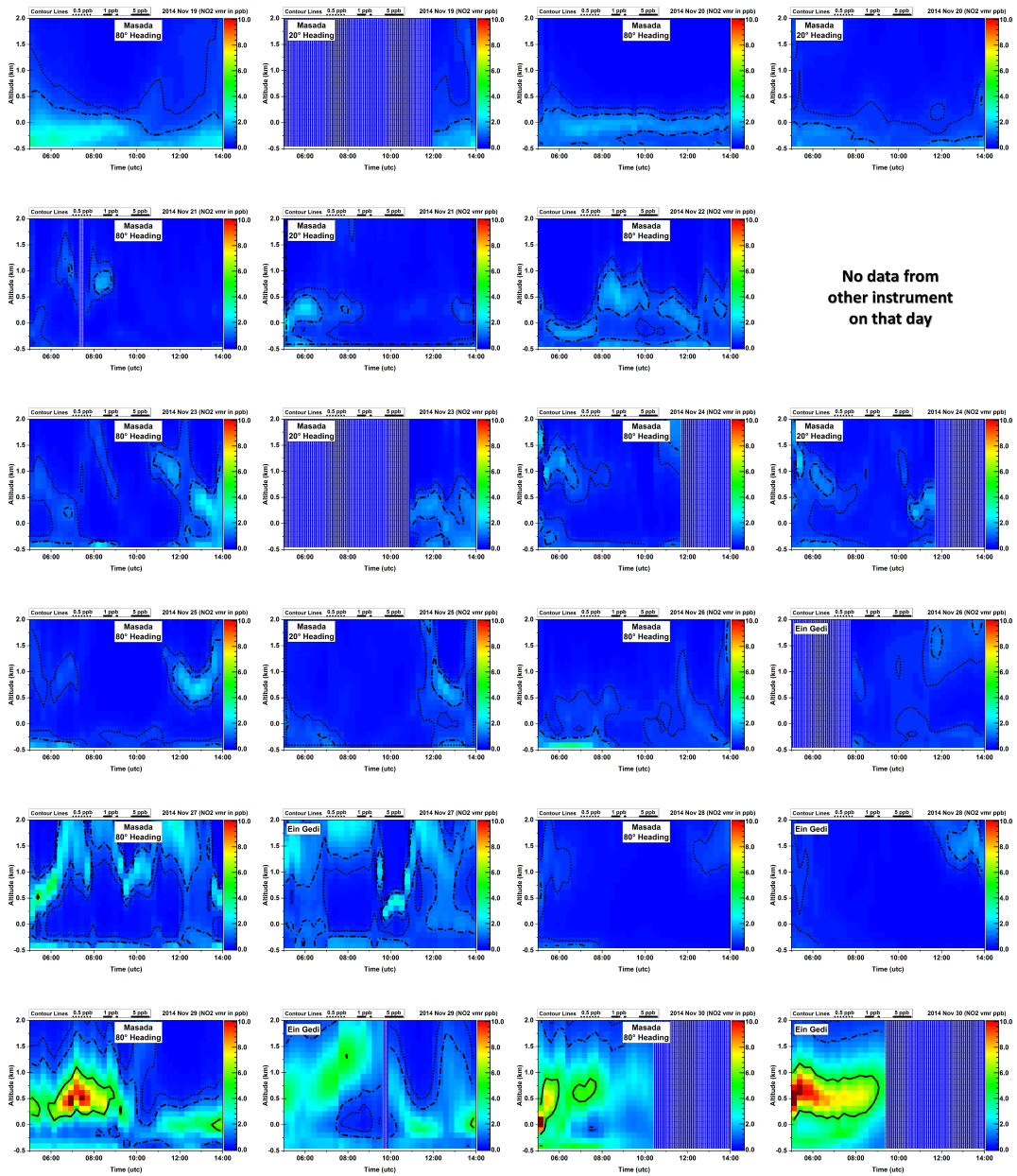
Fig. 9.20: Same as figure 9.19 but for subsequent days.

9.7 Nitrous acid

Nitrous acid (HONO) could only be detected on the days of Nov. 11th, 12th and 13th with the instrument at Masada. Typical mixing ratios were 120 pptv to 200 pptv after sunrise followed by a decrease of approximately 15 pptv/h towards sunset. Figure 9.21 shows time series of surface mixing ratios and vertical column densities while figure 9.22 shows the retrieved vertical profiles. HONO is predominantly located near the surface which explains the similar dynamics of surface mixing ratios and VCDs. Besides the slightly larger total amount of HONO, the vertical extend is also larger in Nov. 12th and 13th compared to Nov. 11th. This might be caused by the cloud coverage which was higher on 12th and 13th than on 11th.
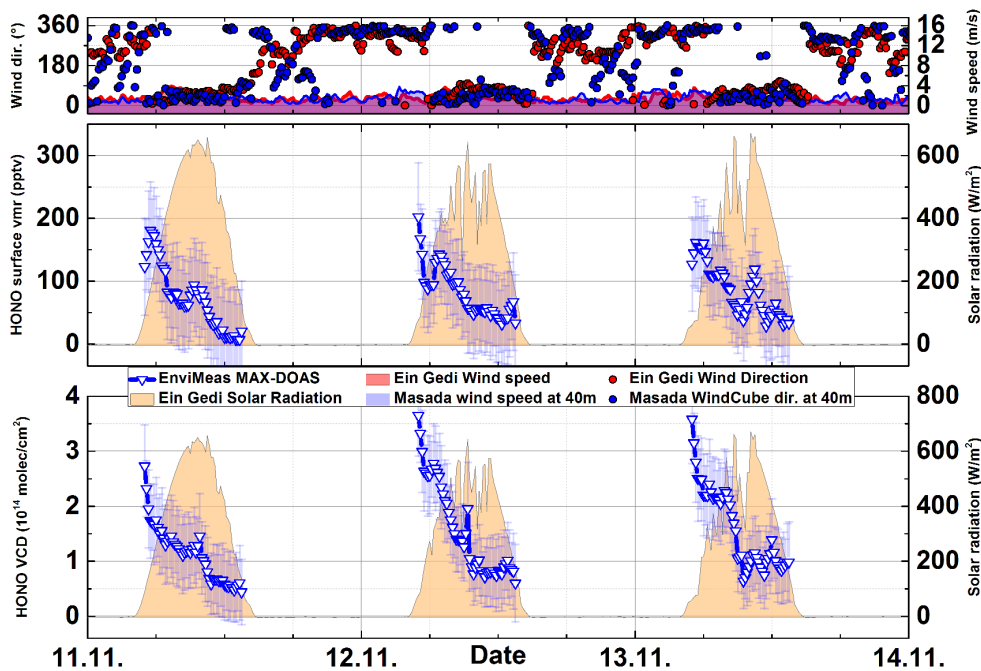
Fig. 9.21: Time series of significant HONO surface mixing ratios and vertical column densities retrieved from MAX-DOAS data at Masada. Plots above the HONO time series show wind data from weather stations at Ein Gedi (red area and dots) and Masada (blue area and dots). Major ticks are at 00:00 UTC. Errors are total retrieval errors.
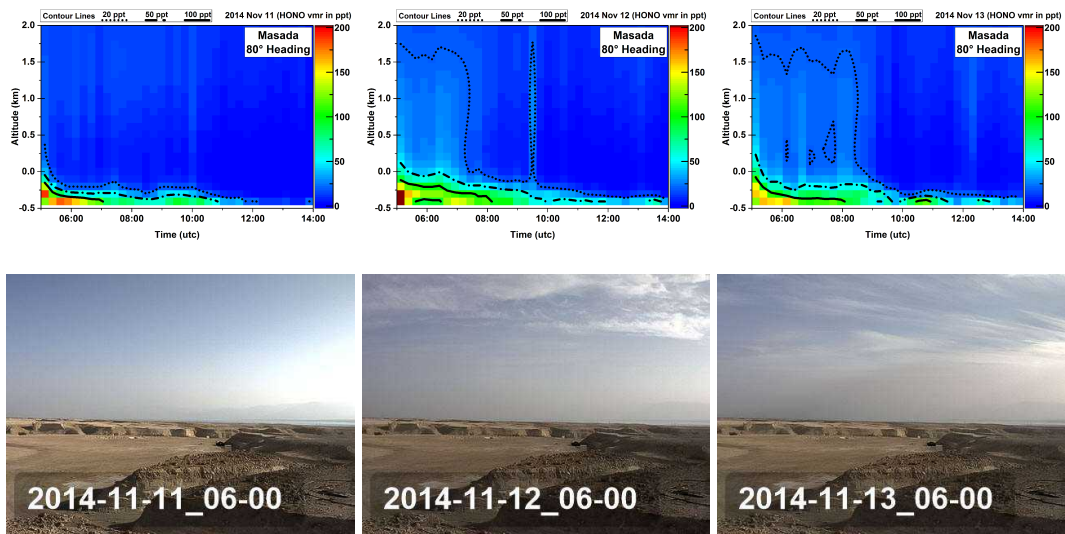
Fig. 9.22: **Top:** *Vertical profiles of HONO volume mixing ratios retrieved from the data of MAX-DOAS at Masada. X-axis displays times from 05:00 to 14:00 UTC. Y-axis represents absolute altitude from -0.5 km to 2 km. Color code is from 0 to 200 pptv with contour lines at 20 pptv, 50 pptv and 100 pptv.* **Bottom:** *Camera pictures of the corresponding days taken on 06:00 UTC each.*

9.8 Formaldehyde

Significant amounts of formaldehyde (HCHO) were detected by all MAX-DOAS instruments on every day of the measurement period with surface mixing ratios ranging from 1 ppbv and 6 ppbv (see figure 9.23). Further, the time series of VCDs in figure 9.23 shows a comprehensive trend of the total amount of HCHO. From Nov. 5th to 15th, a day by day increase in HCHO is observed, where the vertical column density increased by a factor of two with in ten days. On the subsequent days, HCHO decreased again until Nov 17th followed again by several days of increase and decrease of HCHO. The meteorologic data give the impression that HCHO increases are correlated with northerly winds while decreases prevail during southerly winds. Yet, this has to be discussed.

Figure 9.25 shows vertical profiles of HCHO mixing ratios. On days with lower HCHO abundances, the profiles show confined layers of HCHO with minimum at altitudes between surface to -200 m and 0 m absolute altitude. On days where relative large HCHO amounts are observed, the vertical profile is either homogeneously with an extension up to 1.5 km absolute altitude, or with an distinct maximum at 0 m to 500 m absolute altitude (e.g. Nov 13th).
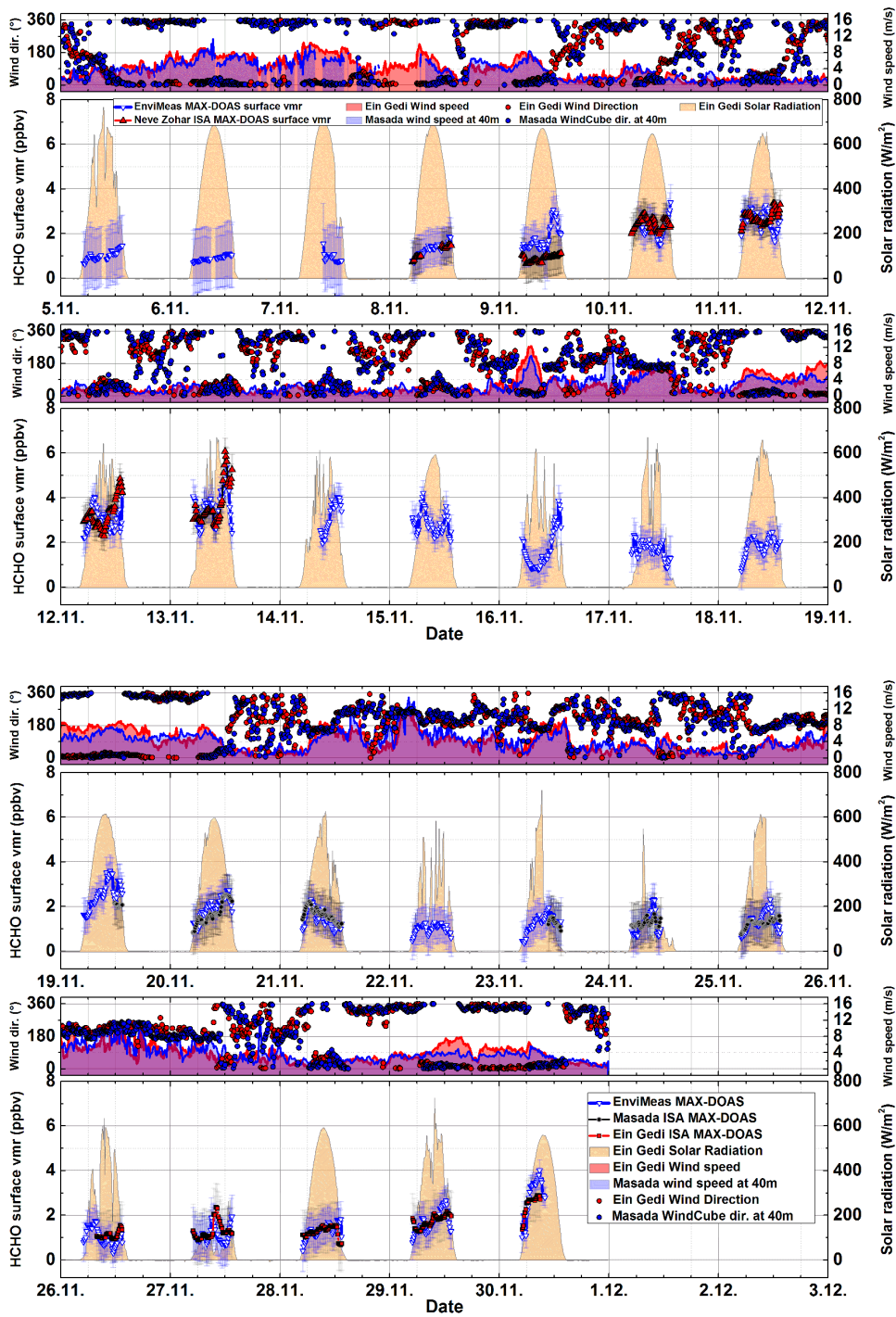
Fig. 9.23: Time series of HCHO surface mixing ratios retrieved from MAX-DOAS data. Solar radiation (orange area), data of the ISA MAX-DOAS at Neve Zohar (red triangles), at Masada (black circles) and at Ein Gedi (red squares) as well as data of the EnviMeS MAX-DOAS at Masada (blue triangles) is shown. Plots above the HCHO time series show wind data from weather stations at Ein Gedi (red area and dots) and Masada (blue area and dots). Major ticks are at 00:00 UTC. Errors are total retrieval errors.
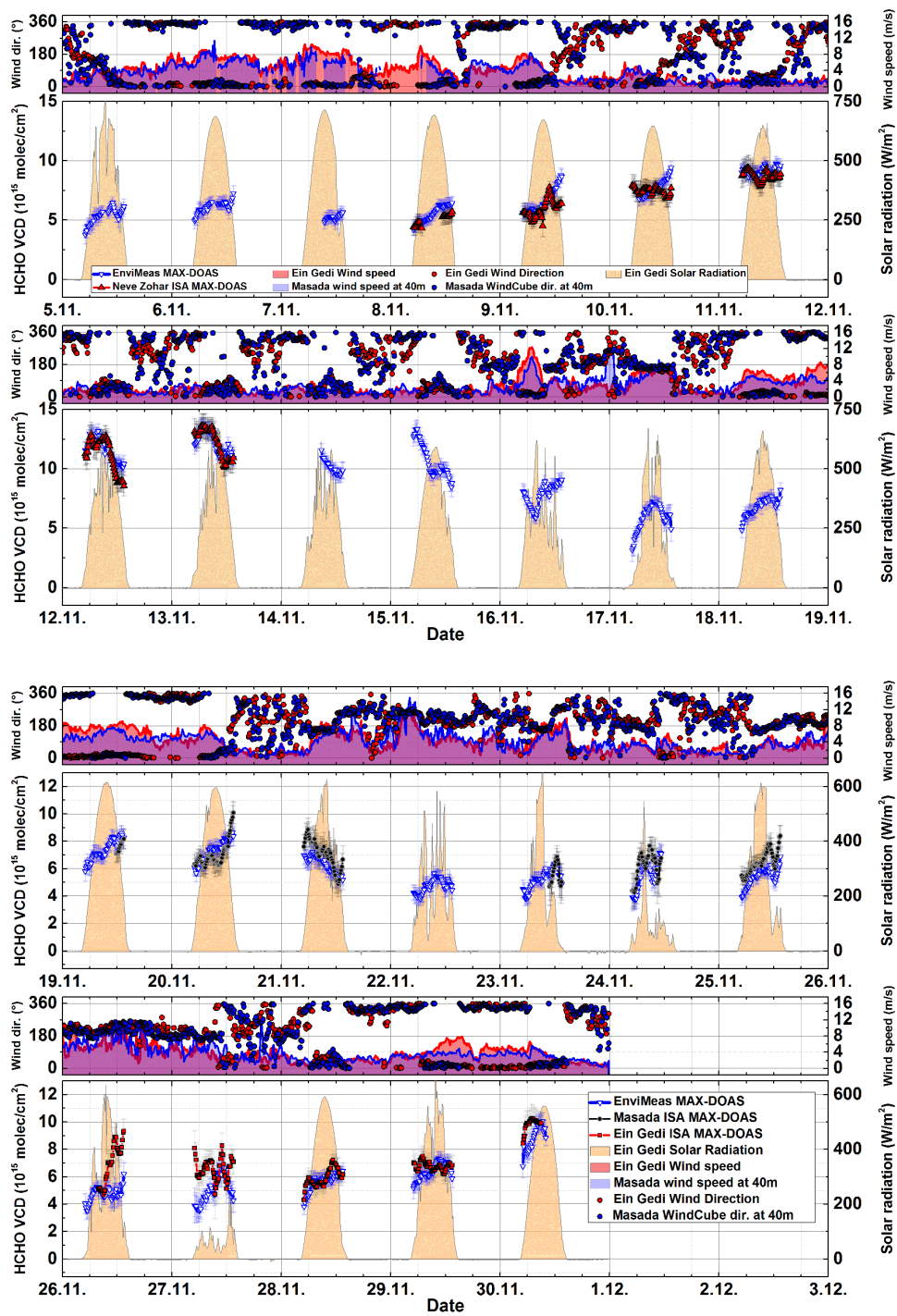
Fig. 9.24: Same as figure 9.23 but for VCDs.
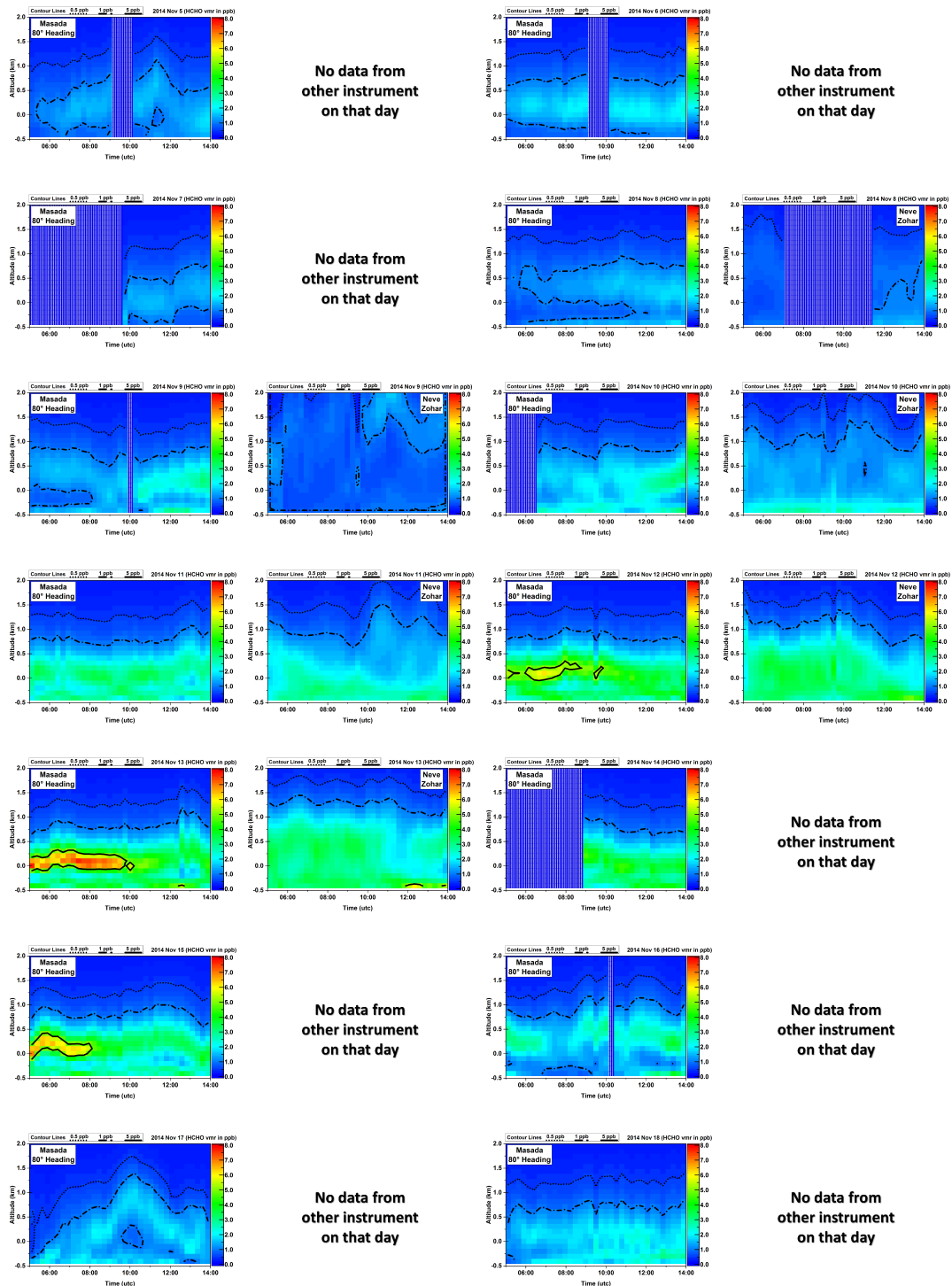
Fig. 9.25: Vertical profiles of HCHO volume mixing ratios retrieved from the data of MAX-DOAS at Masada and the ISA MAX-DOAS (see plot label for details). Neighboring plots from first and second column as well as from third and forth column are from the same day. X-axis displays times from 05:00 to 14:00 UTC. Y-axis represents absolute altitude from -0.5 km to 2 km. Color code is from 0 to 8 ppbv with contour lines at 0.5 ppbv, 1 ppbv and 5 ppbv.
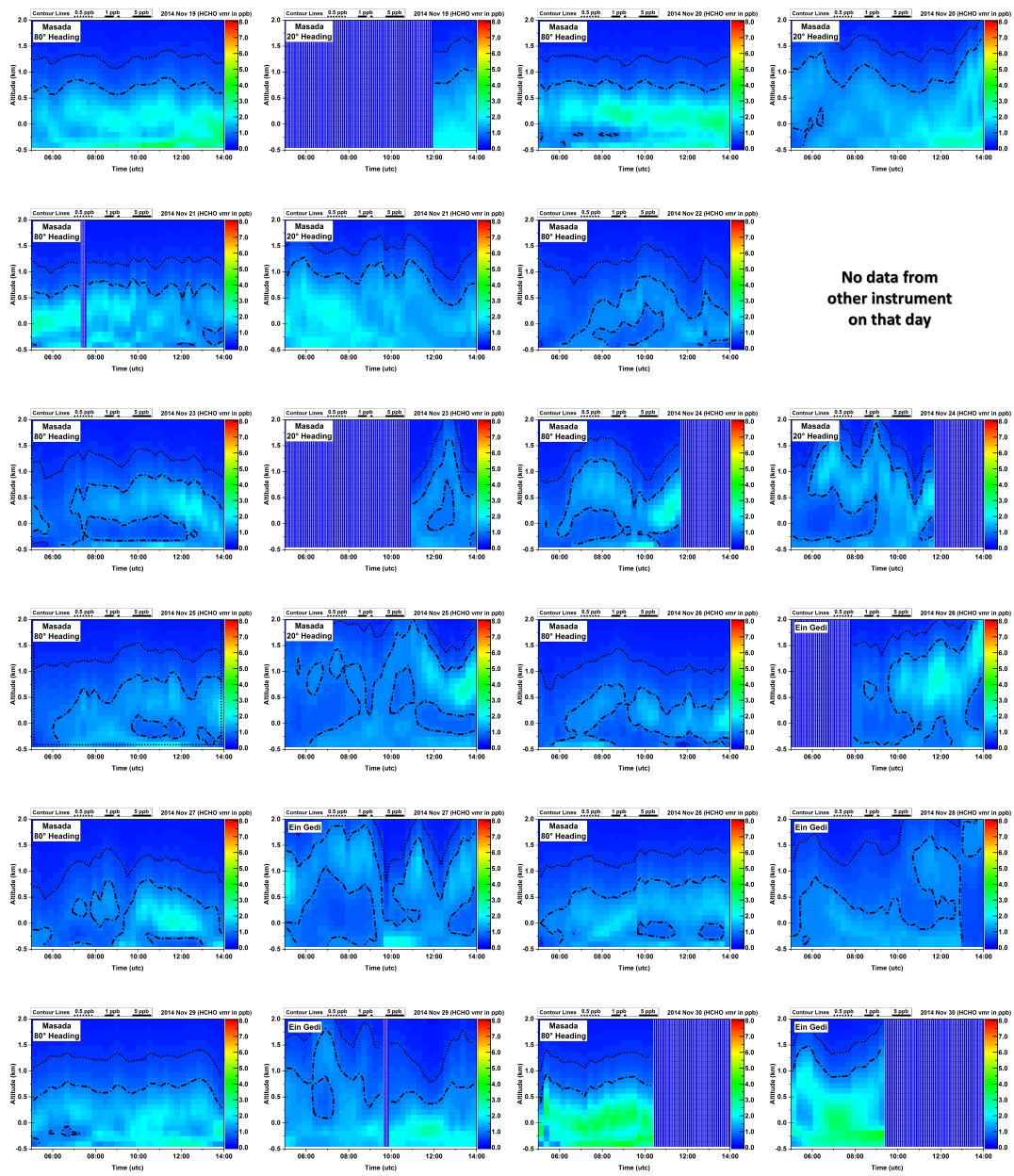
Fig. 9.26: Same as figure 9.25 but for subsequent days.

9.9 Glyoxal

Significant mixing ratios of glyoxal were observed on several days of the measurement campaign. Surface mixing ratios and vertical column densities ranged from 0 pptv to 200 pptv and from 0 to 10^{14} molec/cm^2. The diurnal variation of the VCDs has a slight decrease on most days. Further, strong peaks in mixing ratios and VCDs are occasionally observed during sunrise. Figure 9.27 shows the corresponding time series. Only days with significant data are shown.

The vertical profiles in figure 9.28 illustrate, that on some days, the dominant part of glyoxal is located in altitudes of several hundred meters above the ground. So surface mixing ratios may underestimate the total amount (i.e. on Nov. 12th and 13th). However, on several other days, the vertical extend of glyoxal in homogeneously distributed from the ground level up to 1 km absolute altitude (approximately 1.5 km above ground level). The strong peaks in mixing ratio and VCD after sunrise can be addressed to different altitudes between ground level and 1.5 km absolute altitude.
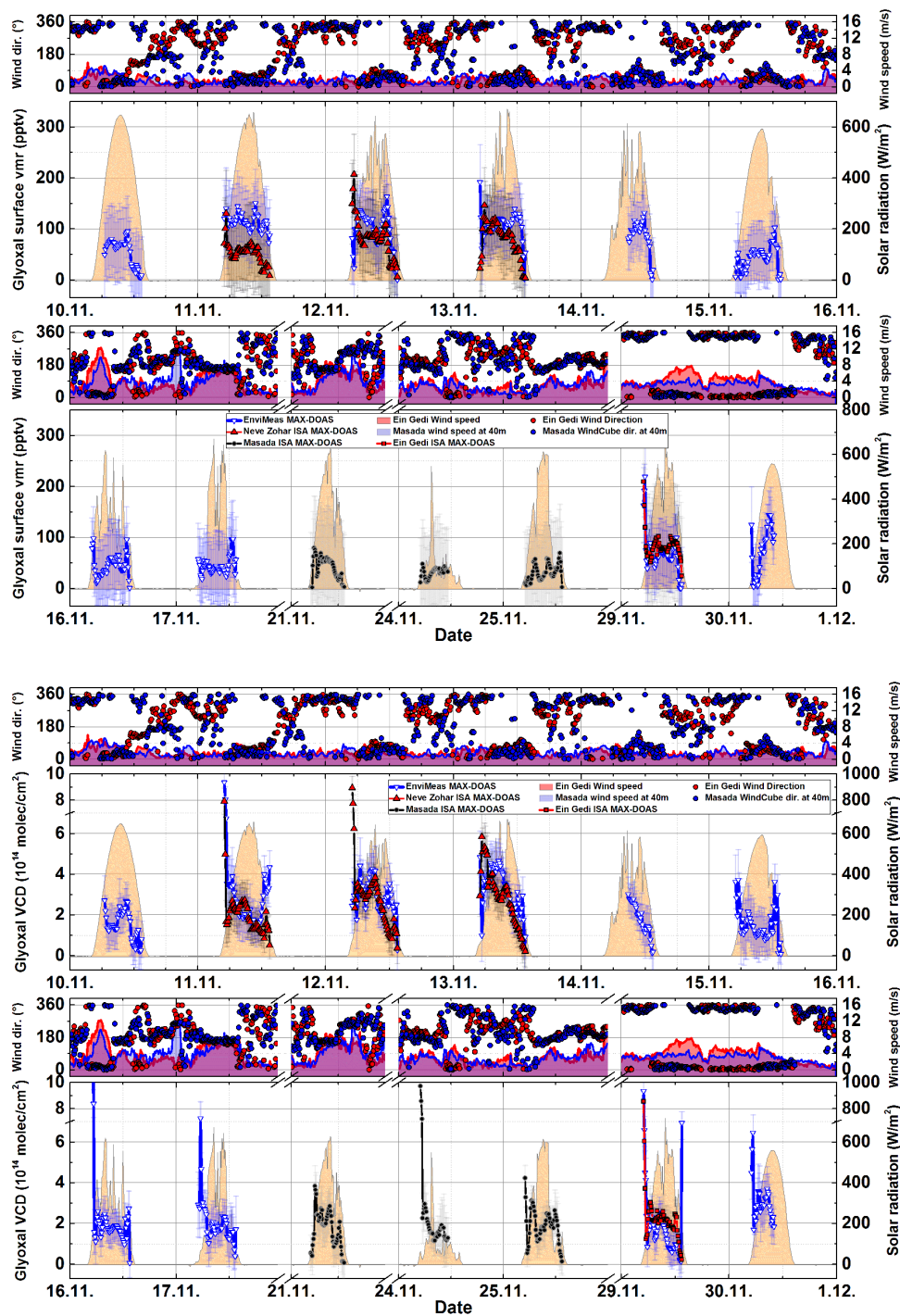
Fig. 9.27: Time series of Glyoxal surface mixing ratios and VCDs retrieved from MAX-DOAS data. Solar radiation (orange area), data of the ISA MAX-DOAS at Neve Zohar (red triangles), at Masada (black circles) and at Ein Gedi (red squares) as well as data of the EnviMeS MAX-DOAS at Masada (blue triangles) is shown. Plots above the Glyoxal time series show wind data from weather stations at Ein Gedi (red area and dots) and Masada (blue area and dots). Major ticks are at 00:00 UTC. Note the breaks in the y-axis to display the large range of Glyoxal vmrs. Errors are total retrieval errors.
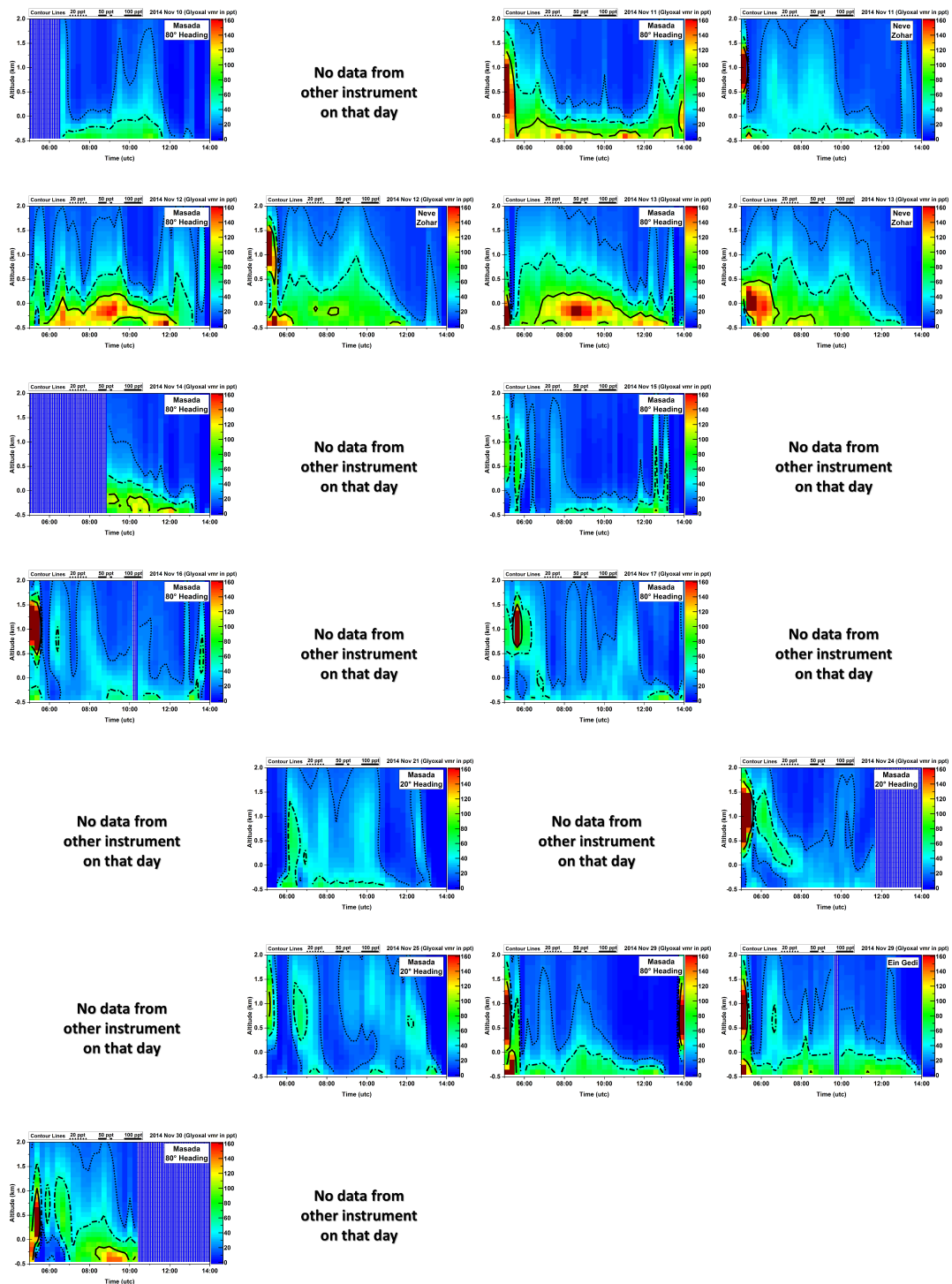
Fig. 9.28: Vertical profiles of Glyoxal volume mixing ratios retrieved from the data of MAX-DOAS at Masada and the ISA MAX-DOAS (see plot label for details). Neighboring plots from first and second column as well as from third and forth column are from the same day. X-axis displays times from 05:00 to 14:00 UTC. Y-axis represents absolute altitude from -0.5 km to 2 km. Color code is from 0 to 160 pptv with contour lines at 20 pptv, 50 pptv and 100 pptv.

Part IV

Synthesis

10

Discussion

10.1 Meteorology

In May 2012, significantly different wind scenarios during daytime and nighttime were observed. At daytime easterly winds at Masada are often accompanied with westerly winds at Ein Bokek. At northerly or southerly winds, usually at higher wind speeds and during nighttime, the two stations observe the same wind direction which indicates a coupled scenario. On May 5th 2012, a change between those two scenarios was observed and is described in detail in the following. This day is chosen, because data of both weather stations was available. The characteristic of this exemplary day is frequently observed by the Masada station throughout the time period of the campaign. Hence, it can be assumed that the meteorological processes can be transferred to other days, although data from the second station at Ein Bokek is missing.

Figure 10.1 shows data from May 5. Between 06:00 UTC and 12:00 UTC, the wind directions at the two stations are nearly contrary. The northern station at Masada measures wind blowing from eastern direction. This can be attributed to sea breeze since the station is located at an western shore line (see map in figure 6.1). At Ein Bokek, wind from south-westerly direction is observed. This may also be caused by local sea breeze, induced by the large land mass separating the two basins in the north-east of the weather station.
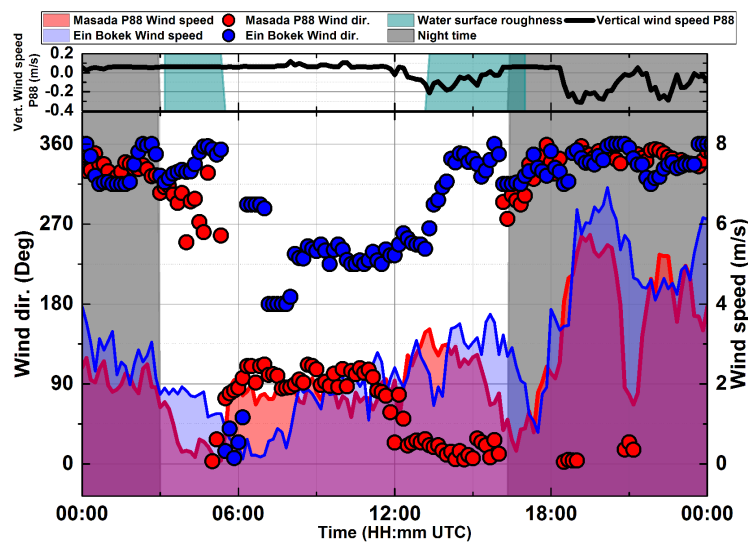
Fig. 10.1: Wind and water surface roughness (WSR) data from May 5th 2012.

At 11:00 UTC a change in wind directions from east to north occurred at Masada. With a current wind speed of about 2 m/s the Ein Bokek weather station observed a change in wind directions from west to north is observed at 13:00 UTC. The distance between the stations is approximately 15 km. This suggests that the air mass which is causing a change in wind direction at Masada reaches the other weather station 2 hours later also causing the wind direction to change to north. This particular example will be important for the interpretation of the observed trace gas dynamics on that day. The dynamics of the measured trace gases (see below) indicate that the northerly wind which is usually observed in the afternoon is most likely "purging" the valley of the Dead Sea.

Given the results from the data of the two measurement campaigns, the meteorology can be described by two main scenarios. Due to their impact on the observed trace gas dynamics, these scenarios are defined as "Enrichment" and "Purging" scenario which are illustrated in figure 10.2:

Wind scenario 1 ("Enrichment scenario")

- Contrary wind directions at Masada and Ein Bokek.

- Possible, but not necessarily local sea breeze scenarios.

- Low wind speeds of 1 to 3m/s.

Wind scenario 2 ("Purging scenario")

- Similar wind directions at Masada and Ein Bokek.

- Northerly or southerly wind direction.

- High wind speeds above 4 m/s.

- Usually, but not necessarily during night time.

The contrary winds, observed during the enrichment scenario indicate a vertical vortexes system (indicated in figure 10.2, top) which may cause air masses to be transported up at the side slopes of the valley and to re-enter from above. In other words, this would cause a reduction in air mass exchange between the Dead Sea valley and its surrounding.

While in May 2012 daytime wind speeds were usually low (1 to 3 m/s) with prevailing sea breeze scenarios, much stronger daytime wind speeds of 4 to 12 m/s were regularly observed in November 2014. Also, in contrast to 2012, the dominating daytime wind directions in 2014 were north and south. Given the two wind scenarios discussed above, one can assume that in Nov. 2014, the Dead Sea Valley is regularly flushed during daytime and thus air masses from the surrounding area are transported into the valley. As a result the halogen chemistry might be affected by enhanced dilution and/or an increased amount of chemical sinks (e.g. nitrogen dioxide, dust). The flushing of the valley during nighttime was observed during both campaigns.
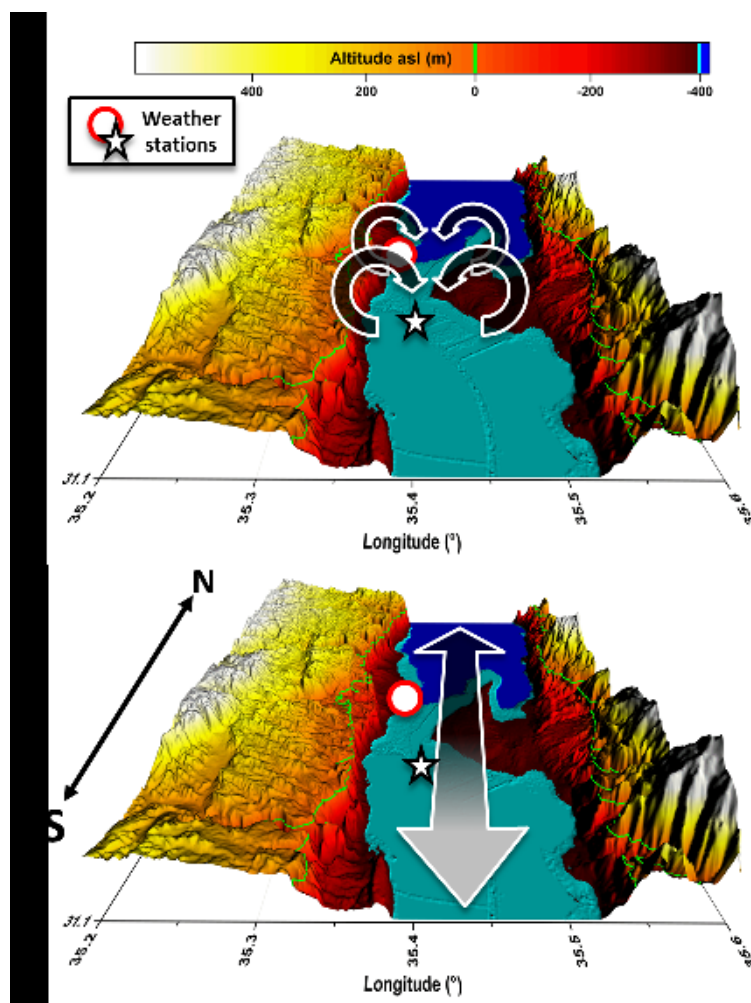
Fig. 10.2: Illustration of the two main wind scenarios. **Top:** Enrichment scenario. Easterly and westerly winds are observed at the weather stations. **Bottom:** Purging scenario. Both weather stations observe the same wind direction at increased wind speed. Data adapted from Shuttle Radar Topographic Mission (SRTM), Jarvis et al. [2008].

Solar radiation has a strong potential impact on the abundance of reactive halogen species by the photolysis of its precursors. Figure 10.3 shows histograms of solar radiation measured during both campaigns. As already mentioned in the results section, most days during the 2012 campaign were cloud free while in Nov. 2014, several days had strong cloud coverage. Together with the lower sun

elevation caused by winter season, the overall solar radiation at the Dead Sea valley was significantly lower than in May 2012. Additionally, the diurnal variation of observed solar radiation was influenced by clouds which caused fast changes within several minutes. This has to be considered for the total abundance as well as the dynamic of observed trace gases in May 2012 and Nov. 2014.
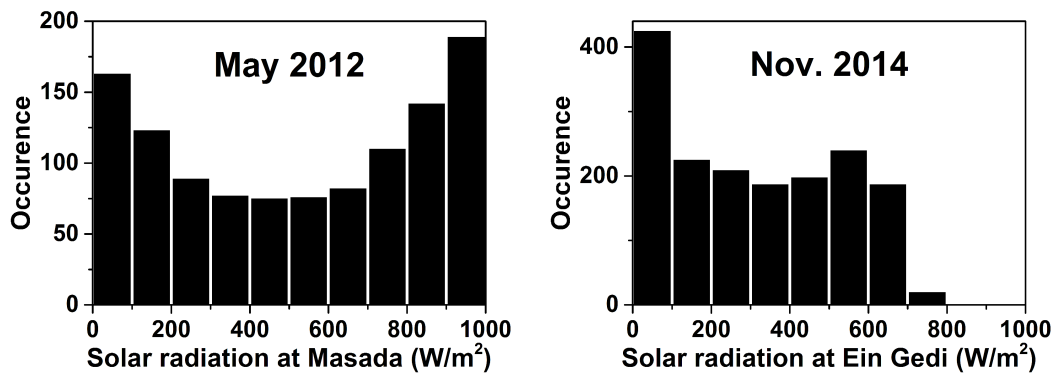
Fig. 10.3: Histograms of solar radiation measured by the weather stations at Masada in May 2012 and Ein Gedi in Nov. 2014.

One can conclude, that during May 2012, the intake of air masses from the surrounding of the valley is reduced during daytime. In Nov. 2014, the atmosphere above the Dead Sea is most likely influenced by air masses which are transported into the valley during daytime as well as during nighttime. Further, in 2014, solar radiation was reduced compared to 2012 due to winter season and cloud coverage.

10.2 Bromine monoxide

The data sets from both campaigns provide different information concerning the observed dynamics of BrO. In 2012, cloud coverage was sparse and solar radiation was similar for each day coming along with significant BrO abundance. Since wind speed and wind directions were very dynamic it was possible to assign dynamics of BrO to different wind scenarios and, hence, gain insight about horizontal and vertical transport processes.

In contrast to 2012, a dynamic cloud coverage in November 2014 lead to very dynamic solar radiation. The wind conditions stayed mostly constant throughout the day and a change between purging and sea breeze wind scenario was rarely observed. Thus, the data is suitable to study the impact of changing solar radiation while other meteorological conditions stay constant.

Figure 10.4 shows histograms of BrO VCDs measured during the campaigns in 2012 and 2014. Further, a brief description of the location of the corresponding instrument is given in the plots. In May 2012 BrO VCDs of up to 11 and $14 \cdot 10^{13}$ molec/cm^2 were observed at Masada and Ein Bokek, respectively. In November 2014, BrO abundance was about a factor of 6 lower with peak VCDs of $3 \cdot 10^{13}$ molec/cm^2 at Masada. On other locations, peak VCDs were around $1.5 \cdot 10^{13}$ molec/cm^2, although being less representative due short measurement periods. It is noticeable that during both campaigns, BrO seems to be more abundant at Masada compared to measurements over the water surface of the northern, natural Dead Sea basin and the southern evaporation ponds, which is an indication for another source of BrO besides the water surface itself.
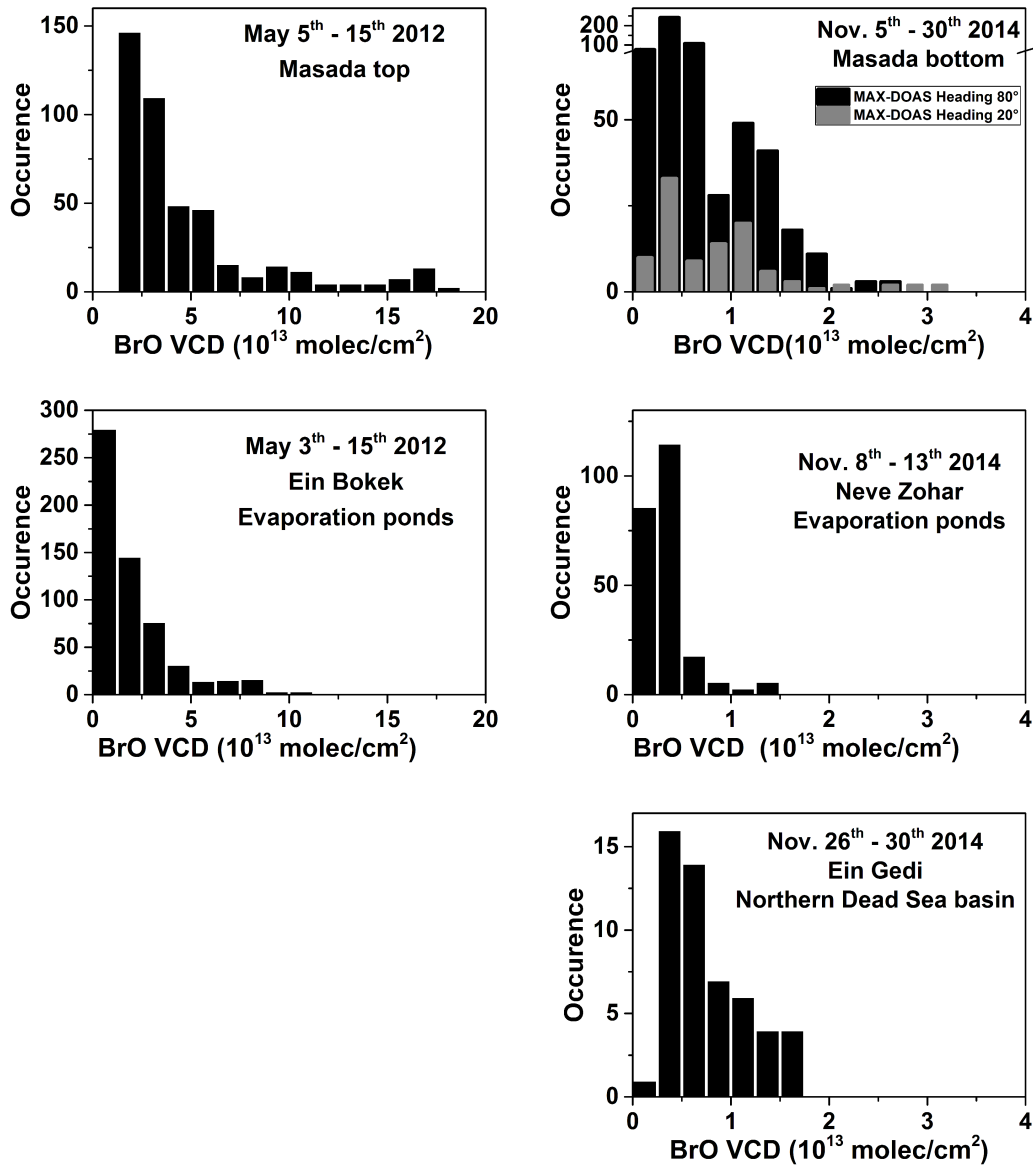
Fig. 10.4: Histograms of BrO VCDs measured during May 2012 and Nov. 2014 at different locations. In 2014 two instruments with different headings measured parallel at Masada for several days, indicated by black and grey bars. Note the different x-axis scales for 2012 and 2014.

10.2.1 Impact of meteorologic transport on observed BrO

The MAX-DOAS at Masada measured significantly larger surface mixing ratios of up to 180 pptv. The peak vmrs at Masada do not necessary coincide with peak values at Ein Bokek indicating a difference of BrO abundance between the two locations and hence, over the land mass between the northern and southern basin and the evaporation ponds at Ein Bokek. Since the influence of vertical dynamics on VCDs is weak, they provide a suitable indicator for the total abundance of a trace gas species within the Dead Sea Valley. Wind roses of BrO vertical column densities at Masada and Ein Bokek are shown in figure 10.5.

The wind roses show that at Masada, the highest BrO VCDs are observed during eastern winds which can be attributed to low wind speeds at sea breeze and thus a possibly reduced exchange in air masses between the valley and its surrounding (compare to "Enrichment Scenario", see section 10.1). When comparing the Ein Bokek VCDs with the wind direction at Masada (figure 10.5 bottom) one can see that the highest values are also observed during eastern winds. The diurnal variation of wind direction in 2014 was more or less constant and barely no change between sea breeze and purging of the valley was observed. Therefore, wind roses of BrO measured in 2014 do not provide any additional information. The largest BrO abundance is observed at wind speeds of 2 m/s both in May 2012 and November 2014 (see figure 10.6), which can be due to dilution and/or the entry of air masses with different chemical composition (e.g. increase of sinks like NO_2).
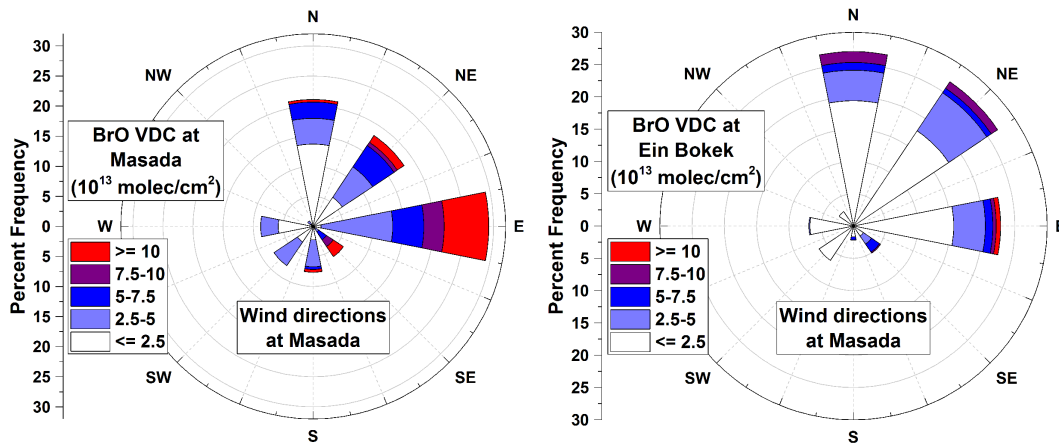
Fig. 10.5: **Left:** Wind rose showing the occurrence of BrO VCDs measured by the Masada MAX-DOAS in 2012 at given wind directions measured by weather station P88. **Right:** BrO VCDs measured at Ein Bokek in 2012 with respect to wind directions measured in Masada. The color code represents the value of measured VCDs.
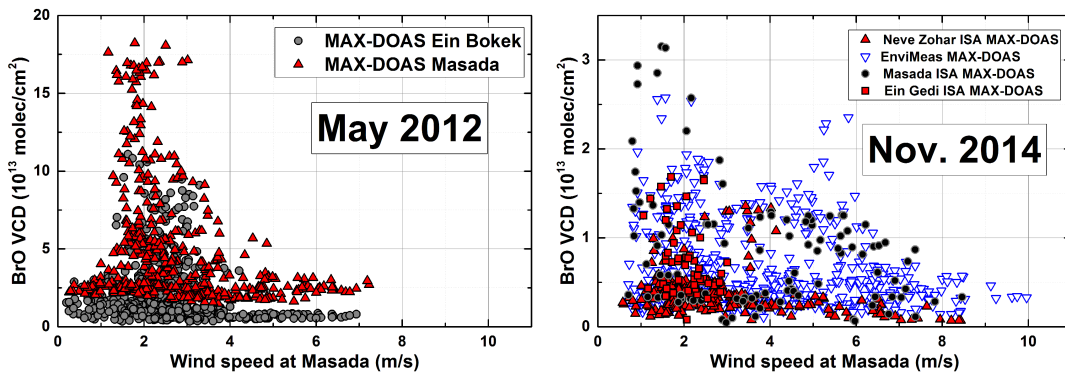
Fig. 10.6: BrO VDCs as a function of wind speed measured in 2012 (left) and 2014 (right) at different locations (see plot legend). Note the different y-axis scales for 2012 and 2014.

Strong evidence for the impact of horizontal transport on the observed BrO abundance was found during both campaigns. Figure 10.7 shows time series of BrO and NO_2 mixing ratios from LP-DOAS data at Ein Bokek on May 5th 2012

as well as mixing ratios and vertical column densities from MAX-DOAS data at Masada on Nov 25th 2014. Further, wind speed and direction as well as solar radiation is shown. The meteorological data from May 5th 2012 has already been discussed above (section 10.1). The BrO time series from LP-DOAS data features a pronounced, "M"-shaped temporal characteristic. The first increase of BrO is observed under contrary wind directions at the two weather stations. At 12:00 UTC, the wind direction at Masada changes from easterly to northerly direction (change from "Enrichment" to "Purging" scenario). Parallel to the change in wind direction, the LP-DOAS observes a decrease in BrO from 55 pptv down to 5 pptv within approximately 90 minutes and a simultaneously increase of NO_2 from below the detection limit (15 pptv) up to 250 pptv, followed by another increase up to 70 pptv within 30 minutes while NO_2 decreases again. Further a second decrease of BrO follows while NO_2 increases.

On November 25th 2014, a similar behavior of BrO and NO_2 VCDs is observed (figure 10.7, bottom right). Between 08:00 and 11:00 UTC, the time series of BrO VCDs at Masada show again an "M"-shaped characteristic. Similar to 2012, BrO increases until wind direction changes, here from northerly to southerly direction. This first increase and decrease is also visible in the observed surface mixing ratios. After 90 minutes the decrease stops and BrO increases again for approximately 40 minutes followed by another decrease. Again, NO_2 VCDs and surface mixing ratios show an inverted temporal behavior, being decreased at elevated BrO and vice versa.

In both cases, the prevailing wind speed is 2 m/s. Further, the time difference between first and the second maximum in BrO is two hours, in both observed cases. Assuming a horizontal transport of (rigid) air masses, this would imply a spatial gap of approximately 10 km which is the extent of the land mass separating the two basins of the Dead Sea.
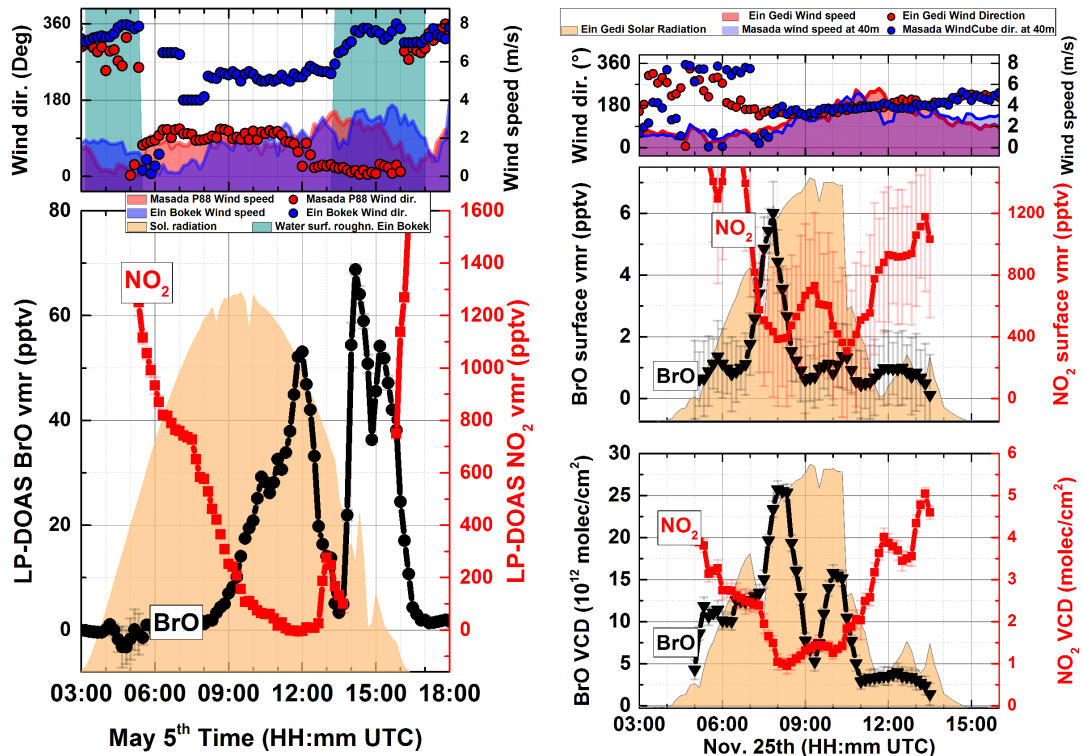
Fig. 10.7: **Left:** *BrO and NO$_2$ mixing ratios from LP-DOAS data and meteorology on May 5th at Ein Bokek.* **Right:** *VCDs and mixing ratios from MAX-DOAS data and meteorology at Masada on Nov 25th 2014. The "M"-shaped temporal characteristics in BrO indicate horizontal transport of BrO enriched air masses from the two basins of the Dead Sea which are separated by a land mass of 10 km extent.*

On Nov. 25th 2014 the "M"-shaped temporal characteristic are barley visible in the time series of the surface mixing ratios, in contrast to the VCDs. This may be explained by an turbulent upwelling of BrO enriched air masses due to increased wind speed coming from the southern basin. The vertical profiles from that day, shown in figure 10.8 support this theory. While the first peak between 07:00 and 08:00 UTC comes along with increased surface mixing ratios, the second peak at 10:00 UTC is exclusively at altitudes between 500 m and 1 km above ground level. Further, the data from the second MAX-DOAS instrument is shown, which measured parallel to the stationary instrument at Masada but under a different

azimuthal heading (see, figure 7.1). While the stationary instruments heading was 80° (almost east), the second instrument was aligned with a heading of 20° and hence, in northerly direction.

Four significant features can be recognized in the profiles of the instrument with heading of 80°. (a) the maximum between 05:00 and 06:00 UTC at 0.4 km absolute altitude, (b) The maximum at 07:00 UTC at -200 m, (c) maximum at 08:00 UTC between and (d) maximum at 10:00 UTC at 0 m absolute altitude. While (a), (b) and (d) can be identified with a temporal delay of approximately 1 hour in the vertical profiles of the instrument with 20° heading, (c) is not clearly recognizable. Further, the northerly headed MAX-DOAS observes another maximum at 08:00 UTC and 1km absolute altitude (called (e) in the corresponding plot) which is not observed by the easterly heading instrument.
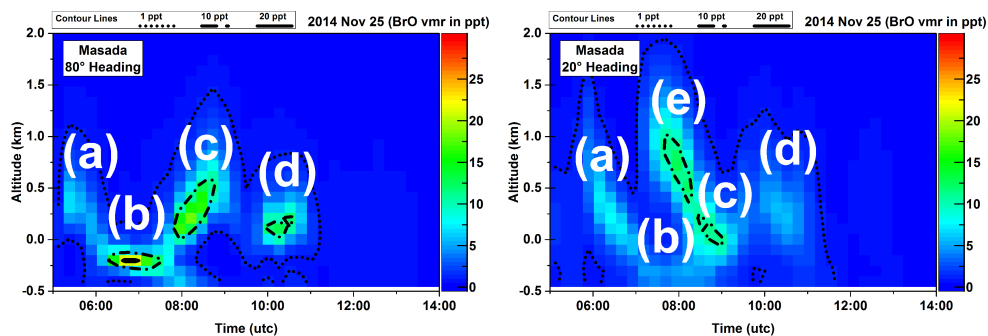
Fig. 10.8: *Vertical profiles of BrO on Nov 25th 2014 measured with at Masada with two MAX-DOAS instruments with different azimuthal headings.* **Left:** *80°.* **Right:** *20°. Letters (a) to (e) mark distinct features which are observed with both instruments and which indicate horizontal transport caused by prevailing northerly winds.*

The observations of meteorology and BrO leads to the following hypothesis: The extent of the landmass between the two basins of the Dead Sea is approximately 10 km. A large construction site of the Dead Sea works company is located on the northern edge of the evaporation ponds at Ein Bokek. Heavy industrial traffic is likely to cause significant abundances of nitrogen oxides and, hence, NO_2. Once

the wind changes to a direction parallel to the orientation of the Dead Sea Valley (northerly or southerly), the NO_2 plume from above the land mass and also the BrO enriched air masses are transported along the valley and are detected by the instruments at Ein Bokek or Masada. The decrease in observed BrO parallel to the increase of observed NO_2 is most likely chemically driven by the formation of $BrONO_2$, which would explain the observations illustrated in figure 10.7.

The data shows that the observed dynamics of BrO and NO_2 is strongly influenced by horizontal transport. Therefore, the consideration of meteorology is critical for the interpretation of ground near measurements at the Dead Sea. Especially if the data serves as starting point for modeling gas phase chemistry, the errors by not taking transport processes into account may be severe. Further, it will be show later that measurements performed near the ground (e.g. LP-DOAS or in-situ, point measurements) do not represent the total amount of trace gases very well which is due to strong vertical gradients.
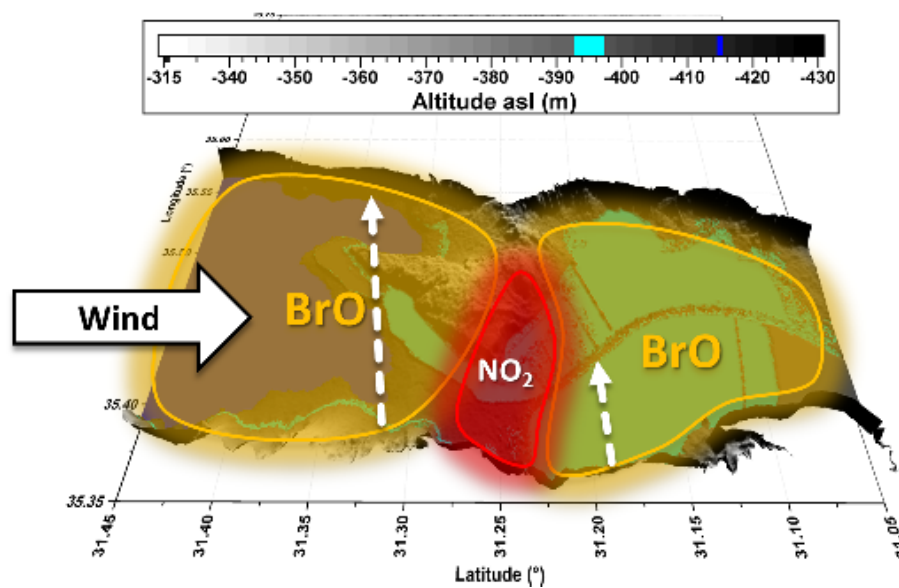
Fig. 10.9: Hypothetical distributions of BrO and NO_2 to explain the dynamics in mixing ratios observed on May 5th 2012 and Nov. 25th 2014. The white arrows represent the viewing direction of the MAX-DOAS at Masada and the LP-DOAS at Ein Bokek.

10.2.2 Comparison with aerosols profiles

In the following section, vertical distributions of BrO are compared with profiles of aerosol extinction. Exemplary days from 2012 and 2014 with large and small vertical extent of BrO and aerosol distributions are discussed. Note again that the altitude of the upper rim of the valley on Jordanian side is approximately at 1 km absolute altitude (see also figure 2.1). This will be important for the following interpretation of vertical transport processes.

For each day, combined profiles of BrO and aerosol extinction are shown. BrO mixing ratios are represented by black solid lines. Aerosol extinction is display by blue dotted lines. For the sake of clarity, values mixing ratios and extinctions are only represented by labels on contour lines in units of pptv (parts per trillion, volume mixing ratio) and km^{-1}, respectively. Date and location of the instrument is described in the corresponding profile plots. On the right side of the profile plots, meteorological data of the corresponding day is shown. For exemplary days in 2014, only data of the instrument at Masada is discussed.

May 3rd 2012 - Elevated BrO at Ein Bokek during sea breeze
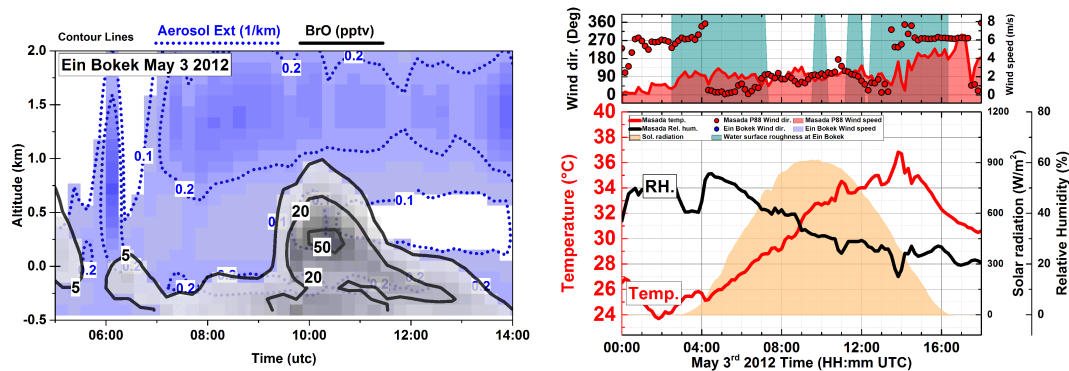
Fig. 10.10: Combined vertical profiles of BrO (black, solid contour lines) and aerosol extinction (blue, contour lines) on May 3rd 2012. Striped area represents missing data.

The BrO profiles of May 3rd show mixing ratios of 5 pptv located in absolute altitudes of up to 0 m (see figure 10.10, left). Aerosol extinctions of 0.1 to 0.2 km^{-1} homogeneously distributed from ground level up to absolute altitudes of 2 km prevailed during that day. After being vertically constraint, BrO shows a fast increase in vertical extension shortly after 09:00 UTC reaching 1 km within 30 minutes. At 09:30 UTC, an increase in water surface roughness is observed at Ein Bokek. Considering the easterly winds observed at Masada, the increase in water surface roughness is most likely caused by enhanced sea breeze winds at Ein Bokek which may transport BrO enriched air masses from absolute altitudes below 0 m up to 1 km (which is approximately the upper rim of the valley on the Jordanian side). At 11:00 UTC, the vertical extent of BrO decreases again. At the same time, wind directions at Masada change from easterly to westerly which may lead to a collapse of the prevailing sea breeze scenario.

May 9th 2012 - increase of BrO during changing wind conditions
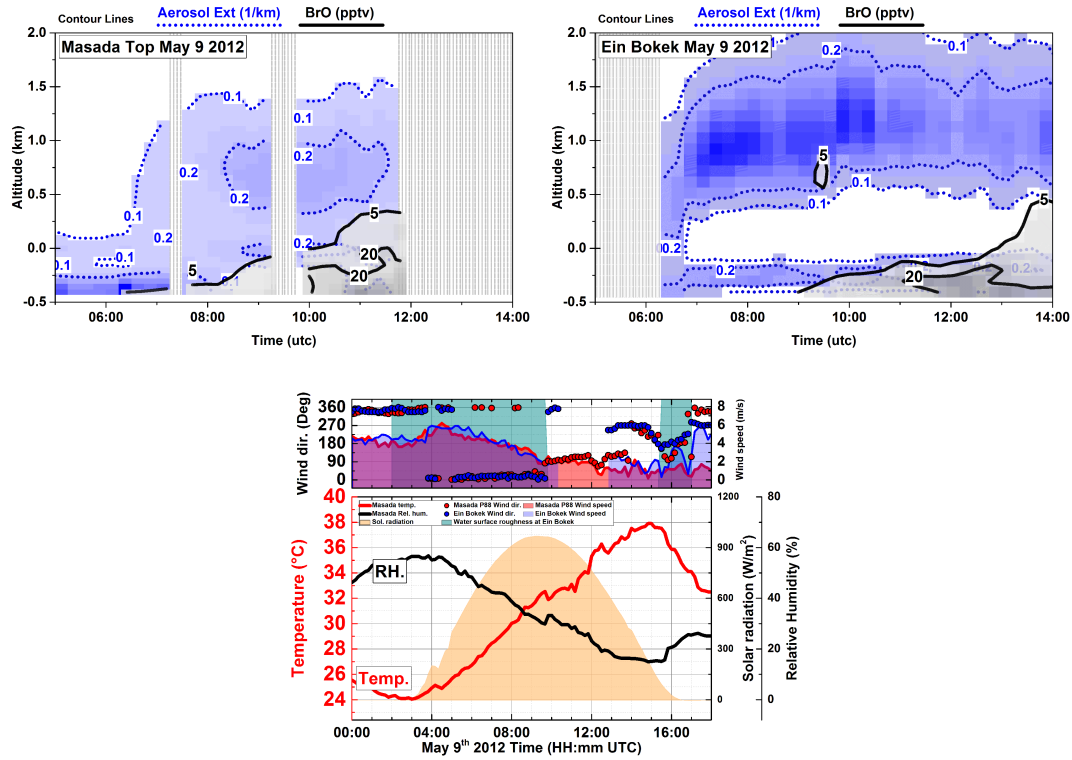
Fig. 10.11: Combined vertical profiles of BrO (black, solid contour lines) and aerosol extinction (blue, contour lines) on May 9th 2012. Striped area represents missing data.

On May 9th, wind speeds start to decrease with sun rise from values of 6 m/s to 2 m/s. Wind directions change from northerly to easterly at 10:00 UTC. Vertical extents of BrO at Masada and Ein Bokek increase at 08:00 and 09:00 UTC, respectively, which is likely to be due to the decreased wind speed and easterly direction.

May 8th, 11th and 12th 2012 - vertically confined BrO at Masada, elevated BrO at Ein Bokek, indications for upwelling of BrO enriched air masses out of the valley caused by sea breeze
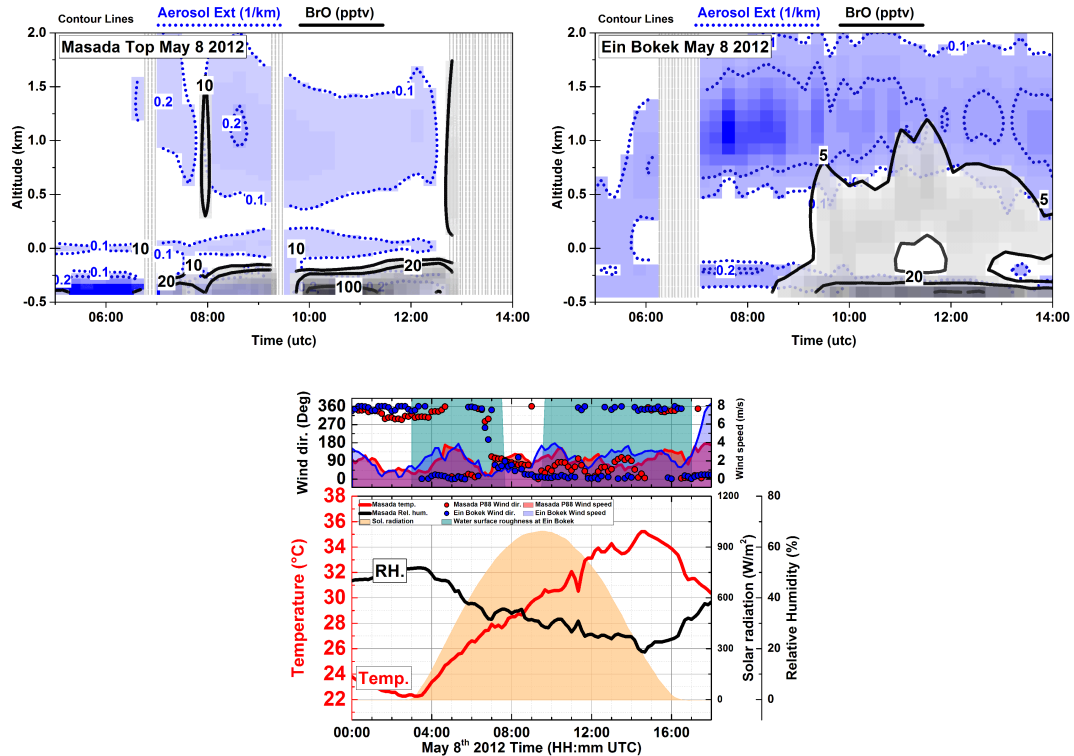
Fig. 10.12: Combined vertical profiles of BrO (black, solid contour lines) and aerosol extinction (blue, contour lines) on May 8th 2012. Striped area represents missing data.

The profiles of aerosol extinction show a pronounced vertical gradient over the first 500 above ground at Masada. Especially on May 8th, the gradient is very pronounced with extinction changing from 0.2 km^{-1} at ground level to below 0.1 km^{-1} within 200 m of altitude. Another layer with 0.1 km^{-1} is located at 0 m absolute altitude. At Masada and Ein Bokek, BrO starts to increase after 07:00 UTC parallel to a change of wind direction from northerly to easterly, sea breeze winds. The vertical BrO distribution at Masada is confined to 200

m above ground with rather high mixing ratios of 100 pptv. Between 07:30 and 08:00 UTC, defined easterly winds prevail at Masada coming along with a breakthrough between the two aerosol layers is followed by an elevated, short timed BrO occurrence of 10 pptv between absolute altitudes of 200 m and 1.5 km. This might indicate that the local wind systems causes an upwelling and ejection of air masses enriched with BrO or its precursors out of the valley into higher altitudes. The coexistence of the elevated BrO abundance with an confined aerosol distribution of approximately the same altitude and vertical extent supports this assumption. At Ein Bokek, surface mixing ratios are 20 pptv but with a larger vertical extent with 5 pptv at absolute altitudes around 1.5 km. The fast increase in total BrO abundance and vertical extent at Ein Bokek almost coincides with a decrease of water surface roughness and, hence, local wind speed.
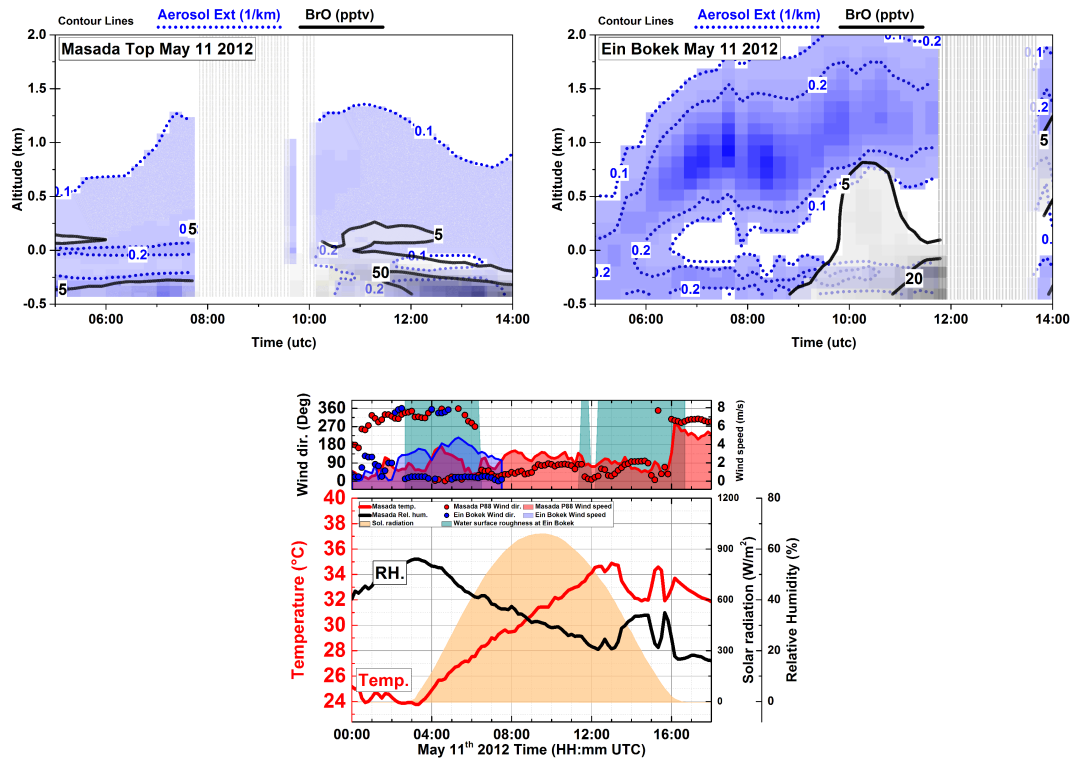
Fig. 10.13: Combined vertical profiles of BrO (black, solid contour lines) and aerosol extinction (blue, contour lines) on May 11th 2012. Striped area represents missing data.

On May 11th, the aerosol abundance at Masada and Ein Bokek is similar to May 8th. Ground mixing ratios above 5 pptv BrO are present from morning time at Masada, while at Ein Bokek, BrO is detected at 09:00 UTC, when winds change from northerly to easterly and water surface roughness at decreases at Ein Bokek. Like on May 8th, BrO apparently rises from ground level to 500 m absolute altitude within 90 minutes. At Masada, the vertical extent also increases slightly to an absolute altitude of 0 m with change to easterly wind speeds at 09:00 UTC. The decrease of high altitude BrO at Ein Bokek co-occur with increasing water surface roughness and change in wind direction at Masada. This indicates that, elevated BrO is restricted to sea breeze scenarios.
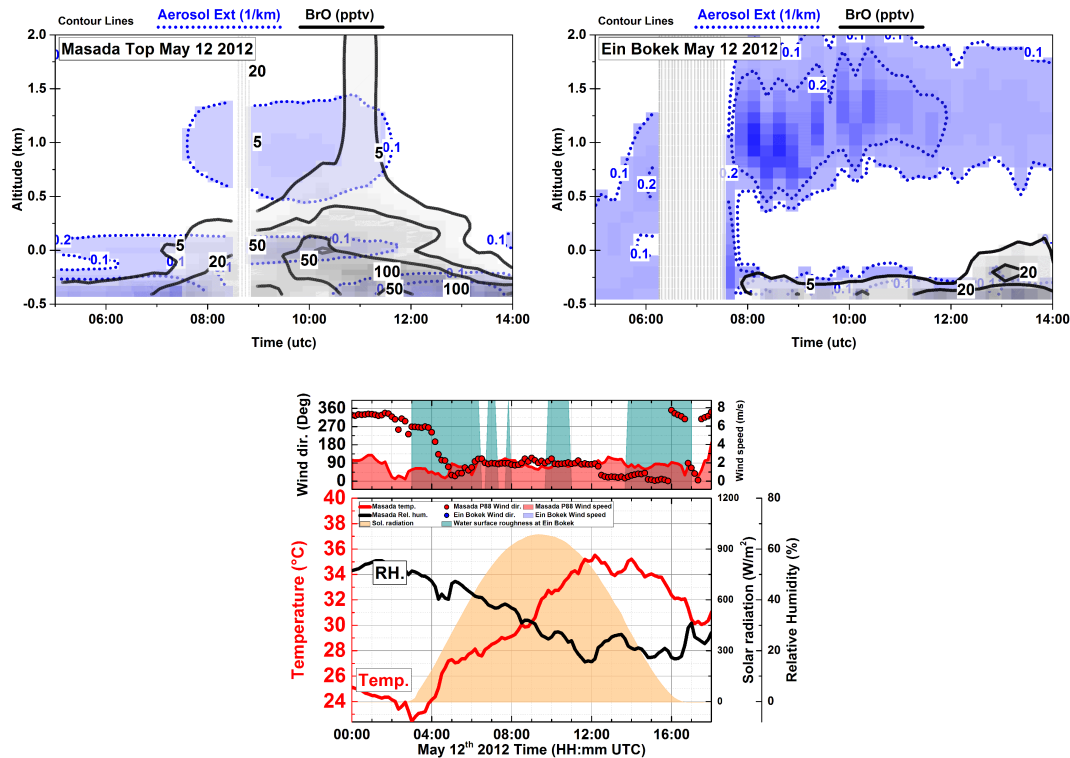
Fig. 10.14: Combined vertical profiles of BrO (black, solid contour lines) and aerosol extinction (blue, contour lines) on May 12th 2012. Striped area represents missing data.

Another indication for the upwelling of BrO enriched air masses during sea breeze is observed on May 12th. Here, stable easterly winds are observed during daytime, indicating a constant sea breeze scenario. Occasionally increased water surface roughness at Ein Bokek indicates high wind speeds (and therefore suppressed build-up of sea breeze) and might be the cause for vertically constrained BrO abundances at Ein Bokek. At Masada, the vertical extent of the 5 pptv front is constantly increasing with rates of approximately 0.1 km/h to absolute altitudes of 0.8 km. At 11:00 UTC, the extent suddenly increases to above 2 km absolute altitude with in a few minutes. Assuming a stable vortex system during sea breeze, this observation can be interpreted as a breaking off of BrO enriched air masses out of the sea breeze system and thus, out of the valley. Around 11:00

UTC, the upper limit of the vertical extent of BrO decreases again down to 200 m followed by changing wind direction indicating a purging of the valley at 12:30 UTC. The northerly winds most likely penetrated the Dead Sea valley from above which leads to a delayed detection by the ground based weather station at Masada. This might explain the decrease of the BrO profile prior to the detection of northerly winds at the ground.

May 10th 2012 - strong southerly winds, high aerosol abundance, large vertical extent of BrO
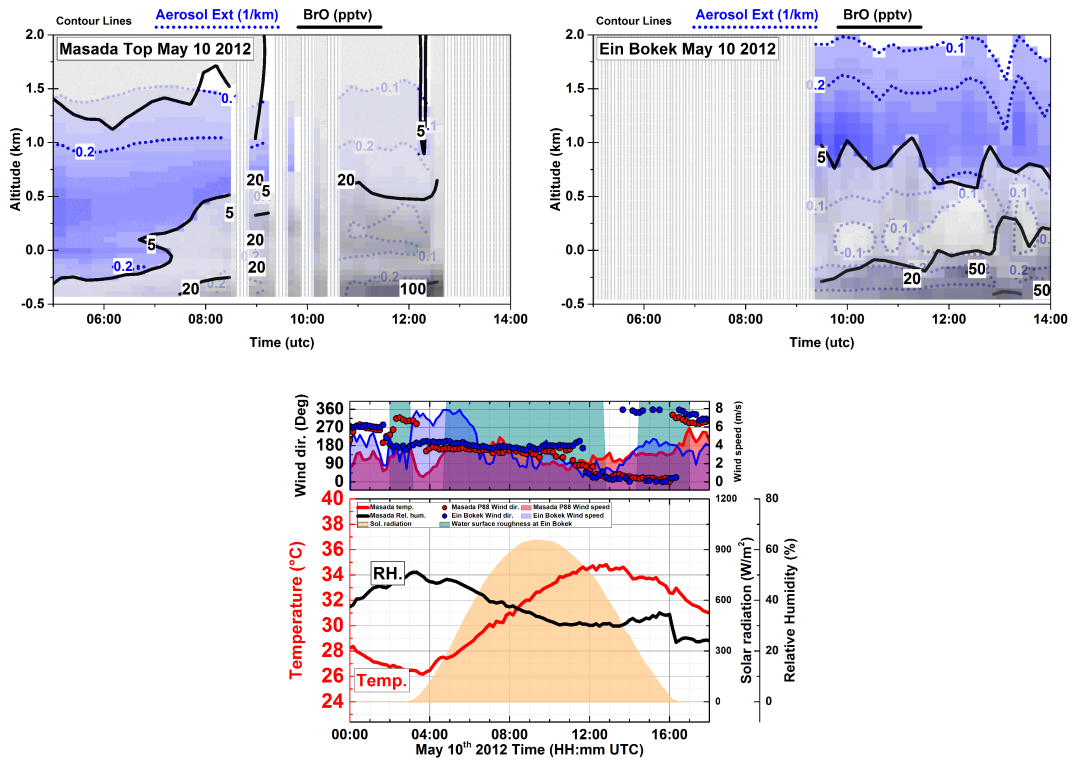
Fig. 10.15: Combined vertical profiles of BrO (black, solid contour lines) and aerosol extinction (blue, contour lines) on May 10th 2012. Striped area represents missing data.

On May 10th, strong southerly winds at speeds of up to 8 m/s prevailed during
sun rise which strongly differs from the meteorological situation on the other
days of the campaign in 2012, where usually northerly and easterly winds at
lower wind speeds were observed. Aerosol profiles at both locations show homo-
geneously distributions with values of 0.1 km^{-1} at absolute altitudes of 1.5 km.
At Ein Bokek, BrO also shows a homogeneously distribution with mixing ratios
of 5 pptv at 1 km absolute altitude and 50 pptv near ground level. At Masada,
the vertical BrO extent is even larger with 5 pptv above absolute altitude of 1.5
km and mixing ratios of 100 pptv near the ground. Between 05:00 and 09:00
UTC a confined layer of 5 pptv BrO is located above the valley between alti-
tudes of 1 km and 2 km. This event is unique for the measurement period in
2012 and may be attributed to the also unique meteorological situation on that
day. Strong southerly winds of 8 m/s during sun rise may lead to an upwelling
of dust, sea salt aerosols or other BrO precursors to higher altitudes. According
to Geever et al. [2005], the source flux F of sea salt aerosol with diameters ≥ 10
nm from the water surface increases approximately by a factor of two if wind
speed increases from 2 m/s to 8 m/s with F depending exponentially on the wind
speed U by the following equation 10.1:

$$F\left(10^6\, m^{-2}\, s^{-1}\right) = (0.099\, U\left(ms^{-1}\right) - 0.73) \qquad (10.1)$$

The large and homogeneous vertical extent of observed aerosol extinctions sup-
ports this assumption for the case of aerosols. A heterogeneous release of BrO
precursors from these aerosols at higher altitudes might explain the observed
BrO profile. Similar to other days discussed above, the vertical extent of BrO
inside the valley increases once wind direction begins to changes from south to
east and at 10:00 UTC.

November 8th 2014 - small vertical extent of BrO and aerosols, low relative humidity
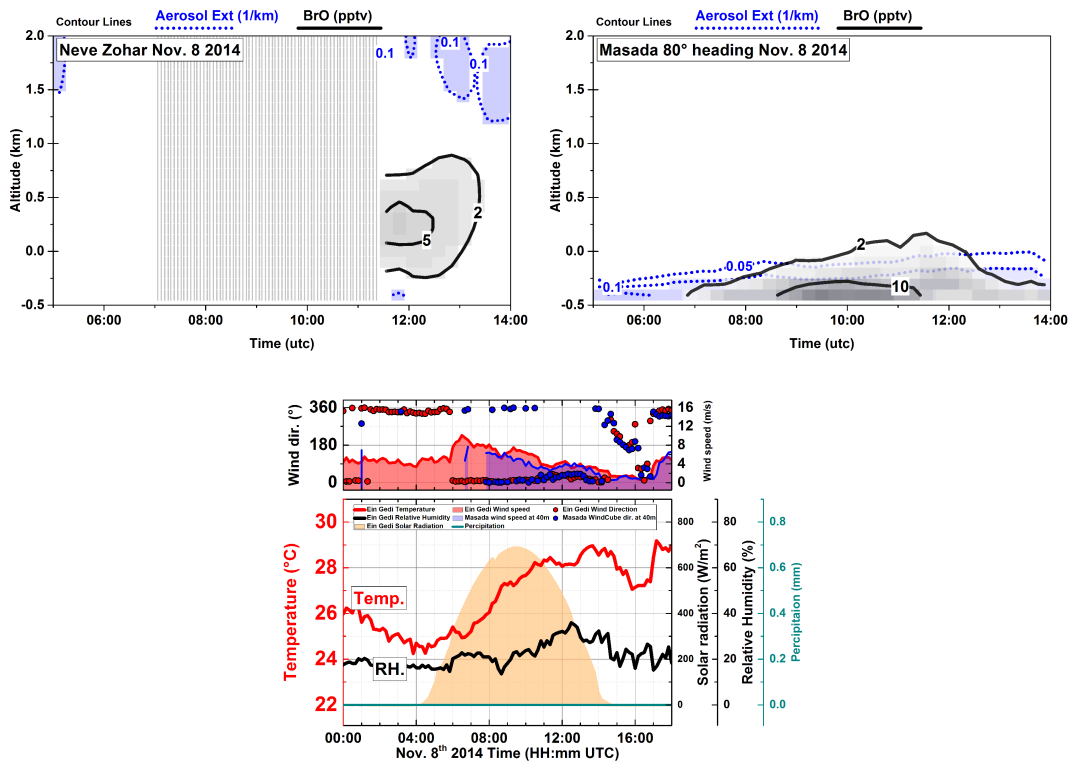
Fig. 10.16: Combined vertical profiles of BrO (black, solid contour lines) and aerosol extinction (blue, contour lines) on Nov. 8th 2014 at Neve Zohar and Masada. Striped area represents missing data. Right plot shows meteorological data.

On Nov. 8th 2014 BrO mixing ratios of 15 pptv were observed at Masada. The vertical distribution shows a limited extent of BrO to approximately 700 m above ground level. In contrast to other days, the maximum mixing ratios are always located within the first 100 m above ground and no elevated layers are observed during the day. The extinction profile shows a similar characteristic with values of 0.05 to 0.1 km^{-1} between altitudes of 0 m to 300 m above ground. Constant northerly winds at wind speeds between 10 m/s in the morning to 4 m/s in the

evening prevailed. While the surface mixing ratio seems to correlate with solar radiation, the data shows a slight increase in vertical extend of BrO along with a decrease in wind speed. Further, the exceptional low relative humidity may contribute to the low aerosol abundance. At Neve Zohar, aerosol abundance was even lower than at Masada, after technical problems due to overheating between 07:00 and 11:15 UTC, the instrument observed an elevated layer of 2 to 5 pptv BrO at around 200 m absolute altitude with no significant mixing ratios near the water surface. Since Neve Zohar is located 20 km south of Masada, the meteorological data may not be transferred. The elevated BrO layer is most likely caused by local sea breeze at Neve Zohar.

November 17th and 25th 2014 - increasing vertical BrO extension during changing solar radiation caused by clouds
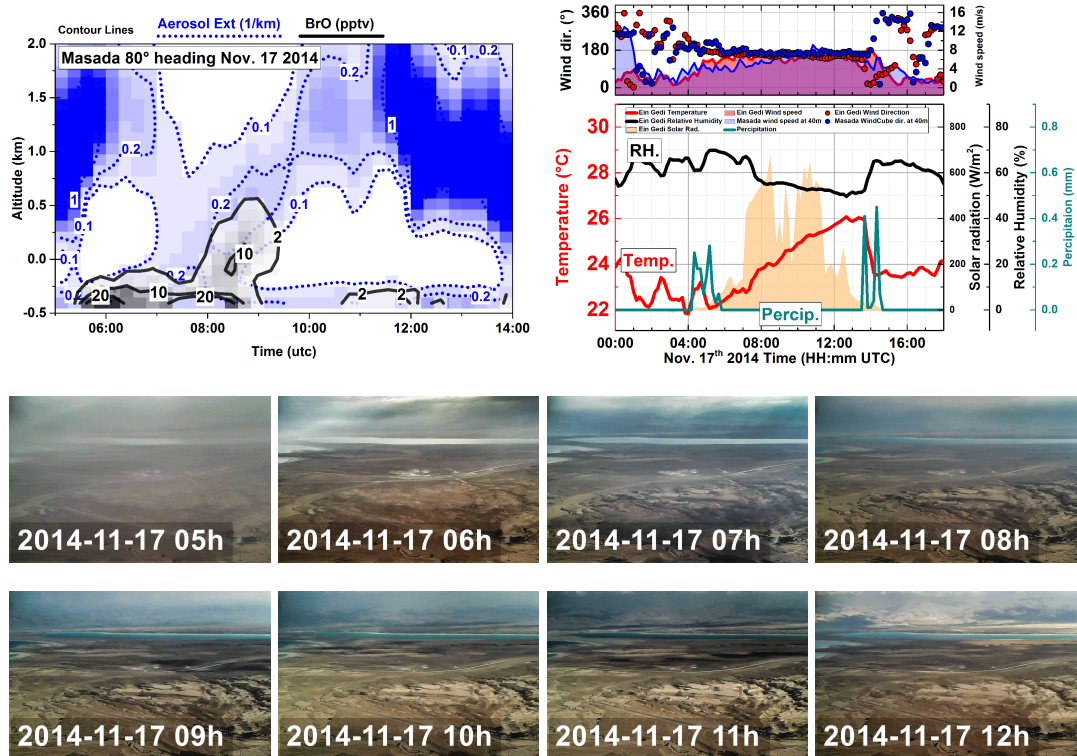
Fig. 10.17: **Top:** *Combined vertical profiles of BrO (black, solid contour lines) and aerosol extinction (blue, contour lines) on Nov. 17th 2014 at Masada. Right plot shows meteorological data.* **Bottom:** *Camera pictures taken at Masada top on 17th 2014. Viewing direction was east. Times in UTC. Increasing visibility indicates decreasing aerosol load.*

Precipitation events were detected during 04:00 and 06:00 UTC as well as during 13:30 and 15:00 UTC. Increased extinctions are clearly visible in the profiles after sunset and in the afternoon indicating optically dense clouds (see also ceilometer data in figure 9.7 in the results section). The aerosol profile shows an aerosol layer at extinctions between 0.1 and 0.2 km^{-1} ascending from the ground up to absolute altitudes of 1 km. Camera pictures taken from Masada top (figure 10.17) confirm an increase in visibility and, hence, a decrease in aerosol abundance.

Shortly after the rain event in the morning BrO starts to increase. While surface mixing ratios of 20 pptv are observed, the vertical BrO extend seems to follow the aerosol distribution by increasing slowly to absolute altitudes of 500 m. Further, a confined maximum of 10 pptv at 0 m is observed. At 09:00 UTC the increase stops and the total amount of BrO decreases to below the detection limit. At the same time, the weather station detects a decrease in solar radiation, caused by clouds. Between 10:00 and 11:00, as solar radiation increases again, 2 pptv of BrO are detected near the surface. Considering constant wind speed and direction, the observations of this indicate that the dynamics of observed BrO is predominantly driven by the dynamics of solar radiation.
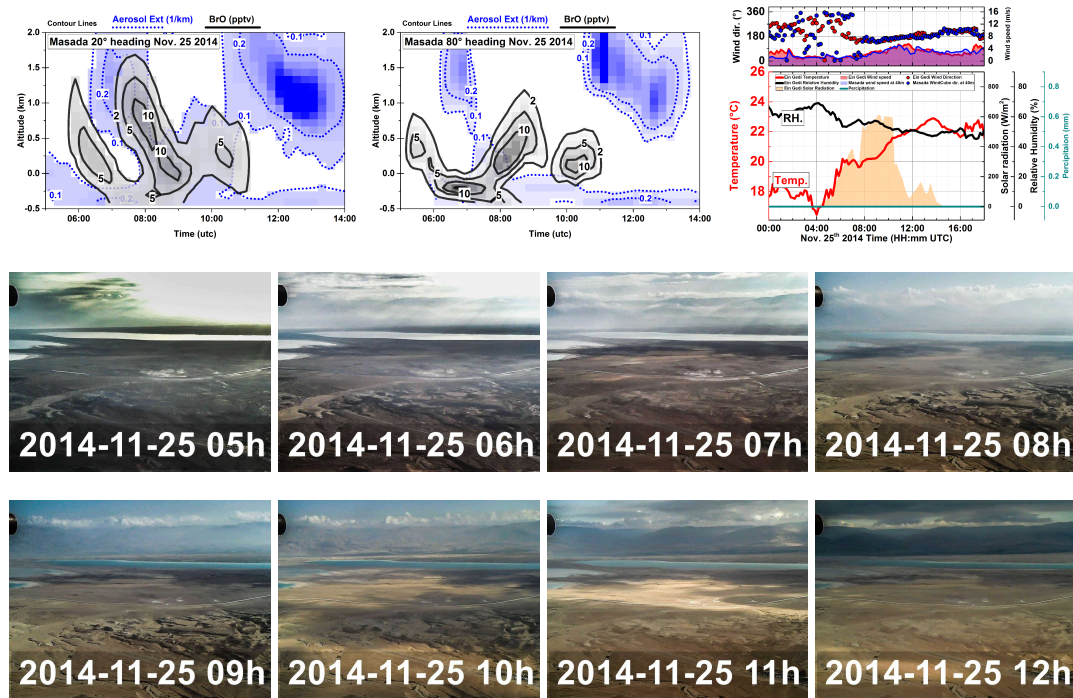
Fig. 10.18: **Top:** Combined vertical profiles of BrO (black, solid contour lines) and aerosol extinction (blue, contour lines) on Nov. 25th 2014 at Masada by instruments with different heading. Right plot shows meteorological data. **Bottom:** Camera pictures taken at Masada top, viewing direction east.

Meteorological conditions on Nov. 25th are similar to Nov 17th, however, no precipitation occurred. Between 05:00 and 06:00 UTC low wind speeds of 2 m/s at undefined directions come along with elevated layer of 2 to 5 pptv BrO mixing ratios. At 06:00 UTC wind directions change to south while a decrease of the vertical extent of BrO is observed. Solar radiation data indicates clouds between 07:00 UTC and 08:00 UTC followed by a formation of an elevated BrO layer with mixing ratios of 10 pptv, similar to Nov 17th, where an increase vertical extend is also observed shortly after cloud occurrence indicated by a drop in solar radiation. This leads to the assumption that decreased solar radiation caused by cloud coverage may lead to longer lifetimes of BrO precursors enabling them to ascent to higher altitudes. Once solar radiation increases again, the release mechanisms are activated at higher altitudes. The fact that no change in wind direction and, hence, most likely no vertical transport is observed, supports this theory.

The elevated BrO layer observed at 05:00 UTC might be caused by the fact that during sunrise, solar radiation increases first in higher altitudes before reaching the ground of the Dead Sea Valley, illustrated in figure 10.19. As already discussed above (section 10.2.1), the second elevated BrO plume observed on 10:00 UTC can be attributed to air masses which are transported to Masada from the southern evaporation ponds where an elevated plume of BrO is formed also by changing solar radiation. Assuming a wind speed of 3 m/s and a time difference of 90 to 120 minutes leads to a transport distance of 15 to 20 km, indicating the evaporation ponds as a possible origin. Further, the dominant features of the aerosol abundance are observed at the same time, while those of the BrO distribution are observed with a delay of about 30 to 60 minutes compared to the instrument with easterly viewing direction. This is another evidence for the horizontal transport of BrO enriched air masses.
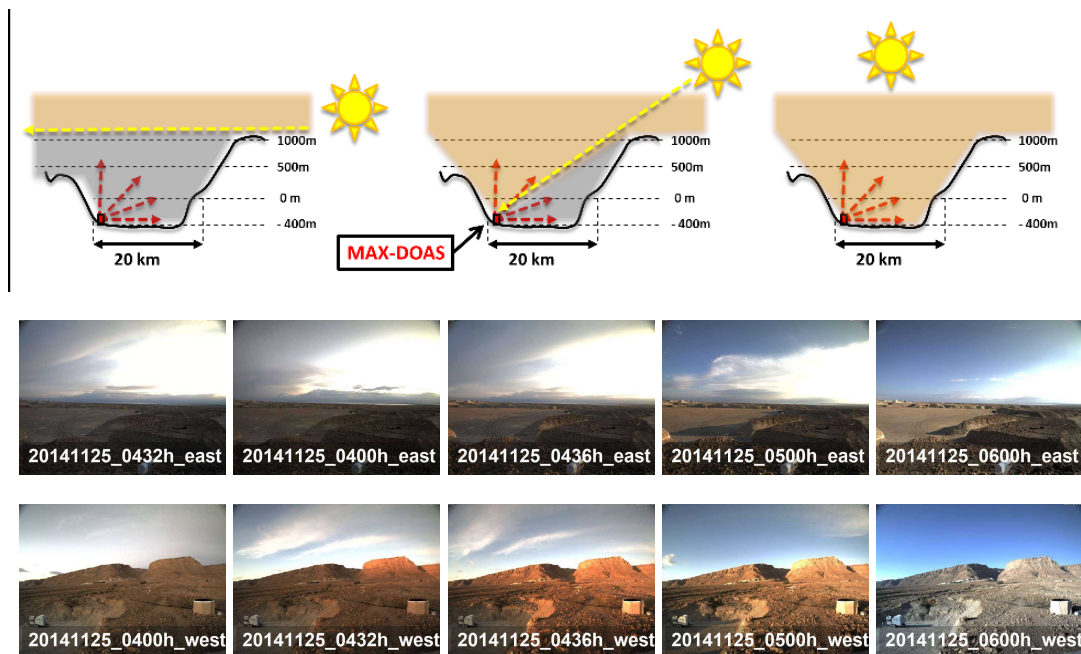
Fig. 10.19: Sketch illustrating the shadow caused by the valley during sunrise. Geological cross section in west-east direction at Masada adapted from Google Earth. ©2015 Google, ©2015 ORION-ME, ©2015 Digital Globe, US Dept of State Geographer. Further, camera pictures taken on Nov 25th at the KIT Cube with viewing direction east and west show the illumination of the valley during sunrise.

November 28th 2014 - small vertical extend of BrO and aerosols, elevated BrO maximum

Meteorological conditions on Nov. 28th were similar to those on Nov. 8th except for a larger amount of aerosols indicated by the vertical profile and the camera pictures in figure 10.20. Wind directions between northerly and easterly prevailed at low speeds of 2 to 3 m/s. Cloud coverage was sparse resulting in continuous solar radiation throughout the day. Similar to Nov. 8th a continuous build-up of BrO near ground level is observed. However, also an elevated, local maximum 300 m above ground level is detected at 07:00 UTC. At the same time, camera pictures and measured aerosol profiles indicate also an elevated aerosol maximum at the same altitude.

The instrument at Ein Gedi observed, low aerosol abundances near ground level and a confined elevated layer 250 m above the water surface in the morning hours. At 08:00 UTC, the aerosol profile shows a unification of ground level aerosols and the elevated layer followed by increased BrO levels of 2 to 10 pptv over an vertical extent of 1 km and a local maximum at 0 m absolute altitude. The slight change of wind directions from northerly to easterly between 08:00 and 12:00 UTC might address the elevated BrO layers to a weak sea breeze scenario.
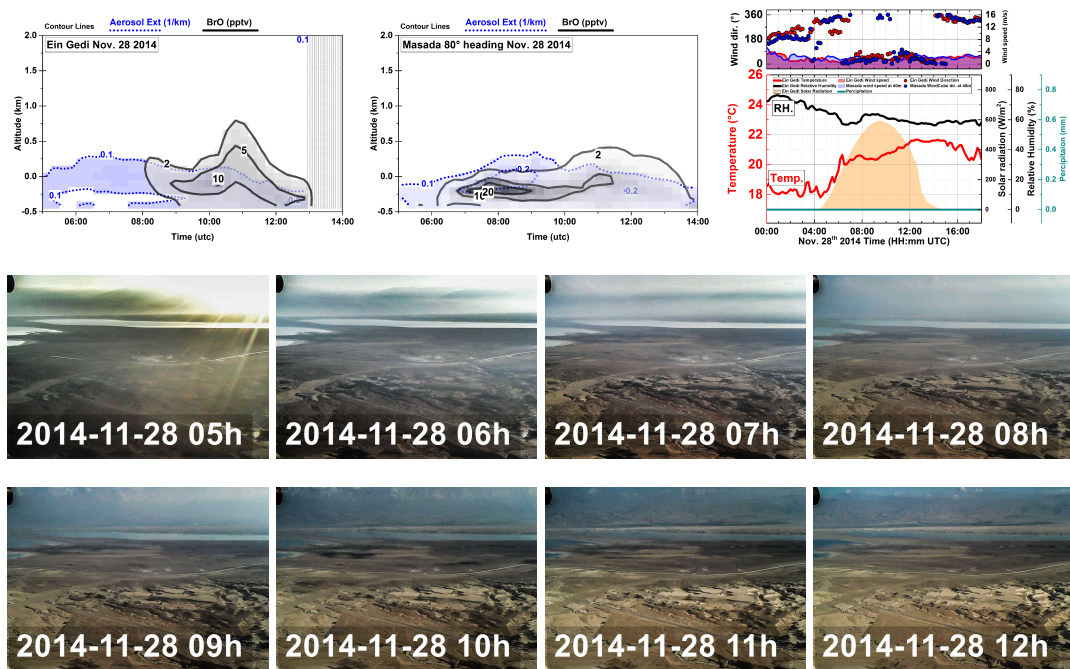
Fig. 10.20: **Top:** Combined vertical profiles of BrO (black, solid contour lines) and aerosol extinction (blue, contour lines) on Nov. 28th 2014 at Ein Gedi and Masada. Right plot shows meteorological data. **Bottom:** Camera pictures taken at Masada top, viewing direction east.

10.2.3 Comparison with NO$_2$ profiles
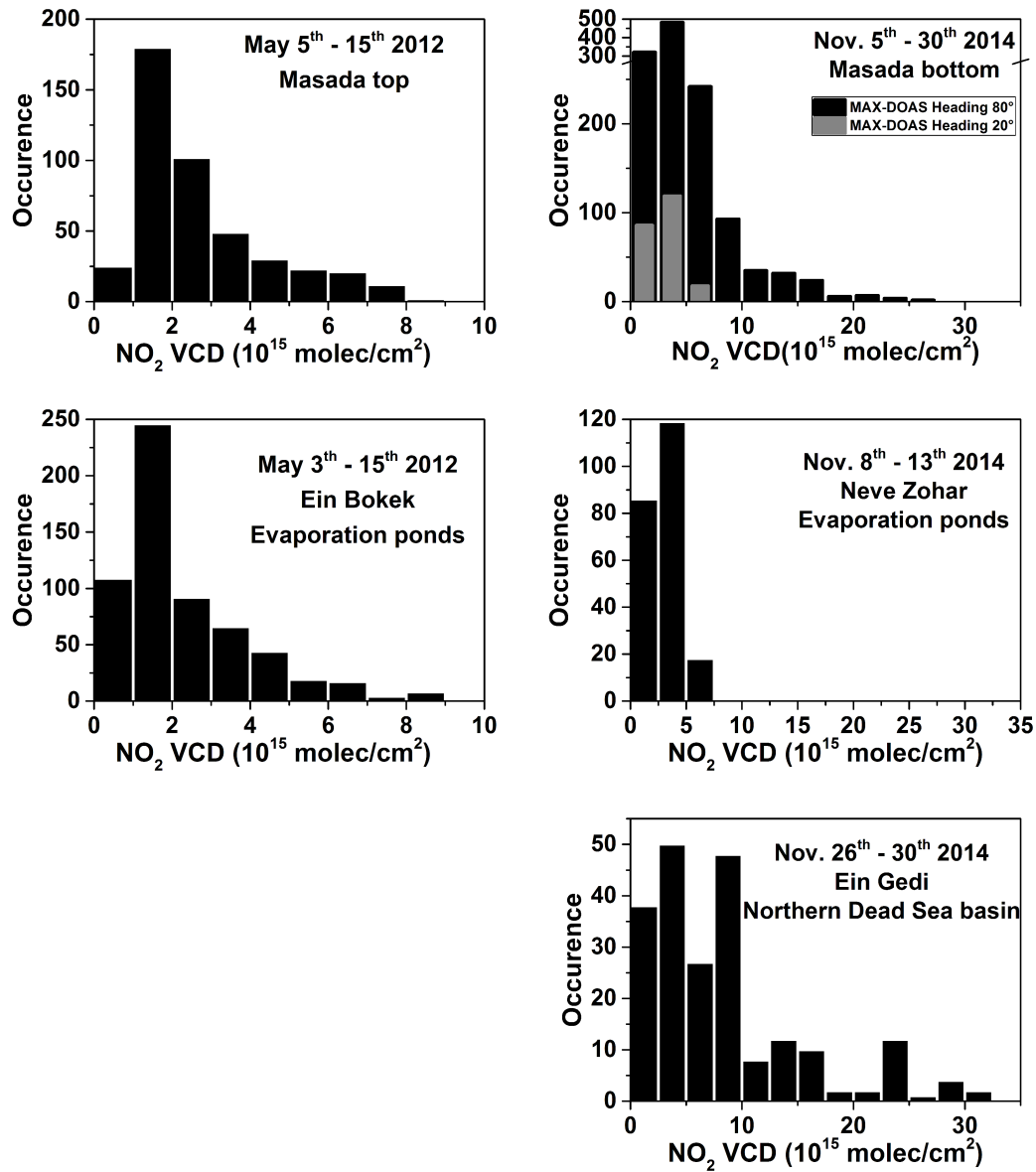
Fig. 10.21: Histograms of NO$_2$ VCDs measured during May 2012 and Nov. 2014 at different locations. In 2014 two instruments with different headings measured parallel at Masada for several days, indicated by black and grey bars. Note the different x-axis scales between 2012 and 2014.

To get an impression of the differences in total NO_2 abundances between may 2012 and November 2014, histograms of VCDs from data of the MAX-DOAS instruments at different locations are shown in figure 10.21. VCDs were about a factor of three higher in November 2014 compared to May 2012. This has to be considered since it is known that nitrogen oxides can have a significant impact in the halogen chemistry (Tas et al. [2008]).

Before comparing vertical trace gas profiles, it has to be considered that the MAX-DOAS instrument integrate over a light path of several km. Thus, trace gas gradients along the line of sight of the telescopes can not be resolved. BrO and NO_2 plumes which are located at different distances from the instrument but are detected by the field of view may be misinterpreted to be coexisting, especially at low wind speeds and wind directions which are parallel to the instruments line of sight (eastern winds during sea breeze). Strong, northerly or southerly winds should reduce the possibility of gradients along the line of sight since the air masses are assumed to be well mixed.

In figure 10.22 combined vertical profile of NO_2 and BrO from exemplary days in 2012 are shown. At Ein Bokek, BrO and NO_2 seem to be strongly mutually exclusive both temporally and spatially (e.g. May 3rd, 10th and 12th). Comparing the overlapping profiles indicates BrO to NO_2 ratios of 5:200 and 10:500 at the boundaries of the trace gas distributions at Masada and Ein Bokek, respectively. Slightly lower BrO to NO_2 ratios are observed at Masada. However, gradients along the instruments line of sight (described above) are likely since it points over the landmass between northern and southern Dead Sea basins, where constructions sites of the Dead Sea Works are located. Further, the Jordanian town Al Mazaraa, located 15 km east of Masada, may have a significant influence on the observed NO_2 signals.

On May 10th, where strong southerly winds prevail assuming well-mixed air masses, the silhouettes of the observed profiles at Masada adapt exceptionally to each other (e.g. 07:00 to 08:00 at -200m absolute altitude). On other days with lower wind speeds and sea breeze scenarios, coexisting mixing ratios of 50 pptv BrO and 200 pptv NO_2 are regularly observed.
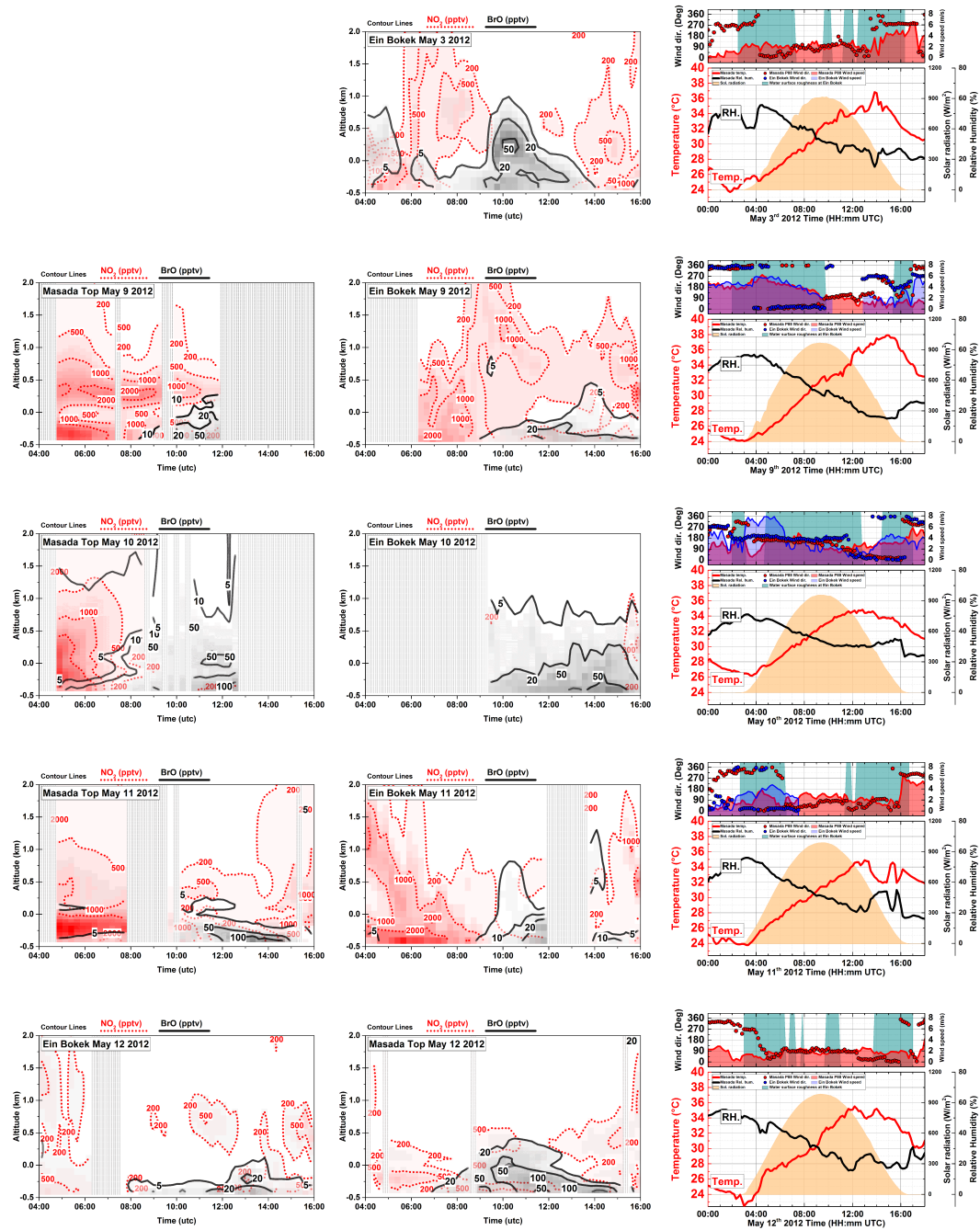
Fig. 10.22: Combined vertical profiles of BrO (black solid lines, pptv) and NO$_2$ (red dotted lines, pptv) measured during May 2012. Exemplary days are shown. For date and location, refer to plot labels.

November 2014
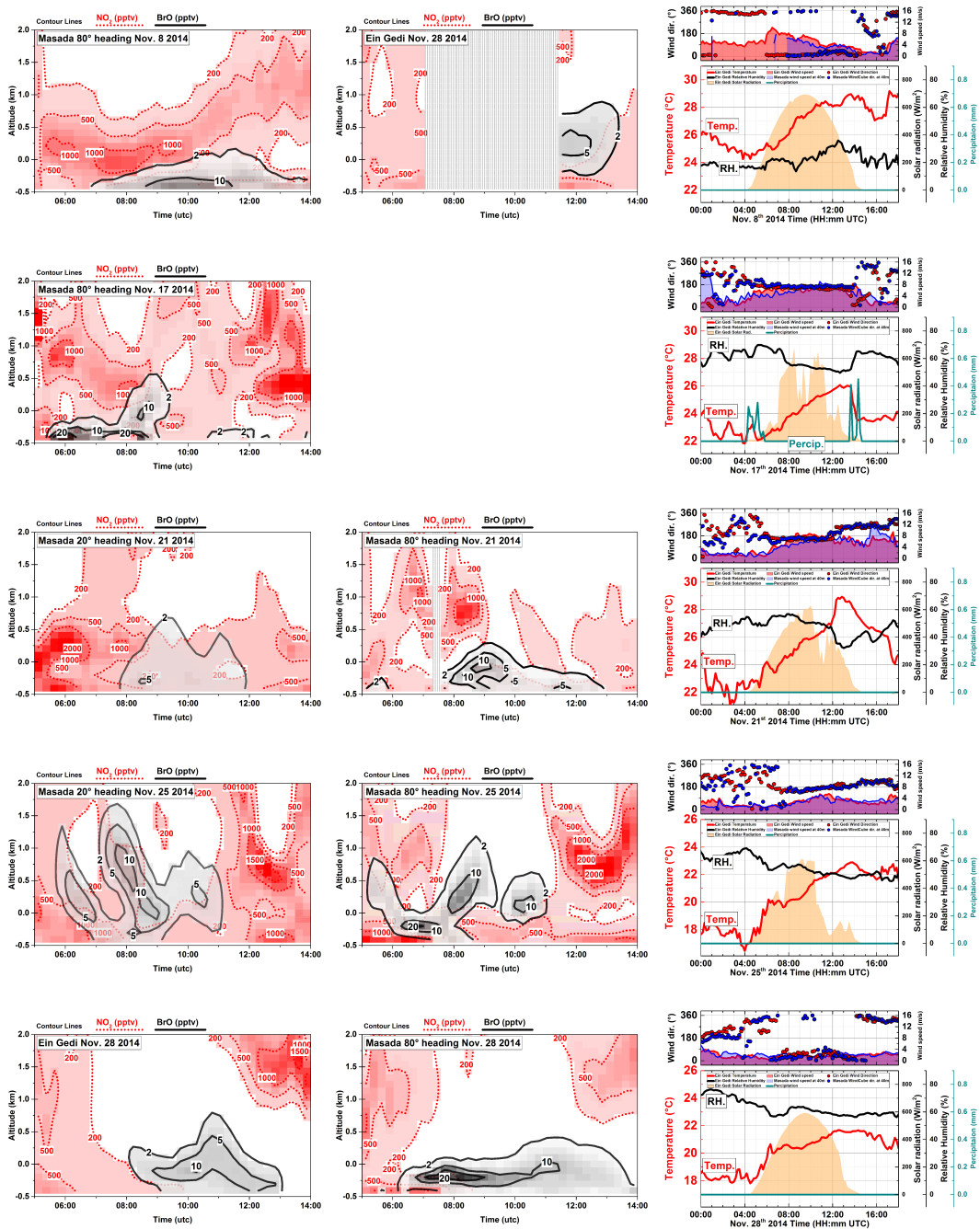
Fig. 10.23: Combined vertical profiles of BrO (black solid lines, pptv) and NO_2 (red dotted lines, pptv) measured during November 2014. Exemplary days are shown. For date and location, refer to plot labels. Northern locations are always in the left column.

As already shown above (figure 10.21), the total NO_2 abundance was significantly larger in Nov. 2014 compared to May 2012. However, the vertical profiles in figure 10.23 show that the major amount of NO_2 is often located in higher altitudes while mixing ratios inside the valley (below 500 m absolute altitude) are often in the range of 200 pptv to 500 pptv and, thus comparable to May 2012. While in 2012, mixing ratios above 1 ppbv NO_2 where exclusively observed after sunset, the data of November 2014 frequently shows elevated layers between 1 and 2 ppbv of NO_2 in the morning, noon and afternoon. The spatial and temporal characteristics of BrO and NO_2 are similar to 2012. Especially data from Nov. 8th and 28th, where moderate northerly wind prevailed, shows a distinct temporally and spatially separation of BrO and NO_2. Typical BrO to NO_2 ratios of 1:100 and below are observed at the boundaries of the profiles, which is a factor of up to three lower than in 2012. Considering the significantly lower solar radiation in 2014 (peaks values of 600 W/m^2 and frequently cloud coverage vs. 1000 W/m^2 and sparse cloud coverage in 2012, see also figure 10.3), this indicates reduced photolysis of $BrONO_2$ leading to lower BrO abundances.

Consideration of $BrONO_2$

The measurements of vertical profiles show, that BrO and NO_2 mostly mutually exclusive both temporally and spatially for BrO above 5 pptv and NO_2 above 200 pptv. The time series of vertical profiles (figures 10.22 and 10.23) show overlap regions, where BrO and NO_2 are coexistent with typical mixing ratios of 2 pptv and 200 pptv, respectively. Figure 10.24 illustrates the NO_2 to BrO ratio by solid blue lines on May 3rd 2012 and Nov. 25th 2014.
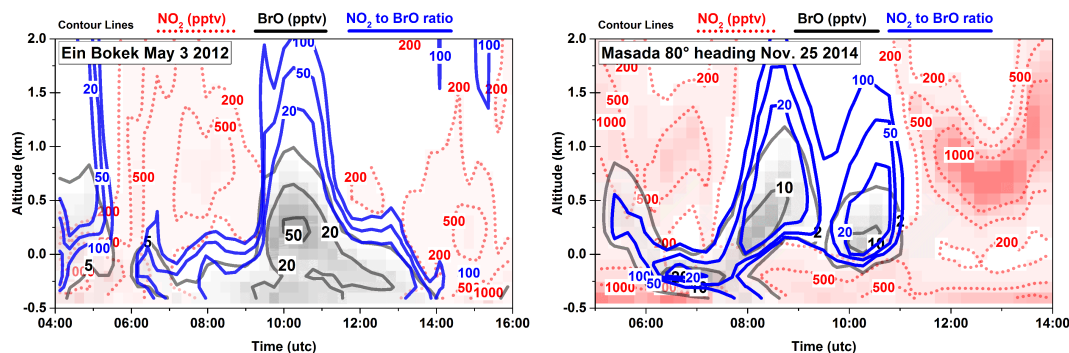
Fig. 10.24: **Top:** *Combined vertical profiles of BrO (black solid lines, pptv) and NO$_2$ (red dotted lines, pptv). Further, the NO$_2$ to BrO ratio is display (blue solid line).*

This observations agree with the findings from Tas et al. [2008]. The authors performed model studies based on data from field measurements. One of the conclusions was, that at below a threshold of 200 pptv NO$_2$, the formation of BrO is increased with increasing NO$_2$, which is caused by the uptake and recycling of BrONO$_2$ on aerosol surface.

However, above this threshold, an increase of NO$_2$ leads to an decrease of BrO which is due to the formation of BrNO$_2$ and BrONO$_2$, in which BrNO$_2$ play a less important role during daytime due to its fast photolysis. Further, the authors showed, that the total amount of bromine species generally increased in the presence of NO$_2$. To estimate the abundance of BrONO$_2$ based on the measurements of BrO and NO$_2$, the major sinks for BrONO$_2$ have to be considered which are:

1. Photolysis

2. Uptake on aerosol surfaces

3. Thermal decomposition.

Deters et al. [1998] calculated the photolysis rates for BrONO$_2$ to be $2.2 \ 10^{-3}$ s^{-1} and $1.3 \ 10^{-3}$ s^{-1} at solar zenith angles (SZAs) of 20° and 60° leading to

lifetimes of 8 and 12 minutes respectively. Figure 10.3 shows histograms of the SZAs during the two measurement campaigns of this work. With noon SZAs of 10° and 50°, the values from Deters et al. [1998] seem suitable to estimate the photolytic life time of $BrONO_2$.
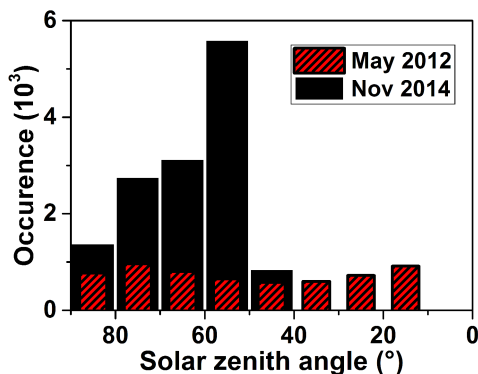
Fig. 10.25: Histogram of solar zenith angles of May 2012 (red shaded bars) and November 2014 (black bars).

Holla et al. [2015] showed that the uptake on aerosol surfaces during hazy conditions (visibility of 5 km) at the Dead Sea is in the order of 10 to 20 minutes for aerosol diameters of 0.4 μm and about 27 minutes for diameters of 1 μm (which are the main diameters modes of aerosol distribution at the Dead Sea according to Levin et al. [2005]). The temperature used for the calculation was 303K (30°C)

Another potential sink is the thermal dissociation of $BrONO_2$ via reaction 10.2. Using thermal decomposition rate by Orlando et al. [1996] leads to lifetimes of several hours. Figure 10.26 shows histograms of calculated lifetimes against thermal decomposition based on temperature data from the weather stations on 2012 and 2014.

$$BrONO_2 + M \xrightarrow{k} BrO + NO_2 + M$$

$$\text{with } k = 2.79\text{x}10^{13} \exp(-103[kJ/mole]/RT) \text{ s}^{-1} \qquad (10.2)$$
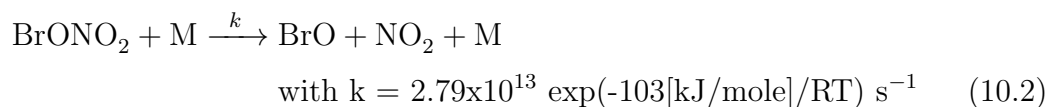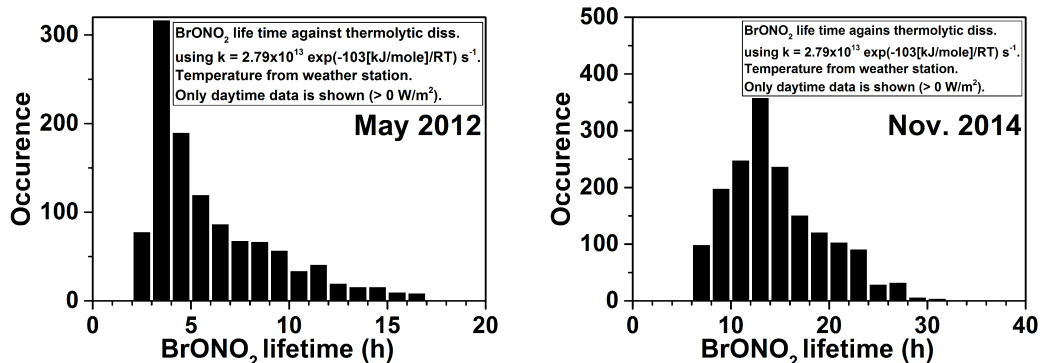
Fig. 10.26: Histograms of BrONO$_2$ life times against thermal decomposition calculated based on temperature data from weather stations in May 2012 (left) and November 2014 (right).

The following table 10.1 summarizes the major BrONO$_2$ sinks and their time scales under Dead Sea condisitons.

Mechanism	corresponding lifetime at Dead Sea conditions
Photolysis	8 - 12 min
Uptake on aerosol surface	10 - 30 min
Thermal decomposition	5 - 10 h

Table 10.1: Summary of the typical sinks and resulting lifetimes of BrONO$_2$ at the Dead Sea.

BrONO$_2$ is formed by the reaction of BrO and NO$_2$ described in equation 10.3 with k$_{10.3}$ taken from Atkinson et al. [2007].

$$BrO + NO_2 \longrightarrow BrONO_2 \quad k_\infty = 1.8 \text{ x } 10^{-11} \text{ cm}^3 \text{ molecule}^{-1} \text{ s}^{-1} \qquad (10.3)$$
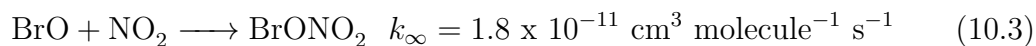
Since this reaction is rather fast, typical lifetimes of BrO with respect to the formation of BrONO$_2$ are in the order of seconds. In figure 10.27, a histogram of BrO life times against the reaction with NO$_2$ are calculated from LP-DOAS

measurements in May 2012 is shown. Only daytime values are shown. The data shows, that the daytime mixing ratios of NO_2 lead to a typical BrO lifetime of below 1 second.
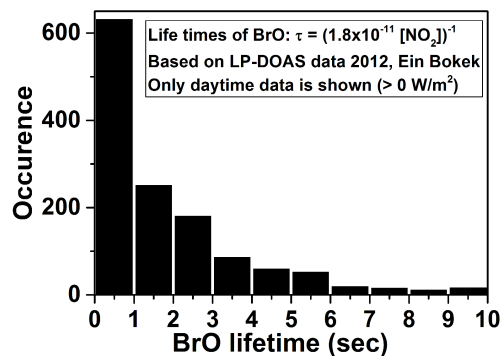
Fig. 10.27: Histogram of BrO life times with respect to the reaction with NO_2 from LP-DOAS data in May 2012. Only daytime values are shown.

Since the formation of $BrONO_2$ is much faster than its depletion, one can assume equilibrium conditions described by

$$0 = \frac{\mathrm{d}}{\mathrm{dt}} [BrONO_2] = k\, [BrO]\, [NO_2] - J_{BrONO_2}\, [BrONO] , \qquad (10.4)$$

leading to

$$[BrONO_2] = \frac{J_{BrONO_2}}{k\, [BrO]\, [NO_2]} \qquad (10.5)$$

to estimate the abundance of $BrONO_2$ from measurement data of BrO and NO_2. Using equation 10.5, profiles of $BrONO_2$ can be calculated from profiles of BrO and NO_2. Two examples are shown in figure 10.28. However, since a constant (noon) photolysis rate is used for the calculation of the profiles, the $BrONO_2$ abundance in during morning and afternoon is most likely underestimated by a factor 6 to 10 (according to $BrONO_2$ photolysis rates by Deters et al. [1998]).
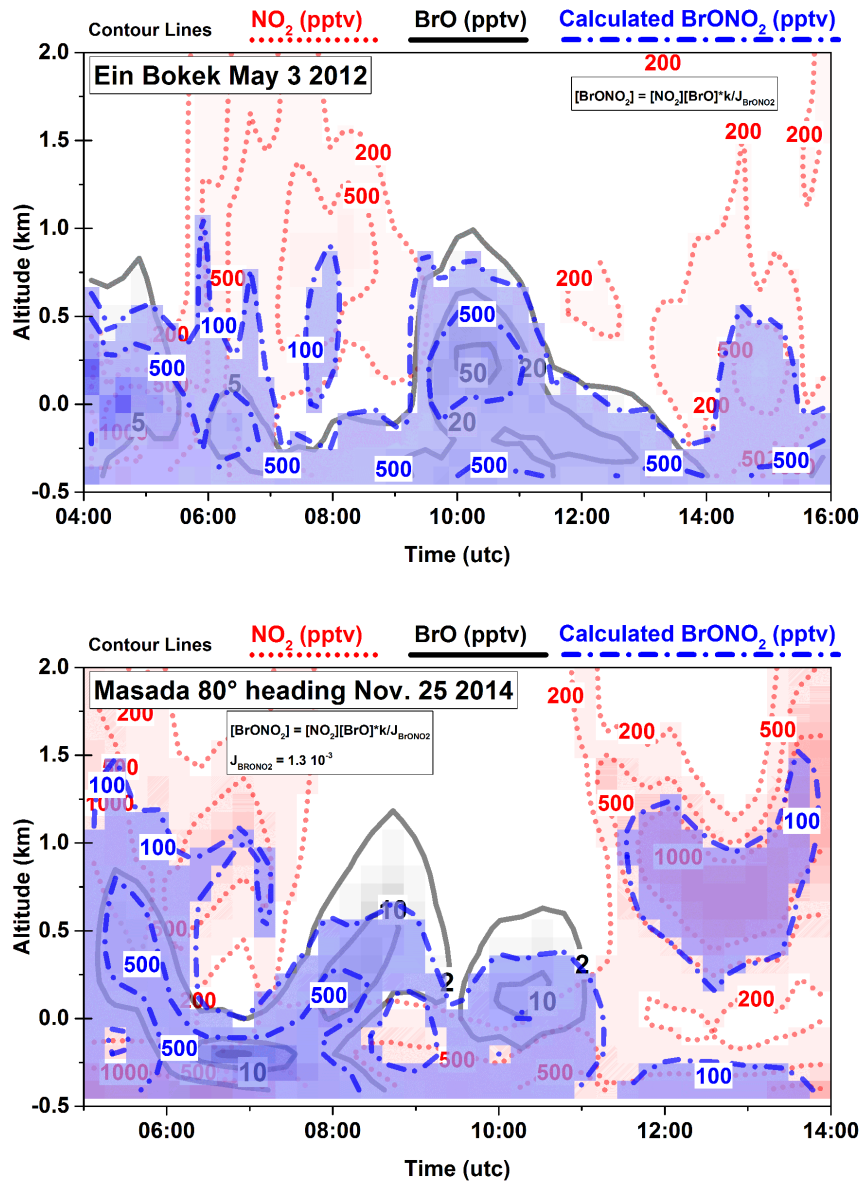
Fig. 10.28: Calculated vertical profiles of $BrONO_2$ from data on May 3rd 2012 (top) and Nov. 25rd 2014 (bottom).

10.3 Iodine monixide

10.3.1 Comparison with meteorology

When investigating the correlation of wind direction and IO VCD (Wind rose plots in figure 10.29) one recognizes that the highest VCDs at Masada (above $3 \cdot 10^{12}$ molec/cm^2) coincide with northerly and southerly winds which are usually correlated to higher wind speeds (see meteorology results in section 8.1). At Ein Bokek, VCDs are lower than at Masada and they are observed at wind directions uniformly between north and east. Thus, highest IO VDCs are observed during the "purging" wind scenario (northerly or southerly winds, increased wind speed) which is contrary to the behavior of observed BrO (see figure 10.5). Further the correlation of mixing ratios by LP-DOAS and MAX-DOAS VCDs with wind speed are shown in 10.29, lower plots. Mixing ratios near ground level seem to be highest at wind speeds between 2 and 4 m/s. However, the total amount of IO, represented by VCDs, seem not to be affected by wind speed.
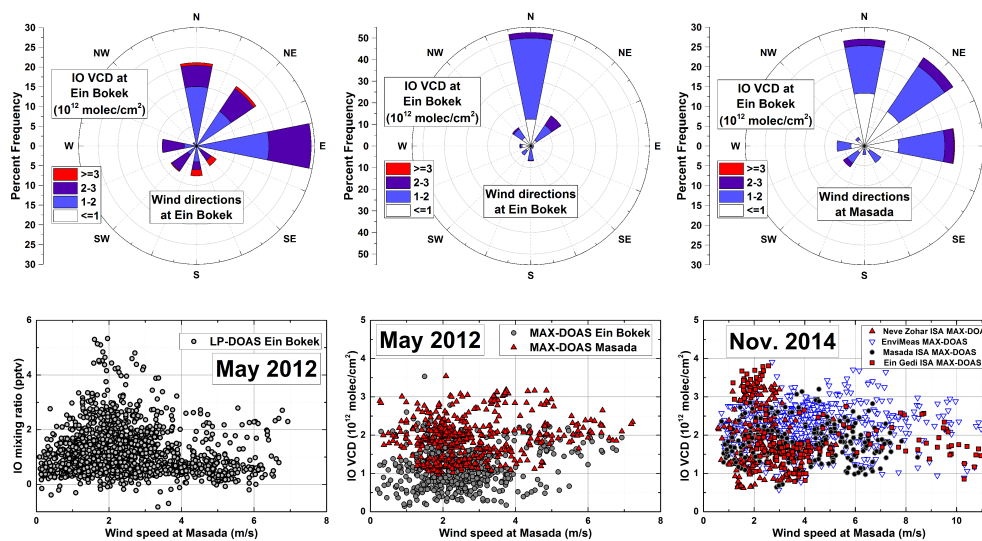
Fig. 10.29: Upper plots show wind rose showing the occurrence of IO VCDs by MAX-DOAS at given wind directions. For locations refer to plot labels. Lower plots show IO mising ratios by LP-DOAS (lower left plot) and VCDs retrieved from MAX-DOAS (lower middle and right plot) as a function of horizontal wind-speed.

10.3.2 Comparison of surface vmrs from MAX-DOAS and LP-DOAS

By comparing the mixing ratios measured by the LP-DOAS with the surface mixing ratios of the nearby MAX-DOAS, one can make assumptions about the vertical distribution of trace gases near the water surface. The height resolution of the profile retrieval is 100 m, the altitude of the MAX-DOAS is 20 m. Since no negative elevation angle is used in the retrieval, the MAX-DOAS surface vmrs are only affected by air masses from 20 m to 100 m (see figure 6.5). Thus the difference between MAX-DOAS and LP-DOAS vmrs provides information about the vertical gradient between 0 to 20 m and 80 to 100 m.
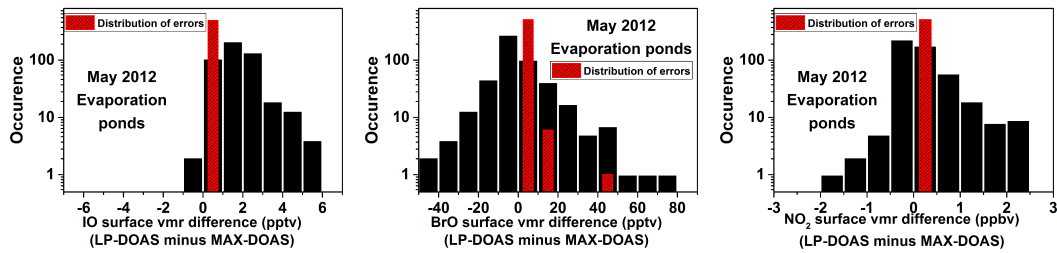
Fig. 10.30: Histogram of differences of surface mixing ratios between LP-DOAS and MAX-DOAS at Ein Bokek. The distribution of errors of the calculated difference (according to gaussian error propagation) is displayed in red.

The retrieved surface vmrs from the MAX-DOAS differ significantly from those measured by the LP-DOAS. Figure 10.30 shows a histogram of the difference between mixing ratios measured by LP-DOAS and surface mixing ratios retrieved by MAX-DOAS at Ein Bokek. While the distribution of BrO and NO_2 differences is roughly centered around zero, the distribution of IO differences is clearly shifted towards positive values. Positive values indicate that the LP-DOAS regularly observes higher amounts of IO.
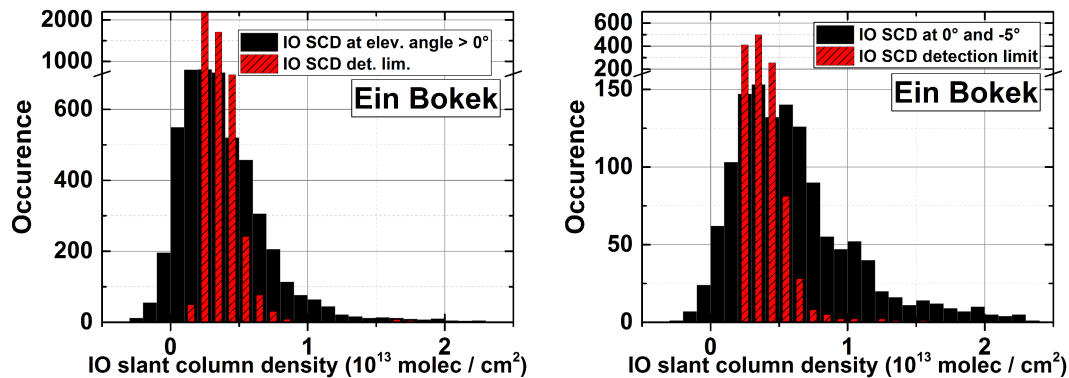
Fig. 10.31: IO slant column densities measured by the MAX-DOAS at Ein Bokek. Left plot shows SCDs of eleavtion angles larger than zero, which were used for the retrieval of volume mixing ratios. Right plot shows SCDs at 0° and -5° which were not used in the retrieval. Red bars indicate the distribution of detection limits, defined by four times the DOAS fit error.

The instrument at Ein Bokek observed significant SCDs of up to $1.2 \cdot 10^{12}$ molec/cm^2 were measured under elevation angles larger than zero (see figure 10.31, upper left plot). Note that only the SCDs of these elevation angles were used in the profile retrieval which leads to the surface vmrs and VCDs discussed in this section. However, large IO column densities were observed at elevation angles of 0° and -5°. The histogram at the bottom right of figure 10.31 shows SCDs measured under telescope elevation angles of 0° and -5° where large SCDs of up to $2 \cdot 10^{12}$ molec/cm^2 were regularly observed. An exemplary fit of IO under -5° can be found in figure 5.23 in section 5.1.6. Figure 10.32 displays the time series of the IO SCDs measured by the MAX-DOAS instrument at Ein Bokek. Zero degrees and downward looking elevation angles are emphasized by cyan and purple colors (for details see plot legends). Elevated IO SCDs values at 0° and -5° are clearly recognizable and significantly larger than under elevation angles larger than zero.
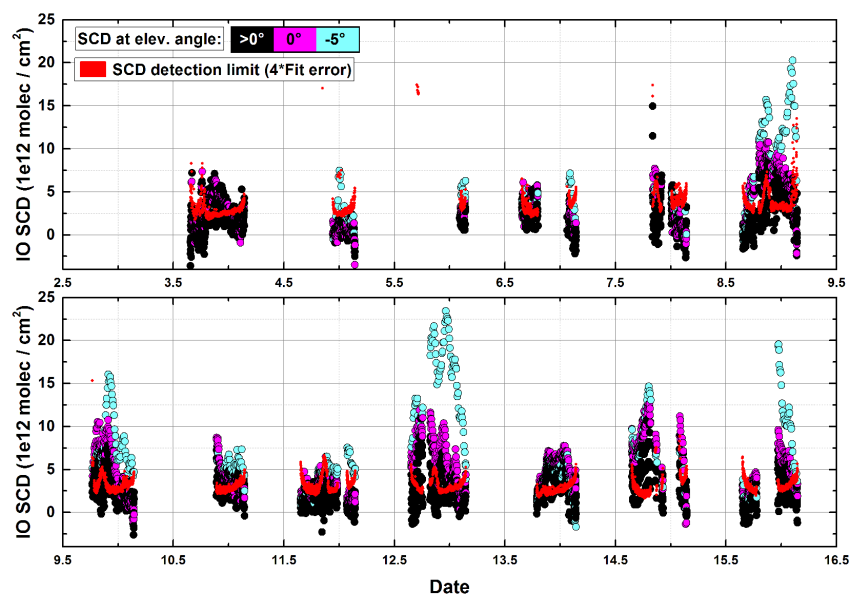
Fig. 10.32: IO slant column densities measured by the MAX-DOAS instrument at Ein Bokek. SCDs at elevation angles 0° and -5° (displayed in purple and cyan) indicate enhanced IO anundance near ground level. Red dots represent the detection limits of all elevations which are defined as 4 times the fit error.

Since the retro reflector of the LP-DOAS is positioned at a lower altitude compared to the telescope, its light path is slightly pointed downwards and air masses below the MAX-DOAS instrument are probed. Comparing the SCDs of elevation angles pointing upwards and downwards with the vmrs measured by the LP-DOAS indicates that a large fraction of the observed IO abundance might be located in the first few meters above the water surface. If the IO abundance would be driven by horizontal transport, significant SCDs would be observed by the MAX-DOAS also at larger telescope elevation angles, which is not the case.

10.3.3 Correlation of IO and water surface roughness

Figure 10.33 shows time series of observed water surface roughness (WSR, see section 6.2 for description) at Ein Bokek and IO mixing ratios measured by LP-DOAS close to the water surface. The data suggests that increased levels of IO correlate with small waves on the water surface. Especially the fast increase of IO with increasing WSR supports this theory.

Data from November 2014 shows a similar correlation. In figure 10.34, IO profiles of Nov. 21th and 28th are displayed together with pictures of the water surface. On Nov. 21th, the water surface appeared darker while on 28th, reflections of the Judean mountains are clearly visible. The observations are compatible with the meteorological data shown in the upper plots of the figure. Strong winds at 8 m/s lead to waves and thus, enhanced water surface roughness, while the low winds on 21th leave the water surface calm.
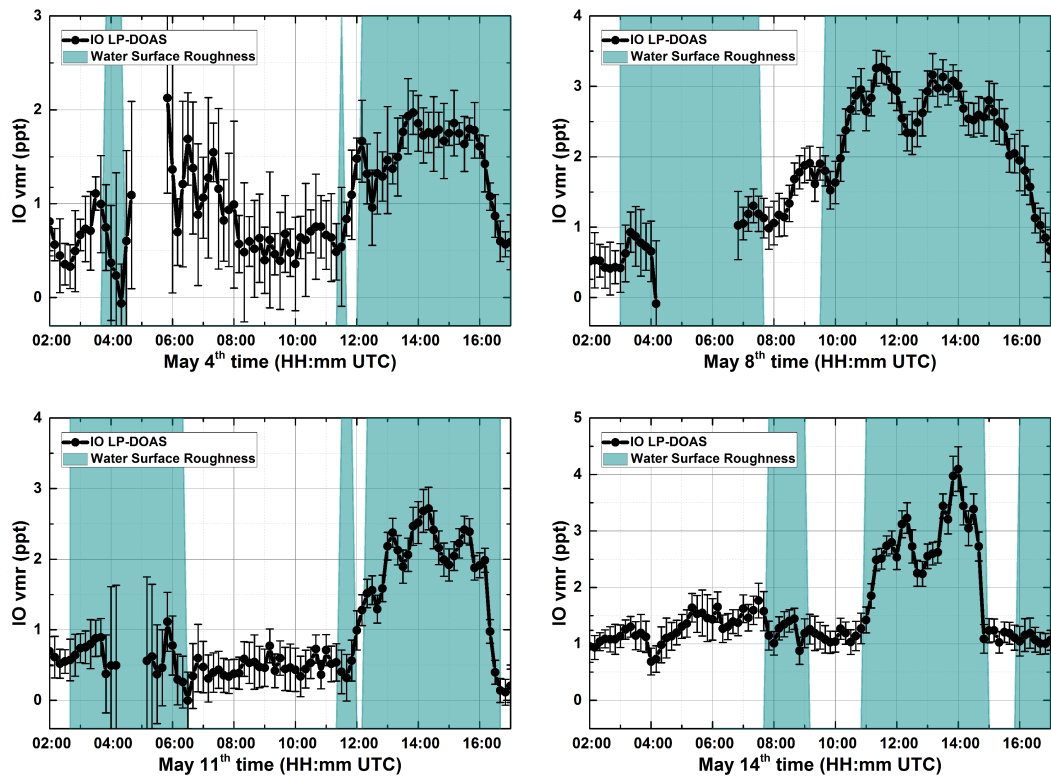
Fig. 10.33: Time series of IO vmrs by LP-DOAS and water surface roughness on the days of May 4th, 8th, 11th and 14th. Black dots represent IO mixng ratio, Cyan area represents waves (enhanced water surface roughness) observed by camera pictures. The time series show a strong correlation between water surface roughness and IO.
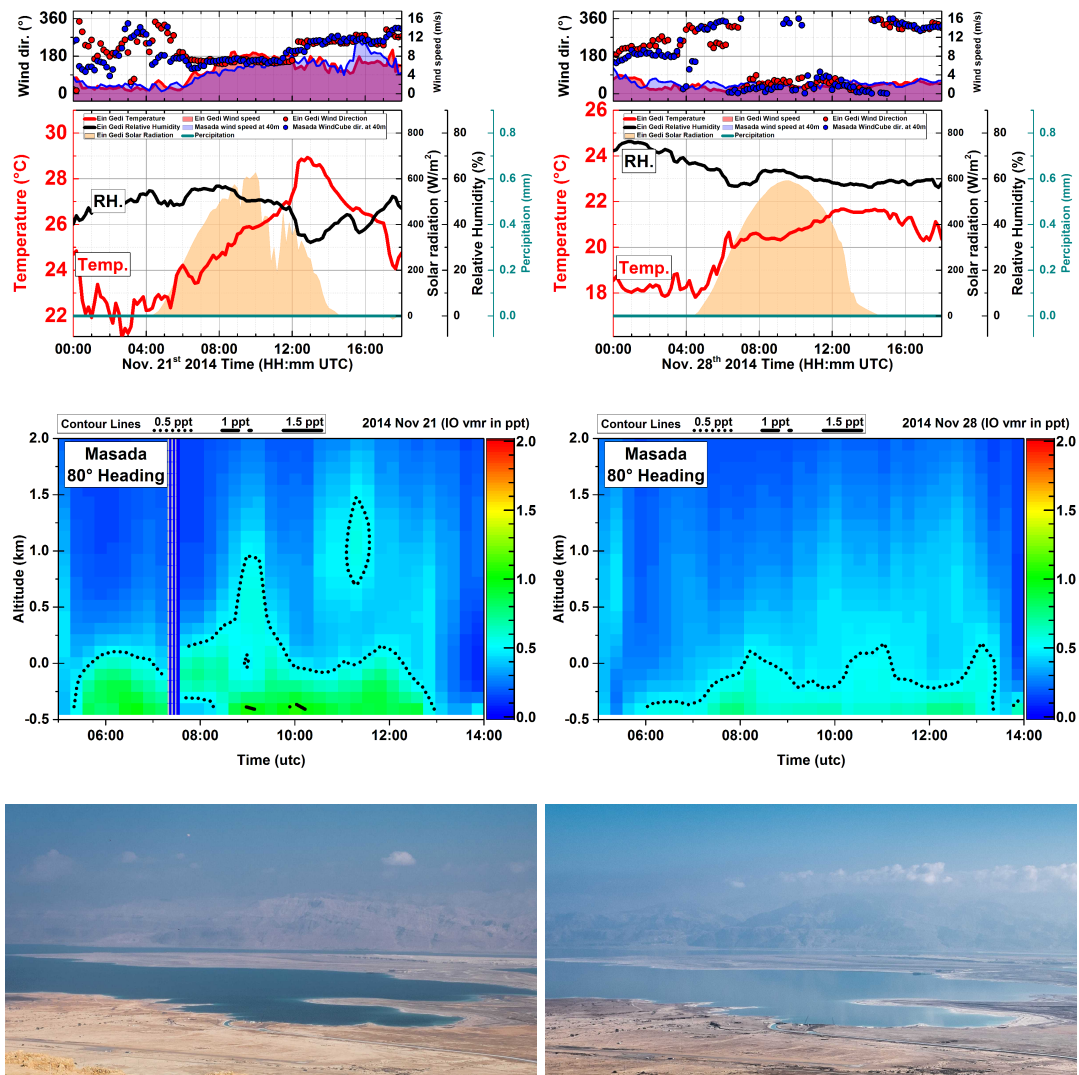
Fig. 10.34: Vertical profiles of IO observed at Masada on Nov. 21th and 28th in 2014. The pictures show the water surface at Masada on 21th 11:30 UTC (left) and 28th 08:11 UTC (right).

Another example of increased IO and wave occurence can be observed at Ein Gedi (figure 10.35) on Nov. 28th. Pictures taken on 06:44 and 06:53 UTC indicate waves on the water surface. By comparing the two pictures, a horizontal movement of the wave front can be observed. This may be caused by vertical winds hitting the water surface and causing waves. The movement of the wave

front may be due to the movement of such a wind system itself, however, this is highly speculative.
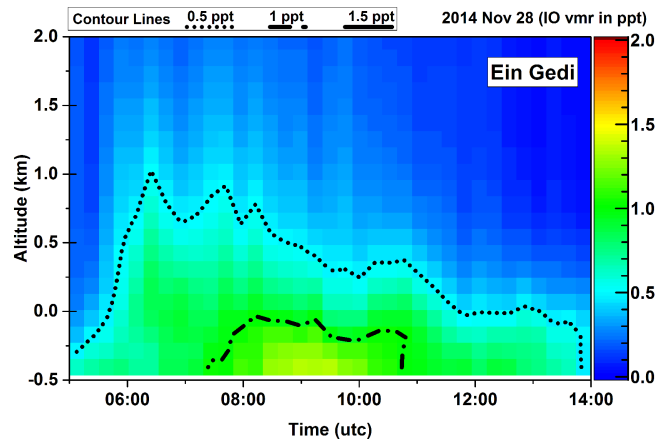
Fig. 10.35: Vertical profiles of IO observed at Ein Gedi on Nov. 28th in 2014. The pictures (taken under viewing direction of the MAX-DOAS(east)) show the water surface 06:44 (left) and 06:53 UTC (right). The dark area on the water surface indicates a wind system of vertical winds hitting the surface. The apparent horizontal movement of the dark area indicates a movement of the wind system in southern direction.

10.3.4 Consideration of IONO$_2$ and I$_2$
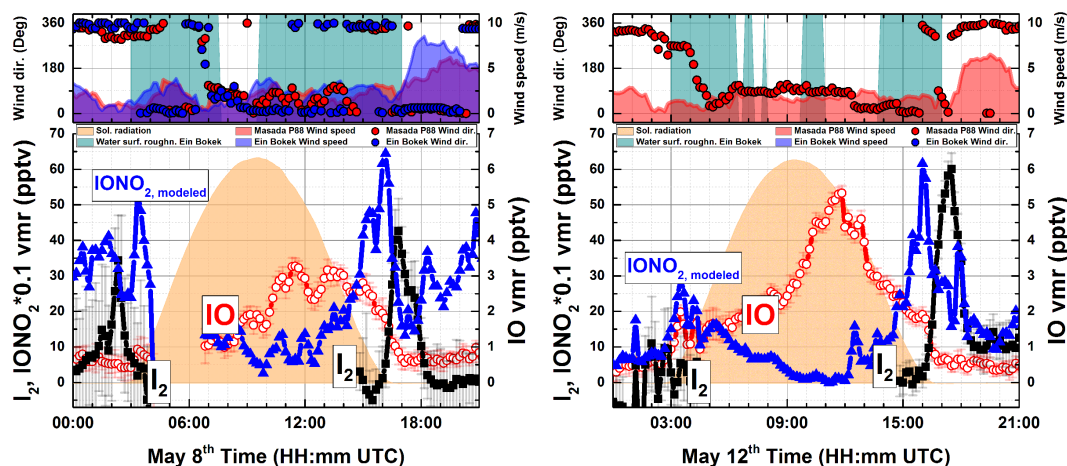
Fig. 10.36: Exemplary days of LP-DOAS data showing I$_2$ mixing ratios of up to 60 pptv after sunset subsequent to increased IO abundance of 3 to 5 pptv during daytime. Note that the of the modeled IONO$_2$ data is scaled by a factor of 0.1.

During the measurements in 2012, the LP-DOAS instrument observed molecular iodine (I$_2$) on several days shortly after sunset with mixing ratios of up to 70 pptv subsequent to increased daytime IO abundance (see figure 8.21 in the results section). IO, I$_2$ and model IONO$_2$ times series of exemplary days are shown in figure 10.36. Due to its short photolytic life time of a few seconds (Saiz-Lopez et al. [2004]), I$_2$ occurs only after sunrise. The dynamics show a characteristic increase and decrease within two hours, which can also be observed on other days of the measurement period. The slope of the increase might be influenced by residual solar radiation which suppresses the formation of iodine. The decreasing slope might be addressed to transport processes due to increasing wind speeds, which occur regularly after sunset and are most likely caused by catabatic winds from the valley slopes (see section 2.1). However, nighttime chemistry is also likely to play an important role. Assuming the photolysis of I$_2$ being the source of daytime IO, significantly higher IO abundances are expected since the photolysis of one iodine molecule can potentially lead to the formation of two iodine radicals

and thus two IO molecules . The fact that only a few pptv of IO are observed indicates that a large amount of reactive iodine is depleted by the formation of other iodine compounds. A potential candidate is the formation of $IONO_2$. Assuming a photolysis rate of J = 3 x 10^{-3} s^{-1} (according to Saiz-Lopez et al. [2004] and a rate coefficient k = 1.6 x 10^{-11} cm^3 $molec^{-1}$ s^{-1} (Atkinson et al. [2007]), the equilibrium mixing ratio of $IONO_2$ can be calculated from measured IO and NO_2 via equation 10.6.

$$[IONO_2] = \frac{k[NO2][IO]}{J} \tag{10.6}$$

The modeled $IONO_2$ mixing ratios are in the range of 100 to 200 pptv during daytime and may explain the "missing" reactive iodine when concerning the observed I_2 mixing ratios.

10.3.5 Conclusion of IO observations

The correlation with the water surface roughness may indicate a thin layer above the surface which is enriched with IO during low wind speeds. At increasing winds this layer may be disturbed by turbulence and the enriched air masses may be transported upwards into the field of view of the LP-DOAS and MAX-DOAS instrument leading to increased IO signals. Another possibility would be the initiation of a chemical mechanism caused by the introduction of air masses with a different chemical composition into the layer near the water surface (e.g. uptake of ozone leading to emission of iodine as stated in Carpenter et al. [2013], and described in section 3.2). Carpenter et al. [2013] also mentioned that surface saturation effect may affect the emission rate of I_2 due to decreased I^- concentration at surface layer. Other works (Sakamoto et al. [2009] and Hayase et al. [2010]), observed these saturation effects with unstirred iodid solutions. The correlation of IO abundance and water surface roughness, which can be compared to "stirring", supports this theory. Figure 10.37 shows a sketch illustrating the proposed mechanism to explain the correlation of waves and IO abundance. Further, the detection of molecular iodine after sunset by LP-DOAS suggests I_2 as a precursor for IO during daytime and is an additional strong indication

of the interaction between the mechanism by Carpenter et al. [2013] and water surface roughness Of the Dead Sea.
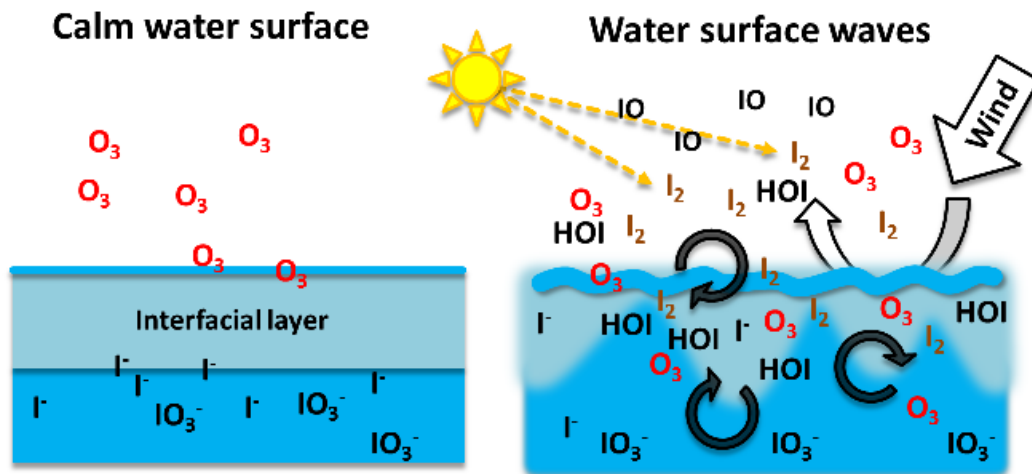
Fig. 10.37: Sketch of a proposed mechanism which explaines the observed correlation of Io and waves at the Dead Sea based on findings by Carpenter et al. [2013]. Waves indicate mixing in the interfacial layer enhancing its iodide content followed by the formation of HOI and I_2 which can degas, being quickly photolyzed and, thus, leading to the formation of IO during daytime.

10.4 Chlorine dioxide

10.4.1 May 10*th* 2012
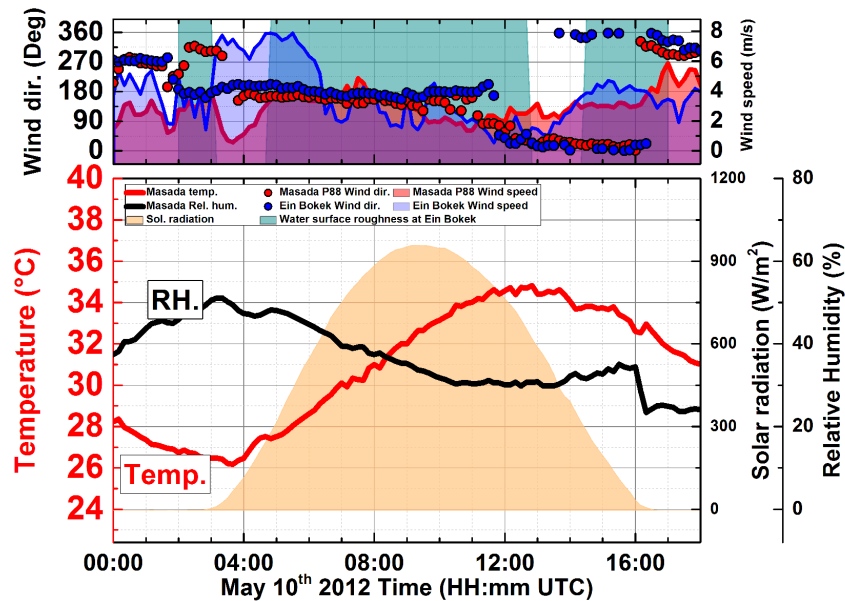
Fig. 10.38: Meteorological data taken on May 10th 2012. Strong southerly winds prevail through out the day, which represents exceptional conditions. Upper plot shows wind direction (dots) and speed (area) at Masada (red) and Ein Bokek (blue). At 12:00 UTC, a change from southerly to northerly winds is observed.

On May 10th 2012, the meteorology was exceptional compared to the rest of the measurement period (see figure 10.38). Strong southerly winds at 4 to 8 m/s prevailed throughout the day and are observed by both weather stations. Changing wind directions and, hence, sea breeze scenarios were not observed. Further, aerosol abundance at Masada showed a large vertical extend from ground level to absolute altitudes of 1 km, supported by camera pictures (see figure 10.39). Due to a failure, the instrument at Ein Bokek was not measuring until 09:00 UTC, however, camera pictures show enhanced aerosol load at Ein Bokek in the morning hours. Thus, it is assumed that the aerosol diurnal variation is similar to other days, where an ascent of aerosols is observed between 06:00 and 08:00 UTC

before settling in an elevated layer at 1 km absolute altitude (compare aerosol profiles in figure 8.6 in the results section). The data suggests that the strong winds lead to 1) the intake of dust particles into the valley from the surrounding or, 2) the mobilization of particles, including sea salt aerosol from the soil or the water surface of the Dead Sea. Both assumptions represent scenarios which differ significantly from the conditions during the other days of the campaign.
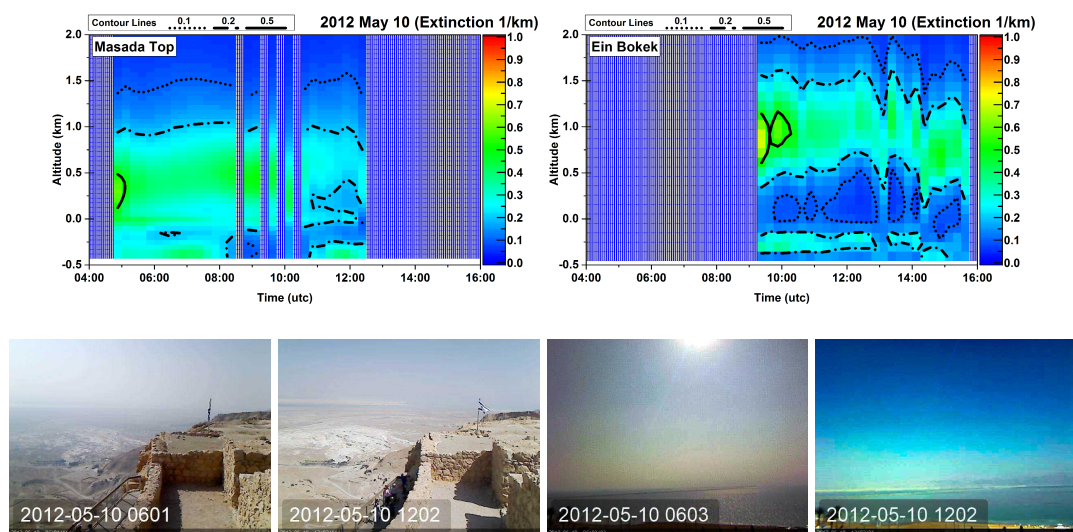
Fig. 10.39: Aerosol profiles and pictures taken at Masada (left) and Ein Bokek (right) on May 10th 2012. Reft pictures are taken at Masada top, right pictures at Ein Bokek. For date and time, see label.

Figure 10.40 shows combined vertical profiles of OClO, BrO and IO from MAX-DOAS measurements at Masada and Ein Bokek on May 10th 2012. The data shows several interesting features. The vertical extension of BrO starts to increase in the morning. The data shows how the 10 pptv front ascends monotonous from ground level to an absolute altitude of 1 km within 5 hours. This behavior is already discussed in section 10.2.3 and can be addressed to the vertical distribution of NO_2 and hence, its chemical interaction with BrO. The spatial and temporal maximum of BrO, 50 pptv at 12:00 UTC and 0 m absolute altitude, coincides with the maximum of OClO (4 pptv), also both in altitude and time.

Further, the vertical distribution of IO seems to show a minimum at increased OClO levels. This behavior suggests that both IO and BrO participate in the formation of OClO via reactions 10.7 and 10.8 which implies the existence of reactive ClO.

$$BrO + ClO \longrightarrow Br + OClO \tag{10.7}$$

$$IO + ClO \longrightarrow I + OClO \tag{10.8}$$

Assuming equilibrium, OClO photolysis $J = 7.2$ x $10^{-2}s^{-2}$ (according to Gliß et al. [2015]), $k_{10.7,298K} = 6.8$ x 10^{-12} cm^3 molec^{-1}s^{-1} by Atkinson et al. [2007]) and neglecting IO, the ClO mixing ratio at the OClO maximum can be calculated resulting in 33 pptv. Equation 10.10 provides a convenient way to calculate the equilibrium ClO mixing ratio at given BrO and OClO by unifying J/k 10.9.

$$[ClO] = \frac{J[OClO]}{k_{10.7}[BrO]} \tag{10.9}$$

$$[ClO]_{pptv} \approx 424\frac{[OClO]_{pptv}}{[BrO]_{pptv}} \tag{10.10}$$
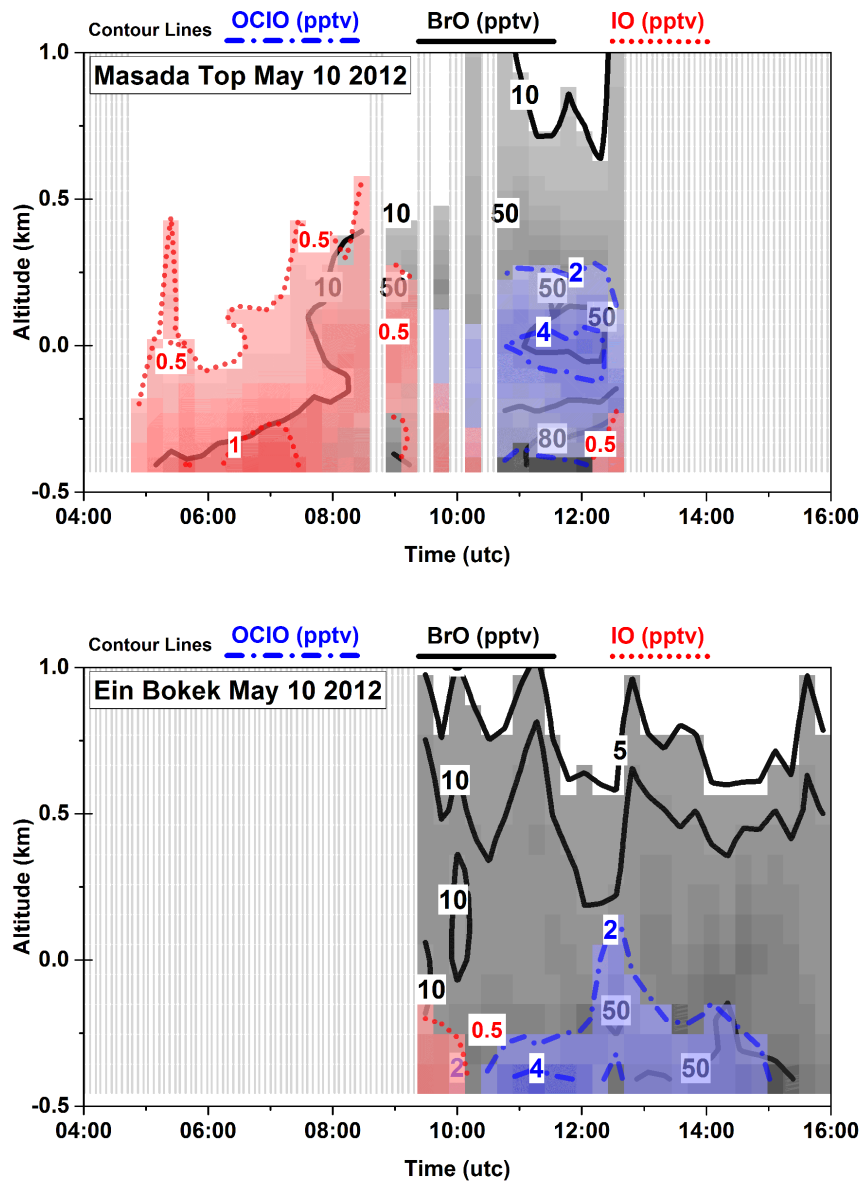
Fig. 10.40: Combined profiles of OClO (blue, dash dots), BrO (black, solid) and IO (red, dotted) measured at Masada top (upper plot) and Ein Bokek (lower plot) on May 10th 2012. Contour lines indicate volume mixing ratios in pptv.

The large vertical extend of the aerosol abundance suggest the mobilization of aerosols from the water surface or the soil of the valley or the intake of dust by mesoscale transport. Given this assumption, the composition of aerosols was

different compared to days with lower wind speeds and sea breeze scenarios, which suppress the intake of air masses from outside the valley. The detection of OClO might be explained by the lower bromine to chlorine ratio of the mobilized aerosols leading to enhanced release of BrCl and Cl_2 and reduced release of Br_2. OClO is predominately formed by the reaction of BrO with ClO. Thus formation of $ClONO_2$ from ClO and NO_2 is likely to happen and can amplify the release of reactive chlorine from aerosols.

At Ein Bokek, OClO is observed between 10:00 and 12:00 UTC at altitudes near the ground. Similar to Masada, OClO and IO seem to be mutually exclusive. The short increase in vertical extent of OClO between 12:00 and 13:00 UTC coincides with a change in wind directions from south over east to north (see figure 10.38). This indicates vertical transport during (a short) sea breeze scenario. This is supported by the decrease of vertical extend after 13:00 UTC, when wind direction is northerly. The different altitudes of the OClO abundance at Masada and Ein Bokek may be due to enhanced convective ascent of air masses over the land mass between northern and southern basin compared to the ascent over the water surface over the evaporation ponds. The fact that at Ein Bokek, OClO is predominantly observed at low altitudes arises the assumption that, the strong southerly winds lead to the formation of sea salt aerosols which are transported in northern direction. Once over the (warm) land mass, air masses under go vertical transport due to convection. Figure 10.41 shows a sketch of the proposed mechanism. At Masada the maximum of OClO is observed within elevated layers. This indicates, that the contribution of mobilized dust from soil is probably small than of sea salt aerosol. Otherwise, OClO would be observed also near ground level at Masada. However, the contribution of dust can not be ruled out by these observations.
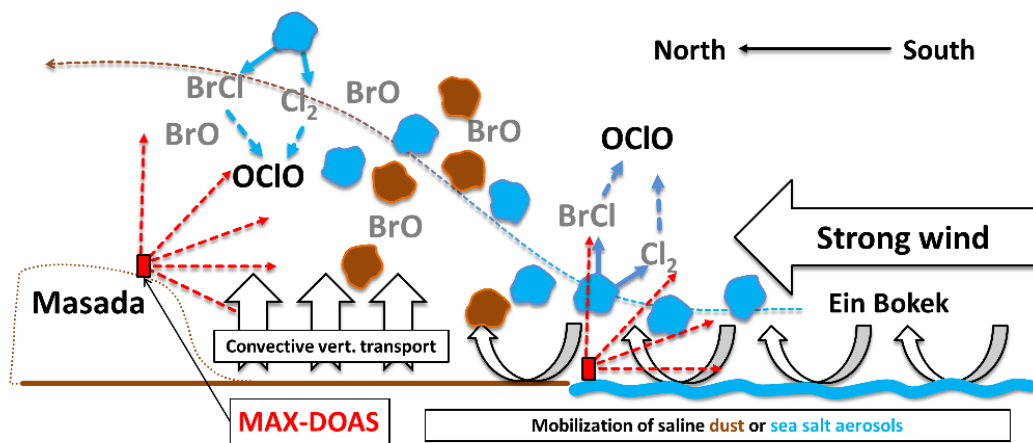
Fig. 10.41: Sketch of the mechanism, which may explain the vertical distribution of OClO during strong southerly winds on May 10th 2012. Strong southerly winds lead to the mobilization of sea salt aerosols and/or dust particles from saline soil which are assumed to release precursors of reactive chlorine.

10.4.2 November 17th 2014
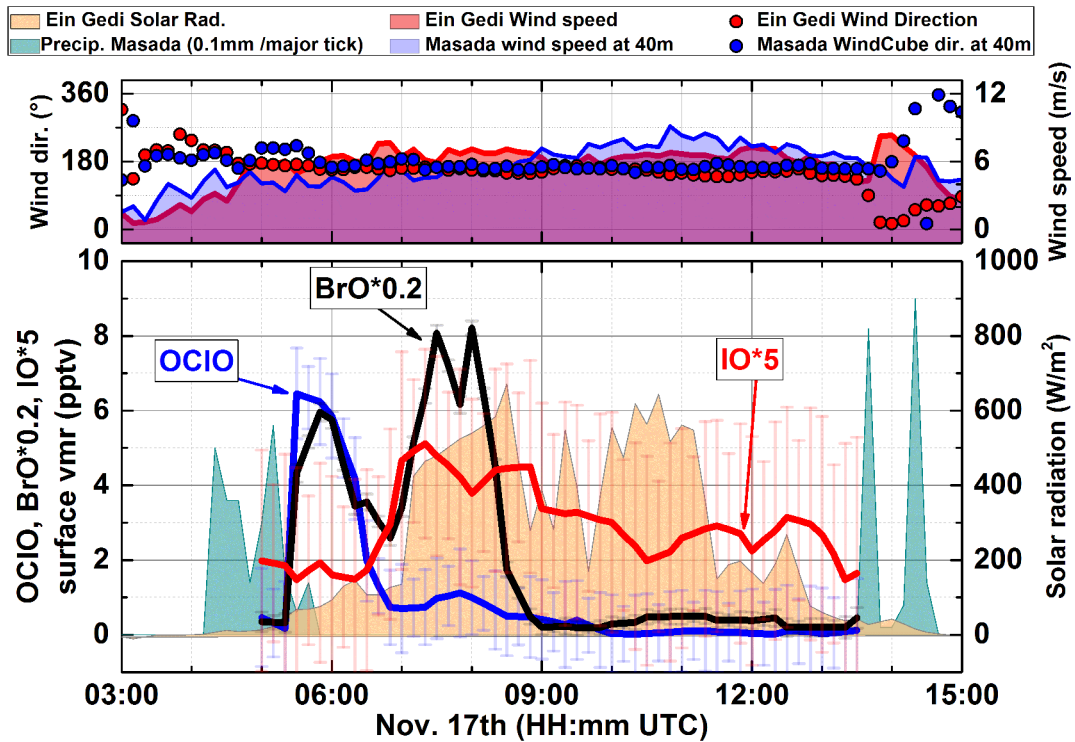
Fig. 10.42: Time series of surface vmrs of OClO (blue), BrO (black scaled by factor 0.2) and IO (red, scaled by factor 10) from MAX-DOAS data at Masada on Nov. 17th 2014. Errors are total retrieval errors (measurement and smoothing error).

During the campaign in 2014, OClO could also be observed on one single day, Nov. 17th, during exceptional meteorological conditions shown in figure 10.42. Similar to the observation of OClO in May 2012, strong southerly winds with constant speeds of 6 m/s prevailed throughout the day. A short precipitation event occurred between 04:00 and 05:30 UTC. Shortly after the rain event, cloud coverage decreases leading to an illumination of the bottom of the valley by solar radiation. Simultaneously, ground level mixing ratios of OClO and BrO rose within 10 minutes from below the detection limit (approx. 1 pptv) to 6.5 pptv and 30 pptv, respectively. Between 06:00 and 07:00 UTC, OClO decreased

down to values of 1 pptv. BrO showed a similar behavior by decreasing to 15 pptv, however increased again to reach 40 pptv between 07:00 and 08:00 UTC. BrO showed an "M"-like temporal dynamic which indicates horizontal transport processes (as already discussed in section 10.2.1).

However, since solar radiation also shows a dynamic behavior due to changing cloud coverage, photochemistry can not be ruled out to drive the observed dynamics of BrO. Further, the increase of IO occurring with the second BrO peak at 07:00 UTC can also be addressed to both horizontal transport and photochemistry by increased solar radiation. Like in 2012, elevated levels of IO (above 1 pptv) seem to exclude OClO. The dynamics of measured solar radiation indicate that the decrease of OClO after 06:00 UTC is most likely driven by its photolysis due to enhanced solar radiation which, on the other hand, is assumed to drive the processes leading to the abundance of IO. This might explain the apparent anti-correlation of OClO and IO in this case.

In contrast to the observations of OClO in May 2012 (see above), where high aerosol abundance (extinction of 0.4 to 0.5 km^{-1}) was already present at sun rise, the rain event in of Nov 17th leads to a relative low aerosol load with observed extinctions between 0.1 and 0.2 km^{-1}. Profiles of aerosol extinction, OClO, BrO and IO are shown in figure 10.43. The low altitude and small vertical extend of OClO (300 m) indicates initial sources of reactive chlorine near the ground level.

Note that the geometry of the MAX-DOAS at Masada in 2014 was different to the one at Masada top in 2012. The measurement path in 2012 had a heading of 118° and only air masses over soil were observed. With a heading of 80°, the instrument in 2014 was also observing air masses above the water surface. Therefore the observed OClO distribution is compatible with the assumption that mobilized sea salt aerosols releasing chlorine species.
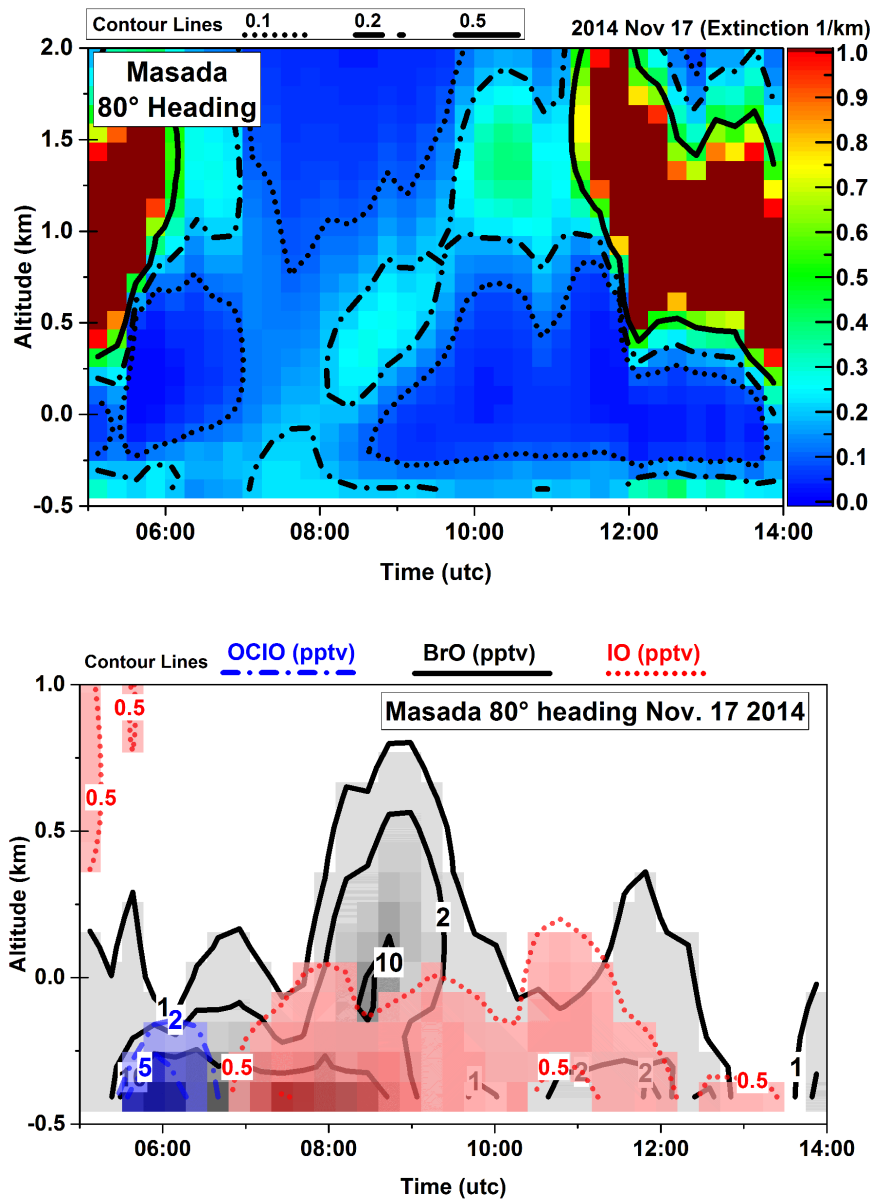
Fig. 10.43: Aerosol extinction profiles (top) and combined profiles of OClO, BrO and IO (bottom) measured at Masada on Nov. 17th 2014. Extinction color coded with a range from 0 to 1 km−1. Note the different y-axis scales of upper and lower plot.
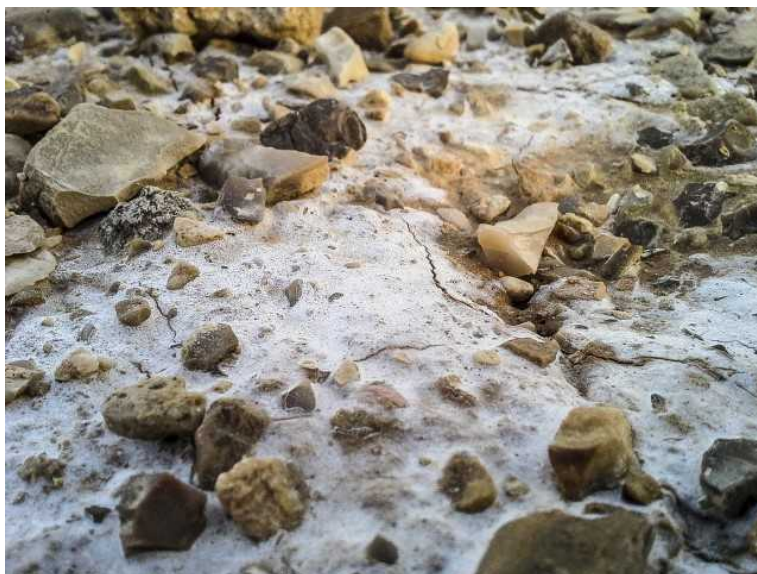
Fig. 10.44: Picture of saline soil recorded on Nov 26th 2014 at Masada.

Observations of the soil around the Dead Sea revealed the abundance of salt deposits probably caused by the evaporation of saline solutions after rain events. Figure 10.44 shows a picture of such a deposit. The picture was taken on Nov. 26th and may be the result of precipitation events on Nov. 17th and 24th (see meteorological data in figure 9.2 in the results sections). This arises the theory that rain events may lead to a mobilization of salt dust or saline soil particles which may have a different chemical composition compared to the particles which are usually observed during hazy conditions at the Dead Sea valley and which coincide with increased BrO abundances. Thus, the release of reactive chlorine species may be favored over the release of reactive bromine.

11

Conclusion and Outlook

Due to its exceptional high content of halides, the Dead Sea Valley (DSV)provides a predestined place to study the chemical processes of RHS in their natural environment. In the past, several measurements were carried out at the DSV, mostly focused on the observation of BrO (Tas et al. [2006], Hebestreit [2001]). The acquired data sets served as initial conditions for model calculations which are intended to provide a deeper insight in the RHS chemistry. Model calculations by Smoydzin and von Glasow [2009] showed the measurements could not be reproduced by models which consider gas phase reactions only. They assumed that heterogeneous processes on aerosol surfaces play a significant role for the total abundance of reactive bromine. Further, they had to reduce the air exchange between the DSV and its surrounding, thus, the strength of dilution, to reproduce the measurements. Also reactive halogen species are predicted to have a strong vertical gradient within the first few ten meters above ground level.

The fact that, vertical gradients, aerosols and meteorology (dilution) have a potentially larger impact on the distributions of RHS at the DSV demands to monitor this parameters parallel to the trace gas dynamics to provide a more suitable starting point for future model simulations. The goal of this thesis was to create such a data set. During two extensive field campaigns in May 2012 and November 2014, several DOAS instruments were deployed to measure vertical distributions of trace gases at a high time resolution of minutes. Together with the comprehensive meteorological data which was simultaneously acquired by the Karlsruhe Institute for Meteorology, the observed trace gas dynamics could

be separated into chemical driven processes and transport processes which are found out to have a large impact.

The measurements of 2012 and 2014 show a strong seasonal difference. In 2012 a strong variability in wind directions and wind speeds was observed. During daytime, wind directions were predominantly moderate with easterly and westerly directions indicating sea breeze scenarios. During night strong northerly winds prevailed. Sparse cloud coverage provided constant solar radiation and high temperatures. In 2014, the wind system was less variable with prevailing northerly and southerly winds at high speeds independent of daytime. However, solar radiation showed a strong variability due to changing cloud coverage. The versatility of the two data sets allows the investigation of variable transport processes at constant solar radiation (2012) as well as the variability of solar radiation at constant transport processes (2014). Further, it shows that short-period measurements do not represent the total RHS emission potential of the Dead Sea Valley.

Increased BrO amounts of up to 150 pptv could be addressed to low wind speeds and hence, low dilution. Further, the wind direction strongly affects BrO in terms of altitude and total abundance. Elevated layers of BrO where mostly observed during sea breeze scenarios. They are characterized by westerly and easterly winds at low wind speeds which lead to vertical transport at the slopes of the valley. Further, this implies sufficiently long lived precursors of reactive bromine which lead to enhanced BrO abundance after being transported to higher altitudes.

Correlations of aerosols and BrO show strong evidence for heterogeneous reaction on aerosol surface. Further, this theory supported by the distinct anti correlation of BrO and NO_2, both in time and in altitude, indicating the formation of $BrONO_2$. Once uptaken by aerosols, $BrONO_2$ is known to enhance the degassing of reactive halogen species from aerosol surfaces.

The knowledge about the abundance of IO at the Dead Sea is still spare. Zingler and Platt [2005] observed up to 10 pptv of IO during LP-DOAS measurements at the evaporation ponds at the southern basin of the Dead Sea. However, the source

of the IO release is unknown. The authors assume the storage of reactive IO in photolabile reservoirs which are photolyzed during daytime. However, this would include the possible transportation of these reservoirs to higher altitudes leading to elevated layer of IO during daytime. In the framework of this thesis vertical profiles of IO were measured. The data shows no significant evidence for elevated IO layers. The comparison of ground near LP-DOAS measurements (2 to 20 m above ground) with MAX-DOAS measurements at the evaporation ponds shows a strong vertical gradient of IO with mixing ratios decreasing from values of 6 pptv down to 1 pptv with in the first 100 m. Further, a strong correlation between water surface roughness and IO abundance could be observed in 2012 and 2014. Carpenter et al. [2013] found out that molecular iodine can be induced by the uptake of ozone by sea water. However, they mentioned laboratory experiments, which showed that saturation effects at the interfacial layer between atmosphere and liquid may occur of the water is not well mixed. Transferring these findings to the Dead Sea provides a possible explanation for the correlation of waves and IO abundance. Within this thesis, I_2 could be detected with mixing ratios of up to 70 pptv after sunset subsequent to increased daytime IO levels which supports the theory by Carpenter et al. [2013].

Another main result of this thesis is the detection of OClO which provides a first direct evidence for reactive chlorine chemistry at the Dead Sea. However, OClO was only observed under exceptional meteorological conditions. Further, on only 2 out of 40 measurement days, significant OClO abundance was observed. Since both observations of OClO coincide with strong winds, it is assumed that OClO is released from mobilized sea salt aerosols.

Besides the outcomes presented above, a comprehensive data set could be acquired with the framework of this thesis which can serve as a starting condition for future model simulations. Table 11.1 provides an overview of its features It includes the following features:

Observable	Vertical profiles (MAX-DOAS)	Ground level (LP-DOAS)	Summer season	Winter season
BrO	X	X*	X	X
IO	X	X*	X	X
I_2		X*	X	
OClO	X	X*	X	X
O_3		X*		X
NO_2	X*	X	X	X
NO_3		X*	X	
HONO	X	X*	X	X
HCHO	X	X*	X	X
SO_2		X*	X	
Solar Radiation	X	X	X	X
Temperature	X	X	X	X
Rel. Humidity	X	X	X	X
Wind direction	X	X	X	X
Wind speed	X	X	X	X

*Table 11.1: Summary of the data set acquired within this thesis. * indicates the additional availability of nighttime data.*

11.1 Outlook

Due to the large number of parameters it is strongly recommended to perform model simulations based on the acquired data set. However, the model of choice must be capable to account for small-scale meteorological processes to embrace the topography of the Dead Sea Valley. Further, gas phase chemistry as well as heterogeneous processes involving reactive halogen species are required.

If available, the application of imaging instruments would provide more insight in the vertical and horizontal distribution and dynamics of RHS at the Dead Sea Valley. Similar instruments for the observation of SO_2 distributions in volcanic plumes already exist Kuhn et al. [2014] and may be adapted to detect BrO, NO_2 or IO. By obtaining 2D information, showing the trace gas dynamics in near real-time, would not only lead to more intuitive understanding but

would also facilitate the data acquisition while still embracing a larger number of parameters.

References

AERONET (2014).

Aguzzi, A. and J. Rossi, M. (1999). The kinetics of the heterogeneous reaction of BrONO2 with solid alkali halides at ambient temperature. A comparison with the interaction of ClONO2 on NaCl and KBr. *Phys. Chem. Chem. Phys.*, 1:4337–4346.

Alicke, B., Hebestreit, K., Stutz, J., and Platt, U. (1999). Iodine oxide in the marine boundary layer. *Nature*, 397(6720):572–573.

Atkinson, R., Baulch, D. L., Cox, R. A., Crowley, J. N., Hampson, R. F., Hynes, R. G., Jenkin, M. E., Rossi, M. J., and Troe, J. (2007). Evaluated kinetic and photochemical data for atmospheric chemistry: Volume III gas phase reactions of inorganic halogens. *Atmospheric Chemistry and Physics*, 7(4):981–1191.

Ball, S. M., Hollingsworth, A. M., Humbles, J., Leblanc, C., Potin, P., and Mc-Figgans, G. (2010). Spectroscopic studies of molecular iodine emitted into the gas phase by seaweed. *Atmos. Chem. Phys.*, 10(13):6237–6254.

Bobrowski, N., von Glasow, R., Aiuppa, A., Inguaggiato, S., Louban, I., Ibrahim, O. W., and Platt, U. (2007). Reactive halogen chemistry in volcanic plumes. *J. Geophys. Res.*, 112:D06311.

Bogumil, K., Orphal, J., Homann, T., Voigt, S., Spietz, P., Fleischmann, O., Vogel, A., Hartmann, M., Kromminga, H., Bovensmann, H., Frerick, J., and Burrows, J. (2003). Measurements of molecular absorption spectra with the {SCIAMACHY} pre-flight model: instrument characterization and reference data for atmospheric remote-sensing in the 230-2380 nm region. *Journal of Photochemistry and Photobiology A: Chemistry*, 157:167 – 184. Atmospheric Photochemistry.

Bussemer, M. (1993). Der Ring- Effekt: Ursachen und Einfluß auf die spektroskopische Messung stratosphärischer Spurenstoffe. Diploma thesis, University of Heidelberg, Heidelberg, Germany.

Butkovskaya, N., Morozov, I., Tal'rose, V., and Vasiliev, E. (1983). Kinetic studies of the bromine-oxygen system: A new paramagnetic particle, BrO2. *Chemical Physics*, 79(1):21 – 30.

Cao, L., Sihler, H., Platt, U., and Gutheil, E. (2014). Numerical analysis of the chemical kinetic mechanisms of ozone depletion and halogen release in the polar troposphere. *Atmos. Chem. Phys.*, 14(7):3771–3787.

Carpenter, L. J., MacDonald, S. M., Shaw, M. D., Kumar, R., Saunders, R. W., Parthipan, R., Wilson, J., and Plane, J. M. C. (2013). Atmospheric iodine levels influenced by sea surface emissions of inorganic iodine. *Nature Geoscience*, 6(2):108–111.

Chance, K. and Kurucz, R. (2010). An improved high-resolution solar reference spectrum for earth's atmosphere measurements in the ultraviolet, visible, and near infrared. *J. Quant. Spec. Rad. Trans.*, 111(9):1289–1295.

Deiber, G., George, C., Le Calvé, S., Schweitzer, F., and Mirabel, P. (2004). Uptake study of clono$_2$ and brono$_2$ by halide containing droplets. *Atmospheric Chemistry and Physics*, 4(5):1291–1299.

Deters, B., Burrows, J. P., and Orphal, J. (1998). UV-visible absorption cross sections of bromine nitrate determined by photolysis of BrONO2/Br2 mixtures. *Journal of Geophysical Research: Atmospheres*, 103(D3):3563–3570.

Eger, P. (2014). Improving Long-Path DOAS measurements with a Laser Driven Light Source and a new fibre configuration. Master's thesis, University of Heidelberg.

Fleischmann, O. C. and Burrows, J. P. (2002). Absorption measurements using a Fourier transform spectrometer; spectral resolution 5 cm$^-$1. University of Bremen, Germany.

Fleischmann, O. C., Hartmann, M., Burrows, J. P., and Orphal, J. (2004). New ultraviolet absorption cross-sections of BrO at atmospheric temperatures measured by time-windowing Fourier transform spectroscopy. *Journal of Photochemistry and Photobiology A: Chemistry*, 168:117 – 132.

Frieß, U. (2001). *Spectroscopic Measurements of Atmospheric Trace Gases at Neumayer-Station, Antarctica.* PhD thesis, University of Heidelberg.

Frieß, U., Sihler, H., Sander, R., Pöhler, D., Yilmaz, S., and Platt, U. (2011). The vertical distribution of BrO and aerosols in the Arctic: Measurements by active and passive differential optical absorption spectroscopy. *J. Geophys. Res.*, 116:D00R04.

Gebel, M. E., , and Finlayson-Pitts, B. J. (2001). Uptake and Reaction of ClONO2 on NaCl and Synthetic Sea Salt. *The Journal of Physical Chemistry A*, 105(21):5178–5187.

Geever, M., O'Dowd, C. D., van Ekeren, S., Flanagan, R., Nilsson, E. D., de Leeuw, G., and Rannik, l. (2005). Submicron sea spray fluxes. *Geophysical Research Letters*, 32(15):n/a–n/a. L15810.

Gliß, J., Bobrowski, N., Vogel, L., Pöhler, D., and Platt, U. (2015). OClO and BrO observations in the volcanic plume of Mt. Etna and implications on the chemistry of chlorine and bromine species in volcanic plumes. *Atmospheric Chemistry and Physics*, 15(10):5659–5681.

Greenblatt, G. D., Orlando, J. J., Burkholder, J. B., and Ravishankara, A. R. (1990). Absorption measurements of oxygen between 330 and 1140 nm. *J. Geophys. Res.*, 95:18577–18582.

Hausmann, M. and Platt, U. (1994). Spectroscopic measurement of bromine oxide and ozone in the high Arctic during Polar Sunrise Experiment 1992. *J. Geophys. Res.*, 99(D12):25399–25413.

Hayase, S., Yabushita, A., Kawasaki, M., Enami, S., Hoffmann, M. R., and Colussi, A. J. (2010). Heterogeneous Reaction of Gaseous Ozone with Aqueous Iodide in the Presence of Aqueous Organic Species. *The Journal of Physical Chemistry A*, 114(19):6016–6021. PMID: 20415500.

Hebestreit, K. (2001). *Halogen oxides in the mid-latitudinal planetary boundary layer.* PhD thesis, University of Heidelberg, Heidelberg, Germany.

Hebestreit, K., Stutz, J., Rosen, D., Matveiv, V., Peleg, M., Luria, M., and Platt, U. (1999). DOAS measurements of tropospheric bromine oxide in mid-latitudes. *Science*, 283(5398):55–57.

Hermans, C., Vandaele, A. C., Fally, S., Carleer, M., Colin, R., Coquart, B., Jenouvrier, A., and Mérienne, M. F. (2002). Absorption cross-section of the collision-induced bands of oxygen from the UV to the NIR. In *NATO Advanced Research Workshop: Weakly Interacting Molecular Pairs: Unconventional Absorbers of Radiation in the Atmosphere*, St. Petersburg, Russia.

Holla, R. (2013). *Reactive Halogen Species above Salt Lakes and Salt Pans.* PhD thesis, University of Heidelberg.

Holla, R., Schmitt, S., Frieß, U., Pöhler, D., Zingler, J., Corsmeier, U., and Platt, U. (2015). Vertical distribution of Bro in the boundary layer at the Dead Sea. *Environmental Chemistry*, 12(4):438–460.

Hönninger, G. (2002). *Halogen Oxide Studies in the Boundary Layer by Multi Axis Differential Optical Absorption Spectroscopy and Active Longpath-DOAS.* PhD thesis, University of Heidelberg.

Hönninger, G., Bobrowski, N., Palenque, E. R., Torrez, R., and Platt, U. (2004a). Reactive bromine and sulfur emissions at salar de uyuni, bolivia. *Geophys. Res. Lett.*, 31:L04101.

Hönninger, G., von Friedeburg, C., and Platt, U. (2004b). Multi axis differential optical absorption spectroscopy (MAX-DOAS). *Atmos. Chem. Phys.*, 4(1):231–254.

Horbanski, M. (2015). *Emissions and Distribution of Reactive Iodine from Seaweed in Coastal Regions*. PhD thesis, University of Heidelberg.

IMK, K. (2012). Webpage of KIT weather station located at Dead Sea Works Pumpstation P88.

Jacobs, D. J. (2007). Lectures on inverse modeling. *Harvard University*.

Jarvis, A., Reuter, H., Nelson, A., and Guevera, E. (2008). Hole-filled seamless SRTM data V4. -.

Joseph, D. M., Ashworth, S. H., and Plane, J. M. C. (2007). On the photochemistry of IONO2 : absorption cross section (240-370 nm) and photolysis product yields at 248 nm. *Phys. Chem. Chem. Phys.*, 9:5599–5607.

Kraus, S. (2006). *DOASIS: A Framework Design for DOAS*. PhD thesis, University of Mannheim.

Kuhn, J., Bobrowski, N., Lübcke, P., Vogel, L., and Platt, U. (2014). A fabry perot interferometer-based camera for two-dimensional mapping of so_2 distributions. *Atmospheric Measurement Techniques*, 7(11):3705–3715.

Lampel, J. (2014). *Measurements of reactive trace gases in the marine boundary layer using novel DOAS methods*. Phd thesis, University of Heidelberg.

Lampel, J., Pöhler, D., Tschritter, J., Frieß, U., and Platt, U. (2014). On the relative absorption strengths of water vapour in the blue wavelength range. *Atm. Meas. Tech. Discuss.*, page in preparation.

Levenberg, K. (1944). A method for the solution of certain non-linear problems in least squares. *Quart. Appl., Math.*, 2:164–168.

Levin, Z., Gershon, H., and Ganor, E. (2005). Vertical distribution of physical and chemical properties of haze particles in the Dead Sea valley. *Atmospheric Environment*, 39(27):4937 – 4945.

Liao, J., Sihler, H., Huey, L. G., Neuman, J. A., Tanner, D. J., Friess, U., Platt, U., Flocke, F. M., Orlando, J. J., Shepson, P. B., Beine, H. J., Weinheimer, A. J., Sjostedt, S. J., Nowak, J. B., Knapp, D. J., Staebler, R. M., Zheng, W., Sander, R., Hall, S. R., and Ullmann, K. (2011). A comparison of Arctic bro measurements by chemical ionization mass spectrometry and long path-differential optical absorption spectroscopy. *J. Geophys. Res.*, 116:D00R02.

Lyday, P. A. (2003). Mineral commodity summaries. *U.S. Geological Survey.*

Marquardt, D. W. (1963). An algorithm for least-squares estimation of nonlinear parameters. *J. Soc. Ind. App. Math.*, 11(2):431–441.

Meller, R. and Moortgat, G. K. (2000). Temperature dependence of the absorption cross sections of formaldehyde between 223 and 323 k in the wavelength range 225-375 nm. *Journal of Geophysical Research: Atmospheres*, 105(D6):7089–7101.

Merten, A. (2008). *Neues Design von Langpfad-DOAS-Instrumenten basierend auf Faseroptiken und Anwendungen der Untersuchung der urbanen Atmosphäre.* PhD thesis, University of Heidelberg.

Merten, A., Tschritter, J., and Platt, U. (2011). Design of differential optical absorption spectroscopy long-path telescopes based on fiber optics. *Appl. Opt.*, 50(5):738–754.

Mettendorf, K. U. (2005). *Aufbau und Einsatz eines Multibeam Instrumentes zur DOAS-tomographischen Messung zweidimensionaler Konzentrationsverteilungen.* PhD thesis, University of Heidelberg.

Nasse, J.-M. (2014). Retrieval of aerosol and trace gas vertical profiles in the Antarctic troposphere using helicopter- and ship-borne MAX-DOAS measurements. Master's thesis, University of Heidelberg.

Niemi, T. M., Ben-Avraham, Z., and Gat, J. R., editors (1997). *The Dead Sea The Lake and Its Setting.* Oxford University Press.

Nissenbaum, A. (1977). Minor and trace elements in Dead Sea water. *Chemical Geology*, 19(1):99 – 111.

O'Dowd, C. and Hoffmann, T. (2005). Coastal new particle formation: A review of the current state-of-the-art. *Environ. Chem.*, 3(1):245–255.

Ofner, J., Kamilli, K. A., Held, A., Lendl, B., and Zetzsch, C. (2013). Halogen-induced organic aerosol (XOA): a study on ultra-fine particle formation and time-resolved chemical characterization. *Faraday Discuss.*, 165:135–149.

Oren, A. (2010). The dying Dead Sea: The microbiology of an increasingly extreme environment. *Lakes & Reservoirs: Research & Management*, 15(3):215–222.

Orlando, J. J., , and Tyndall, G. S. (1996). Rate Coefficients for the Thermal Decomposition of BrONO2 and the Heat of Formation of BrONO2. *The Journal of Physical Chemistry*, 100(50):19398–19405.

Papayannis, D., Kosmas, A. M., and Melissas, V. S. (1999). Ab initio calculations for (BrO)2 system and quasiclassical dynamics study of BrO self-reaction . *Chemical Physics*, 243(3):249 – 262.

Penth, L. (2014). Developement of the Inertial Sensor-based Attitude compensating MAX-DOAS Instrument. Master's thesis, University of Heidelberg.

Pillar, E. A., Guzman, M. I., and Rodriguez, J. M. (2013). Conversion of iodide to hypoiodous acid and iodine in aqueous microdroplets exposed to ozone. *Environmental Science & Technology*, 47(19):10971–10979. PMID: 23987087.

Platt, U. and Janssen, C. (1995). Observation and role of the free radicals NO_3, ClO, BrO and IO in the troposphere. *Faraday Discuss.*, 100:175–198.

Platt, U. and Lehrer, E. (1997). Arctic tropospheric ozone chemistry (ARC-TOC). *Final Report to the European Union.*

Platt, U., Perner, D., and Pätz, H. W. (1979). Simultaneous measurement of atmospheric CH_2O, O_3, and NO_2 by differential optical absorption. *J. Geophys. Res.*, 84(C10):6329–6335.

Platt, U. and Stutz, J. (2008). *Differential optical absorption spectroscopy.* Springer Verlag.

Pöhler, D. (2010). *Determination of two-dimensional trace gas distributions using tomographic LP-DOAS measurements in the city of Heidelberg, Germany.* PhD thesis, University of Heidelberg.

Pöhler, D. (2014). *EnviMeS MAX-DOAS Systems Instrument Description.*

Pöhler, D., Vogel, L., Frieß, U., and Platt, U. (2010). Observation of halogen species in the Amundsen Gulf, Arctic, by active long-path differential optical absorption spectroscopy. *PNAS.*

Rodgers, C. D. (2000). *Inverse methods for atmospheric sounding, theory and practice.* Series on Atmospheric, Oceanic and Planetary Physics. World Scientific.

Rothman, L., Gordon, I., Babikov, Y., Barbe, A., Benner, D. C., Bernath, P., Birk, M., Bizzocchi, L., Boudon, V., Brown, L., Campargue, A., Chance, K., Cohen, E., Coudert, L., Devi, V., Drouin, B., Fayt, A., Flaud, J.-M., Gamache, R., Harrison, J., Hartmann, J.-M., Hill, C., Hodges, J., Jacquemart, D., Jolly, A., Lamouroux, J., Roy, R. L., Li, G., Long, D., Lyulin, O., Mackie, C., Massie, S., Mikhailenko, S., Müller, H., Naumenko, O., Nikitin, A., Orphal, J., Perevalov, V., Perrin, A., Polovtseva, E., Richard, C., Smith, M., Starikova, E., Sung, K., Tashkun, S., Tennyson, J., Toon, G., Tyuterev, V., and Wagner, G. (2013). The {HITRAN2012} molecular spectroscopic database. *Journal of Quantitative Spectroscopy and Radiative Transfer*, 130:4 – 50. {HITRAN2012} special issue.

Rothman, L., Gordon, I., Barber, R., Dothe, H., Gamache, R., Goldman, A., Perevalov, V., Tashkun, S., and Tennyson, J. (2010). Hitemp, the high-temperature molecular spectroscopic database. *Journal of Quantitative Spectroscopy and Radiative Transfer*, 111(15):2139 – 2150. {XVIth} Symposium on High Resolution Molecular Spectroscopy (HighRus-2009)XVIth Symposium on High Resolution Molecular Spectroscopy.

Rozanov, A., Bovensmann, H., Bracher, A., Hrechanyy, S., Rozanov, V., Sinnhuber, M., Stroh, F., and Burrows, J. (2005). NO_2 and BrO vertical profile retrieval from SCIAMACHY limb measurements: Sensitivity studies. *Adv. Space Res.*, 36(5):846–854.

Rozanov, V., Buchwitz, M., Eichmann, K.-U., de Beek, R., and Burrows, J. (2002). Sciatran - a new radiative transfer model for geophysical applications in the 24-2400 {NM} spectral region: the pseudo-spherical version . *Advances in Space Research*, 29(11):1831 – 1835.

Saiz-Lopez, A., Plane, J. M. C., Baker, A. R., Carpenter, L. J., von Glasow, R., Gomez Martin, J. C., McFiggans, G., and Saunders, R. W. (2012). Atmospheric chemistry of iodine. *Chem. Rev.*, 112(3):1773–1804.

Saiz-Lopez, A., Saunders, R. W., Joseph, D. M., Ashworth, S. H., and Plane, J. M. C. (2004). Absolute absorption cross-section and photolysis rate of i_2. *Atmospheric Chemistry and Physics*, 4(5):1443–1450.

Sakamoto, Y., Yabushita, A., Kawasaki, M., and Enami, S. (2009). Direct Emission of I2 Molecule and IO Radical from the Heterogeneous Reactions of Gaseous Ozone with Aqueous Potassium Iodide Solution. *The Journal of Physical Chemistry A*, 113(27):7707–7713. PMID: 19530668.

Sansonetti, C. J., Salit, M. L., and Reader, J. (1996). Wavelengths of spectral lines in mercury pencil lamps. *Appl. Opt.*, 35(1):74–77.

Schmitt, S. (2011). A compact long path DOAS instrument based on fibre-optics and LEDs. Diploma thesis, University of Heidelberg.

Schmitz, S. (2009). Untersuchung thermisch induzierter Hang- und Talwindsysteme am Toten Meer und deren Kopplung an größere Skalen.

Segal, M., Mahrer, Y., and Pielke, R. A. (1983). A study of meteorological patterns associated with a lake confined by mountains - the Dead Sea case. *Quarterly Journal of the Royal Meteorological Society*, 109(461):549–564.

Seinfeld, J. H. and Pandis, S. N. (1998). *Atmospheric Chemistry and Physics*. John Wiley and Sons, Inc.

Seinfeld, J. H. and Pandis, S. N. (2006). *Atmospheric Chemistry and Physics: From Air Pollution to Climate Change, 2nd Edition*. John Wiley and Sons, Inc.

Serdyuchenko, A., Gorshelev, V., Weber, M., Chehade, W., and Burrows, J. P. (2014). High spectral resolution ozone absorption cross-sections - part 2: Temperature dependence. *Atmos. Meas. Tech.*, 7(2):625–636.

Sihler, H. (2007). Light-Emitting Diodes as Light Sources in Spectroscopic Measurements of Atmospheric Trace Gases. Master's thesis, University of Heidelberg.

Sihler, H., Platt, U., Beirle, S., Marbach, T., Kühl, S., Dörner, S., Verschaeve, J., Frieß, U., Pöhler, D., Vogel, L., Sander, R., and Wagner, T. (2012). Tropospheric BrO column densities in the Arctic derived from satellite: retrieval and comparison to ground-based measurements. *Atmos. Meas. Tech.*, 5(11):2779–2807.

Simon, F., Schneider, W., Moortgat, G., and Burrows, J. (1990). A study of the clo absorption cross-section between 240 and 310 nm and the kinetics of the self-reaction at 300 k. *Journal of Photochemistry and Photobiology A: Chemistry*, 55(1):1 – 23.

Simpson, W. R., von Glasow, R., Riedel, K., Anderson, P., Ariya, P., Bottenheim, J., Burrows, J., Carpenter, L. J., Frieß, U., Goodsite, M. E., Heard, D., Hutterli, M., Jacobi, H.-W., Kaleschke, L., Neff, B., Plane, J., Platt, U., Richter, A., Roscoe, H., Sander, R., Shepson, P., Sodeau, J., Steffen, A., Wagner, T., and Wolff, E. (2007). Halogens and their role in polar boundary-layer ozone depletion. *Atmos. Chem. Phys.*, 7(16):4375–4418.

Smoydzin, L. and von Glasow, R. (2009). Modelling chemistry over the dead sea: bromine and ozone chemistry. *Atmos. Chem. Phys.*, 9(14):5057–5072.

Spietz, P., Gómez Martín, J., and Burrows, J. P. (2006). Effects of column density on i_2 spectroscopy and a determination of i_2 absorption cross section at 500 nm. *Atmospheric Chemistry and Physics*, 6(8):2177–2191.

Spietz, P., Martin, J. C. G., and Burrows, J. P. (2005). Spectroscopic studies of the I2/O3 photochemistry: Part 2. improved spectra of iodine oxides and analysis of the {IO} absorption spectrum. *Journal of Photochemistry and Photobiology A: Chemistry*, 176:50 – 67. In Honour of Professor Richard P. Wayne.

Stutz, J., Kim, E. S., Platt, U., Bruno, P., Perrino, C., and Febo, A. (2000). UV-visible absorption cross sections of nitrous acid. *Journal of Geophysical Research: Atmospheres*, 105(D11):14585–14592.

Stutz, J. and Platt, U. (1996). Numerical analysis and estimation of the statistical error of differential optical absorption spectroscopy measurements with least-squares methods. *Appl. Opt.*, 35(30):6041–6053.

Stutz, J. and Platt, U. (1997). Improving long-path differential optical absorption spectroscopy with a quartz-fiber mode mixer. *Appl. Opt.*, 36(6):1105–1115.

Tas, E., Peleg, M., Pedersen, D. U., Matveev, V., Biazar, A. P., and Luria, M. (2008). Measurement-based modeling of bromine chemistry in the Dead Sea boundary layer - part 2: The influence of NO_2 on bromine chemistry at mid-latitude areas. *Atmos. Chem. Phys.*, 8(16):4811–4821.

Tas, E., Peleg, M., Pedersen, D. U., Matveev, V., Pour Biazar, A., and Luria, M. (2006). Measurement-based modeling of bromine chemistry in the boundary layer: 1. bromine chemistry at the Dead Sea. *Atmos. Chem. Phys.*, 6(12):5589–5604.

Thalman, R. and Volkamer, R. (2013). Temperature dependent absorption cross-sections of O_2-O_2 collision pairs between 340 and 630 nm and at atmospherically relevant pressure. *Phys. Chem. Chem. Phys.*, 15:15371–15381.

Tuckermann, M., Ackermann, R., Gölz, C., Lorenzen-Schmidt, H., Senne, T., Stutz, J., Trost, B., Unold, W., and Platt, U. (1997). DOAS-observation of halogen radical-catalysed arctic boundary layer ozone destruction during the ARCTOC-campaigns 1995 and 1996 in Ny-Ålesund, Spitsbergen. *Tellus*, 49(5):533–555.

Vandaele, A. C., Hermans, C., Fally, S., Carleer, M., Colin, R., Marienne, M.-F., Jenouvrier, A., and Coquart, B. (2002). High-resolution Fourier transform measurement of the NO2 visible and near-infrared absorption cross sections: Temperature and pressure effects. *Journal of Geophysical Research: Atmospheres*, 107(D18):ACH 3–1–ACH 3–12. 4348.

Vandaele, A. C., Hermans, C., Simon, P. C., Carleer, M., Colin, R., Fally, S., Mérienne, M. F., Jenouvrier, A., and Coquart, B. (1998). Measurements of the NO2 absorption cross-section from 42,000 cm^{-1} to 10,000 cm^{-1} (238-1000 nm) at 220 K and 294 K. *J. of Quant. Spectrosc. and Rad. Transfer*, 59:171–184.

Vogt, R., Crutzen, P. J., and Sander, R. (1996). A mechanism for halogen release from sea-salt aerosol in the remote marine boundary layer. *Nature*, 383(6598):327–330.

Volkamer, R., Spietz, P., Burrows, J., and Platt, U. (2005). High-resolution absorption cross-section of glyoxal in the UV-vis and {IR} spectral ranges. *Journal of Photochemistry and Photobiology A: Chemistry*, 172(1):35 – 46.

von Glasow, R. and Crutzen, P. J. (2007). *Tropospheric Halogen Chemistry*, volume 4.02, chapter Treatise on Geochemistry, pages 1 – 67. Pergamon.

Yilmaz, S. (2012). *Retrieval of Atmospheric Aerosol and Trace Gas Vertical Profiles using Multi-Axis Differential Optical Absorption Spectroscopy.* PhD thesis, University of Heidelberg.

Yokelson, R. J., Burkholder, J. B., Fox, R. W., Talukdar, R. K., and Ravishankara, A. R. (1994). Temperature dependence of the no3 absorption spectrum. *The Journal of Physical Chemistry*, 98(50):13144–13150.

Zielcke, J. (2015). *Observations of reactive bromine, iodine and chlorine species in the Arctic and Antarctic with Differential Optical Absorption Spectroscopy.* PhD thesis, University of Heidelberg.

Zingler, J. and Platt, U. (2005). Iodine oxide in the dead sea valley: Evidence for inorganic sources of boundary layer io. *J. Geophys. Res.*, 110:D07307.

List of Figures

List of Tables

Part V

Appendix

.1 Histograms of mixing ratios measured by LP-DOAS
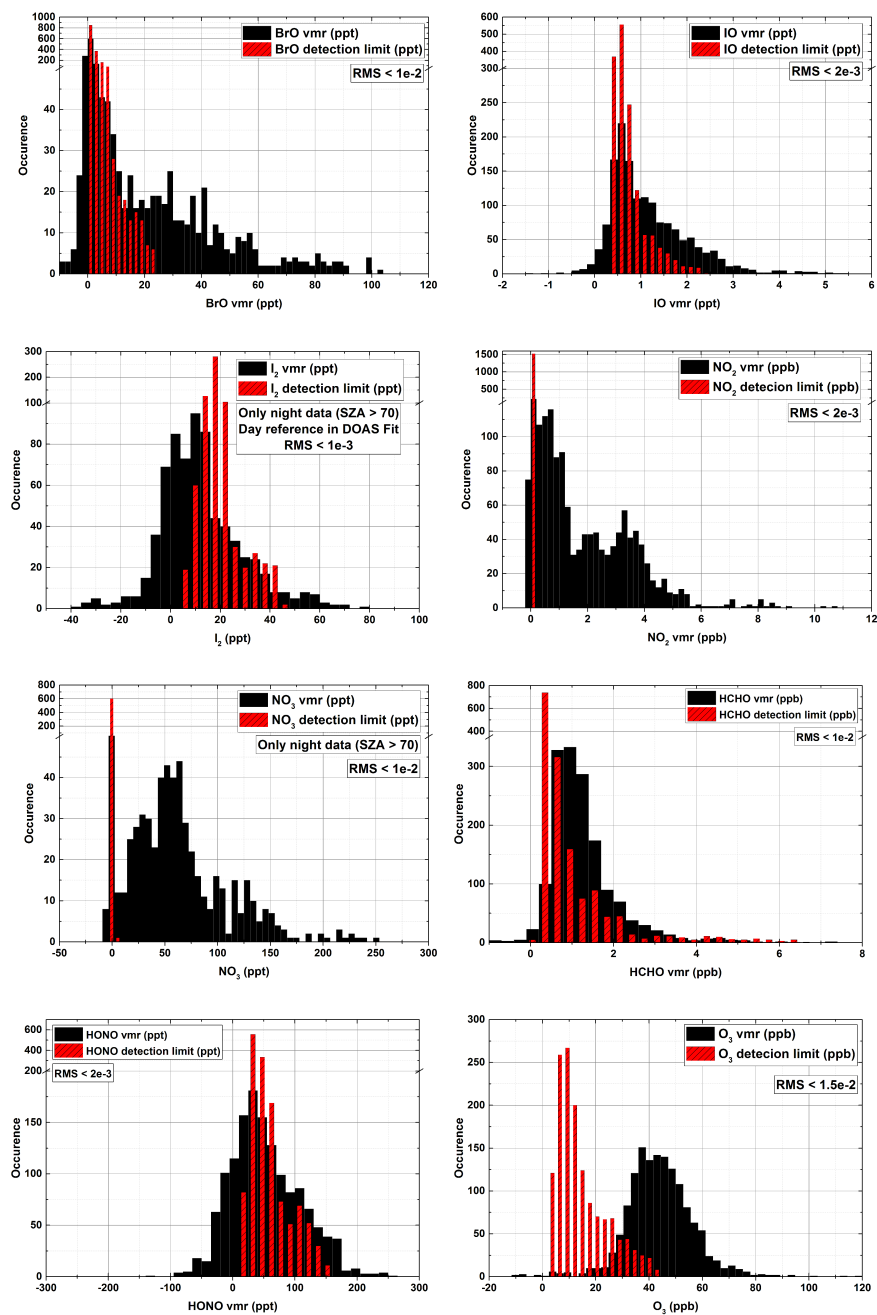
Fig. .1: Histograms of mixing ratios (black bars) and corresponding detection limits (red bars) from LP-DOAS data in May 2012.
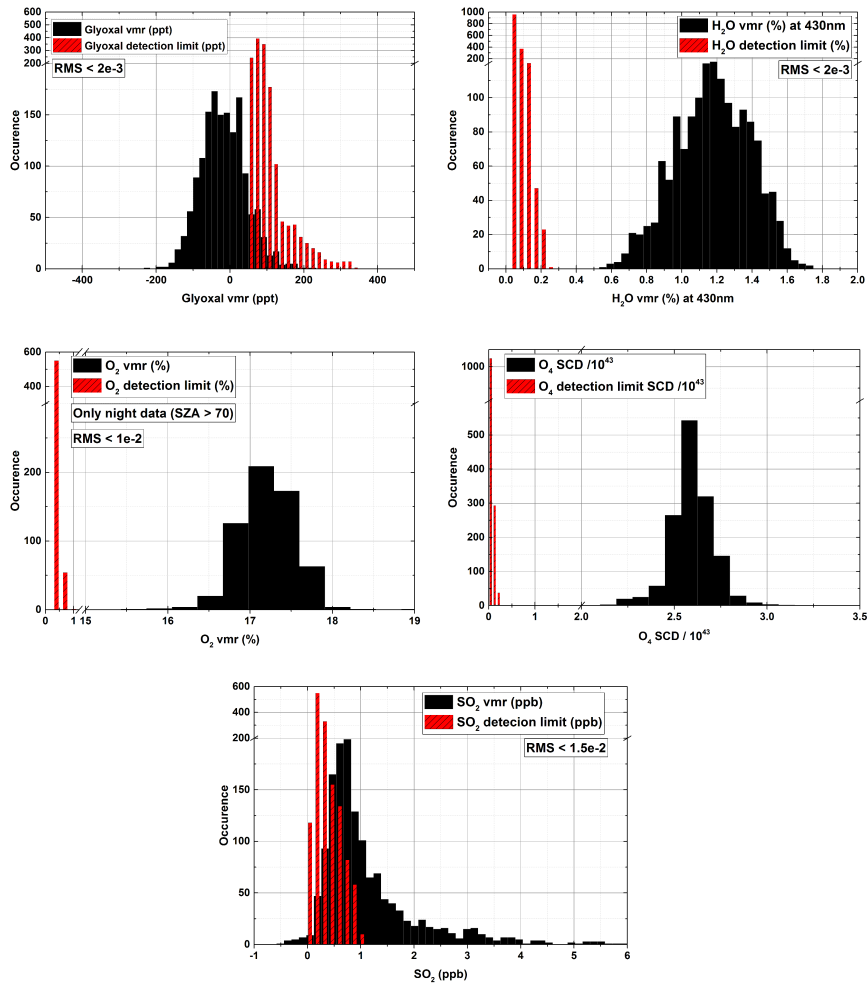
Fig. .2: Histograms of mixing ratios (black bars) and corresponding detection limits (red bars) from LP-DOAS data in May 2012.

.2 Histograms of slant column densities measured by MAX-DOAS in Ein Bokek
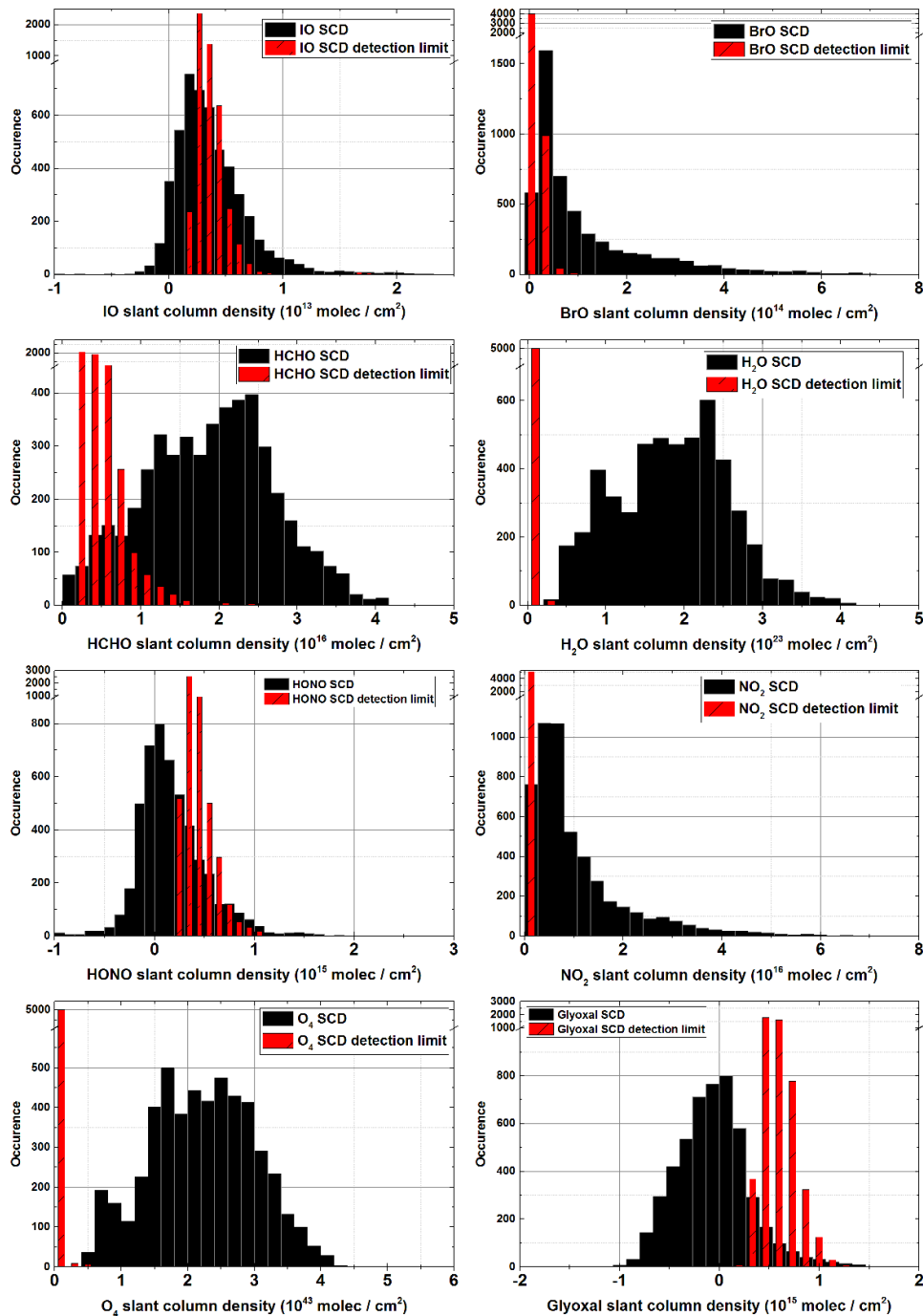
Fig. .3: *Histograms of slant column densities (black) and corresponding detection limits (red) retrieved from the data of the Ein Bokek MAX-DOAS during the Dead Sea campaign in November 2012. All elevation angle are shown.*
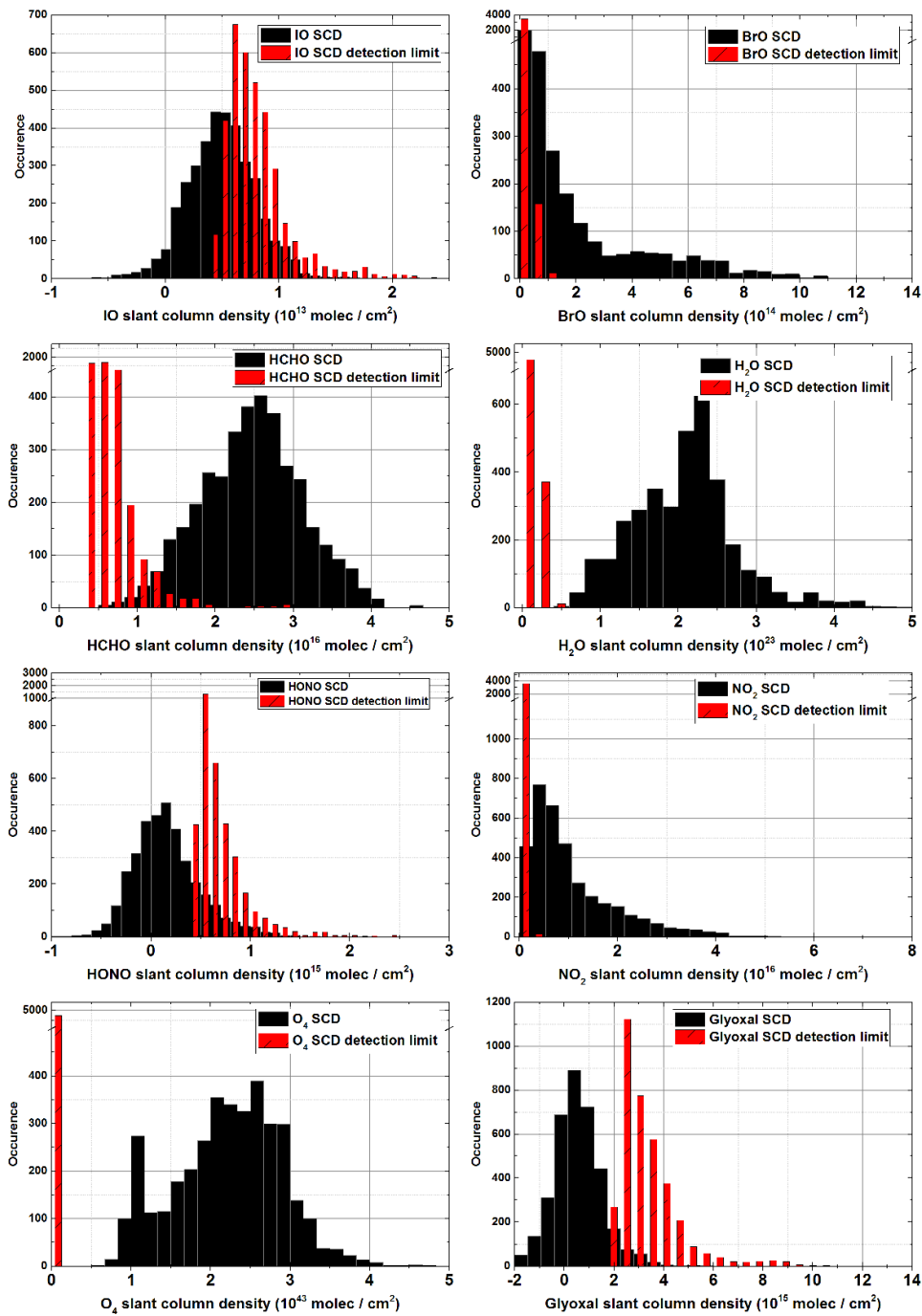
Fig. .4: Histograms of slant column densities (black) and corresponding detection limits (red) retrieved from the data of the Masada top MAX-DOAS during the Dead Sea campaign in November 2012. All elevation angles are shown.

.3 MAX-DOAS Slant column densities

.3.1 May 2012
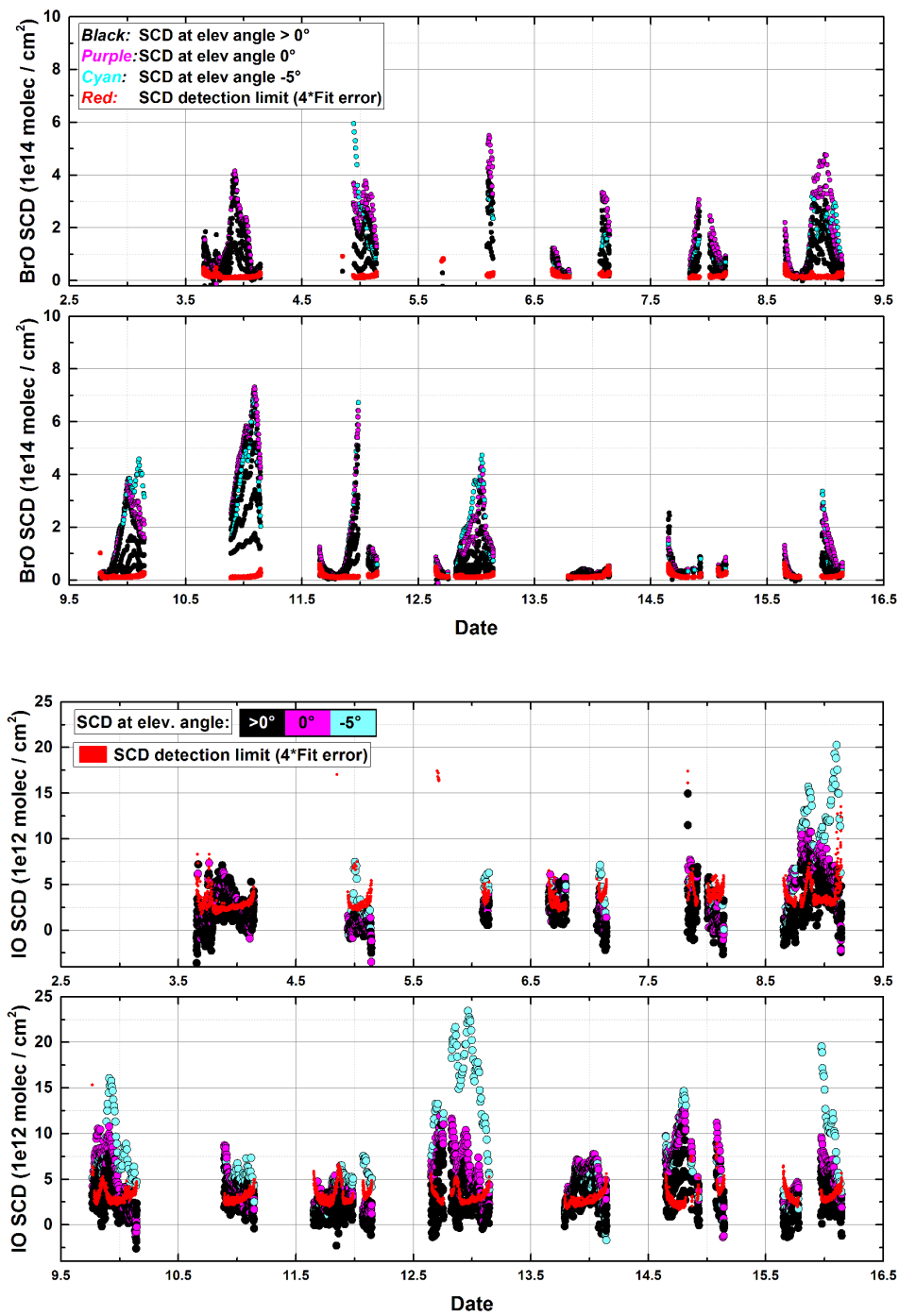
Fig. .5: Ein Bokek MAX-DOAS time series of BrO and IO SCDs.
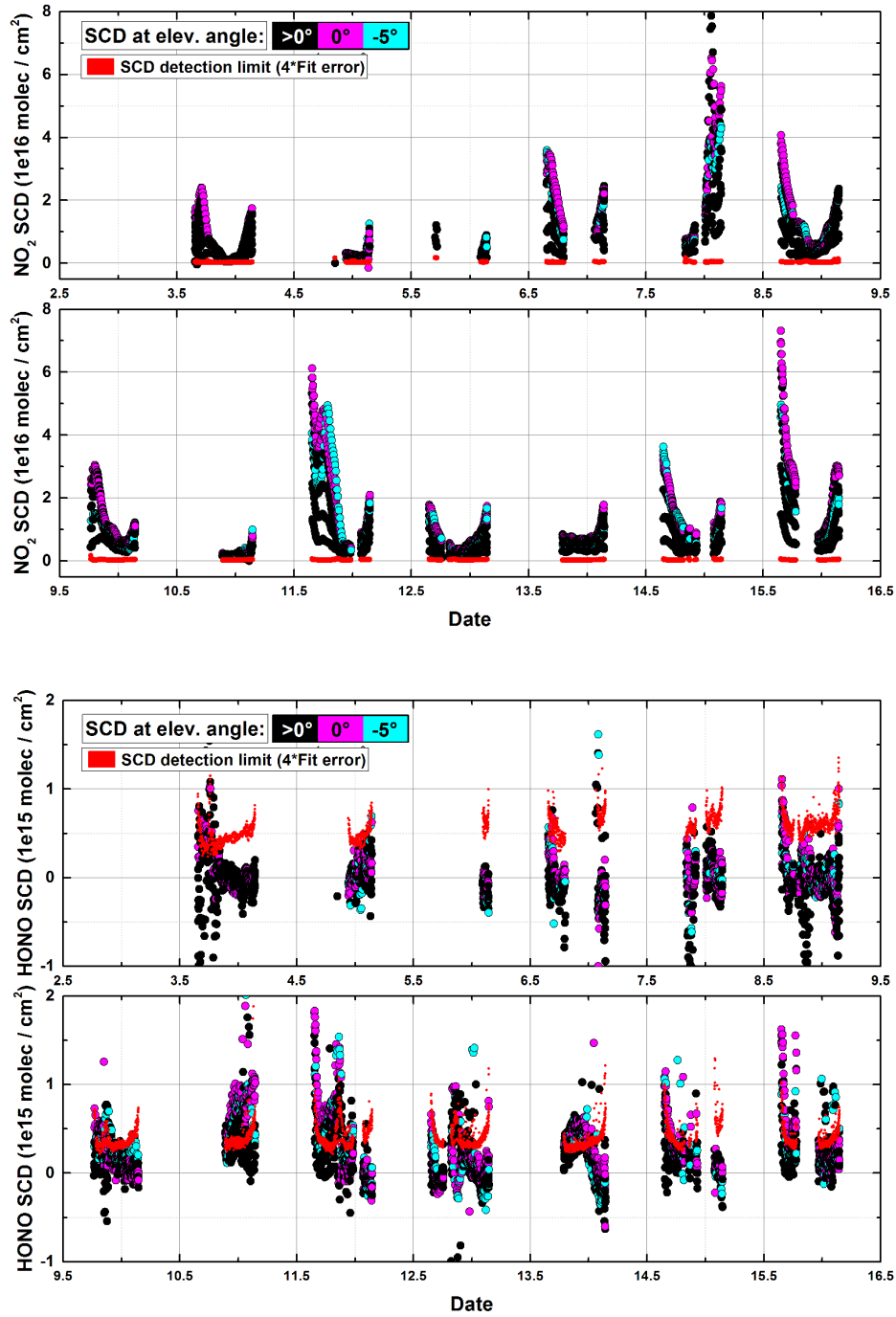
Fig. .6: Ein Bokek MAX-DOAS time series of NO2 and HONO SCDs.
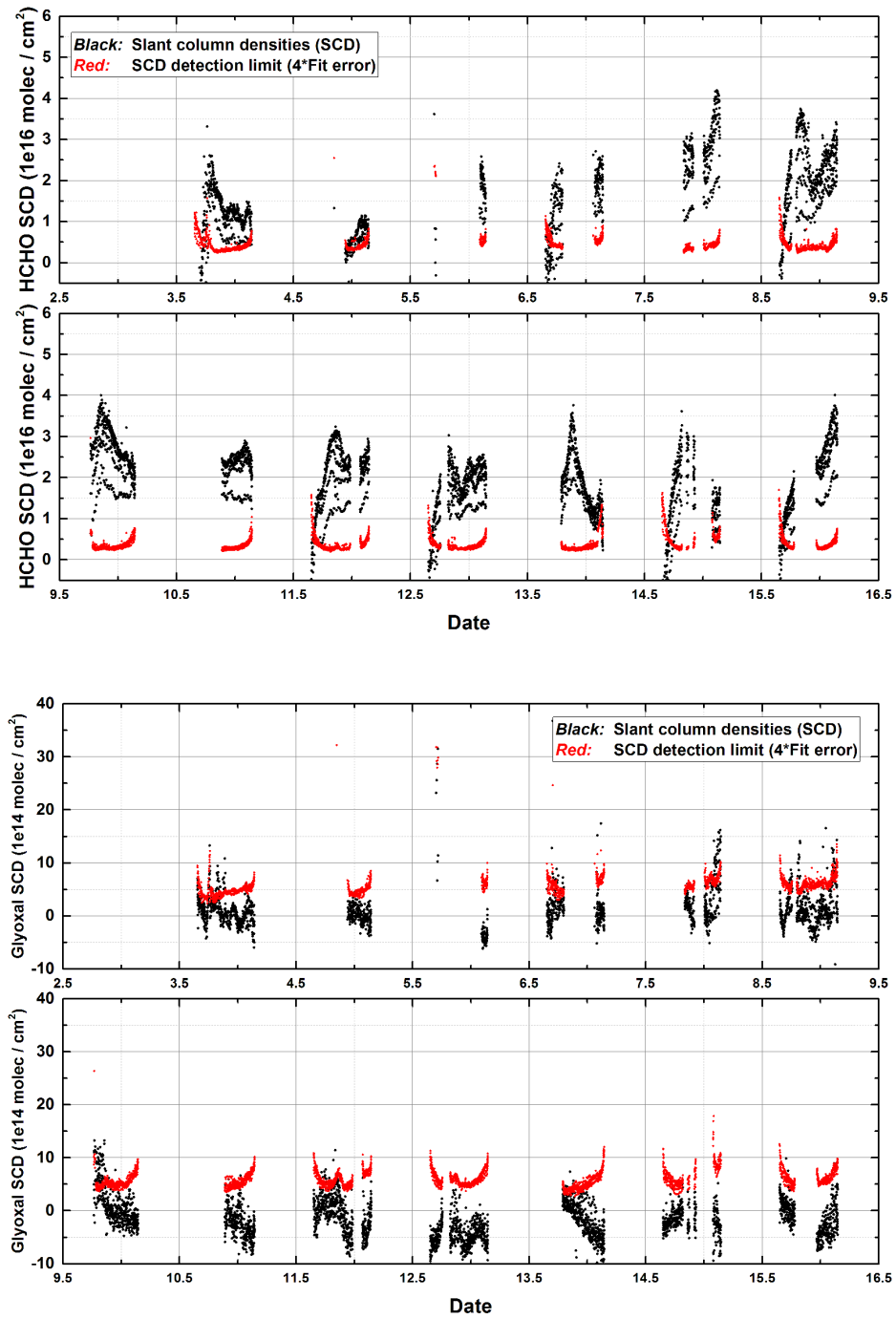
Fig. .7: Ein Bokek MAX-DOAS time series of HCHO and Glyoxal SCDs.
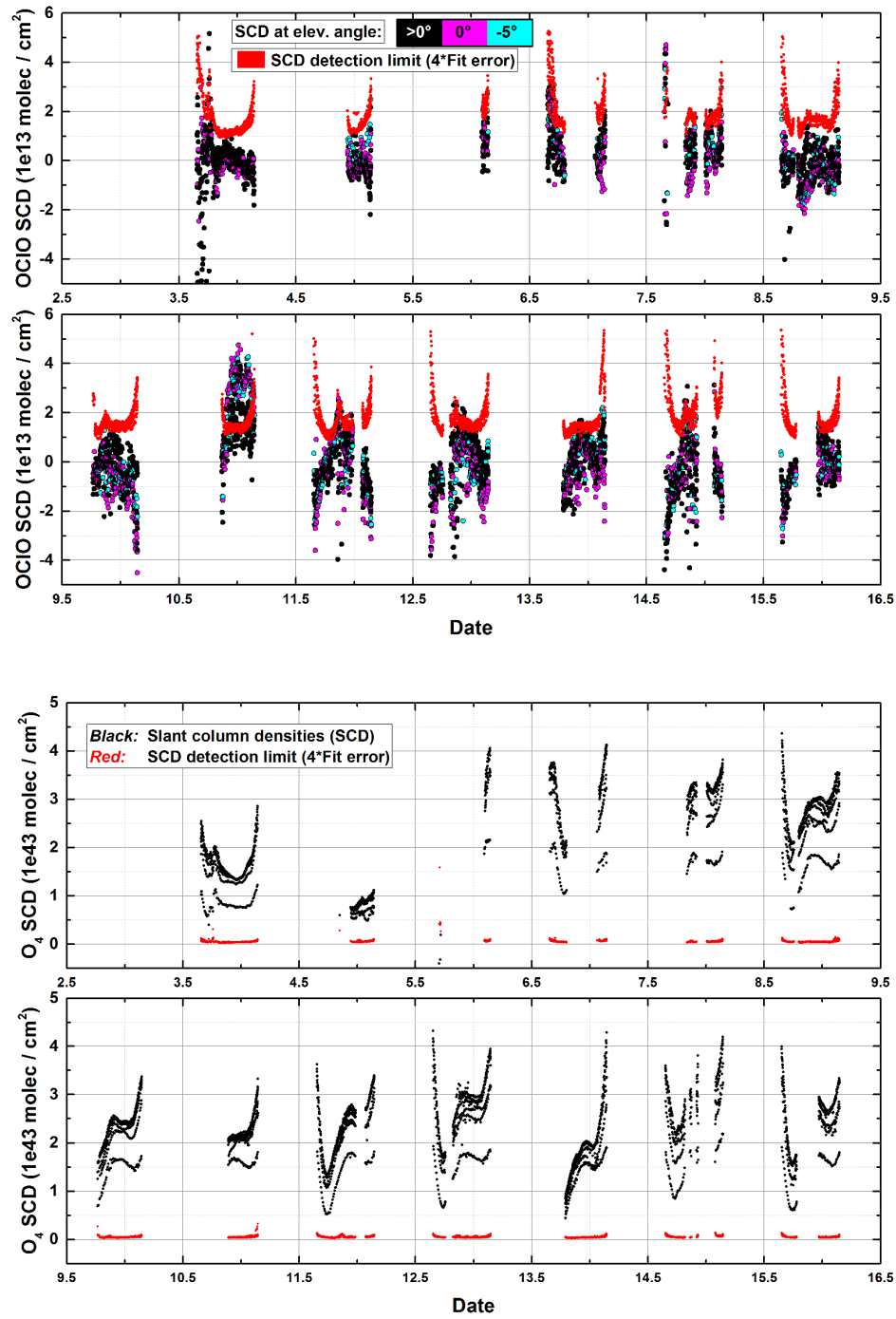
Fig. .8: Ein Bokek MAX-DOAS time series of OCLO and O_4 SCDs.
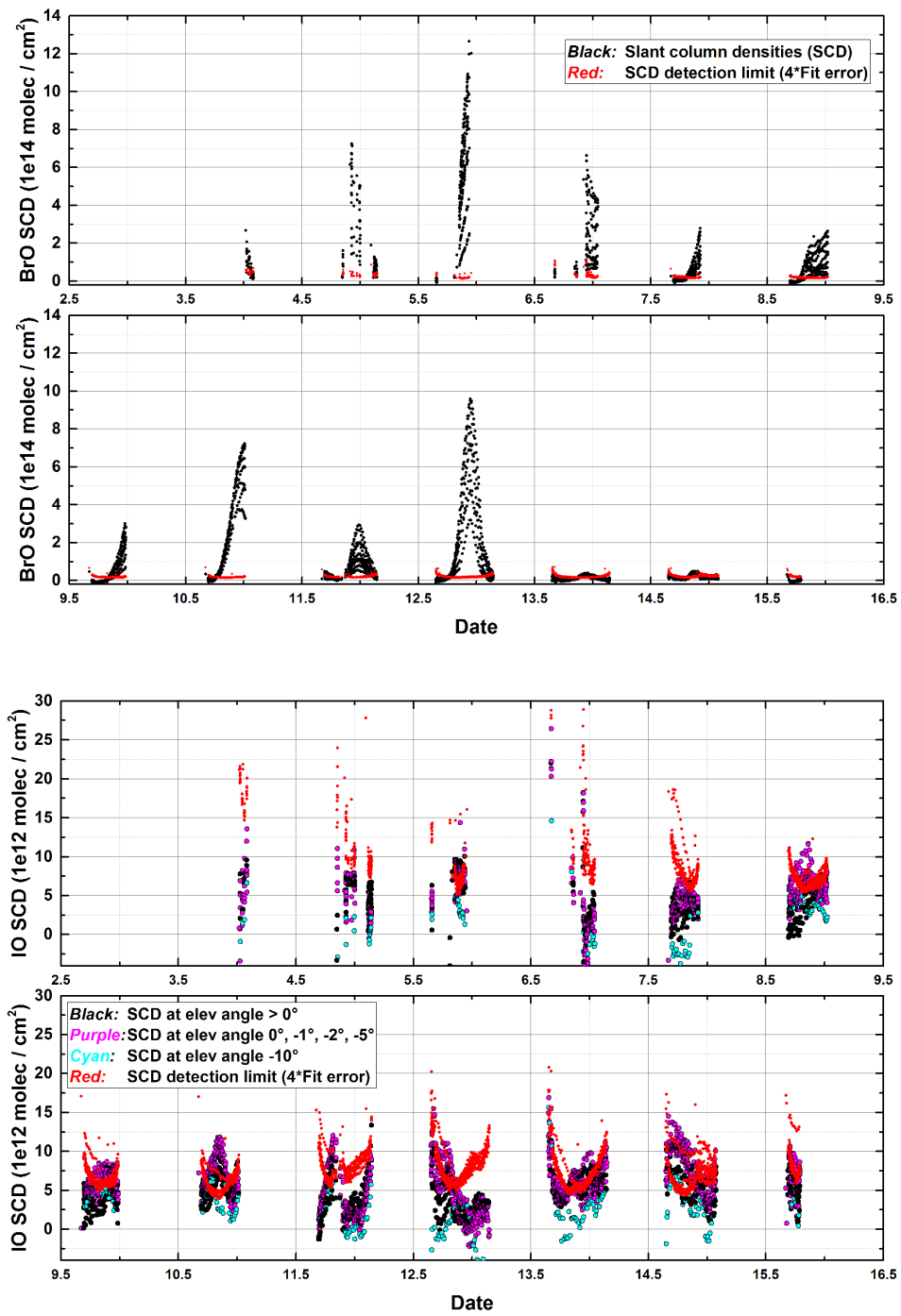
Fig. .9: Masada top MAX-DOAS time series of BrO and IO SCDs.
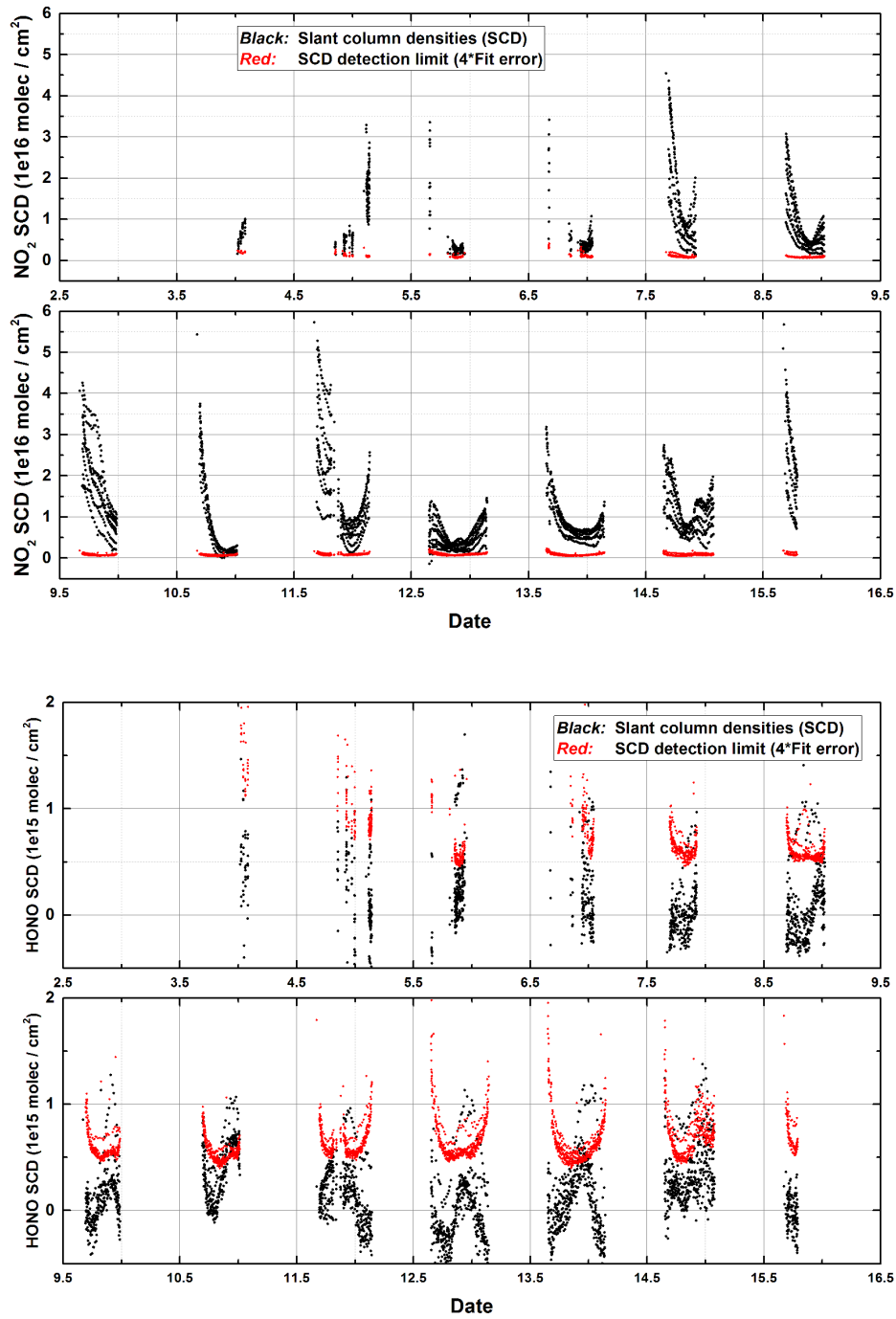
Fig. .10: Masada top MAX-DOAS time series of NO2 and HONO SCDs.
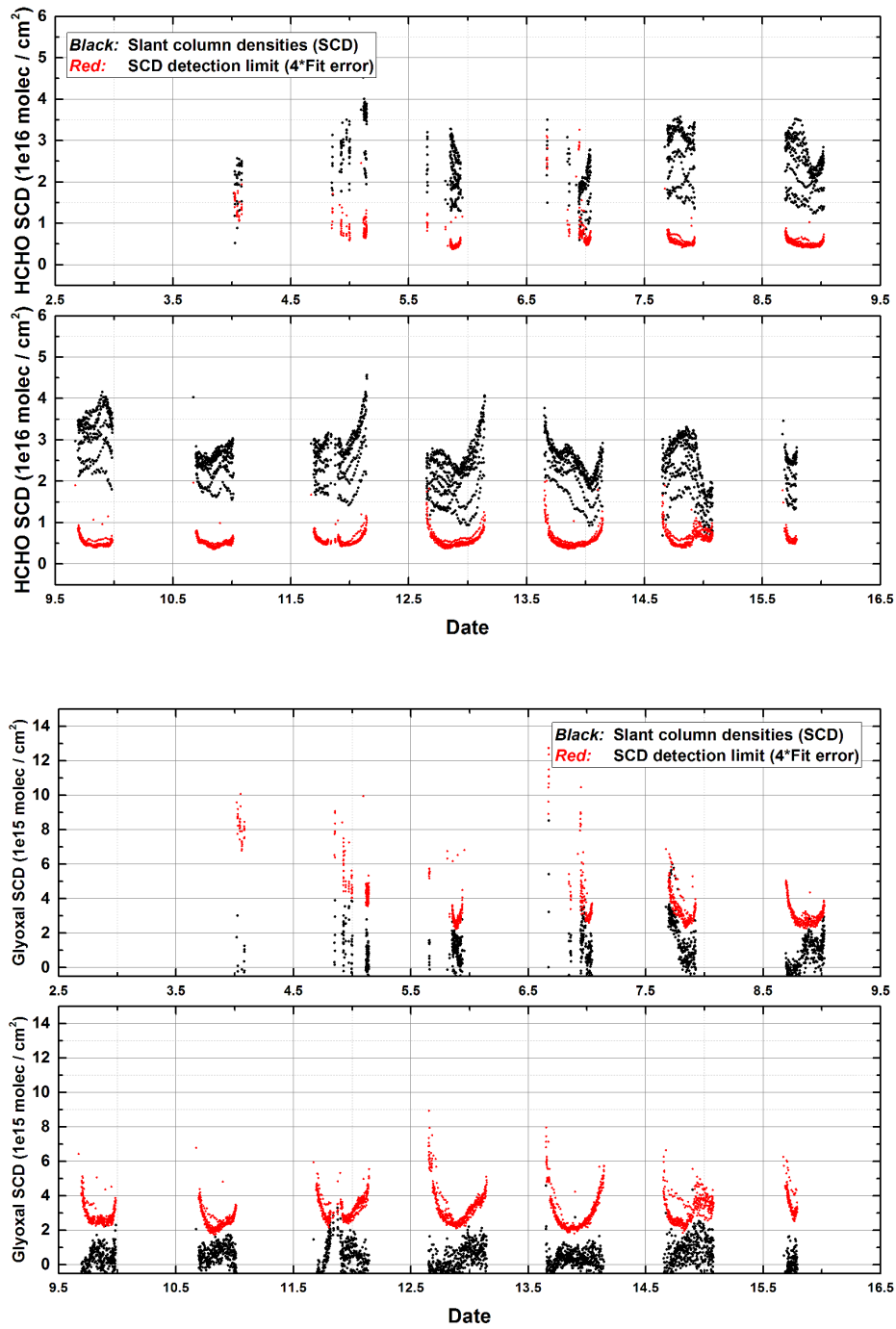
Fig. .11: Masada top MAX-DOAS time series of HCHO and Glyoxal SCDs.
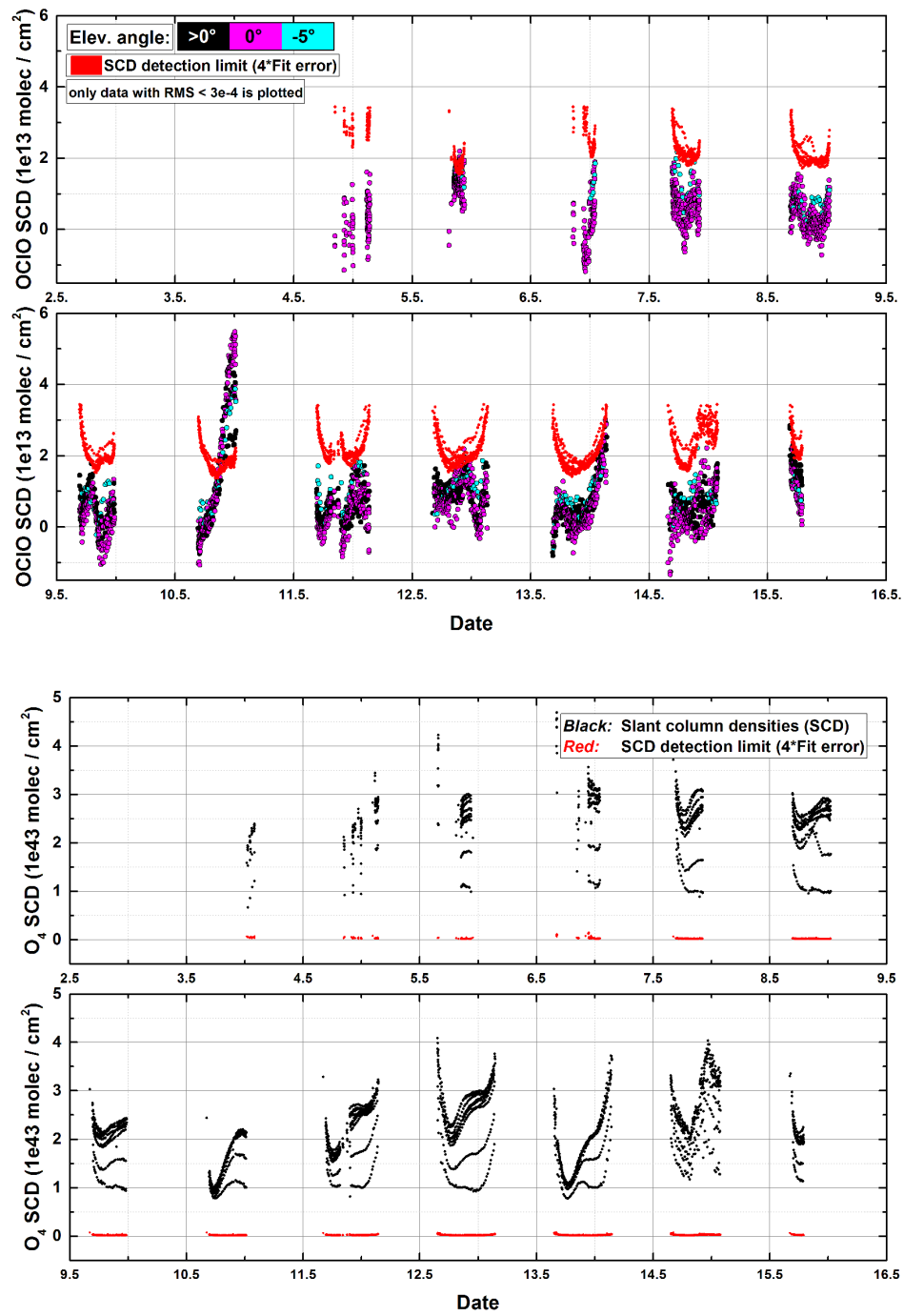
Fig. .12: Masada top MAX-DOAS time series of OClO and O_4 SCDs.

.3.2 November 2014
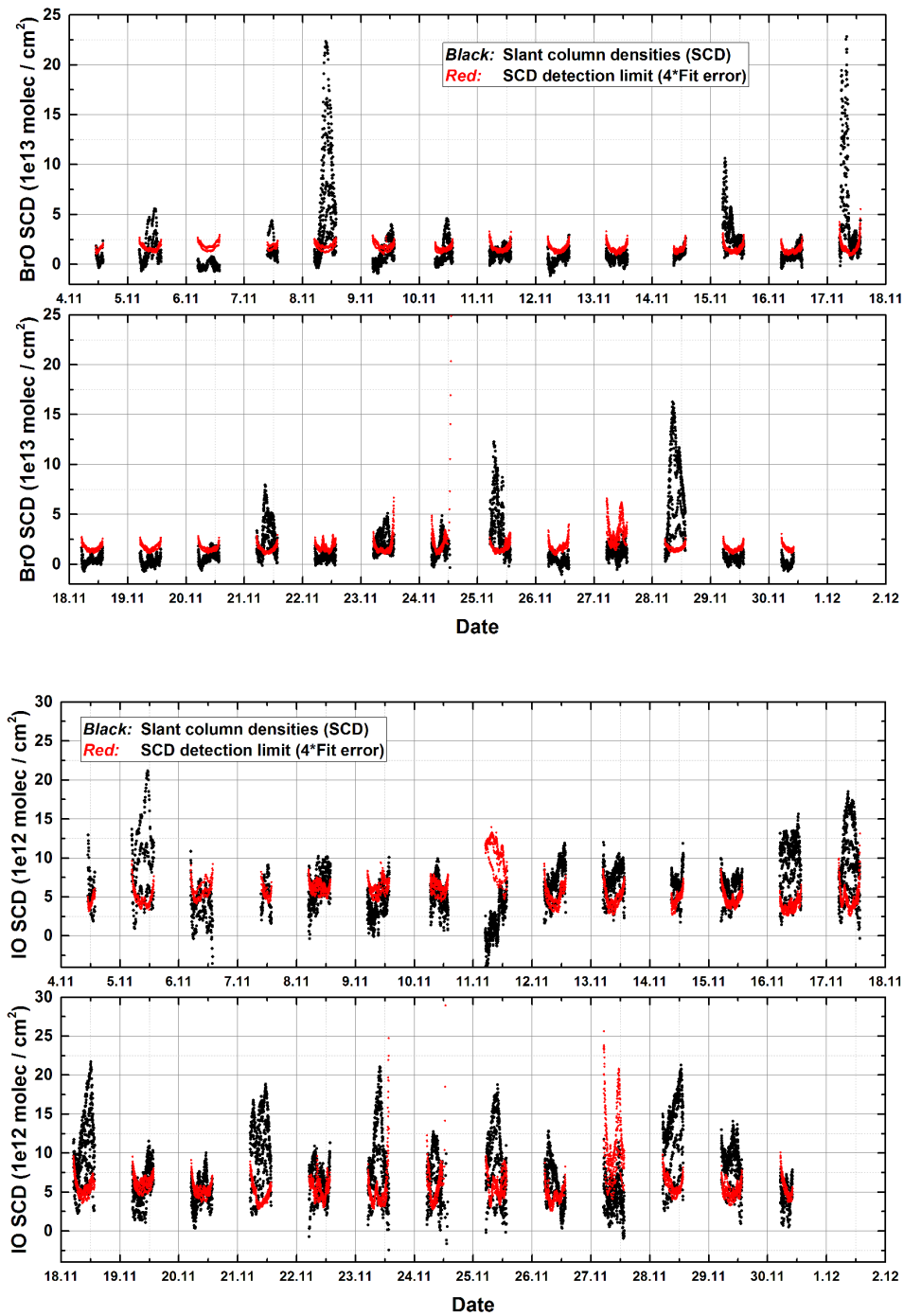
Fig. .13: Masada MAX-DOAS time series of BrO and IO SCDs.
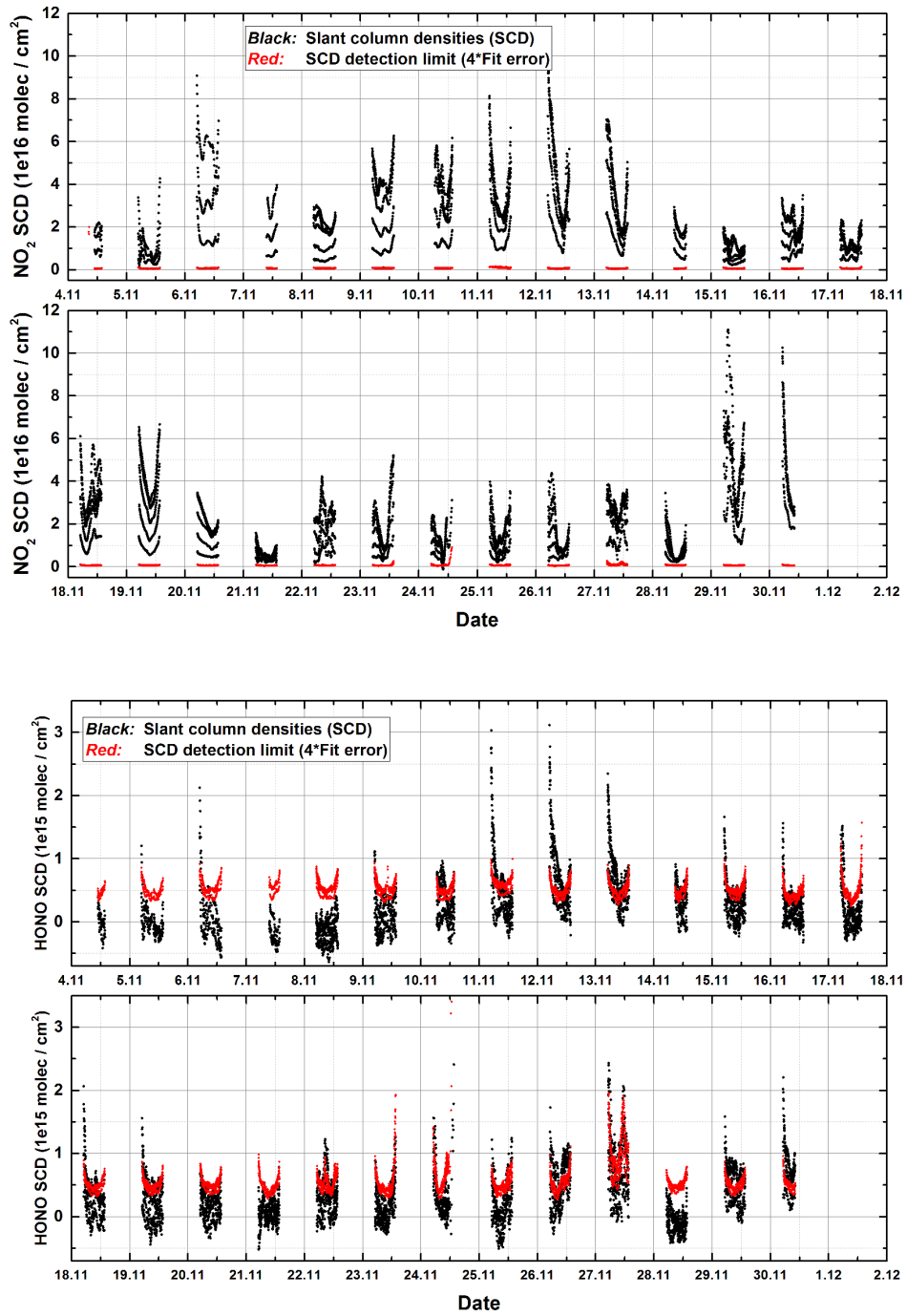
Fig. .14: Masada MAX-DOAS time series of NO2 and HONO SCDs.
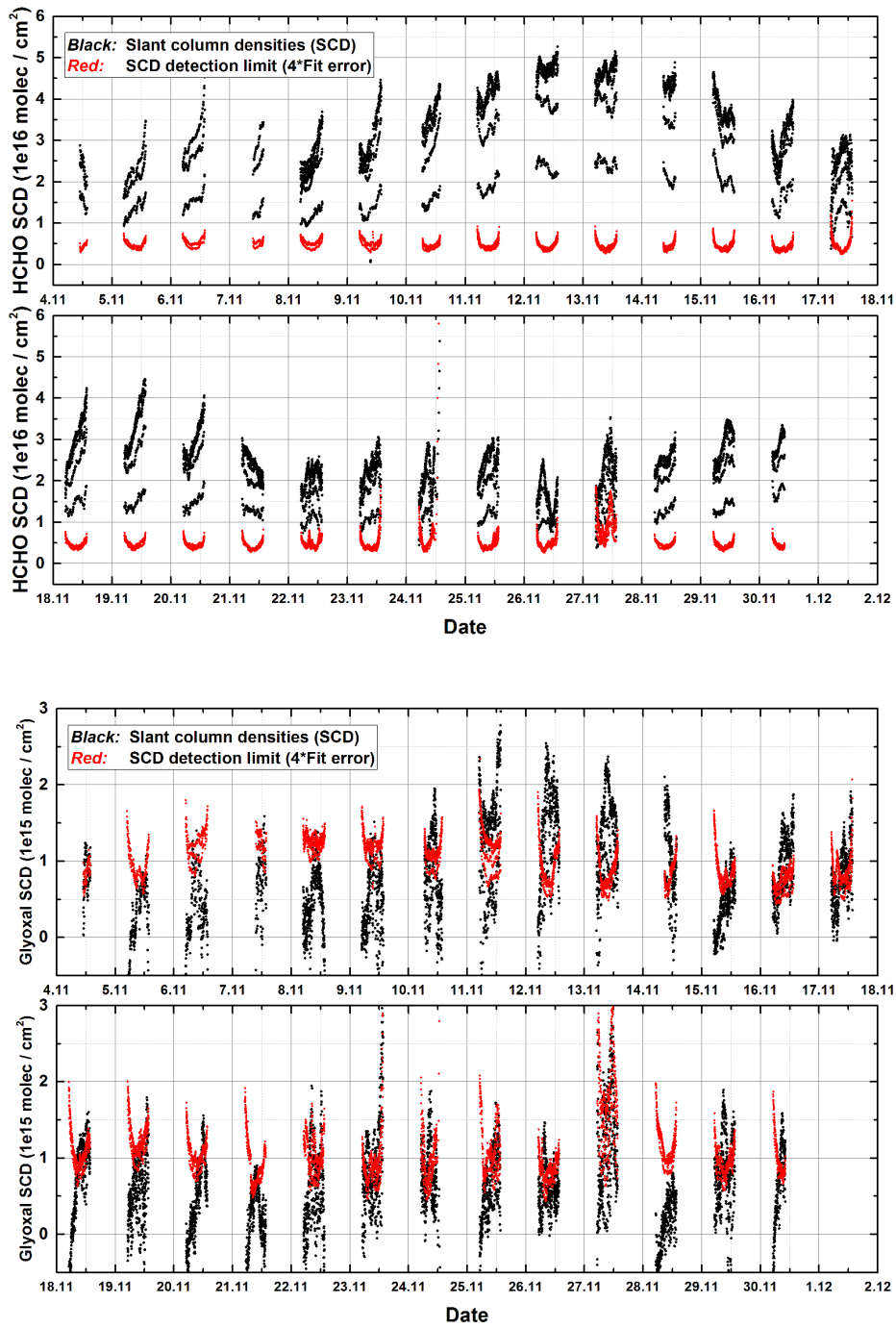
Fig. .15: Masada MAX-DOAS time series of HCHO and Glyoxal SCDs.
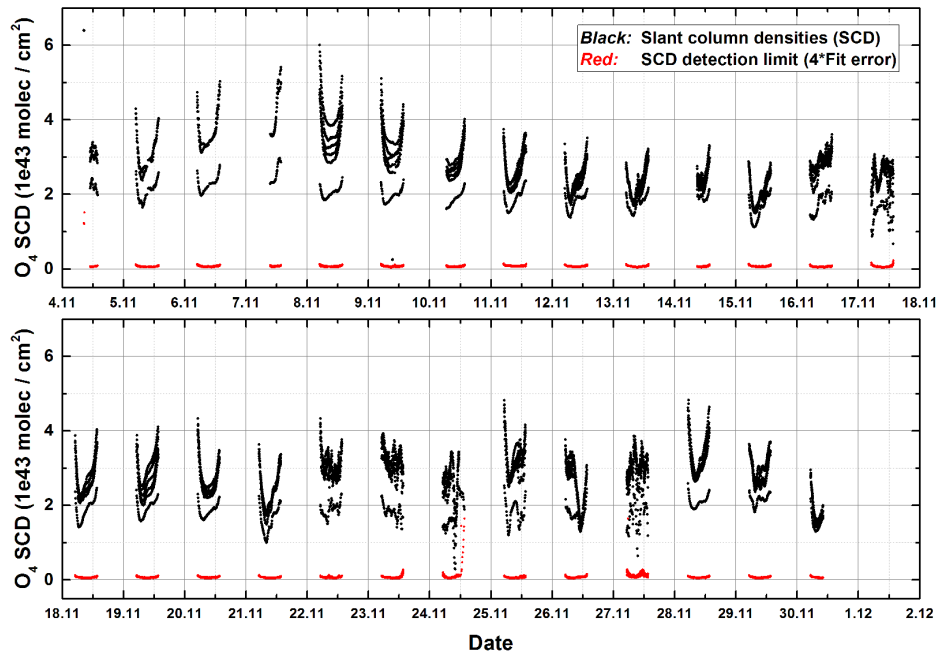
Fig. .16: Masada MAX-DOAS time series of O4 SCDs.
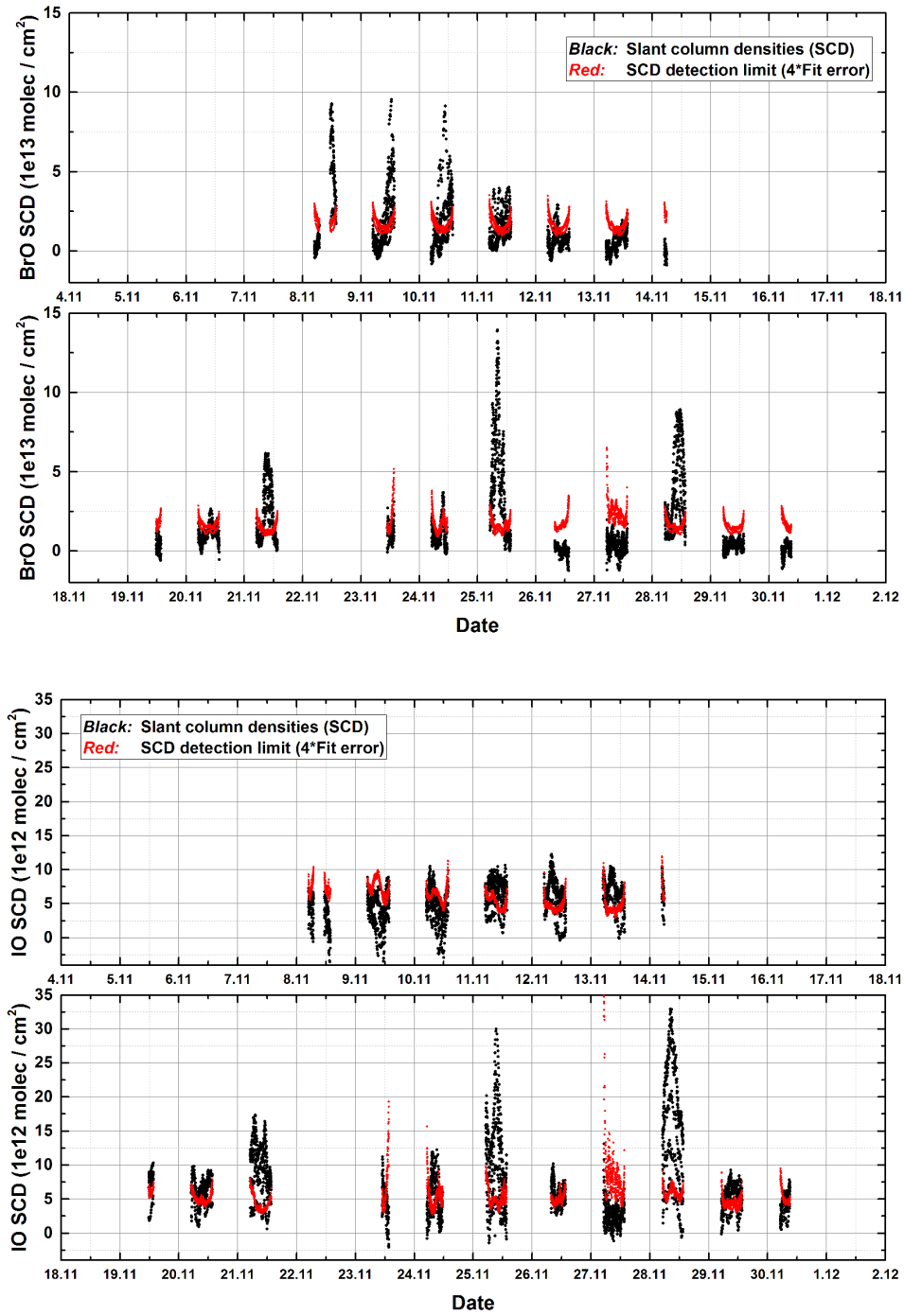
Fig. .17: ISA MAX-DOAS time series of BrO and IO SCDs.
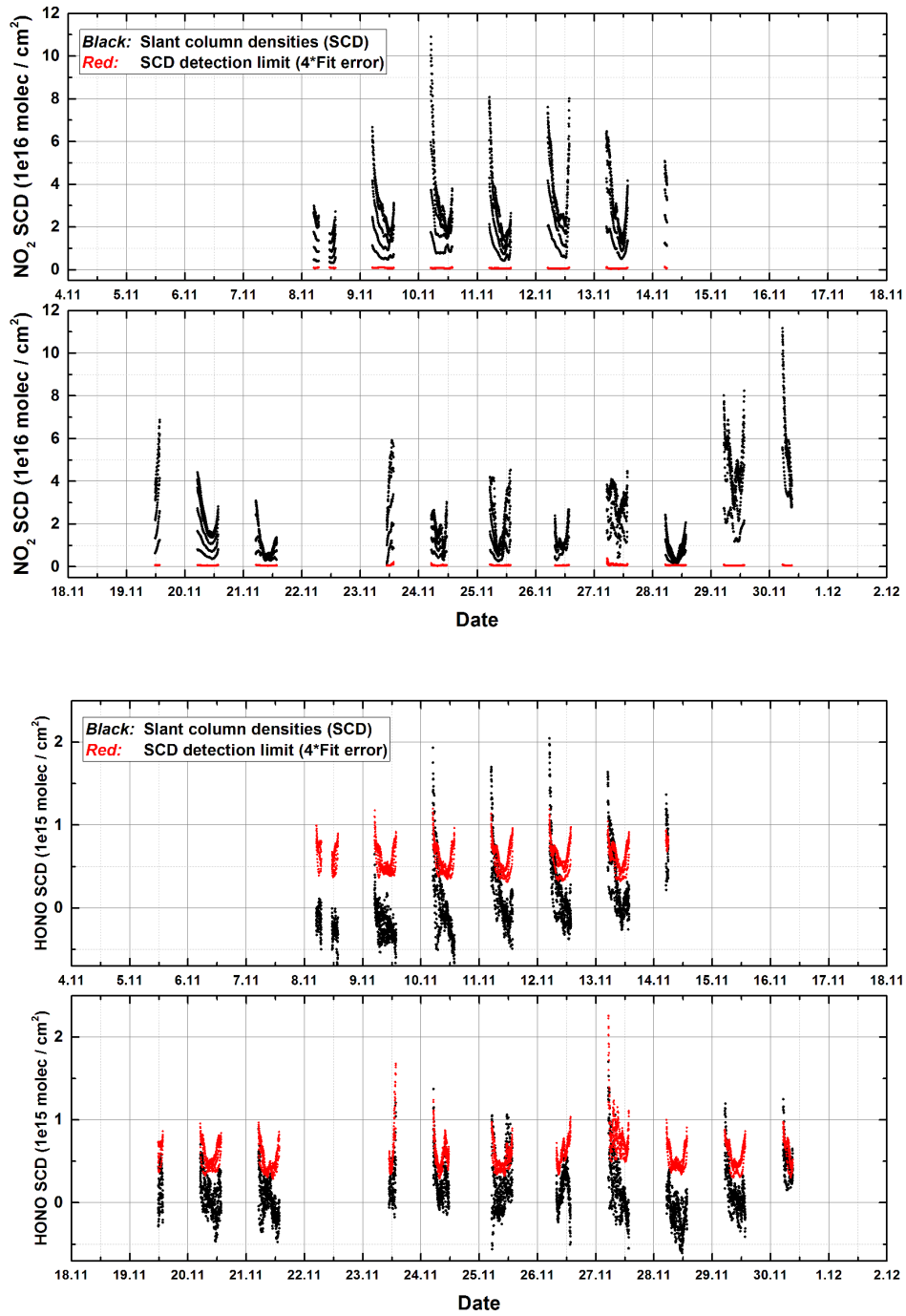
Fig. .18: ISA MAX-DOAS time series of NO2 and HONO SCDs.
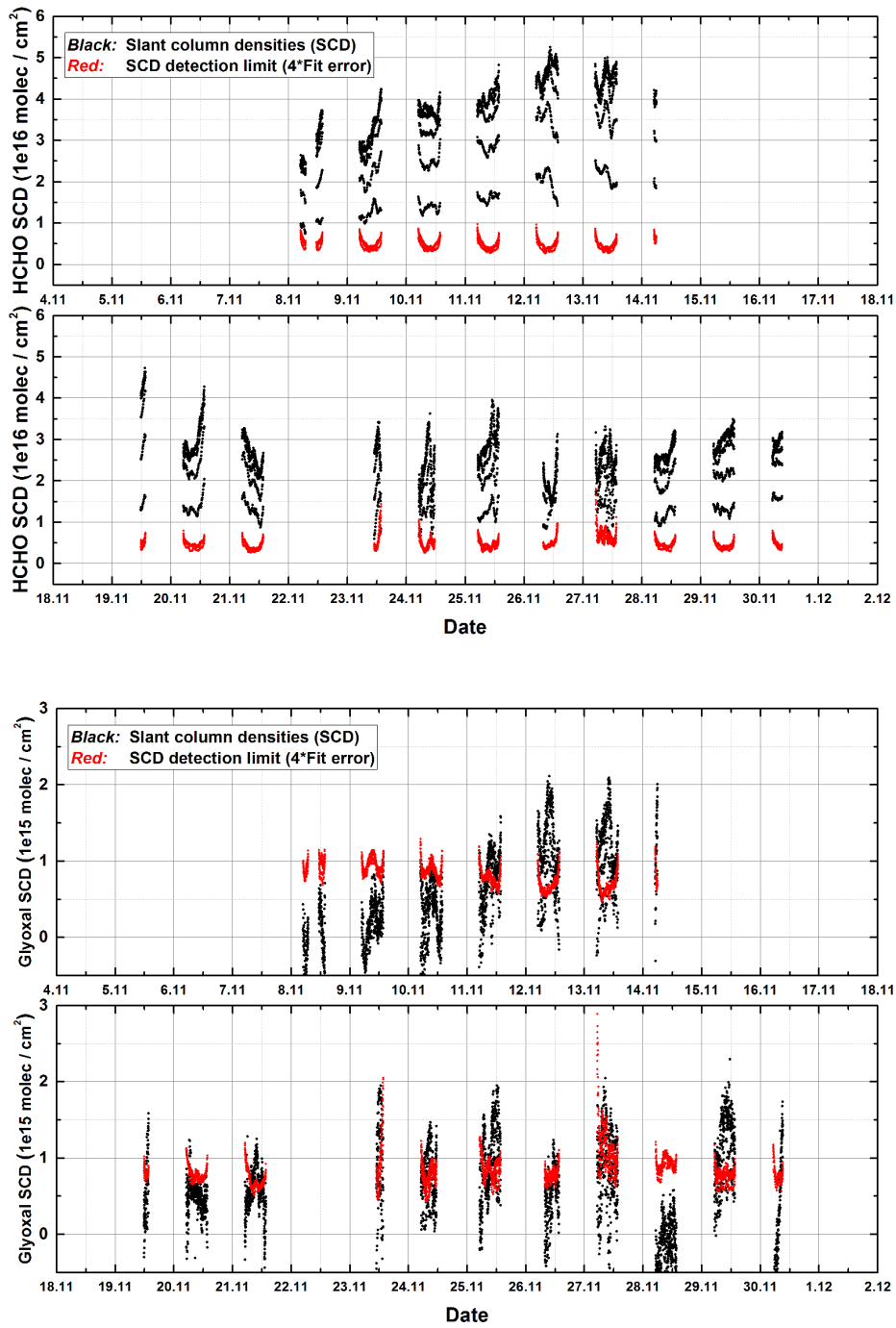
Fig. .19: ISA MAX-DOAS time series of HCHO and Glyoxal SCDs.
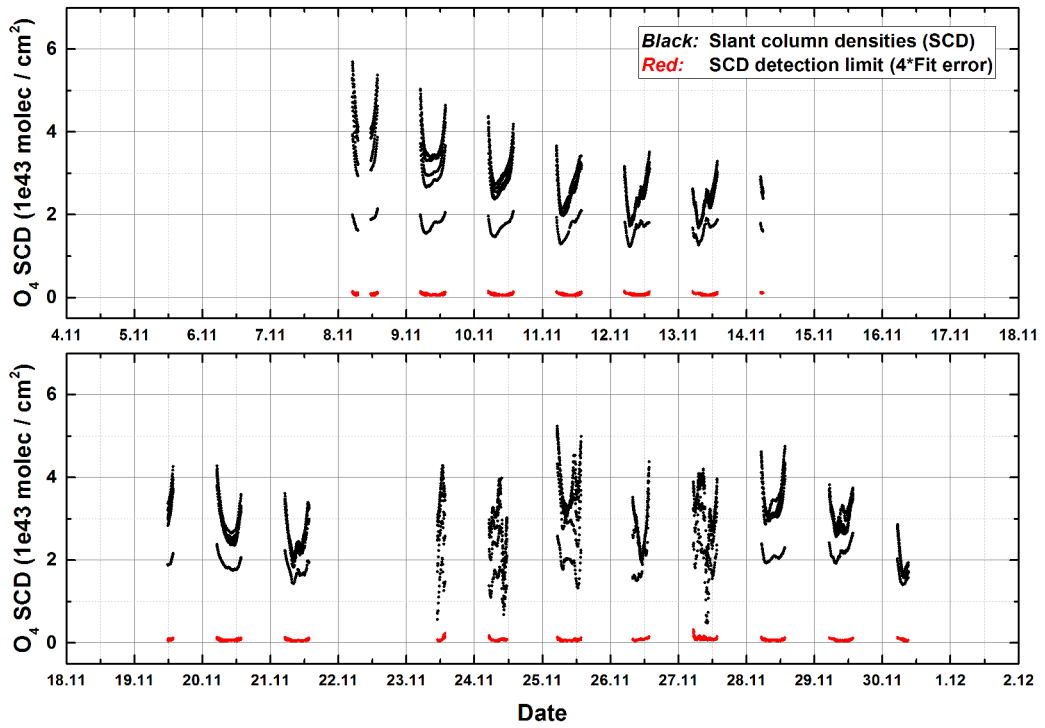
Fig. .20: Masada top MAX-DOAS time series of O4 SCDs.

Acknowledgments

Ganz herzlich danken möchte ich

- Meinem Doktorvater Herrn Prof. Ulrich Platt für die Möglichkeit zur selbstbestimmten Forschung am Toten Meer und vielen anderen Regionen der Welt und das damit verbundene Vertrauen in die eigene Arbeit. Desweiteren für die inspirierende Begeisterung für physikalische und technische Probleme aller Art.

- Herrn Prof. Bernd Jähne, für die Übernahme des Zweitgutachtens.

- Johannes Zielcke für die MAX-DOAS Sensitivitätsstudien, den gemeinsamen Kampf mit dem hauseigenen Inversionsalgorithmus und die Diskussionen zwischen Wahnsinn und Wissenschaft, ich hoffe auf weitere Zusammenarbeit!

- Jutta Zingler für die Unterstützung während der Kampagne am Toten Meer.

- Udo für die Motivation und Unterstützung beim Schreiben von Anträgen.

- Denis und Martin für den stüdigen Instrumentellen Support während der etlichen Messkampagnen in Israel, Irland und Bayreuth

- Robert und Kathi für die entspannte Zusammenarbeit und den Humor während der Messkampagne 2012 am Toten Meer

- Lennard für die Zeit am Toten Meer 2014, was für ein Trip (Put the lime in the coconut!)